Surface and interface contributions to III-V/Si hetero-epitaxial growth : Theory and Experiments

Ida Lucci

UNIVERSITE MATIERE BRETAGNE MOLECULES LOIRE ET MATERIAUX

INSA RENNES

THESE DE DOCTORAT DE

L'INSTITUT NATIONAL DES SCIENCES APPLIQUEES RENNES
COMUE UNIVERSITE BRETAGNE LOIRE

ECOLE DOCTORALE N° 596
Matière, Molécules, Matériaux
Spécialité : « science des matériaux»

Par

« Ida LUCCI »

« Surface and interface contributions to III-V/Si hetero-epitaxial growth: Theory and Experiments »

Thèse présentée et soutenue à « l'INSA de Rennes », le « 26/02/2019»
Unité de recherche : INSTITUT FOTON (UMR 6082 / CNRS)
Thèse N° : 19ISAR 02 / D19 - 02

Rapporteurs avant soutenance :

Pierre MULLER
Professeur, CINaM, Université d'Aix Marseille
Magali BENOIT
Directrice de recherche CNRS, CEMES, Toulouse

Composition du Jury :

Président Jean-Christophe HARMAND
Pierre MULLER
Professeur, CINaM, Université d'Aix Marseille / Rapporteur
Magali BENOIT
Directrice de recherche CNRS, CEMES, Toulouse / Rapporteur
Kerstin VOLZ
Professor, Philipps-Universität Marburg / Examinateur
Jean-Christophe HARMAND
Directeur de recherche CNRS, C2N / Examinateur
Charles CORNET
MCF HDR, Institut FOTON, INSA de Rennes / Directeur de thèse
Laurent PEDESSEAU
MCF, Institut FOTON, INSA de Rennes / Co-encadrant de thèse
Pascal TURBAN
MCF, IPR, Université de Rennes 1 / Co-encadrant de thèse

UNIVERSITE MATIERE BRETAGNE MOLECULES LOIRE ET MATERIAUX

INSA RENNES

Intitulé de la thèse :

Surface and interface contributions to III-V/Si hetero-epitaxial growth: Theory and Experiments

Ida LUCCI

En partenariat avec :

A mio marito Fabrizio, la mia forza.

A Zizzi, so che saresti stata fiera di me.

Acknowledgements

First of all, I want to thank my thesis supervisors Charles Cornet, Laurent Pedesseau and Pascal Turban for giving me the chance to pursue my Ph.D. as part of the ANTIPODE project.

I felt very lucky to be advised and supported by Charles during these years. Thanks to his advice I was able to get through the many difficulties encountered during my Ph.D. I really appreciated his availability for helping me when needed and his ability to transfer to me his knowledge.

Thanks to Laurent, for always supporting me and also for introducing me to the Density Functional Theory (DFT) world. Without his support, I would not have been able to overcome the complex calculations-related obstacles I went through during my Ph.D.

Thanks to both of you for your suggestions, all the meetings (with a lot of good laughs too). This experience will be a solid starting point for a new exciting chapter of my life.

Thanks to Pascal Turban and my colleague Simon Charbonnier for their useful contributions to my Ph.D. work.

Thanks to the committee members Jean-Christophe Harmand, Magali Benoit, Pierre Muller and Kerstin Volz for their questions and suggestions for improving my thesis work.

Thanks to all the members of the ANTIPODE project I worked with. It was a pleasure for me to meet you and share each time ideas to advance my research. In particular, I want to thank Anne Ponchet who gave me precious advice for improving my thesis work results.

I want to thank also Rozenn Gautheron-Bernanrd for the help and everything you taught me during the experimental part of my work. I felt very lucky to have the chance to work with you. I learned how important is to work with people who transmit their curiosity, their passion for learning and their creativity. You have definitely been one of them for me.

I want to thank Thomas for the nice talks about football and do not forget always FORZA NAPOLI!. I also want to thank Isabelle and Alexandrine for having shared some really funny moments together which made easier for me to spend hard work days in the lab.

I want to thank all my colleagues Gaelle, Alejandro, Daniel, Tore and Michael for the nice time together and in particular I want to thank Ronan, the best colleague for sharing the office with. We helped each other, we shared ideas and we also spent funny moments together. Thank you for having been a friend more than a simple colleague at work.

Finally, I want to thank all the Foton institute members for the nicest work environment where I could have ever spent four years of my life starting with an internship and finishing as a Dr.

Now it's time to switch in Italian for my family and my Italian family in Rennes.

Grazie ai miei genitori e mia sorella sempre pronti a supportarmi durante tutti i miei traguardi raggiunti nonostante la lontananza e grazie per il loro amore incondizionato. Grazie ai miei

genitori per essermi stati vicino in un giorno cosi speciale e a mia sorella che è riuscita ad essere presente nonostante non abbia potuto raggiungermi a Rennes.

Grazie alla mia amica Lavinia per aver sempre creduto in me.

Grazie a tutti gli amici di Rennes. In particolare, Arianna, Claudia e Melania con le quali ho condiviso tante risate e tanto affetto riuscendo a formare un legame speciale in così poco tempo. Grazie a Khaled e Francesca per avermi fatto rivivere momenti di spensieratezza donandomi attimi di pausa dal duro lavoro. Grazie ad Elena e Raimondo per tutte le serate in super stile italiano (soprattutto per le pizze). Grazie per la vostra continua disponibilità, siete delle persone speciali. Un grazie particolare va alla mia piccola famiglia di Rennes (o meglio il "Gruppo unito") Steph, Riccardo, Rosa e Fausta. Loro, il mio anti-stress. Grazie per tutti i bellissimi momenti insieme.

Voglio infine ringraziare mio marito Fabrizio, la mia forza e la mia ispirazione. E' anche grazie a lui se sono arrivata fin qui. Lui che mi è accanto da 12 anni e che mi ha sempre supportata. Grazie per essermi stato sempre vicino, per credere in me e nelle mie potenzialità.

E' stata una bellissima esperienza.

Grazie, merci à tous!

Table of contents

General introduction

Silicon photonics, which consists in the integration of photonic components and circuits on Silicon On Insulator (SOI) wafers, comes from the idea of applying the benefits of low-cost silicon manufacturing to photonics. It also aims to overcome the electrical interconnections limits by on-chip and intra-chip high speed optical communications. Since the pioneering work of Soref *et al.* in 1985 [1], the silicon photonics researches have been boosted with the realization of many integrated photonic devices, such as modulators or photodetectors. A major advance in the CMOS integrated nanophotonic technology was reported in 2012 by IBM, integrating side-by-side in a 90nm fabrication process electrical and optical components [2]. So far, the integration of lasers on chip is still a challenge. Nevertheless, in the context of the photonics integrated on chip, the III-V on Si co-integration is a strategy proposed to improve the photonic devices performances [3]. Indeed, it combines the good optical properties of III-V semiconductors with the mature silicon technology [4]. Especially, the monolithic approach is a very promising integration technique, as reminded in 2018 by INTEL (ECOC conference). Indeed, it allows the direct growth of III-Vs on silicon in a "front-end" scheme with the advantage to be compatible with very large scale integration (VLSI) applications [4]. Nevertheless, it has to face different challenges such as defects formation due to the III-V/Si lattice mismatch, or the formation of antiphase domains (APDs) due to the epitaxial growth of polar-III-Vs on non-polar silicon [5]. Thus, even if III-V/Si templates are already commercially available at the NAsP for instance [6] the control and understanding of defects generation and propagation at the early stage of III-V/Si growth is a subject of interest for a lot of research groups.

This thesis is part of the "Advanced aNalysis of III-V/Si nucleaTIon for highly integrated PhOtonic Devices" (ANTIPODE) project (supported by the French National Research Agency – Grant No. 14-CE26-0014-01), which aims to deeply understand what happens during the initiation step of the III-V epitaxy on Si. Especially, it should clarify the interplay between 3D-growth mode, strain relaxation and APDs generation. Thus, the ANTIPODE project main objectives are the understanding of: (i) the 3D nucleation mechanism of III-V semiconductors on silicon (including generation of defects during coalescence) and the associated strain

relaxation mechanisms (ii) the nature and role of the interfacial charges on the growth and defects generation (iii) the influence of the initial silicon surface.

In the context of the ANTIPODE project, this thesis focuses especially on the GaP on Si 3D-growth. Such a system, because of its low lattice mismatch (0.3%), is interesting for photonics and photovoltaic applications [7]–[9]. Nevertheless, antiphase domains are a big issue limiting the GaP-based devices performances [5], [9]–[12]. Thus, the thesis aims i) to determine, by density functional theory (DFT) calculations, the absolute surface and interface energies in the GaP/Si materials system, ii) to understand their role in the GaP/Si 3D-growth mode and iii) to compare these energy values with other III-V-based on Si systems. Finally, it aims to study experimentally the silicon surface structure for subsequent III-V overgrowth.

Dissertation overview:

Chapter 1 presents the state-of-art of different III-V on Si integration approaches and photonic and photovoltaic devices developed through the different integration techniques. The monolithic integration of III-V semiconductors on Silicon and its challenges (such as lattice mismatch and defects formation) are presented. Finally, a particular attention is given to the antiphase domains showing the works performed by different research groups to try to control or annihilate them.

Chapter 2 presents the atomistic simulations performed by DFT to determine the absolute surface and interface energies of the GaP/Si(001) system. Si(001) surface energies are first determined. Then, GaP non-polar (001) and polar (114) and (136) surface energies are computed. Finally, both abrupt and compensated absolute GaP/Si interface energies are determined.

Chapter 3 aims to clarify the main steps at the very early stage of the III-V on Si growth. For this reason, three different III-V/Si materials systems presenting 3D-monodomain islands morphologies are first studied. The GaP/Si wetting properties are investigated on the basis of surface and interface energies determined by DFT calculations over the full range of phosphorus chemical potential, as showed in Chapter 2. The contributions of these energies and of the elastic relaxation of strain, to free energy change during the III-V/Si epitaxy are compared.

Finally, the main steps of the III-V/Si 3D-growth and the defects generation by coalescence are clarified.

Chapter 4 focuses on finding experimentally new strategies for developing a Si(001) surface compatible with III-V overgrowth. Thus, we investigate strategies to control the silicon surface steps organization and to protect the silicon surface from contaminants. Different growth parameters are varied for achieving a monodomain silicon surface on nominal and vicinal Si(001) substrates. Furthermore, GaP samples were grown on the same silicon substrate to study the efficiency of a thin AlGaP marker layers to control APDs vertical propagation. Finally, preliminary results on the electrical properties of antiphase boundaries are presented.

Chapter 5 focuses on the context of energy conversion applications such as the photoelectrochemical (PEC) water splitting. Indeed, the formation by surface energy engineering of textured GaP templates, monolithically grown on Si, is investigated. This study is supported by experimental results and DFT calculations presented in Chapter 2. The advantages of using such a textured surface in the PEC water splitting application are also discussed.

References

[1] R. A. Soref and J. P. Lorenzo, 'Single-crystal silicon: a new material for 1.3 and 1.6 µm integrated-optical components', *Electronics Letters*, vol. 21, no. 21, pp. 953–954, Oct. 1985.

[2] S. Assefa *et al.*, 'A 90nm CMOS integrated Nano-Photonics technology for 25Gbps WDM optical communications applications', in *Electron Devices Meeting (IEDM), 2012 IEEE International*, 2012, pp. 33.8.1-33.8.3.

[3] D. T. Spencer *et al.*, 'An optical-frequency synthesizer using integrated photonics.', *Nature*, vol. 557, no. 7703, pp. 81–85, May 2018.

[4] C. Cornet, Y. Léger, and C. Robert, *Integrated Lasers on Silicon*. ISTE-Elsevier, 2016.

[5] H. Kroemer, 'Polar-on-nonpolar epitaxy', *J. Cryst. Growth*, vol. 81, no. 1–4, pp. 193–204, Feb. 1987.

[6] 'About us - NAsP'. [Online]. Available: https://www.nasp.de/about_us.html.

[7] E. E. Barton, D. M. Rampulla, and A. B. Bocarsly, 'Selective Solar-Driven Reduction of CO2 to Methanol Using a Catalyzed p-GaP Based Photoelectrochemical Cell', *J. Am. Chem. Soc.*, vol. 130, no. 20, pp. 6342–6344, mai 2008.

[8] O. Supplie, M. M. May, H. Stange, C. Höhn, H.-J. Lewerenz, and T. Hannappel, 'Materials for light-induced water splitting: In situ controlled surface preparation of GaPN epilayers grown lattice-matched on Si(100)', *Journal of Applied Physics*, vol. 115, no. 11, p. 113509, Mar. 2014.

[9] K. Volz *et al.*, 'GaP-nucleation on exact Si (0 0 1) substrates for III/V device integration', *Journal of Crystal Growth*, vol. 315, no. 1, pp. 37–47, Jan. 2011.
[10] A. C. Lin, M. M. Fejer, and J. S. Harris, 'Antiphase domain annihilation during growth of GaP on Si by molecular beam epitaxy', *Journal of Crystal Growth*, vol. 363, pp. 258–263, Jan. 2013.
[11] E. Tea *et al.*, 'Theoretical study of optical properties of anti phase domains in GaP', *Journal of Applied Physics*, vol. 115, no. 6, p. 063502, Feb. 2014.
[12] O. Supplie *et al.*, 'Atomic scale analysis of the GaP/Si(100) heterointerface by in situ reflection anisotropy spectroscopy and ab initio density functional theory', *Phys. Rev. B*, vol. 90, no. 23, p. 235301, décembre 2014.

Chapter 1 : III-V on silicon for photonics and energy applications

In the following chapter we provide an overview of the III-V on Si devices developed so far through different integration techniques. To this aim, we first explain the interest in growing III-V semiconductors on Si. Then, we explain the different integration approaches which are hybrid and monolithic. Finally, we will thoroughly describe the main challenges of the monolithic integration approach due to crystal defects at the III-V/Si interface that can deteriorate the device performances.

1.1.Silicon: a material with limited optical properties

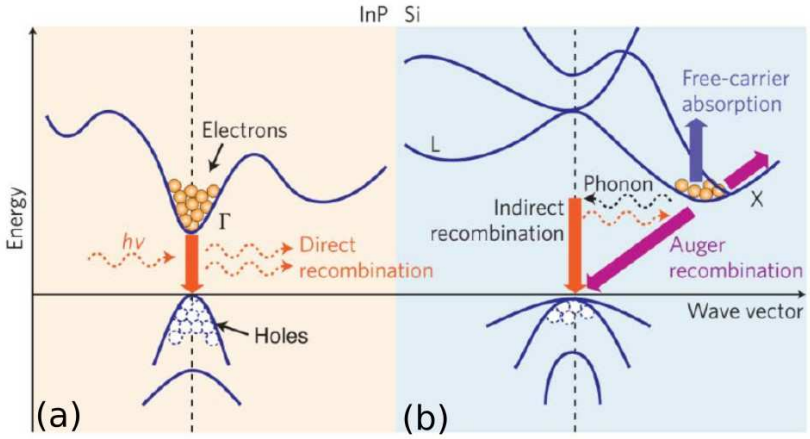

Figure 1.1 Energy bandgap diagram of (a) direct bandgap semiconductors, *e.g.* InP semiconductor, where electrons-holes recombinations take place transferring the energy to emitted photons (b) indirect semiconductors, *e.g.* Si semiconductor, where the little photon emission is a result of the co-existence of electrons-holes recombinations, assisted by the absorption or emission of phonons, together with Auger recominations. Courtesy of [1]

The main reason why silicon is not a good light emitter material is because of its electronic structure which features an indirect band gap, leading to inefficient radiative recombination. Indeed, light emission happens when an electron from an excited state moves

to a lower energy state, in other words, it radiatively recombines with a hole by emitting a photon. It happens in direct bandgap semiconductors, where the lower energy level of the conduction band and the higher energy level of the valence band correspond to the same wave vector value. It is called zero momentum Γ point. Instead, for indirect bandgap semiconductors, the probability that recombination happens is very low because it requires a phonon-assisted transition in order to satisfy the momentum conservation as shown in **Figure 1.1**. It is the case of silicon, where the X valley, which corresponds to the lowest energy of the conduction band, is not aligned with the Γ point corresponding to the maximum energy of the valence band. This results in a poor internal quantum efficiency of light emission in Si and also, in limited optical absorption properties. In contrast to silicon, many III-V compounds are direct band-gap semiconductors such as GaAs, or InP. This physical property of semiconductors is a main concern for different applications. Indeed, in the general context of integrated photonics on chip, the silicon material cannot be used to develop an efficient laser source, while III-V semiconductors are the materials of choice.

For photovoltaic applications crystalline silicon is also not the most efficient material due to its indirect bandgap that provides, in addiction to slow recombination and a long charge carrier lifetime, low absorption properties. Nevertheless, high efficiency silicon based solar cells have been developed, with 26.7% record efficiency achieved by Kaneka in early 2017, see ref. [2] and references therein for instance. On the other hand, the III-V direct bandgap is translated into a very short absorption distance and high photocurrent. Moreover, the III-V compounds bandgap can be tuned to improve the solar cells quality. Efficiency up to 46% for III-V multijunction concentrator solar cells has been recently achieved [3], [4]. Nevertheless, their high costs limit their applications. Thus, III-V on Si integrated solar cells have been studied in order to drastically lower the costs while achieving a comparable efficiency [5]–[7]. Thus, many research efforts were given in the last 20 years on the integration of III-V semiconductors on Si substrate.

1.2.III-V/SI integration approaches

Many different strategies were used to co-integrate III-V semiconductors and silicon in the field of photonics and energy. To illustrate this idea, we will here show some of the advanced integration strategies that have been developed in the field of on-chip integration of photonics. In order to combine the high technology of silicon-based integrated circuits (ICs) with III-V-based components realizing photonics integrated circuits (PICs) on silicon, different integration schemes have been developed. Three of them are: front-side, front-end and back-side. They are shown in **Figure 1.2**

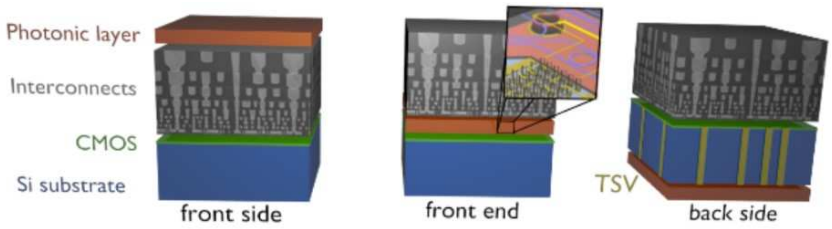

Figure 1.2 Three schemes to integrate photonic layer and CMOS technology. Courtesy of [8]

In the front-side scheme, the photonic devices are embedded in the last level of the metallization pattern of the complementary metal-oxide semiconductors (CMOS) fabrication process. This scheme enables off-chip optical communications. Nevertheless, beside the additional costs needed to introduce some modifications to the CMOS fab-line, it may reduce the thermal budget of the electronics due to the additional layer added on the top thermal path [8], [9]. The back-side scheme, proposed in the pHotonics ELectronics functional Integration on CMOS (HELIOS) project [10], consists in integrating the photonic devices on the substrate backside. The connections between CMOS and photonic layer are achieved by through-silicon-vias (TSV). In both the approaches explained above, the electronic and photonic parts can be processed independently. The front-end scheme allows the fastest connection between the photonic components and CMOS technology due to their vicinity. This scheme was realized by Luxtera [11], MIT [12] and IBM [13]. In this case, all components are fabricated at the same time. Thus, it increases the process complexity.

For each strategy, basically two integration paths may be considered. The hybrid one, which consists in “sticking” or “bonding” optical layers or devices directly on the silicon chip, or

the monolithic one, which consists in growing epitaxially photonic devices on the silicon, and process it afterwards to define the photonic layer. In particular, front-side and back-side schemes are compatible with hybrid integration while the front-end scheme is more adapted to the monolithic integration approach. The principle of hybrid and monolithic integration approaches will be described in the next sections.

1.2.1. Hybrid integration

The hybrid approach consists in bonding the III-V semiconductors on Si or Silicon On Insulator (SOI) platforms (at the wafer or die level). The bonding process can be achieved by direct bonding (molecular-assisted), adhesive bonding (polymer-assisted) or metal-assisted bonding.

The molecular-assisted bonding is based on Van der Walls intermolecular forces and hydrogen bonds. A proper surface cleaning, before the bonding process, is necessary for promoting a flat and clean substrate in order to have a high-quality III-V on Si interface. Then, the surface is chemically treated to be either hydrophobic (-H terminated) or hydrophilic (-OH terminated). After that, the bonding process occurs. The two wafers are bonded via hydrogen bonds independently of the kind of surface treatment. Finally, thermal annealing permits to strengthen the bonding in order to achieve stable and permanent bonds at the interface [8].

In 2006 A. W. Fang *et al.* of the Bowers group [14] realized a hybrid laser where the III-V quantum wells (QWs) layers are connected to the SOI waveguides by O_2 plasma-assisted molecular bonding. The system is based on an evanescent coupling where the optical mode is mainly confined in the SOI waveguide (75%) and interacts just for a few percentage (3%) with the III-V semiconductor layers [14]. The device scheme is shown in **Figure 1.3**. This continuous wave laser presents, at room temperature, a threshold current of 65mA and an output power on the order 1.8mW [14]. The same group improved the device performances by reducing of 30%-40% the threshold current density and threshold voltage. Moreover, they showed that the overlap of the optical mode with the III-V QWs layer can be tailored as a function of the waveguide dimensions [15].

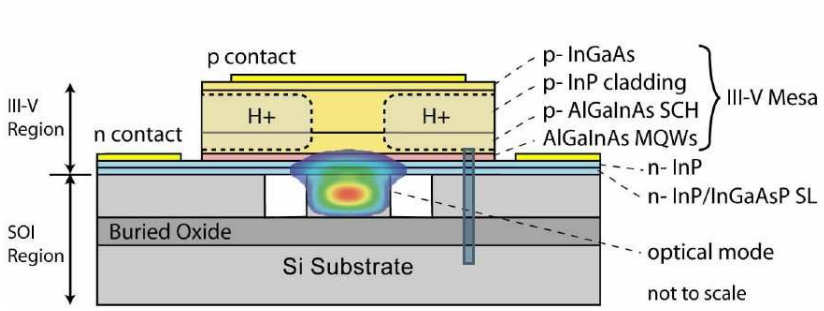

Figure 1.3 Schematic drawing of the hybrid laser structure developed by Bowers group. Courtesy of [14]

Another kind of hybrid integration is the polymer-assisted bonding or adhesive bonding. This technique is less limiting with respect to the molecular bonding, on the surface roughness. Nevertheless, the surface cleaning is always the first step before the bonding process. Benzocyclobutene (BCB) is a typical polymer used for achieving the bonding. It is first spin-coated on the SOI wafer then, it is baked at 150°C to evaporate the solvent. Indeed, it is applied to the wafer, before the spin-coating, to improve the adhesion of the polymer. After the BCB polymerization, the structure is cooled down to form a solid well-bonded device [8]. A Fabry-Pérot cavity laser based on this approach, was realized by IMEC-Ghent University group in 2006 [16] (**Figure 1.4**). As in the case mentioned above [14], the optical mode is mainly present in the Si waveguide. Moreover, 300nm-thick BCB connects the III-V layers to the inverted tapered SOI waveguide where light coupling occurs. The device presented a high threshold current (150mA) in a pulsed mode. One of the reasons of this high value was the high thickness of the BCB layer [16]. Stankovic *et al.*[17], [18] improved the system by realizing a Fabry-Pérot laser bonded to the Si substrate through a thinner adhesive BCB (40-50nm).

The heterogeneous bonding is another example of hybrid integration. It differs from the structures presented just above, because of the optical mode which is mainly confined in the III-V layers. Lamponi *et al.*[19] first presented such a laser by realizing a InP/SOI laser integrated by adhesive bonding approach. It presents a threshold current of 30mA at 20°C and a maximum output power of 4mW [19], [20]. The novelty of the system is the development of a double tapered region which enhances the coupling efficiency of nearly 95% [20]. The scheme is presented in **Figure 1.5(a)**. Another laser structure (**Figure 1.5(b)**) based on the heterogeneous

approach is the microdisk integrated on the SOI waveguide either by molecular or polymer-assisted bonding [21]. The III-V microdisk experiences a whispery gallery mode which is evanescently coupled to the SOI waveguide. Their shallow threshold current (0.45mA achievable with a diameter of 7.5µm) [23] and their compact size make the microdisk lasers very promising for on-chip interactions [23], [24].

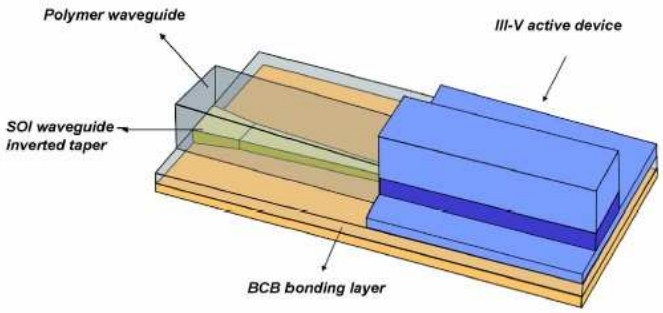

Figure 1.4 Scheme of the Fabry-Perot laser adhesive bonded to the SOI waveguide. Realized by the IMEC-Ghent University group [16]

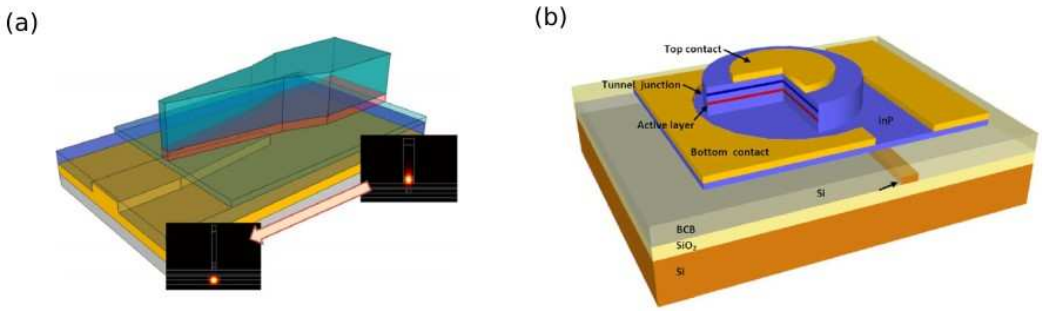

Figure 1.5 Heterogeneous integration based devices: (a) scheme of InP double tapered laser developed by Lamponi *et al.*[19] (b) scheme of a InP microdisk presented by [22]

The last approach presented in this paragraph is the metallic bonding strategy which consists in using a metal alloy with a specific eutectic point. The metal alloy is deposited on the wafers and it melts when the system is heated up at a temperature greater than the eutectic

one. Once melted, the metal will cover all the bonding area and when the temperature is cooled down, a strong bond is realized through its solidification. The metal alloy choice depends on different factors such as its eutectic point, the thermal expansion coefficient of the III-V semiconductors and the thermal budget of the bonding post-processing steps. Lasers structures based on this approach were proposed in [25]–[27].

In the field of photovoltaics, high efficiencies have been achieved through wafer bonded III-V/Si solar cells, such as 32% being the current record for Si-based two-junctions solar cells and 35.9% for three junctions III-V//Si solar cells under one-sun illumination fabricated by NREL and CSEM [6] while 33% for a two-terminal III-V//Si triple-junction cell under 1-sun AM1.5G was recently obtained in [5]. Instead, FhG-ISE, SOITEC, CEA-LETI [3] jointly developed a four-junction solar cell, obtained growing a GaInP/GaAs//GaInAsP/GaInAs cell on InP substrate, with a record efficiency of 46% at 312*x*AM1.5d.

1.2.2. Monolithic integration

The monolithic integration consists in growing the III-V semiconductors directly on Si substrate. This approach has different advantages with respect to the hybrid one, such as low fabrication costs and time. It also enables the very large scale integration of III-V devices on Si which cannot be achieved through the hybrid integration. Nevertheless, the primary challenge is to reach a high III-V/Si interface crystal quality. In the plot of **Figure 1.6** the bandgap energies of different III-Vs are presented as a function of their lattice constant. It shows that III-V alloys such as GaAs, GaSb or InP, typically used in this approach, have a direct bandgap but a large lattice mismatch to the silicon. It can cause defects formation, decreasing the system efficiency. On the other hand, III-Vs such as AlP or GaP are quasi-lattice-matched to the silicon but, they have an indirect bandgap which can limit as well the device performances. In particular, when growing lattice mismatched III-Vs on Si substrate the integration is called metamorphic, otherwise it is pseudomorphic. These integration approaches and the strategies used to overcome the related growth issues are presented in the following paragraphs.

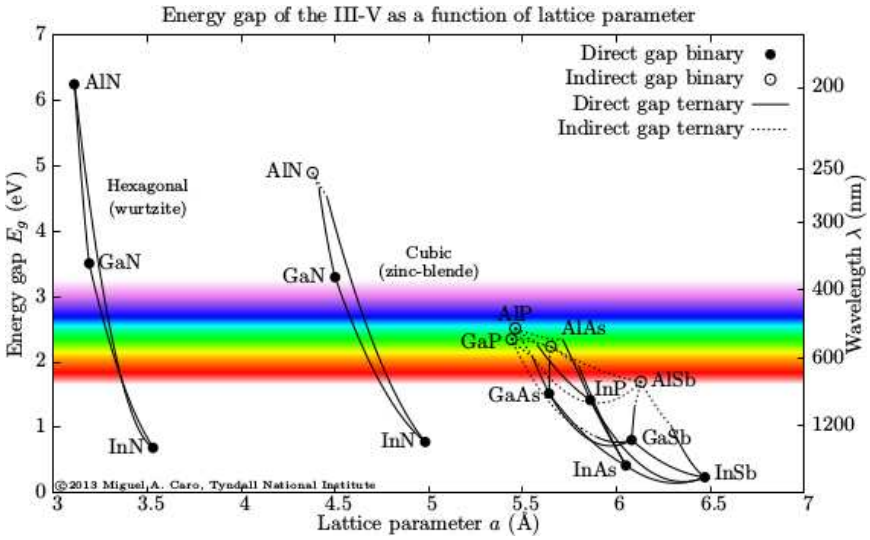

Figure 1.6 Plot of the energy gap as a function of the lattice parameter of binary III-V semiconductors. Courtesy of [28]

1.2.2.1. Metamorphic integration

The metamorphic approach consists in the mismatched epitaxial growth of III-V semiconductors on silicon substrate. The main advantage of III-V semiconductors, such as GaAs or InP, is their low and direct bandgap but, as introduced just above, they present a large lattice mismatch to the silicon. As a consequence the dislocations formation is unavoidable. These defects act as non-radiative recombination centres in the structure. Thus, their density has to be minimized (< 10^4 cm^{-2}) to increase the device performances. **Figure 1.7** shows an example of dislocations distribution in a GaAs on Si epilayer [29].

In order to improve the device performances, tremendous efforts have been done to grow high quality III-V epitaxial layers on Si substrate. One approach consists in the self-organization of dislocations when using for example Sb-based compounds which have a very large lattice mismatch to the Si (such as GaSb 12% or AlSb 13%). Indeed, strain energy due to the large mismatch is immediately relieved into the III-V epilayer by the formation of interfacial misfit dislocations (IMD) arrays [30], [31]. An example is given by the growth of AlSb on Si substrate which results in the formation of planar array of 90 ° misfit dislocations partly confined at the interface as shown in **Figure 1.8**. The very low threading dislocation density

(~7x10^{5}cm^{-2}) achieved though this growth procedure highlights the potential of this approach in the monolithic integration. Kim *et al.* and Akahane *et al.* [32], [33] improved the crystal quality of the GaSb/Si interface by using an AlSb nucleation layer. Indeed, GaSb-based devices have also been realized in [34], [35].

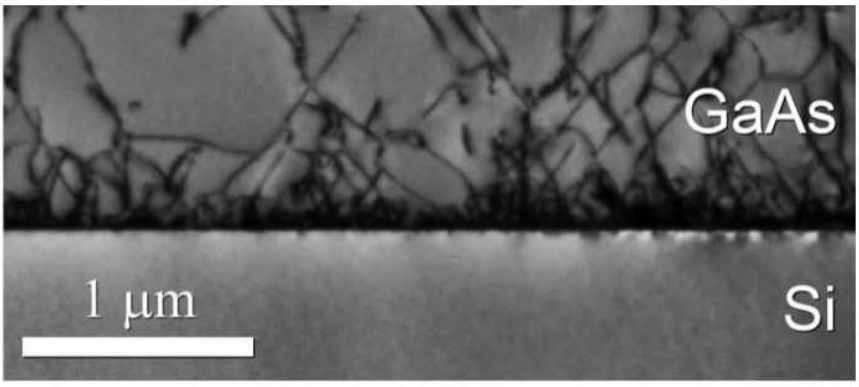

Figure 1.7 Cross-sectional TEM image of dislocations propagating through the GaAs grown on Si. Courtesy of [29]

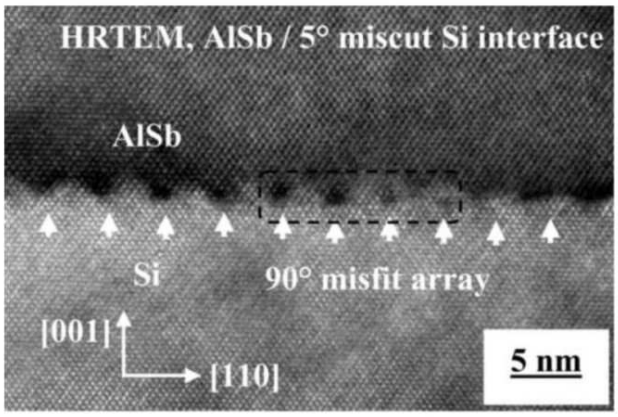

Figure 1.8 Cross-sectional HRTEM image of planar 90° misfit array at the AlSb/Si interface. Courtesy of [30]

Another effective strategy to reduce the threading dislocations is the use of strained layer superlattice (SLS) and short period superlattice (SPL) [36]. The effectiveness of this approach has been demonstrated by growing high quality InGaAs quantum-dots (QDs) on Si

substrate and also by growing InP-on-Si heterostructures [29], [37]. An example of this approach is shown in **Figure 1.9**.

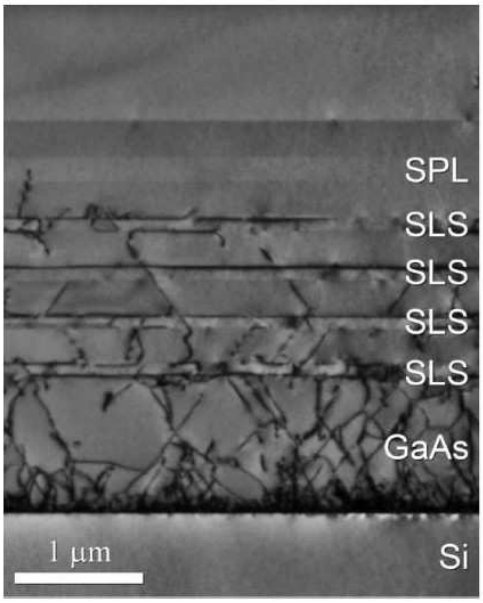

Figure 1.9 Cross-sectional TEM image showing the suppression of threading dislocations through the grow of strained superlattice (SPS) and short period superlattices (SPL). Courtesy of [29]

Another approach highly investigated is the adaptation of the lattice parameter by compositionally graded buffers, such as $Si_xGe_{(1-x)}$/Si pseudo substrate [38] to reduce the dislocation density at the GaAs/Si interface. High performance GaAs-based solar cells [39] and laser structures [40] have been realized. This strategy was also used to grow lattice mismatched $GaAs_{0.7}P_{0.3}$ solar cells on Si substrate [41].

The selective-area-heteroepitaxy is another approach for controlling the propagation of dislocations by using masks which restrict the III-V growth in pre-defined areas. An example is called selective area growth (SAG) where dielectric masks (typically made by SiO_2) are formed by small windows (of the order of dozens to hundreds of nanometres [42]–[44]) at the silicon substrate. The III-V overgrowth will occur in these openings taking advantage of the defect ”necking effect” [45]. It makes dislocations trapped in tranches in between two SiO_2 walls. The effectiveness of this approach is illustrated in **Figure 1.10** where a InP nanolaser has been grown on Si(001) substrate by metal–organic chemical vapor deposition process (MOCVD) [42]. In this

case, the mask is fabricated by deposing, through the Shallow-Trench-Isolation (STI) process, SiO_2 forming 100nm-thick tranches used for the III-V overgrowth. In order to reduce the lattice mismatch related to the III-V on Si deposition, before the overgrowth, a Ge seed layer is grown in the openings on the Si substrate.

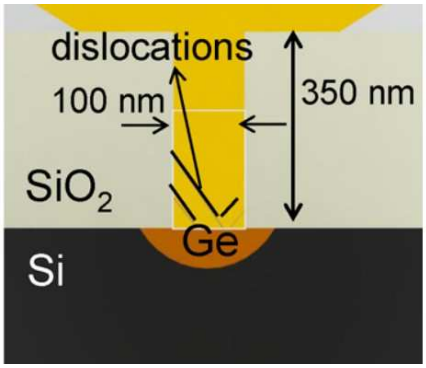

Figure 1.10 Cross-section scheme of the SAG approach used to grow the InP nanolaser to the Si substrate. Courtesy of [42]

Another kind of selective growth, which is considered as a special case of SAG, is the epitaxial lateral overgrowth (ELO). It consists in growing the III-V semiconductors directly on Si substrate. The high density of dislocations (of the order of $10^9 cm^{-2}$ due to the large lattice mismatch [46]) is then filtered by the deposition of a patterned mask whose windows are defined for the subsequent III-V lattice matched epitaxial overgrowth [46], [47]. Smaller is the thickness of the mask windows, less is the chance of the threading dislocations to pass through them, benefiting from the "neckling effect" [45]. An example is the InP ELO on Si using a SiO_2 mask in **Figure 1.11.**

Growing III-V on a V-groove Si(001) substrate has demonstrated its efficiency in the improvement of the GaAs/Si interface quality by reducing the dislocation density and also by growing antiphase domains (APDs)-free III-V layers [48]–[50].

Finally another strategy largely used is the growth of III-V on Si nanowires generally considered to be APDs-free [51]. It consists in growing III-V core-shell nanowires through catalyst–assisted (such as catalyst Au nanoparticles) or a catalyst-free processes [52], [53].

In the photovoltaics context, a quadruple-junctions inverted metamorphic (4J-IMM) solar cell was developed in 2015 by NREL with an efficiency of (43.8 ± 2.2)% at 327-sun concentration [4].

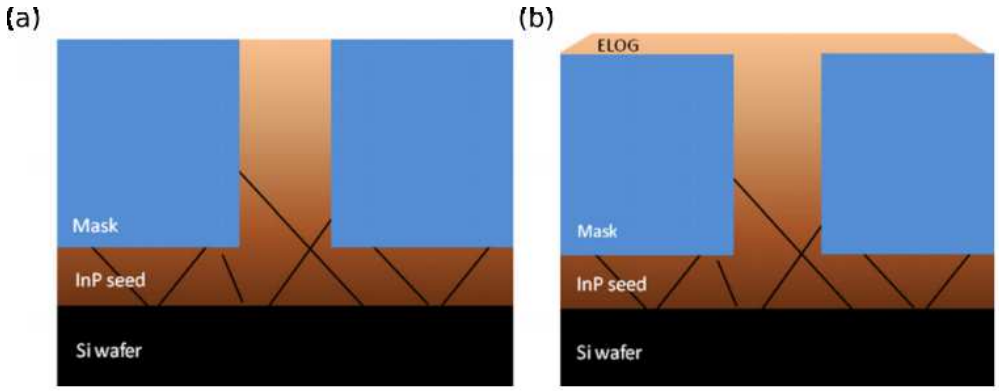

Figure 1.11 Scheme of the ELO growth process of InP layer grown on Si wafer: (a) defect-necking effect and (b) epitaxial lateral overgrowth. Courtesy of [47]

1.2.2.2. Pseudomorphic integration

The pseudomorphic integration consists in growing III-V semiconductors lattice matched on the Si substrate, in order to avoid the formation of misfit dislocations for achieving a perfect crystalline quality. The low lattice mismatch between the III-Vs (such as GaP and AlP) and the silicon surface allows avoiding misfit dislocations formation until a critical thickness of around 100 nm. One of the best candidates for this approach is definitively the GaP. Indeed, thanks to its very low lattice mismatch (0.37%) to the Si, good atoms alignments [54] can be achieved as shown in **Figure 1.12(a)**. By choosing the right growth conditions, it is possible to avoid defects formation such as microtwins (MTs) and to annihilate antiphase domains [55] as shown in **Figure 1.12(b)** where most of the antiphase boundaries (APBs) are annihilated within 10 nm from the GaP/Si interface. Nevertheless, the performances of GaP-based laser devices are limited by the indirect nature of its band structure. Many materials developments were published with the aim of achieving high structural quality. For instance, Takagi *et al.* [56] were able to reduce the defects formation and to improve the surface roughness by migration enhanced epitaxy (MEE). Volz *et al.* [57] were able to grow a defect-free GaP/Si(001) after

almost 50 nm GaP layer thickness. Also, Grassman *et al.* presented a two-step growth process consisting in growing GaP on Si(001) by low temperature MEE followed by molecular beam epitaxy (MBE) [58]. In this way, they were able to achieve a very smooth and defect-free GaP/Si interface. Lasing on Silicon was even demonstrated with GaAsPN quantum wells [59]. In order to overcome the band structure problem, it has been demonstrated that the incorporation of Nitrogen (N) can convert the GaP indirect bandgap into a pseudo direct one. Moreover, by taking advantages from the III-V-N compounds lattice matched to the silicon, dislocation-free III-V-N-based QWs structures, such as $GaAs_yP_{1-x-y}N_x$ /$GaP_{0.98}N_{0.02}$, can be formed with a percentage of N typically less than 3% [60], [61].

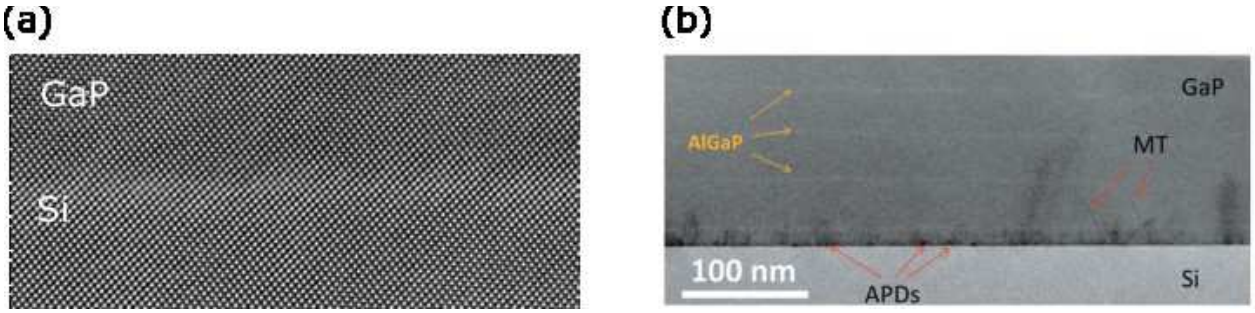

Figure 1.12 Cross-secton (a) HRSTEM-HAADF image of GaP grown on Si hilighting the good atoms alignment at the interface. Courtesy of [54] (b) STEM-BF image hilighting the annihilation of APDs at 10nm from the interface. Courtesy of [55]

1.3.Monolithic integration challenges: III-V/Si interfacial issues

In the monolithic integration context, different materials challenges have to be taken into account during the direct growth of III-Vs on Si substrate in order to reach a III-V/Si high crystal quality interface. In the following paragraphs, they are discussed in details.

1.3.1. Surface preparation

Si substrate surface preparation is important in order to remove any kind of contaminant before the III-V deposition. Indeed, impurities can act as preferential nucleation site resulting in a high defects density in the III-V epilayer. That is why, the Si surface preparation is the first step in the III-V on Si growth process, because it strongly impacts on the III-V/Si interface quality. It

was highlighted in [54]. Basically, two strategies are proposed in the literature: (i) growing homoepitaxially a Si buffer layer to bury the contaminants and promote the step organization, or (ii) chemically prepare the Si substrate to remove contaminants and start the III-V growth in good conditions. The first strategy (silicon homoepitaxial buffers) was adopted by different groups [57], [62] improving III-V structural properties. It provides the ability to get reproducible experimental conditions, and control of the process. In the second strategy, the Si surface can be either oxidized or hydrogenated. Before the III-V growth, O_2 or H_2 can be thermally removed by loading the Si wafer in the growth chamber and heating it up to 900°C and 650°C respectively. This part will be discussed further in Chapter 4.

1.3.2. Lattice mismatch and thermal expansion coefficient

The quality of the monolithic integration of III-V on Si can be limited by the large lattice mismatch and the different thermal expansion coefficients between III-Vs and Si. Indeed, the lattice mismatch is unavoidable in the most commonly used III-V compounds which have a lattice constant significantly different than that of the silicon. The lattice mismatch, f, is defined by the following equation [63]:

$$f = \frac{a_s - a_f}{a_s} \qquad \textbf{(1.1)}$$

Where a_f is the lattice constant of the thin film deposited on a semiconductor substrate with a lattice constant a_s.The strain generated can be accommodated elastically or plastically. For a small lattice mismatch, the elastic energy is stored through a biaxial strain of the epilayer to match the in-plane lattice parameter of the substrate (**Figure 1.13(a)**). The film material is coherently strained to the substrate which means that the lattices planes are continuous at the interface. In this case, the epitaxial film is compressively strained if its lattice constant is larger than that of the substrate, otherwise it is tensily strained. Instead, the plastic relaxation occurs for larger mismatch or thicker epitaxial films (**Figure 1.13(b)**). In the latter case, when the epitaxial film thickness reaches a critical value called “critical thickness”, elastic energy is

released through the creation of the so-called misfit dislocations. The GaP/Si critical thickness estimated to be less than 90nm according to Soga *et al.* [64], between 45-95nm according to Takagi *et al.*[65] and 64nm by Skibitzki *et al.* [66].

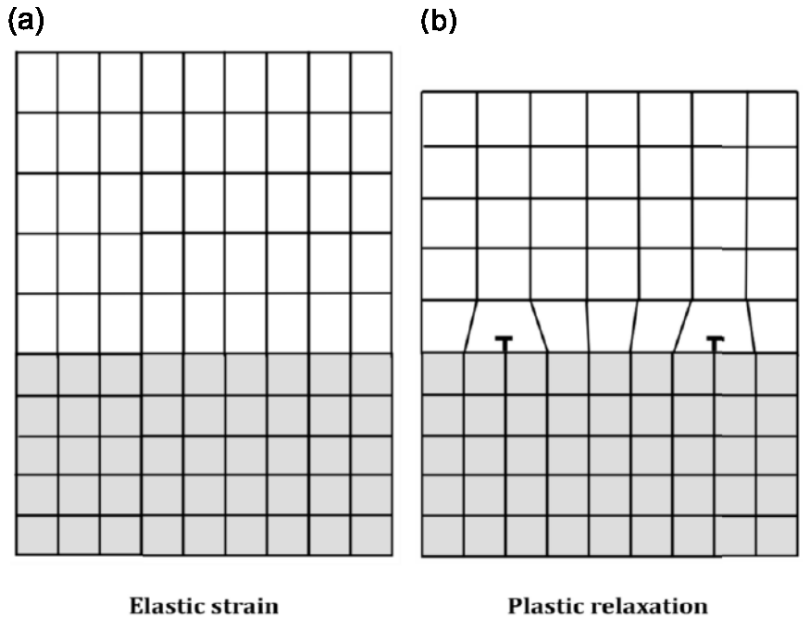

Figure 1.13 Scheme of (a) elastically and (b) plastically strained films in a mismatched semiconductor interface [67]

Furthermore, the lattice constant can vary with the temperature. Thus, another issue that can deteriorate the device performances is the thermal expansion coefficient. It is a property that characterizes each semiconductor and it can be very different from one to another [68]. Microcracks can appear in a III-V semiconductor epilayer if it undergoes to a large tensile or compressive stress due to its temperature related lattice constant change from room temperature to growth temperature (which varies in the range of 350°C to 1000°C). An example is represented by the GaP with a thermal expansion coefficient which is almost the double with respect to that of the silicon (α_{GaP}=4.65 x 10^{-6}/K and α_{Si}=2.4 x 10^{-6}/K). It means that at growth temperature the GaP will be more compressively strained. In particular at 580°C, typical GaP/Si MBE growth temperature, the lattice mismatch is 0.52% while it is 0.36% at room temperature.

1.3.3. 3D-growth

The existence of the heterogeneous III-V on Si 3D growth mode was already suggested in pioneering works such as the one performed by Ernst *et al.* in 1988 [69]. Indeed, different III-V/Si systems experience islands formation at the very early stage of growth. It constitutes a critical issue since it hampers the formation of a very smooth III-V surface at the very beginning of the III-V growth that reduces the hope to reach integration of photonic functions very near the III-V/Si interface. Some examples of III-V on Si 3D islanding are shown in **Figure 1.14**.

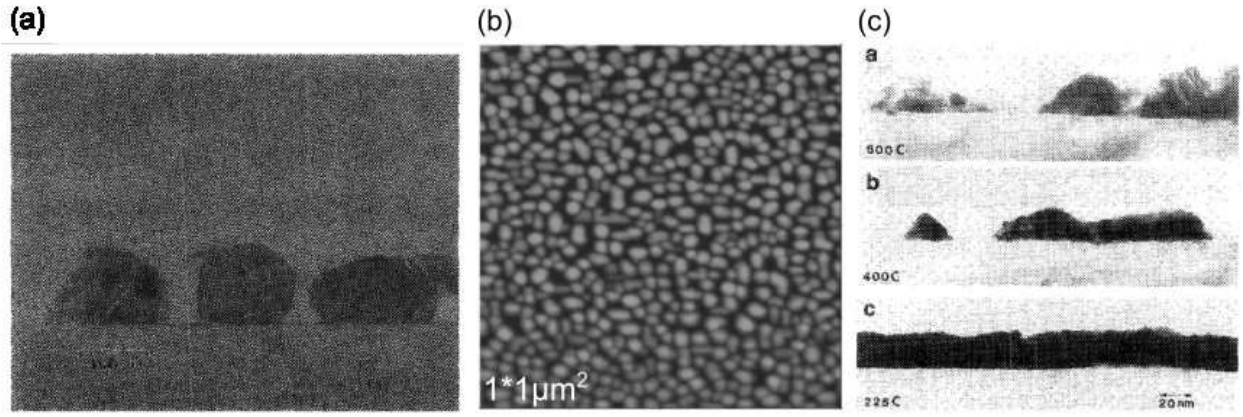

Figure 1.14 3D islands formation in different III-V/Si systems: (a) TEM image of GaP on (001) Si epitaxial growth at the very early stage. Courtesy of [69] (b) AFM image of 3nm-thick AlSb/Si. Courtesy of [32] and (c) TEM image of GaAs/Si. Courtesy of [70]

Islands have been observed in the GaP on Si deposition as it is shown in the transmission elecron microscopy (TEM) image [69] of **Figure 1.14(a)** where the GaP on Si 3D epitaxial growth, at the very early stage, is presented. The atomic force microscopy (AFM) image in **Figure 1.14(b)** shows AlSb/Si 3D growth presented by Akhane *et al.*[32]. Finally, the 3D island was also reported in the GaAs/Si system [70] by TEM in **Figure 1.14(c)**. To avoid this 3D growth mode, low temperature alternated growth techniques were proposed [56]–[58]. In order to improve the III-V on Si interface quality, one must understand what is at the origin of the 3D growth which has been sometimes attributed to strain relaxation processes, since most of III-Vs are lattice mismatched to the Si as in the case of GaAs [71], [72]. This part will be discussed in detail in Chapter 3.

1.3.4. Polar on non-polar epitaxy

When a polar semiconductor such as a III-V compound is heteroepitaxially grown on a non-polar one such as the silicon, some defects can be generated due to the mismatch of their crystal symmetries. They are usually named in the literature stacking faults (SFs), microtwins (MTs) and antiphase domains (APDs).

1.3.4.1. Stacking faults and microtwins

A stacking fault is a planar defect which alters the crystallographic plane order. Indeed, they are found in close-packed structures where atomic layers are arranged in a certain stacking order. Most of the III-V semiconductors crystallize in the zinc-blende structure which is formed by two cubic face centered (cfc) sublattices. Its crystallographic order in the (111) plane is an atomic sequence that can be expressed as a ABCABCABC ordering. Stacking faults are formed when the sequence is altered and it is modified as ABC**AC**ABC or ABC**ABA**BCABC which are called respectively intrinsic or extrinsic stacking faults (**Figure 1.15**). Moreover a stacking fault is

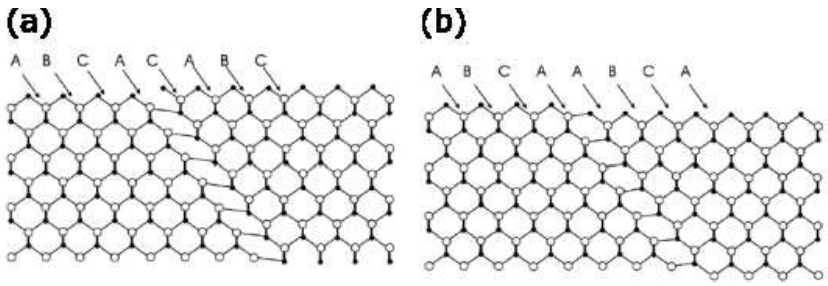

Figure 1.15 Representation of (a) intrinsic (b) extrinsic stacking faults. Courtesy of [73]

bounded by two partial dislocations given by the dissociation of a perfect dislocation (which has a higher energy). If the crystallographic order is changed so that the atoms arrange in a mirror symmetric-like order, the stacking fault formed is called microtwin. The microtwins can be described as a 60° or 180° crystal rotation with respect to the <1 1 1> (**Figure 1.16**).

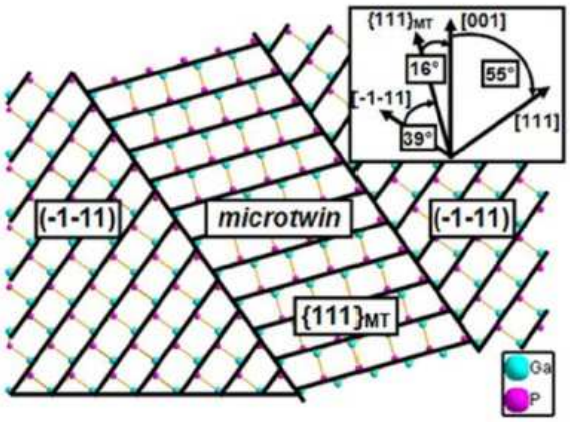

Figure 1.16 Schematic representation of a microtwin model in a zinc-blend GaP structure. Courtesy of [66]

1.3.4.2. Antiphase domains

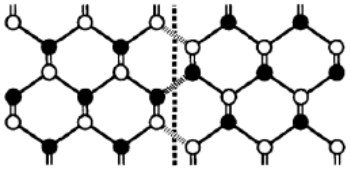

Figure 1.17 Antiphase boundaries represented by the dashed line composed of wrong V-V or III-III bonds. Courtesy of [74]

The III-V zinc blende materials structure is polar which means that each group-III atom is bounded to four group-V atoms, while the Si diamond crystal structure is non-polar, indeed each Si atom is bounded to other four Si atoms. In the polar-on-non-polar epitaxy, antiphase domains can form bounded by antiphase boundaries (APBs). The latter are highlighted by the reversal of the III-V bond polarity (‘‘dumbbells’’) across them. A scheme is presented in **Figure 1.17**. The APDs formation has been generally attributed to two different cases [74]. The first is an uncomplete group-III or group-V coverage of a smooth Si surface that can happen for example during MBE growth processes. In this case, two crystal domains will form having a perpendicular orientation with respect to each other (**Figure 1.18(a)**). The other case is due to single atomic layers on the Si substrate. Indeed, in most cases the silicon surface presents

monoatomic steps which favor the APBs formation. The steps height is equal to $a_0/4$ while in the case of the zinc blende III-V compound, the closest distance between two equal lattice planes is $a_0/2$. That is why, in correspondence of each Si terraces edge, antiphase boundaries can appear and they can propagate through the whole structure degrading the device performances. For this reason, their size control or total suppression have always attracted much attention from different research groups worldwide, since it would be very interesting for various applications such as lasers, photovoltaics and non-linear photonics.

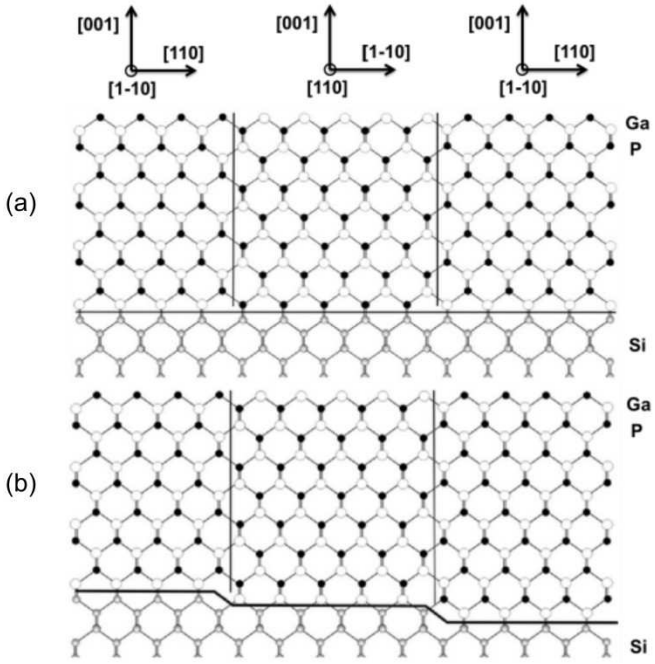

Figure 1.18 Antiphase domains formation due to (a) group-III or group-V incomplete coverage of the Si substrate or (b) single step formation on the Si surface. Courtesy of [73]

Already in the 1987 Kroemer proposed a way to avoid APDs formation which consisted in the use of a bi-step silicon substrate [74]. Since then, it has been considered as the main motivation for using substrates with a miscut, in order to form biatomic steps at the Si surface for the subsequent III-V growth process. In fact, the results presented in Chapter 3 strongly challenge this view. Anyway, much works have been proposed on the control and annihilation of APDs. Indeed, in systems such as the GaP on Si where, thanks to the low lattice mismatch, it is possible to avoid the dislocations formation, different groups still observed APD and have

tried to control them by MBE [75]–[77] and by MOCVD/MOVPE [65], [69], [78]–[81]. We will here limit the discussion to the GaP/Si case, as the absence of misfit dislocations allow ideal electronic microscopy observation conditions of APDs. But this problem is encountered during all III-V/Si semiconductors integration.

In 1997 Takagi *et al.* grew GaP layers on a Si substrate oriented 4° towards the [011] by using MBE and MEE growth techniques. They demonstrated the ability to annihilate the APDs with both processes and in particular they were also able to reduce defects density by MEE [56]. Volz *et al*. [57] have demonstrated the annihilation of APDs during the first 40-50 nm on nominal silicon by MOCVD and are able to provide commercially GaP/Si templates through the NAsP company [82], [83]. Grassman *et al.* [58] used a two-step growth process. They grew GaP on Si(001) 6°-offcut starting by MEE followed by MBE. They obtained a high quality GaP/Si interface without any nucleation-related defect, such as APDs, stacking faults and microtwins. Also, they achieved similar results growing GaP on Si by MOCVD [84]. Harris group annihilated APDs through a MBE-based two-step growth process which consisted in a nucleation step followed by the overgrowth of GaP on Si(001) 4° offcut oriented towards the [110] direction[85], [86]. They also showed how the annihilated APDs size impacts on the surface roughness [85].

At the FOTON institute Y. Ping Wang *et al.* [54] highlighted the importance of the surface cleaning process by showing the resulting GaP on Si very good atoms alignment (**Figure 1.12**). They were also able to annihilate APDs at just 10nm from the GaP/Si interface by using AlGaP markers layers (see **Figure 1.19**) [55], [87].

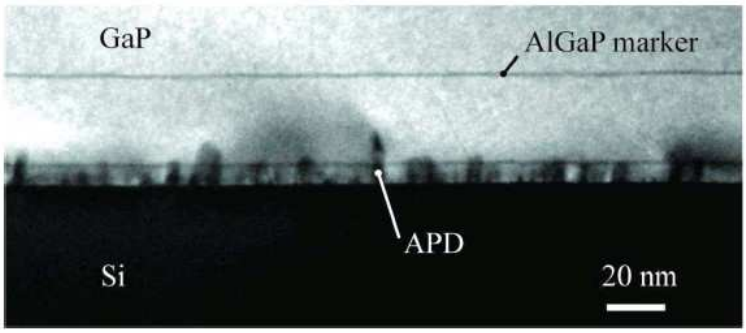

Figure 1.19 Annihilation of domains at 10nm from the GaP/Si interface. Courtesy of [87]

Recently, other groups have shown to improve the GaP on Si quality (using Si 2°, 4° and 6° offcut oriented towards the (111) plane) under AsH_3 flux by MOCVD [88]–[90]. In particular, NREL group demonstrated to obtain a Si surface free from C and O contaminants by annealing under AsH_3. Thanks to this treatment, APDs-free GaP films were grown on As/Si surface without the need of a homo-epitaxial Si buffer layer [88]. A. Navarro *et al.* [90] studied the effect of Si(001) (2°-off) surface annealing under AsH_3 and PH_3 flux, by varying the pre-exposure time and the growth temperature, on 50-nm thick GaP overgrowth. They confirmed to observation of a defect-free GaP layer, when the Si substrate is annealed at high temperature under AsH_3 flux before the III-V overgrowth.

All these work demonstrate that it is possible to achieve a good quality GaP epilayer on the top of the Si substrate. Nevertheless, the total suppression or precise control of APD generation at the early stages of growth has yet to completely be demonstrated. A deep understanding of APDs generation mechanism was not yet given.

1.4.Conclusions

In summary, we have presented different approaches developed to integrate III-Vs on Si for both photonics and photovoltaics. In the latter context, the III-V on Si integration has the aim to reduce the costs related to the III-V multifunction cells production while achieving a comparable efficiency. It also permits to reach a higher efficiency with respect to Si-based solar cells where it is limited to 27%. In the photonics context, the hybrid approach is the most mature to develop lasers on Si. The monolithic approach is compatible with VLSI applications but it faces some challenges related to the materials direct growth on the substrate. The defects related to the mismatched epitaxial growth could be avoided with the pseudomorphic approach. Nevertheless, understanding defects generation and how to control or to suppress it, is still challenging.

References

[1] D. Liang and J. E. Bowers, 'Recent progress in lasers on silicon', *Nat. Photonics*, vol. 4, no. 8, pp. 511–517, août 2010.

[2] K. Yoshikawa *et al.*, 'Silicon heterojunction solar cell with interdigitated back contacts for a photoconversion efficiency over 26%', *Nat. Energy*, vol. 2, no. 5, p. 17032, May 2017.

[3] F. Dimroth *et al.*, 'Four-Junction Wafer-Bonded Concentrator Solar Cells', *IEEE J. Photovolt.*, vol. 6, no. 1, pp. 343–349, Jan. 2016.

[4] R. M. France *et al.*, 'Quadruple-Junction Inverted Metamorphic Concentrator Devices', *IEEE J. Photovolt.*, vol. 5, no. 1, pp. 432–437, Jan. 2015.

[5] R. Cariou *et al.*, 'III–V-on-silicon solar cells reaching 33% photoconversion efficiency in two-terminal configuration', *Nat. Energy*, vol. 3, no. 4, pp. 326–333, Apr. 2018.

[6] S. Essig *et al.*, 'Raising the one-sun conversion efficiency of III–V/Si solar cells to 32.8% for two junctions and 35.9% for three junctions', *Nat. Energy*, vol. 2, no. 9, p. 17144, Sep. 2017.

[7] M. Feifel *et al.*, 'Direct Growth of III–V/Silicon Triple-Junction Solar Cells With 19.7% Efficiency', *IEEE J. Photovolt.*, vol. 8, no. 6, pp. 1590–1595, Nov. 2018.

[8] C. Cornet, Y. Léger, and C. Robert, *Integrated Lasers on Silicon*. Elsevier, 2016.

[9] J. S. Orcutt, R. J. Ram, and V. Stojanović, 'Integration of silicon photonics into electronic processes', in *Silicon Photonics VIII*, 2013, vol. 8629, p. 86290F.

[10] J. M. Fedeli *et al.*, 'Electronic-photonic integration in the helios project', in *10th International Conference on Group IV Photonics*, 2013, pp. 146–147.

[11] C. Kopp *et al.*, 'Silicon Photonic Circuits: On-CMOS Integration, Fiber Optical Coupling, and Packaging', *IEEE J. Sel. Top. Quantum Electron.*, vol. 17, no. 3, pp. 498–509, mai 2011.

[12] J. S. Orcutt, R. J. Ram, and V. Stojanović, 'Integration of silicon photonics into electronic processes', 2013, vol. 8629, pp. 86290F-86290F–12.

[13] S. Assefa *et al.*, 'A 90nm CMOS integrated Nano-Photonics technology for 25Gbps WDM optical communications applications', in *2012 International Electron Devices Meeting*, 2012, pp. 33.8.1-33.8.3.

[14] A. W. Fang, H. Park, O. Cohen, R. Jones, M. J. Paniccia, and J. E. Bowers, 'Electrically pumped hybrid AlGaInAs-silicon evanescent laser', *Opt. Express*, vol. 14, no. 20, pp. 9203–9210, Oct. 2006.

[15] M. J. . Heck *et al.*, 'Hybrid Silicon Photonics for Optical Interconnects', *IEEE J. Sel. Top. Quantum Electron.*, vol. 17, no. 2, pp. 333–346, Apr. 2011.

[16] G. Roelkens, D. V. Thourhout, R. Baets, R. Nötzel, and M. Smit, 'Laser emission and photodetection in an InP/InGaAsP layer integrated on and coupled to a Silicon-on-Insulator waveguide circuit', *Opt. Express*, vol. 14, no. 18, pp. 8154–8159, Sep. 2006.

[17] S. Stankovic, R. Jones, M. N. Sysak, J. M. Heck, G. Roelkens, and D. V. Thourhout, '1310-nm Hybrid III–V/Si Fabry–Pérot Laser Based on Adhesive Bonding', *IEEE Photonics Technol. Lett.*, vol. 23, no. 23, pp. 1781–1783, Dec. 2011.

[18] S. Stankovic, R. Jones, M. N. Sysak, J. M. Heck, G. Roelkens, and D. V. Thourhout, 'Hybrid III–V/Si Distributed-Feedback Laser Based on Adhesive Bonding', *IEEE Photonics Technol. Lett.*, vol. 24, no. 23, pp. 2155–2158, Dec. 2012.

[19] M. Lamponi *et al.*, 'Low-Threshold Heterogeneously Integrated InP/SOI Lasers With a Double Adiabatic Taper Coupler', *IEEE Photonics Technol. Lett.*, vol. 24, no. 1, pp. 76–78, Jan. 2012.
[20] M. Lamponi *et al.*, 'Heterogeneously integrated InP/SOI laser using double tapered single-mode waveguides through adhesive die to wafer bonding', in *7th IEEE International Conference on Group IV Photonics*, 2010, pp. 22–24.
[21] G. Roelkens *et al.*, 'III-V/silicon photonics for on-chip and intra-chip optical interconnects', *Laser Photonics Rev.*, vol. 4, no. 6, pp. 751–779, Nov. 2010.
[22] D. V. Thourhout *et al.*, 'Nanophotonic Devices for Optical Interconnect', *IEEE J. Sel. Top. Quantum Electron.*, vol. 16, no. 5, pp. 1363–1375, Sep. 2010.
[23] T. Spuesens, J. Bauwelinck, P. Regreny, and D. V. Thourhout, 'Realization of a Compact Optical Interconnect on Silicon by Heterogeneous Integration of III–V', *IEEE Photonics Technol. Lett.*, vol. 25, no. 14, pp. 1332–1335, Jul. 2013.
[24] L. Liu *et al.*, 'Compact Multiwavelength Laser Source Based on Cascaded InP-Microdisks Coupled to One SOI Waveguide', in *Optical Fiber Communication Conference/National Fiber Optic Engineers Conference (2008), paper OWQ3*, 2008, p. OWQ3.
[25] T. Creazzo *et al.*, 'Integrated tunable CMOS laser', *Opt. Express*, vol. 21, no. 23, pp. 28048–28053, Nov. 2013.
[26] T. Hong *et al.*, 'A Selective-Area Metal Bonding InGaAsP–Si Laser', *IEEE Photonics Technol. Lett.*, vol. 22, no. 15, pp. 1141–1143, Aug. 2010.
[27] K. Tanabe, D. Guimard, D. Bordel, S. Iwamoto, and Y. Arakawa, 'Electrically pumped 1.3 µm room-temperature InAs/GaAs quantum dot lasers on Si substrates by metal-mediated wafer bonding and layer transfer', *Opt. Express*, vol. 18, no. 10, pp. 10604–10608, May 2010.
[28] M. A. Bayo Caro, 'Theory of elasticity and electric polarization effects in the group-III nitrides', Ph. D thesis, University College Cork, 2013.
[29] I. J. Luxmoore *et al.*, 'III-V quantum light source and cavity-QED on Silicon', *Sci. Rep.*, vol. 3, online février 2013.
[30] S. H. Huang, G. Balakrishnan, A. Khoshakhlagh, L. R. Dawson, and D. L. Huffaker, 'Simultaneous interfacial misfit array formation and antiphase domain suppression on miscut silicon substrate', *Appl. Phys. Lett.*, vol. 93, no. 7, p. 071102, Aug. 2008.
[31] A. Jallipalli, G. Balakrishnan, S. H. Huang, A. Khoshakhlagh, L. R. Dawson, and D. L. Huffaker, 'Atomistic modeling of strain distribution in self-assembled interfacial misfit dislocation (IMF) arrays in highly mismatched III–V semiconductor materials', *J. Cryst. Growth*, vol. 303, no. 2, pp. 449–455, May 2007.
[32] K. Akahane, N. Yamamoto, S. Gozu, A. Ueta, and N. Ohtani, 'Initial growth stage of GaSb on Si(001) substrates with AlSb initiation layers', *J. Cryst. Growth*, vol. 283, no. 3, pp. 297–302, Oct. 2005.
[33] Y. H. Kim *et al.*, 'Growth mode and structural characterization of GaSb on Si (001) substrate: A transmission electron microscopy study', *Appl. Phys. Lett.*, vol. 88, no. 24, p. 241907, Jun. 2006.
[34] J. R. Reboul, L. Cerutti, J. B. Rodriguez, P. Grech, and E. Tournié, 'Continuous-wave operation above room temperature of GaSb-based laser diodes grown on Si', *Appl. Phys. Lett.*, vol. 99, no. 12, p. 121113, Sep. 2011.

[35] L. Cerutti, J. B. Rodriguez, and E. Tournie, 'GaSb-Based Laser, Monolithically Grown on Silicon Substrate, Emitting at 1.55 m at Room Temperature', *IEEE Photonics Technol. Lett.*, vol. 22, no. 8, pp. 553–555, Apr. 2010.
[36] M. Yamaguchi, T. Nishioka, and M. Sugo, 'Analysis of strained-layer superlattice effects on dislocation density reduction in GaAs on Si substrates', *Appl. Phys. Lett.*, vol. 54, no. 1, pp. 24–26, Jan. 1989.
[37] K. Samonji *et al.*, 'Reduction of threading dislocation density in InP-on-Si heteroepitaxy with strained short-period superlattices', *Appl. Phys. Lett.*, vol. 69, no. 1, pp. 100–102, Jul. 1996.
[38] E. A. Fitzgerald *et al.*, 'Totally relaxed GexSi1−x layers with low threading dislocation densities grown on Si substrates', *Appl. Phys. Lett.*, vol. 59, no. 7, pp. 811–813, Aug. 1991.
[39] C. L. Andre *et al.*, 'Investigations of high-performance GaAs solar cells grown on Ge-Si/sub 1-x/Ge/sub x/-Si substrates', *IEEE Trans. Electron Devices*, vol. 52, no. 6, pp. 1055–1060, Jun. 2005.
[40] M. E. Groenert *et al.*, 'Monolithic integration of room-temperature cw GaAs/AlGaAs lasers on Si substrates via relaxed graded GeSi buffer layers', *J. Appl. Phys.*, vol. 93, no. 1, pp. 362–367, Dec. 2002.
[41] J. F. Geisz, J. M. Olson, M. J. Romero, C. s Jiang, and A. G. Norman, 'Lattice-mismatched GaAsP Solar Cells Grown on Silicon by OMVPE', in *2006 IEEE 4th World Conference on Photovoltaic Energy Conference*, 2006, vol. 1, pp. 772–775.
[42] Z. Wang *et al.*, 'Polytypic InP Nanolaser Monolithically Integrated on (001) Silicon', *Nano Lett.*, vol. 13, no. 11, pp. 5063–5069, Nov. 2013.
[43] T. Orzali *et al.*, 'GaAs on Si epitaxy by aspect ratio trapping: Analysis and reduction of defects propagating along the trench direction', *J. Appl. Phys.*, vol. 118, no. 10, p. 105307, Sep. 2015.
[44] J. Z. Li, J. Bai, C. Major, M. Carroll, A. Lochtefeld, and Z. Shellenbarger, 'Defect reduction of GaAs/Si epitaxy by aspect ratio trapping', *J. Appl. Phys.*, vol. 103, no. 10, p. 106102, May 2008.
[45] T. A. Langdo, C. W. Leitz, M. T. Currie, E. A. Fitzgerald, A. Lochtefeld, and D. A. Antoniadis, 'High quality Ge on Si by epitaxial necking', *Appl. Phys. Lett.*, vol. 76, no. 25, pp. 3700–3702, Jun. 2000.
[46] S. Lourdudoss, 'Heteroepitaxy and selective area heteroepitaxy for silicon photonics', *Curr. Opin. Solid State Mater. Sci.*, vol. 16, no. 2, pp. 91–99, avril 2012.
[47] Z. Wang, C. Junesand, W. METAFERIA, C. Hu, L. Wosinski, and S. Lourdudoss, 'III–Vs on Si for photonic applications—A monolithic approach', *Mater. Sci. Eng. B*, vol. 177, pp. 1551–1557, Oct. 2012.
[48] W. Guo *et al.*, 'Selective metal-organic chemical vapor deposition growth of high quality GaAs on Si(001)', *Appl. Phys. Lett.*, vol. 105, no. 6, p. 062101, Aug. 2014.
[49] Q. Li *et al.*, '1.3-μm InAs quantum-dot micro-disk lasers on V-groove patterned and unpatterned (001) silicon', *Opt. Express*, vol. 24, no. 18, pp. 21038–21045, Sep. 2016.
[50] Q. Li, K. W. Ng, and K. M. Lau, 'Growing antiphase-domain-free GaAs thin films out of highly ordered planar nanowire arrays on exact (001) silicon', *Appl. Phys. Lett.*, vol. 106, no. 7, p. 072105, Feb. 2015.

[51] C. P. T. Svensson *et al.*, 'Monolithic GaAs/InGaP nanowire light emitting diodes on silicon', *Nanotechnology*, vol. 19, no. 30, p. 305201, 2008.
[52] G. Koblmüller and G. Abstreiter, 'Growth and properties of InGaAs nanowires on silicon', *Phys. Status Solidi RRL – Rapid Res. Lett.*, vol. 8, no. 1, pp. 11–30, Jan. 2014.
[53] T. Mårtensson *et al.*, 'Epitaxial III−V Nanowires on Silicon', *Nano Lett.*, vol. 4, no. 10, pp. 1987–1990, Oct. 2004.
[54] Y. P. Wang *et al.*, 'Abrupt GaP/Si hetero-interface using bistepped Si buffer', *Appl. Phys. Lett.*, vol. 107, no. 19, p. 191603, Nov. 2015.
[55] Y. Ping Wang *et al.*, 'Quantitative evaluation of microtwins and antiphase defects in GaP/Si nanolayers for a III–V photonics platform on silicon using a laboratory X-ray diffraction setup', *J. Appl. Crystallogr.*, vol. 48, no. 3, pp. 702–710, Jun. 2015.
[56] Y. Takagi, H. Yonezu, K. Samonji, T. Tsuji, and N. Ohshima, 'Generation and suppression process of crystalline defects in GaP layers grown on misoriented Si(1 0 0) substrates', *J. Cryst. Growth*, vol. 187, no. 1, pp. 42–50, Avril 1998.
[57] K. Volz *et al.*, 'GaP-nucleation on exact Si (001) substrates for III/V device integration', *J. Cryst. Growth*, vol. 315, no. 1, pp. 37–47, Jan. 2011.
[58] T. J. Grassman *et al.*, 'Control and elimination of nucleation-related defects in GaP/Si(001) heteroepitaxy', *Appl. Phys. Lett.*, vol. 94, no. 23, p. 232106, juin 2009.
[59] S. Liebich *et al.*, 'Laser operation of Ga(NAsP) lattice-matched to (001) silicon substrate', *Appl. Phys. Lett.*, vol. 99, no. 7, p. 071109, 2011.
[60] Y. Fujimoto, H. Yonezu, A. Utsumi, K. Momose, and Y. Furukawa, 'Dislocation-free GaAsyP1−x−yNx/GaP0.98N0.02 quantum-well structure lattice- matched to a Si substrate', *Appl. Phys. Lett.*, vol. 79, no. 9, pp. 1306–1308, Aug. 2001.
[61] H. Yonezu, 'Control of structural defects in group III–V–N alloys grown on Si', *Semicond. Sci. Technol.*, vol. 17, no. 8, p. 762, 2002.
[62] T. Quinci *et al.*, 'Defects limitation in epitaxial GaP on bistepped Si surface using UHVCVD–MBE growth cluster', *J. Cryst. Growth*, vol. 380, pp. 157–162, Oct. 2013.
[63] J. E. Ayers, T. Kujofsa, P. Rago, and J. Raphael, *Heteroepitaxy of Semiconductors : Theory, Growth, and Characterization, Second Edition*. CRC Press, 2016.
[64] T. Soga, T. Jimbo, and M. Umeno, 'Dislocation generation mechanisms for GaP on Si grown by metalorganic chemical vapor deposition', *Appl. Phys. Lett.*, vol. 63, no. 18, pp. 2543–2545, Nov. 1993.
[65] Y. Takagi, Y. Furukawa, A. Wakahara, and H. Kan, 'Lattice relaxation process and crystallographic tilt in GaP layers grown on misoriented Si(001) substrates by metalorganic vapor phase epitaxy', *J. Appl. Phys.*, vol. 107, no. 6, p. 063506, Mar. 2010.
[66] O. Skibitzki *et al.*, 'GaP collector development for SiGe heterojunction bipolar transistor performance increase: A heterostructure growth study', *J. Appl. Phys.*, vol. 111, no. 7, p. 073515, Apr. 2012.
[67] T. T. Nguyen, 'Sillicon photonics based on monolithic integration of III-V nanostructures on silicon', phdthesis, INSA de Rennes, 2013.
[68] U. W. Pohl, *Epitaxy of Semiconductors: Introduction to Physical Principles*. Springer Science & Business Media, 2013.

[69] F. Ernst and P. Pirouz, 'Formation of planar defects in the epitaxial growth of GaP on Si substrate by metal organic chemical-vapor deposition', *J. Appl. Phys.*, vol. 64, no. 9, pp. 4526–4530, Nov. 1988.
[70] D. K. Biegelsen, F. A. Ponce, A. J. Smith, and J. C. Tramontana, 'Initial stages of epitaxial growth of GaAs on (100) silicon', *J. Appl. Phys.*, vol. 61, no. 5, pp. 1856–1859, Mar. 1987.
[71] C.-H. Choi, R. Ai, and S. A. Barnett, 'Suppression of three-dimensional island nucleation during GaAs growth on Si(100)', *Phys. Rev. Lett.*, vol. 67, no. 20, pp. 2826–2829, Nov. 1991.
[72] R. Hull and A. Fischer-Colbrie, 'Nucleation of GaAs on Si: Experimental evidence for a three-dimensional critical transition', *Appl. Phys. Lett.*, vol. 50, no. 13, pp. 851–853, Mar. 1987.
[73] I. Nemeth, 'Transmission electron microscopic investigations of heteroepitaxial III/V semiconductor thin layer and quantum well structures', 2008, Ph.D. Thesis of Marburg University.
[74] H. Kroemer, 'Polar-on-nonpolar epitaxy', *J. Cryst. Growth*, vol. 81, no. 1–4, pp. 193–204, Feb. 1987.
[75] S. L. Wright, H. Kroemer, and M. Inada, 'Molecular beam epitaxial growth of GaP on Si', *J. Appl. Phys.*, vol. 55, no. 8, p. 2916, 1984.
[76] H. Kawanami, T. Sakamoto, T. Takahashi, E. Suzuki, and K. Nagai, 'Heteroepitaxial Growth of GaP on a Si (100) Substrate by Molecular Beam Epitaxy', *Jpn. J. Appl. Phys.*, vol. 21, no. 2A, p. L68, Feb. 1982.
[77] S. L. Wright, M. Inada, and H. Kroemer, 'Polar-on-nonpolar epitaxy: Sublattice ordering in the nucleation and growth of GaP on Si(211) surfaces', *J. Vac. Sci. Technol.*, vol. 21, no. 2, pp. 534–539, Jul. 1982.
[78] J. M. Olson, M. M. Al-Jassim, A. Kibbler, and K. M. Jones, 'MOCVD growth and characterization of GaP on Si', *J. Cryst. Growth*, vol. 77, no. 1, pp. 515–523, Sep. 1986.
[79] T. Soga, H. Nishikawa, T. Jimbo, and M. Umeno, 'Characterization of Antiphase Domain in GaP on Misoriented (001) Si Substrate Grown by Metalorganic Chemical Vapor Deposition', *Jpn. J. Appl. Phys.*, vol. 32, no. 11R, p. 4912, Nov. 1993.
[80] T. Soga, T. George, T. Jimbo, and M. Umeno, 'Nucleation mechanisms for compound semiconductors grown on Si by MOCVD', *J. Cryst. Growth*, vol. 115, no. 1, pp. 418–422, Dec. 1991.
[81] Y. Takano, T. Takagi, Y. Matsuo, and S. Fuke, 'Surface Evolution of GaP Grown on Si Substrates Using Metalorganic Vapor Phase Epitaxy', *Jpn. J. Appl. Phys.*, vol. 49, no. 3R, p. 035502, Mar. 2010.
[82] Y. Wan *et al.*, 'O-band electrically injected quantum dot micro-ring lasers on on-axis (001) GaP/Si and V-groove Si', *Opt. Express*, vol. 25, no. 22, pp. 26853–26860, Oct. 2017.
[83] Y. Song and M. Larry Lee, 'InGaAs/GaP quantum dot light-emitting diodes on Si', *Appl. Phys. Lett.*, vol. 103, no. 14, p. 141906, Sep. 2013.
[84] T. J. Grassman *et al.*, 'Nucleation-related defect-free GaP/Si(100) heteroepitaxy via metal-organic chemical vapor deposition', *Appl. Phys. Lett.*, vol. 102, no. 14, pp. 142102-142102–4, Apr. 2013.
[85] A. C. Lin, M. M. Fejer, and J. S. Harris, 'Antiphase domain annihilation during growth of GaP on Si by molecular beam epitaxy', *J. Cryst. Growth*, vol. 363, pp. 258–263, Jan. 2013.
[86] A. C. Lin, J. S. Harris, and M. M. Fejer, 'Two-dimensional III-V nucleation on Si for nonlinear optics', 2011, vol. 29, p. 03C120.

[87] P. Guillemé *et al.*, 'Antiphase domain tailoring for combination of modal and 4^{-} -quasi-phase matching in gallium phosphide microdisks', *Opt. Express*, vol. 24, no. 13, pp. 14608–14617, Jun. 2016.
[88] E. L. Warren, A. E. Kibbler, R. M. France, A. G. Norman, P. Stradins, and W. E. McMahon, 'Growth of antiphase-domain-free GaP on Si substrates by metalorganic chemical vapor deposition using an in situ AsH3 surface preparation', *Appl. Phys. Lett.*, vol. 107, no. 8, p. 082109, août 2015.
[89] W. E. McMahon *et al.*, 'Surfaces and interfaces governing the OMVPE growth of APD-free GaP on AsH3-cleaned vicinal Si(100)', *J. Cryst. Growth*, vol. 452, pp. 235–239, Oct. 2016.
[90] A. Navarro, E. García-Tabarés, B. Galiana, P. Caño, I. Rey-Stolle, and C. Ballesteros, 'MOVPE growth of GaP on Si with As initial coverage', *J. Cryst. Growth*., vol. 464, pp. 8-13, Apr. 2017.

Chapter 2 : Surface and Interface energies by density functional theory

In order to explain in terms of thermodynamics the III-V on Si 3D-islands formation at the very beginning of the growth (Chapter 3) and the GaP surface texturation (Chapter 5), surfaces and interfaces energies have been computed by density functional theory (DFT). In particular, GaP and Si most stable surfaces have been investigated together with abrupt and compensated GaP/Si interfaces. This work was performed under the supervision of L. Pedesseau and C. Cornet.

In this chapter, after a brief introduction to the basic concepts of the DFT, the flat and stepped Si(001) surfaces studies are presented. The different approaches to determine the non-polar GaP(001) and the two polar GaP(114) and GaP(136) surface energies are explained. Finally, abrupt and compensated GaP(001)/Si(001) interfaces energies are determined.

2.1.Introduction to density functional theory

The density functional theory [1], [2] is the most successful quantum mechanical approach used for describing the electronic structure of matter. It was introduced by the discovery of the Hohenberg-Kohn theorem in 1964 [1] and the formulation of the Kohn-Sham equations one year later [2]. To better understand what density functional theory is about, it is useful to recall some elementary quantum mechanics, according to which a system can be described by its wave function Ψ. Eigen functions and energies are found by solving the Schrödinger equation:

$$\hat{H}\Psi = E\Psi \qquad \textbf{(2.1)}$$

where $\hat{H}$ is the Hamiltonian operator, Ψ is the wave function and E is its energy. This equation is hard to compute in the many-electrons wave function case, which contains 3N variables (N is the number of electrons). That is why, many powerful methods have been introduced to facilitate informal resolution of this problem.

In 1927, Hartree [3] introduced a simplification to the wave functions calculations, by considering the electrons independent and interacting only on an average static spherical field due to other electrons. He managed to transform the 3N dimensional many body Schrödinger equation to a set of single particle equations. Nevertheless, this method didn't satisfy the Pauli Exclusion Principle because of the function symmetry. To overcome this problem, in 1930 Hartree and Fock took into account the asymmetry of the system representing the wave function with the Slater determinant [4]. Meanwhile, in 1927 Thomas [5] and Fermi independently proposed an approximation to express the total energy completely as a function of the electron density. This method was then improved by Dirac [6]. Due to the fact that the wave function was described by its density, it constitutes a predecessor of the density functional theory, simplifying the N-body system problem by decreasing the degrees of freedom from 3N to only 3 variables. Despite all these approximations, the major breakthrough which led to the formulation of the density functional theory was the Hohenberg-Kohn theorem in 1964 [1].

2.1.1. Hohenberg-Kohn theorem

In 1964, Hohenberg and Kohn [1] proved that the full many particles ground system is a unique functional of the electron density $\rho(\boldsymbol{r})$. Therefore, its total energy can be expressed as:

$$E = E[\rho(\boldsymbol{r})] \tag{2.2}$$

More precisely:

$$E[\rho] = T[\rho] + V_{EE}[\rho] + V_{\mathrm{N-e}}[\rho] = F_{\mathrm{HK}}[\rho] + \int dr^3\, \rho(\boldsymbol{r}) V_{N-e}(\boldsymbol{r}) \tag{2.3}$$

where $F_{\mathrm{HK}}[\rho]$ is a universal functional that contains the functional for the kinetic energy of interacting electrons T[ρ] and the functional for the electron-electron interaction, $V_{EE}[\rho]$. $V_{\mathrm{N-e}}[\rho]$ represents the total external potential due to the nucleus which are considered clamped. The explicit form of the functional $F_{\mathrm{HK}}[\rho]$ is the major challenge of DFT.

2.1.2. Kohn-Sham approach

Kohn and Sham [2] replaced the system with a fictitious non-interacting system that generates the same ground state electron density than the real system of interacting electrons. They introduced the following functional $E_{\mathrm{XC}}[\rho]$ redefining $F_{\mathrm{HK}}[\rho]$ as:

$$F_{KS}[\rho] = T_s[\rho] + V_H[\rho] + E_{XC}[\rho] \tag{2.4}$$

where $T_s[\rho]$ is the kinetic energy functional of non-interacting electrons, $V_H[\rho]$ is the Hartree potential functional and $E_{XC}[\rho]$ is the exchange and correlation energy. The associated potential to the latter is:

$$V_{xc}(\boldsymbol{r}) = \left.\frac{\delta E_{xc}[\rho]}{\delta \rho}\right|_{\rho(\boldsymbol{r})} \tag{2.5}$$

So, the equation to solve is the following:

$$\left[\frac{1}{2}\nabla^2 + V_{N-e}(\boldsymbol{r}) + V_H(\boldsymbol{r}) + V_{xc}(\boldsymbol{r})\right]\varphi_i(\boldsymbol{r}) = \epsilon_i\varphi_i(\boldsymbol{r}) \tag{2.6}$$

It is known as the Kohn-Sham (KS) equation. All the terms are known except $V_{xc}(\boldsymbol{r})$. We need to introduce some approximations to determine it. The accuracy of the electronic density of the system investigated will depend on these approximations. The most commons are the Local Density Approximation (LDA) [2] and the Generalized Gradient Approximation (GGA) [7], [8].

2.1.3. The LDA approximation

In the local density approximation [2], a general inhomogeneous system is divided into infinitesimal volumes. The electron density in each volume is considered as constant. The exchange correlation energy for the density within each volume is approximated to be the exchange-correlation energy of a homogeneous gas of that density. Thus, the total exchange-correlation energy of the system can be written as:

$$E_{xc}^{LDA}[\rho]=\int \rho(\boldsymbol{r})\,\epsilon_{XC}[\rho(\boldsymbol{r})]d\boldsymbol{r} \quad \textbf{(2.7)}$$

where $\epsilon_{XC}[\rho(\boldsymbol{r})]$ is the exchange-correlation energy per particle of the interacting uniform electron gas of density $\rho(\boldsymbol{r})$.

2.1.4. The GGA approximation

The generalized gradient approximation [7], [8] attempts to incorporate the effects of the local density inhomogeneities by including the gradient of the electron density through a general function of $\rho(\boldsymbol{r})$ and $\nabla\rho(\boldsymbol{r})$:

$$E_{xc}^{GGA}[\rho]=\int f(\rho(\boldsymbol{r}),\nabla\rho(\boldsymbol{r}))d\boldsymbol{r} \quad \textbf{(2.8)}$$

In this work, the GGA approximation in the Perdue-Burke-Ernzerhof (PBE) form [7] was used.

2.1.5. Self-consistent total energy and relaxation calculations

The self-consistent total energy calculation aims to minimize the electron density for fixed atomic positions until a specific energy criterion is fulfilled. In order to solve the KS equation, one must estimate an initial electron density to use as input, ρ[in]. Once it has been specified, the KS equation can be solved through a self-consistent calculation. When the atomic positions are also relaxed, than the self-consistent total energy calculation is done for each new atomic position. The algorithm of relaxation will stop at specific force criteria. This method is used for system such as bulk material, slab for surfaces and interfaces studies. To this aim, relaxation calculations have been computed. They consist in finding the surface atomic reconstruction which minimizes the total energy of the system. We note here that a local minimum is targeted, implying that the choice of atomic positions in the initial state will strongly impact the nature of the final surface/interface reconstruction found. These two self-consistent calculations are schemed in **Figure 2.1**

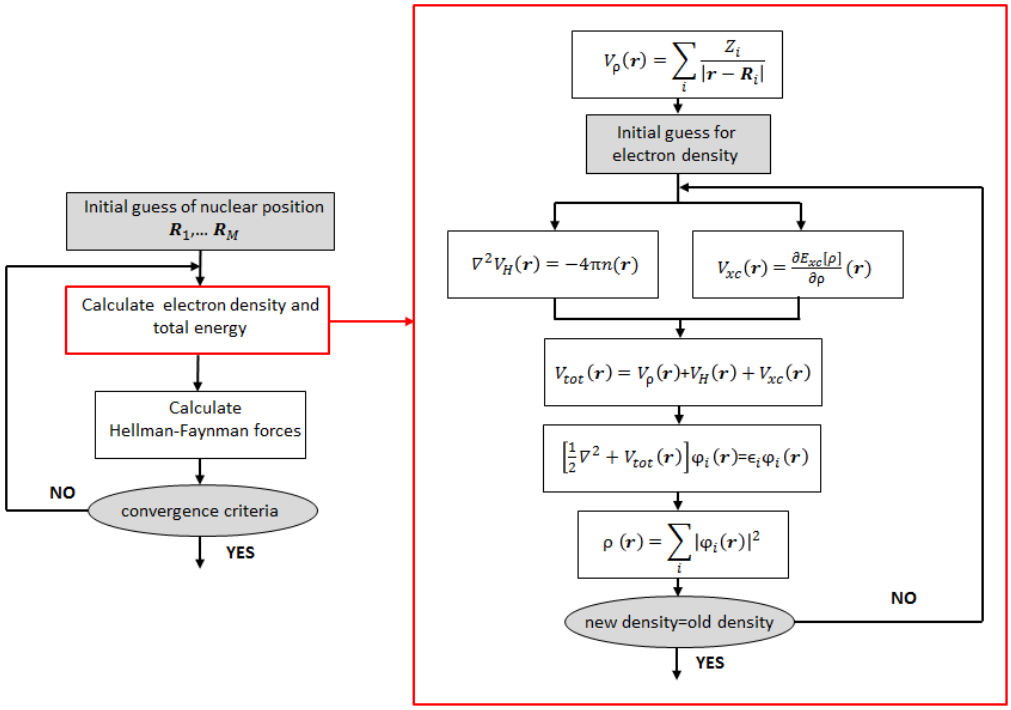

Figure 2.1 The scheme on the left refers to DFT self-consistent calculation for relaxation and structure optimization. The scheme on the right, in the red frame, is the self-consistent total energy calculation

2.1.6. Siesta Code: basis sets, pseudopotential and k-points

In this thesis, all the DFT calculations were performed by using SIESTA code [9], [10]. This code allows to find the electronic structure for large atoms clusters and to perform *ab initio* molecular dynamic simulations of molecules and periodic systems.

Moreover, Siesta code is an N-order method which means that it is possible to treat a large number of atoms since the computational load scales linearly with the system size. Furthermore, the code uses a finite-range of numerical pseudo atomic orbitals basis sets [11] which allows simplifying calculations for systems with vacuum regions. Indeed, no basis functions are required to describe region where the wave functions are negligibly small. It

decreases dramatically the computational time. For this reason, SIESTA is more suitable than plane-wave methods are to treat vacuum.

Periodic Boundary Conditions (PBCs), in all spatial directions, are imposed in the Siesta code when working on crystals. Indeed, a crystal is formed by atoms organized in a periodic arrangement called unit cell. Therefore, it is convenient to represent the system investigated by a fictitious supercell, whose shape and size will depend on the symmetry of the crystal. For surfaces and interfaces analysis, the supercells are made by including a vacuum region and a periodic system called slab in the (a,b) plane. Then, the slab surfaces are orthogonal to the c-axis. The vacuum region has to be thick enough to avoid any interaction between slabs surfaces. So, convergence tests have been done for every slab of this thesis to reach acceptable error on the energy (less than 2meV) of the system. To take into account the system periodicity, the Bloch functions are used:

$$\varphi_{\boldsymbol{k}}(\mathbf{r}) = e^{i\boldsymbol{k}.\boldsymbol{r}} u_{\boldsymbol{k}}(\mathbf{r}) \qquad \textbf{(2.9)}$$

where $u_{\boldsymbol{k}}(\mathbf{r})$ is a function with the same lattice periodicity $u_{\boldsymbol{k}}(\mathbf{r}) = u_{\boldsymbol{k}}(\mathbf{r}+\mathbf{R})$ so that:

$$\varphi_{\boldsymbol{k}}(\mathbf{r}+\mathbf{R}) = e^{i\boldsymbol{k}.\boldsymbol{R}} \varphi_{\boldsymbol{k}}(\mathbf{r}) \qquad \textbf{(2.10)}$$

where **k** is a reciprocal lattice vector of the Brillouin zone and **R** is a translation vector of the lattice. The electron density for periodic systems may be expressed as an integral over **k**:

$$\rho(\mathbf{r}) = \sum_{\rho} \int \mathrm{d}\mathbf{k} \, |\varphi_{\boldsymbol{k}}(\mathbf{r})|^2 \qquad \textbf{(2.11)}$$

where the integration limits concern the Brillouin zone. Thus, we need to choose enough **k**-points to get accurate results. In particular, the number of required **k**-points is inversely proportional to the real-space extension of the supercell.

Finally, Siesta code uses pseudopotentials method that permits to decrease the computational time by considering just the valence electrons outside a certain cutoff radius from the nuclei. Indeed, it is based on the assumption that the core electrons are chemically inert and just the valence electrons are involved in the chemical bonding. In this thesis, we used the Perdue-Burke-Ernzerhof (PBE) [7], Troullier–Martins pseudopotentials [12].

2.2.General surface energy equation

The general equation used to determine the surface energy is:

$$\gamma_{surface} 2A = E_{slab} - \sum_i \mu_i N_i \quad \textbf{(2.12)}$$

where $\gamma_{surface}$ is the surface energy, A the surface area, E_{slab} is the slab energy calculated by DFT (after relaxation calculations), μ_i is the chemical potential of the species *i* and N_i is the number of particles of the species *i* of the slab. The temperature dependence is ignored since we do not take into account the vibrational surface aspect. This relation will be upgraded depending on the different surface polarity.

2.3.Si and GaP bulk

The Si and GaP semiconductors crystallize in a diamond and a zinc-blende crystal structure respectively. Their experimental lattice constant at 300K are respectively 5.43Å [13] 5.45Å [14] For our study, firstly we needed to calculate by DFT their equilibrium lattice constant. Indeed, it is necessary to determine the theoretical equilibrium volume of each crystal at 0K, which means to find the lattice constant corresponding to the minimum total bulk energy. For this reason, a single-point simulation for energy minimization has been computed on both Si and GaP bulk materials. Their total bulk energy has been plotted as a function of the lattice constant. The polynomial fitting is shown in **Figure 2.2**. We found for the Si lattice constant at 0K a value of 5.46Å, and a value of 5.57Å for the GaP.

2.4.Silicon surface

The Si(001) surface has been widely studied since decades [15]–[18]. Indeed, it is well known that the Si(001) (2x1) reconstruction is the most stable configuration which minimizes its surface energy [16], [19], [20]. In particular, the surface atoms arrange themselves in dimers aligned along the [110] or the [1-10] direction. As a consequence, two kinds of stepped configurations form on the surface leading to the so-called double- and single-step surfaces.

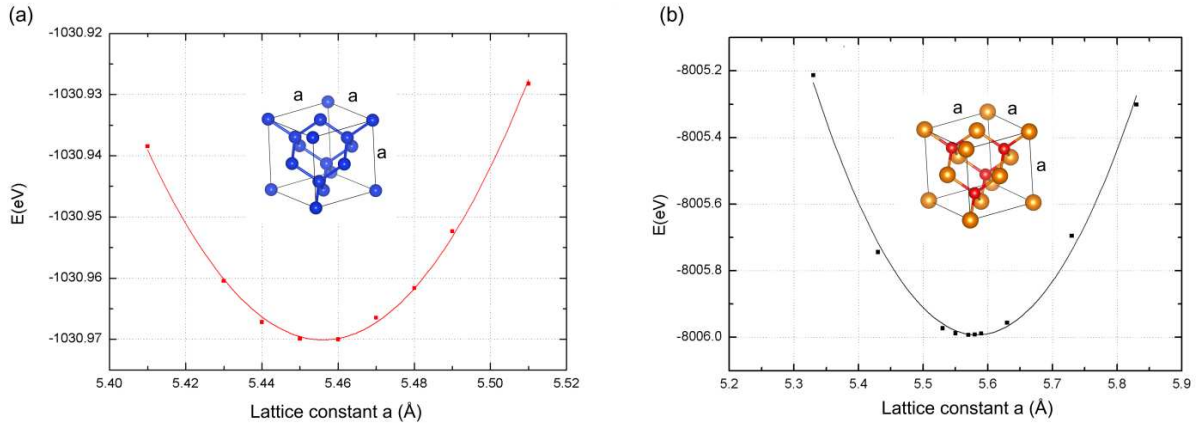

Figure 2.2 Single-point simulation to find the lattice constant corresponding to the minimum energy for a) bulk Si and b) bulk GaP.

They are called D_A, D_B and S_A, S_B respectively. The subscripts "$_A$" and "$_B$" are referred to the upper terrace dimer orientation, perpendicular ("$_A$") and parallel ("$_B$") with respect to the step edge (following the Chadi's convention[15], [16]). Furthermore, it has also been studied that, to reduce the surface energy, the dimers buckling occurs by forming different kinds of reconstructions [19], [21]. The buckling is classically described in DFT at 0K, but is usually averaged in real epitaxial temperature conditions, due to vibrations at the surface, leading to the observation of simple (2x1) surface reconstructions when using in situ diffraction tools.

In the following, the computational details to determine the energy of the flat Si(001) surface with and without step are presented.

2.4.1. Common computational details and surface energy calculations

In order to study by DFT the Si(001) surface energy, atomic relaxations have been done using a double-ζ polarized basis set [22] with an energy shift of 50 meV and a real space mesh grid energy cutoff of 150 Rydberg. The geometries were optimized until the forces were smaller than 0.005eV.Å^{-1}. The electronic structure was converged using a (6x6x2) Monkhorst-Pack grid [23] in the case of the flat Si(001) surface and a (1x1x1) Monkhorst-Pack grid for the Si(001) surface with a step. As already introduced previously, all surfaces investigated have been

modeled with the supercell approach which consists in defining a supercell made by a vacuum region and a crystal structure (a slab), with a periodicity in the (a,b) plane. By convention, the slab surfaces are orthogonal to the c axis. A vacuum of 400Å has been chosen to avoid too much interaction between the surfaces. Each slab thickness is at least about 15Å.

In the case of the flat Si(001) surface, the basis vectors are 15Å long. The D_B-step, S_B-step, S_A-step Si(001) surfaces consist of two terraces which extend over a rectangular surface whose long-side dimension is 65.2Å, 38.6Å, 38.6Å respectively, while the short-side is about 15.4Å for each one. The Si(001) surface is a non-polar surface which means that the two surfaces on the top and bottom of the slab are the same by symmetry. For this reason, they have been treated identically. For each slab, a minimum of 4Å on the top and bottom of the surfaces were allowed to relax, while the atoms of the bulk have been frozen. The bulk lattice constant of 5.46Å was used in the silicon surface calculations. To determine the silicon surface energy, eq.**(2.12)** has been used and adjusted to match the non-polar surface condition (i.e. the energy of one surface is half the total energy of the back and the top surface):

$$\gamma_{surf} = \frac{E_{slab} - N_{Si}\mu_{Si-bulk}}{2A} \qquad \textbf{(2.13)}$$

where E_{slab} is the total energy of the slab when its surfaces are reconstructed, N_{Si} is the number of Si atoms in the slab, $\mu_{Si-bulk}$ is the chemical potential of the bulk silicon, A is the surface area.

2.4.2. Flat Si(001) surface reconstruction

As it is presented in literature [21], [24], among all the stables reconstructions of the flat Si(001) surface, the minimum minimorum of surface energy is the c(4x2), where *c* stands for *centered* because the dimers are centered buckled in a (4x2) configuration. To study the surface energy associated to this reconstruction, we built a periodic slab on the [1-10] and the [110] directions, whose top surface is orthogonal to the [100] direction. The slab is composed by a Si bulk sandwiched between two symmetric surfaces (see **Figure 2.3(b)**). In the cross-sectional view presented in **Figure 2.3(a),** it is possible to have a better view of the buckling behavior of the dimers, while in **Figure 2.3(c)** the c(4x2) primitive cell is highlighted by dashed lines on the

reconstruction top view. The surface energy of the Si(001) c(4x2) reconstruction was found to be 92.8meV/Å^2.

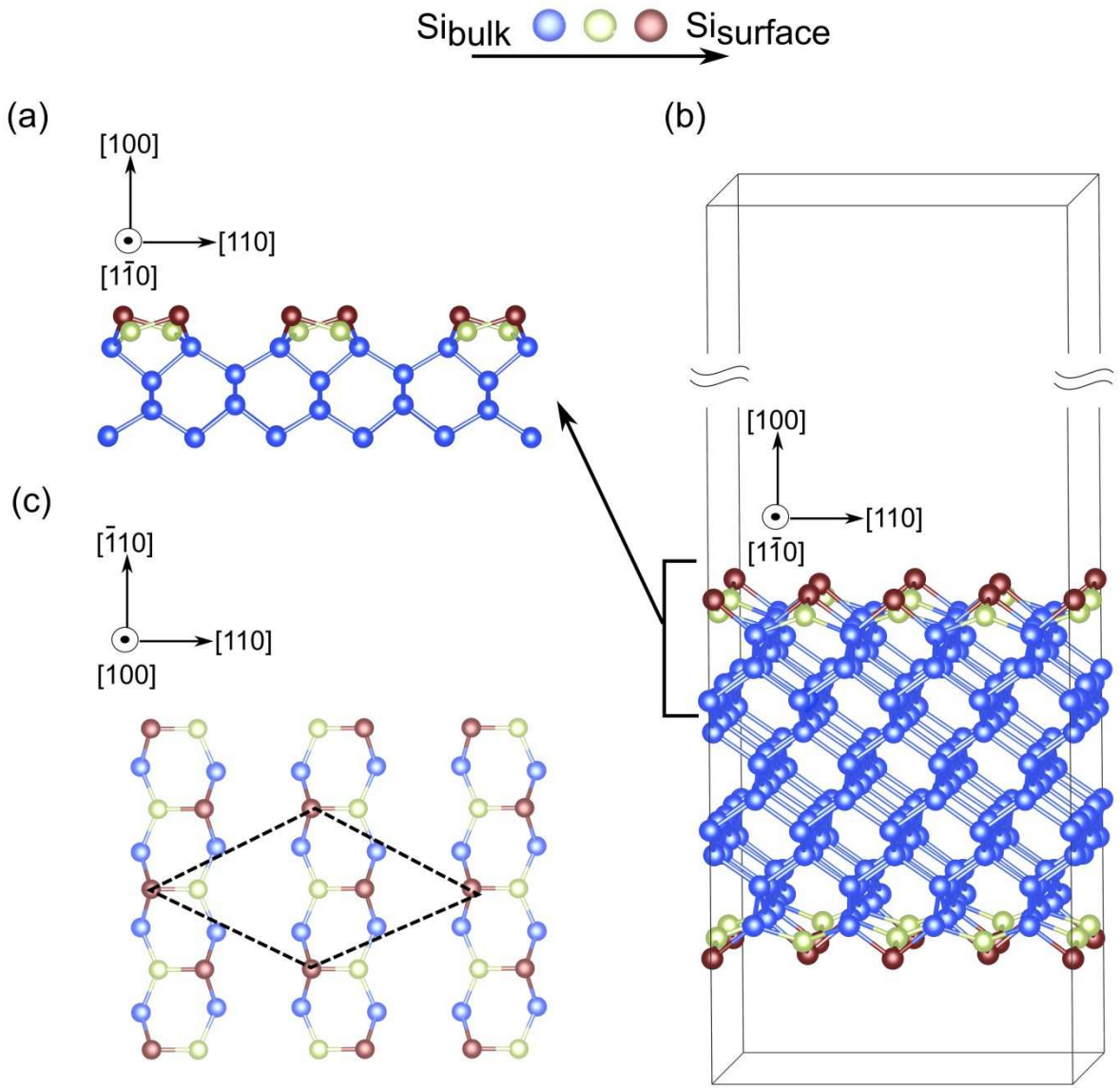

Figure 2.3 Study of the Si(001) flat surface energy: (a) side view of the c(4x2) reconstructed surface (b) slab with symmetric surfaces realized for DFT calculations (c) surface top view with the primitive cell indicated by dashed lines.

2.4.3. Stepped Si(001) surface

We now focus on the flat Si(001) surfaces with three different steps which are S_A, S_B and D_B steps (with a terrace length corresponding to at least a miscut below or equal to 6°) and we computed the most stable reconstruction already known from the literature for each step[16], [19], [20]. The D_A-step surface has not been considered since it has been already proved in the literature that it is the most unstable among all the surfaces investigated [25].

2.4.3.1. Steps interactions

Before determining the stepped surfaces energies, we had to verify the convergence criterion to avoid any interaction between two adjacent step edges. For this reason, three different D_B-stepped surfaces were built with different long-side surface dimension at 65.2Å, 46.2Å, and 38.6Å for the same short-side of 15.44Å. Their surface energies were determined by DFT calculations. The calculated values are 89.3meV/Å^2, 89.9meV/Å^{2}and 90.3meV/Å^2 respectively. In **Figure 2.4** we plotted these surface energies as a function of $1/d^2$ (as already shown for NaCl [26]) where d is the lower terrace length which corresponds to 32.8Å, 23.2Å, and 19.3Å respectively. The plot in **Figure 2.4** permits to know the ledge energy E_{Ledge} which is the stepped surface energy taking into account the step-step interactions. Indeed, it is given by the sum $\mathrm{E_{step}} + \mathrm{B}/d^2$, where $\mathrm{E_{step}}$ is the isolated step formation energy and B/d^2 is the step-step interaction between neighbouring steps [26]. Considering the equation resulting from the linear fitting (illustrated in **Figure 2.4**), $\mathrm{E_{step}}$ corresponds to 88.82meV/Å^2, while the constant term B is equal to 587.66meV/Å^2. For the isolated step case (d→∞, no step-step interaction), $\mathrm{E_{Ledge}} = \mathrm{E_{step}} = 88.82\mathrm{meV/Å^2}$. This value can be expressed as the sum of the flat surface energy γ (92.8meV/Å^2) and the energy due to the isolated step formation λ_0 thus, $\gamma + \lambda_0 = 88.82\mathrm{meV/Å^2}$. Through this equation we found that λ_0 is equal to 3.98 meV/Å^2, which means that the formation of the D_B-step stabilizes the flat surface of about 3.98 meV/Å^2.

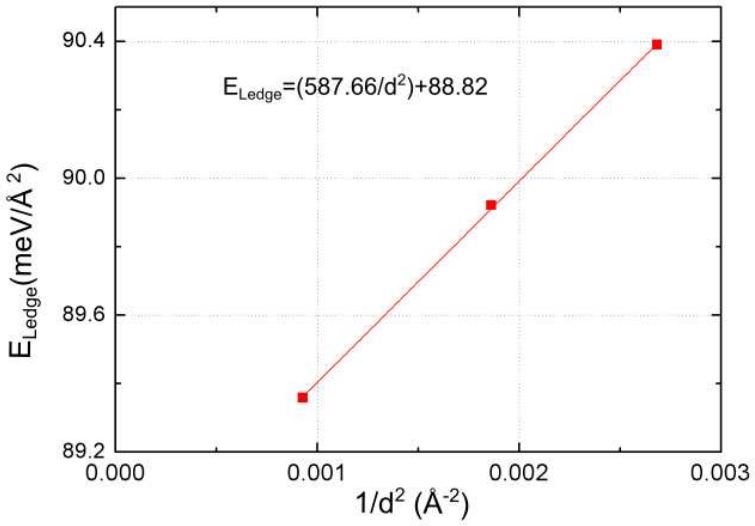

Figure 2.4 D_B stepped surface energies as a function of $1/d^2$

2.4.3.2. Stepped Si(001) surface reconstructions

The surface reconstructions consist in asymmetric (2x1) altering buckled dimers configurations which are more specifically: the *rebonded* p(2x2) for both the D_B- and S_B-step Si(001) and finally the c(4x2) in the case of the S_A-step Si(001) [19]. The D_B-, S_B- and S_A-stepped reconstructed surfaces top views are shown in **Figure 2.5(a),(c) and (e)** while the 3D views are depicted in **Figure 2.5(b),(d) and (f)** where the buckling dimer structure is also highlighted.

2.4.4. Energies of the flat Si(001) with and without steps

The surface energy values for each reconstruction are reported in **Table 2.1**. In accordance with ref. [25], we found that the S_A-step c(4x2) Si(001) is the most stable reconstruction with a value of 87.1 meV/Å^2. The S_B- and D_B-step *rebounded* p(2x2) Si(001) surfaces energies differ from each other of just 0.2 meV/Å^2. In agreement with the conclusion of the section 4.3.1, the c(4x2) reconstruction of the flat Si(001) surface is the most unstable one, with a value of 92.8meV/Å^2.

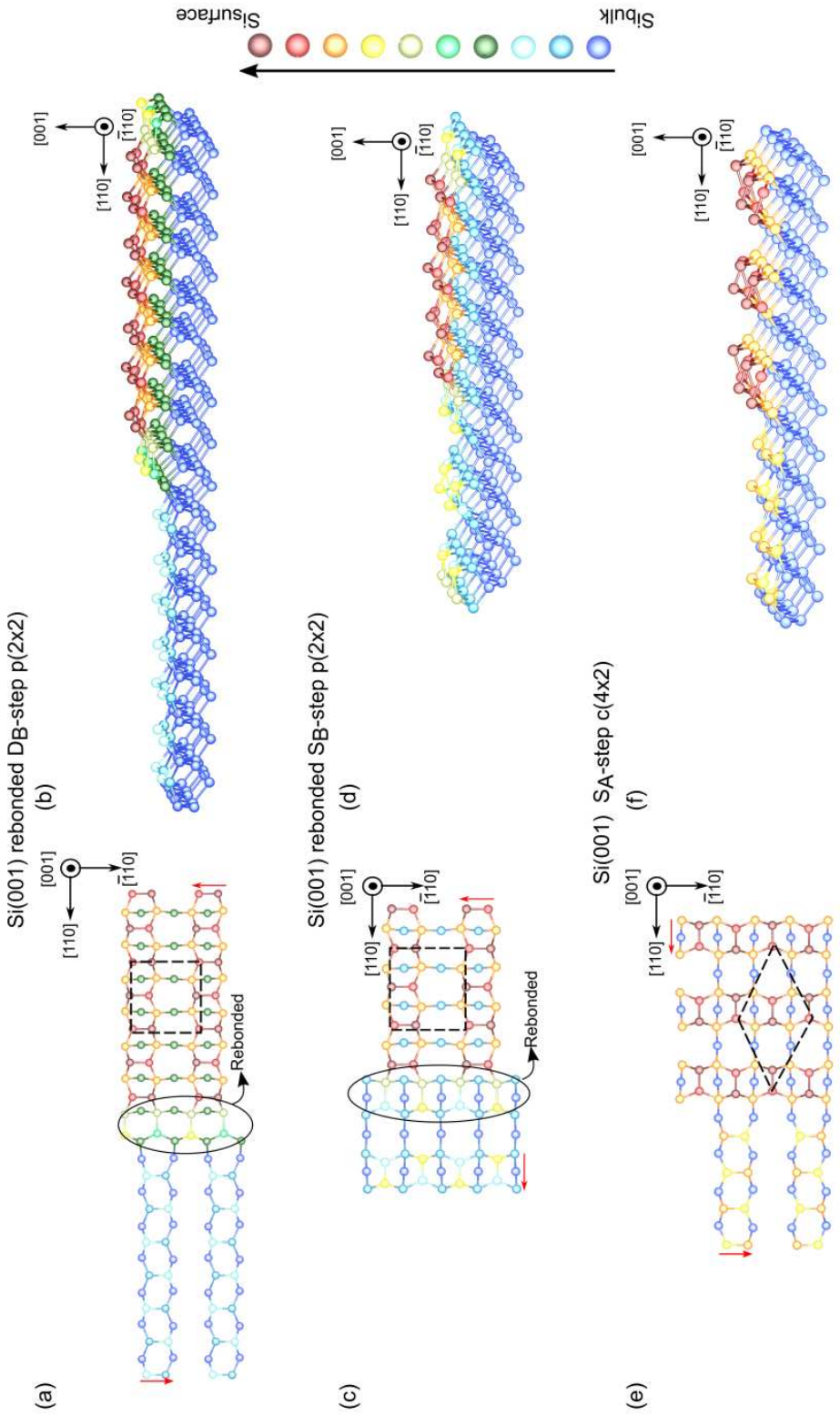

Figure 2.5 *Rebonded* p(2x2) D_B-step top view(a) and 3D view (b), *rebonded* p(2x2) S_B-step top view(c) and 3D view (d) and c(4x2) S_A-step top view(e) and 3D view (f). Primitive cells of the reconstruction are surrounded by dashed lines in each top view.

As a general conclusion, one can clearly see that these energy values are very close to each other within an interval of 5meV/Å^2 which means that the Si steps do not impact too much the surface energy values.

	Reconstruction	Surface Energy (meV/Å^2)
Si(001)	c(4x2)	92.8
S_B-step Si(001)	p(2x2)	89.1
S_A-step Si(001)	c(4x2)	87.1
D_B-step Si(001)	p(2x2)	89.3

Table 2.1 Si(001) surface energies computed by DFT

2.5.Polar and non-polar GaP surfaces

The GaP(001), GaP(114) and GaP(136) surface energies calculations are presented here. In this case, the electron counting model [27] has been taken into account to find the most stable surfaces configurations. Then, two different strategies have been applied for studying the non-polar GaP(001) and the polar GaP(114) and GaP(136) surfaces. Their energies are finally plotted as a function of the chemical potential of the species. A detailed description of the methods used is presented in this section.

2.5.1. Electron counting model

The electron counting model (ECM) plays an important role in the study of the compound semiconductors surfaces reconstructions [27]. Indeed, it represents a mandatory stability criterion which must be satisfied for analyzing surface and interface energies. It states that a surface structure will have the lowest energy when the number of available electrons in the surface layer, will first exactly fill the dangling bond of the electropositive elements in the valence band (VB), and will also left empty the ones on the electronegative elements in the conduction band (CB). It will result in a no net surface charge and the surface will likely be

semiconducting. Otherwise, partially filled dangling bond would lead to metallic surfaces, and will tend to increase the surface energy.

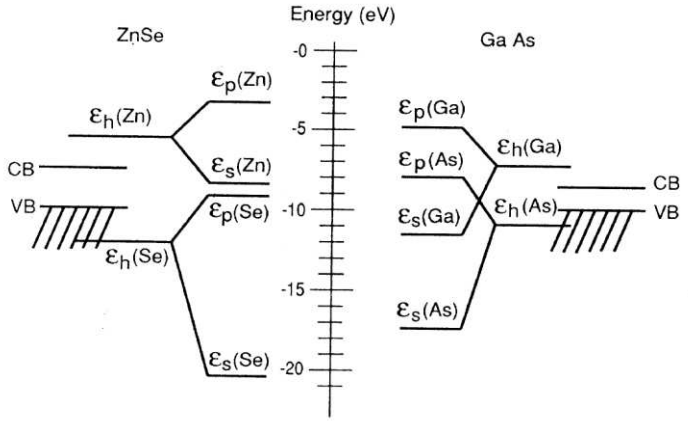

Figure 2.6 Energy level ε_h of the sp^3 dangling-bond states GaAs and ZnSe. Each ε_h level is derived from the energy of the s (ε_s) and p (ε_p) orbitals. In particular, the dangling-bond energies corresponding to Ga and Zn are above the conduction-band minimum (CB) while in the case of As and Se, they are below the valence-band maximum (VB). Figure extracted from Ref. [27].

A diagram representing the energy of these dangling bonds was reported for GaAs [27] . The schematic drawing is depicted in **Figure 2.6**. It shows the surface energy levels ε_h of the sp^3 dangling-bond states of GaAs and ZnSe. They are derived from the energy of the s and p orbitals, ε_s and ε_p respectively [27]. Pashley, in the same article, presented a clear explanation of the ECM applied to the GaAs(001) anion-rich (2xN) and the cation-rich (Nx2) surface reconstructions, which are similar to the GaP surface structures investigated in this thesis. So, to verify the ECM, the first step is to count up the electrons available in the reconstructed unit cell under study. Then, the number of electrons available must be equal to the number of electrons needed to form each bond in the surface unit cell (dimers, dangling bonds and first-to-second surface layer bonding). For the anion-rich (2xN) and cation-rich (Nx2) reconstructions, the following equations [27] are respectively determined:

$$6D + 8D = 2V_n D + V_p N \qquad \textbf{(2.14)}$$

$$6D + 8N = 2V_p D + V_n N \qquad \textbf{(2.15)}$$

where N is the periodicity of the surface unit cell, D is the number of dimers in the unit cell, V_n and V_p are the number of the valence electrons of the electronegative and electropositive element respectively. In each equation, the left terms represent the electrons needed in all the bonds of the surface unit cell, while the right terms indicate the numbers of the electrons available. We referred to the following methodology to check the ECM stability criterion for all the GaP surfaces reconstructions investigated in our work.

2.5.2. Common DFT computational details

In terms of computational details, all the structures relaxations and electronic structure calculations have been done using a double-ζ polarized basis sets [11] with an energy shift of 50 meV and a real space mesh grid energy cutoff of 150 Rydberg. The geometries were optimized until the forces were smaller than 0.005eV.Å^{-1}. The electronic structure was converged using 8x8x8, 8x2x6, 8x4x8, 2x2x1, 4x4x1 and 3x2x1 Monkhorst-Pack grids[23] of the Brillouin zone for the GaP bulk, the black Phosphorus, α-Ga phase [28]–[30] and for GaP(001), GaP(114) and GaP(136) slabs respectively.

The surfaces were modeled in periodic slab geometry. As explained above for Si surfaces, the slab has been built to be periodic within the plan (a,b) and also to reveal the surface orthogonally to the c axis. In this case, a vacuum of 450Å has been chosen for the same reasons as in the case of the Si surfaces. Each surface fulfills the electron counting model [27] as originally well-established for GaAs and ZnSe. Finally, GaP material, black Phosphorus and the α-Ga phase have been considered in bulk materials and minimized from their experimental data [28]–[30]. The black phosphorus and the α-Ga phase materials were used to estimate their intrinsic chemical potential that is needed for calculating the surface energy of GaP surfaces.

2.5.3. Chemical potential

The chemical potentials μ_P and μ_{Ga} are defined as the variables that each element can have within the bulk or surface of the GaP material. The thermodynamic conditions, to which

the chemical potentials have to obey to, are the following: the upper limit of μ_P and μ_{Ga} is reached when each element is in its own pure bulk phase

$$\mu_P < \mu_P^{P-bulk} \quad \textbf{(2.16)}$$

$$\mu_{Ga} < \mu_{Ga}^{Ga-bulk} \quad \textbf{(2.17)}$$

Moreover, at thermodynamic equilibrium the sum of μ_P and μ_{Ga} must be equal to the chemical potential $\mu_{GaP}^{GaP-bulk}$ of the GaP bulk phase:

$$\mu_{Ga} + \mu_P = \mu_{GaP}^{GaP-bulk} \quad \textbf{(2.18)}$$

$$\mu_{GaP}^{GaP-bulk} = \mu_{Ga}^{Ga-bulk} + \mu_P^{P-bulk} + \Delta H_f(\mathrm{GaP}) \quad \textbf{(2.19)}$$

where ΔH_f(GaP) is the heat of formation of the GaP material. μ_P^{P-bulk} and $\mu_{Ga}^{Ga-bulk}$ are the chemical potentials of the species P and Ga from the black P and α-Ga phase respectively. In this work, the value of -0.928 eV has been determined for $\Delta H_f(\mathrm{GaP})$, in agreement with the literature [31]–[33].

In this thesis, we therefore establish the GaP(001), GaP(114) and GaP(136) surface energies as a function of the phosphorus chemical potential variation $\Delta\mu_P$=$\mu_P - \mu_P^{P-bulk}$. Thus, by combining **(2.16)**, **(2.17)** and **(2.19)**, the extreme thermodynamic conditions for $\Delta\mu_P$ are given by:

$$\Delta H_f(GaP) < \Delta\mu_P < 0 \quad \textbf{(2.20)}$$

To summarize, when $\Delta\mu_P$ equals the heat of formation $\Delta H_f(GaP)$, the extreme Ga-rich limit is reached (i.e. bulk Ga will form preferentially). Contrary to that, when $\Delta\mu_P$ equals 0, the extreme P-rich limit is reached (i.e. bulk P will form preferentially). From these considerations, it is clear that experimental conditions reached during the epitaxial growth of GaP are between the Ga-rich and the P-rich limit.

2.5.4. Non-polar GaP(001) surfaces

The GaP(001) surface is non-polar which means that the top and the bottom surfaces of the slab are symmetric. Also, they are rotated of 90° with respect to each other. As a consequence, to determine the non-polar GaP(001) surfaces energy, the bottom and top surfaces have been treated identically with the same reconstruction which decreases the error on the determination of the surface energy. This symmetry can be clearly seen in the slabs realized for each surface investigated. The slabs built in this case are depicted in **Figure 2.7 (b) and (d)** and **Figure 2.8 (b)**. The thicknesses of the slab are about 17Å and 23Å for the P-rich and Ga-rich GaP(001) surfaces respectively. The top and bottom surfaces were allowed to relax about 6Å into their minimum energy configuration and all the others atoms were kept frozen in the bulk position. The top and bottom surfaces have been checked to be the same by a 90° rotation after relaxation of atomic positions (i.e. when the minimum of energy has been reached).

2.5.4.1. GaP(001) surface reconstructions

For the non-polar GaP surfaces, GaP(001), (2x1) and (2x4) reconstructions are computed. We studied the most stable structures of the (2x4) configurations which obey the ECM and we verified the relative instability of the P-rich (2x1) which, instead, does not satisfy it.

In particular, for the Ga-rich GaP(001) surface, the GaP(001)md(2x4) reconstruction [34], [35] (where md stands for mixed dimers) is assumed. This reconstruction is often considered for Ga- rich conditions in the literature [36]–[38]. The side view and top view are shown in **Figure 2.7(c), (d), and (f)** respectively (with the unit cell in dashed lines). For the P–rich GaP(001)(2x4) surface, different stable structures were proposed [39]. In this work, we studied a simple anion P-rich GaP(001)(2x4) surface that fulfills the ECM criteria as proposed for GaAs [27]. Its side view is depicted in **Figure 2.7(a) and (b)** while the top view, where the unit cell is highlighted, can be seen in **Figure 2.7(e)**.

The P-rich (2x1) reconstruction is depicted in **Figure 2.8**. Its side view and slab, in **Figure 2.8(a) and (b)**, look very similar to the (2x4) in **Figure 2.7(a) and (b).** However, the difference

from this structure is given by the additional dimer line which can be seen in the top view of the (2x1) reconstructed unit cell (**Figure 2.8(c)**) with respect to **Figure 2.7(e)**.

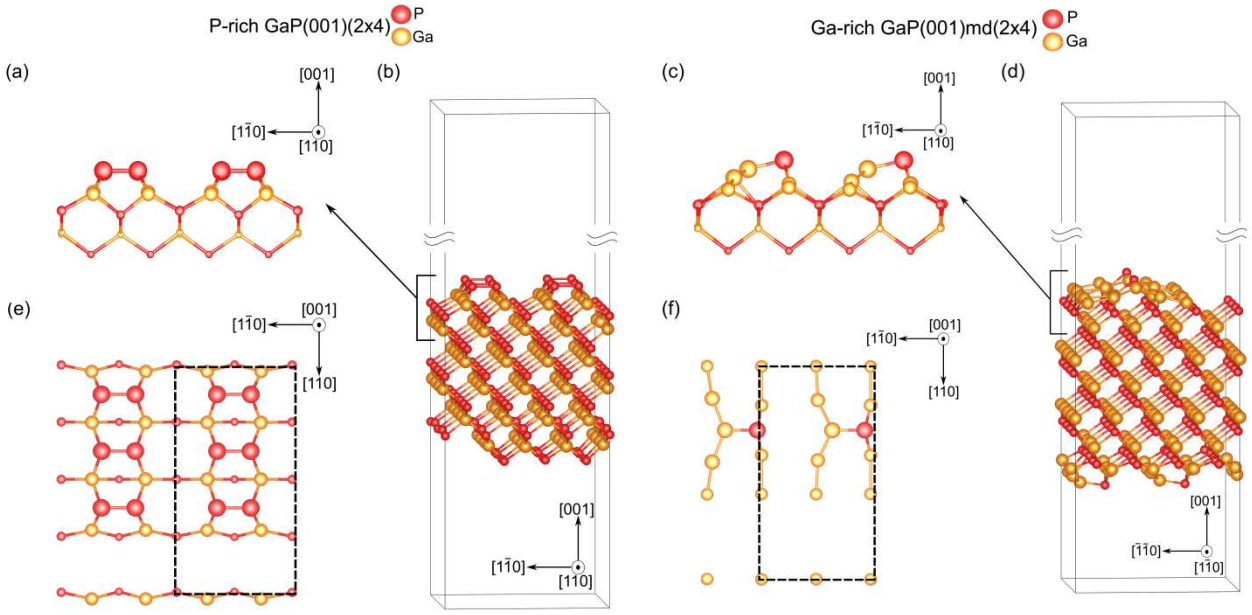

Figure 2.7 **(**a) Side profile and (e) top view for P-rich GaP(001)(2x4) surface. (c) Side profile and (f) top view for Ga-rich GaP(001)(2x4)md surface. The unit cells of the reconstructions are indicated by dashed lines in the top views. The slab realized for P-rich GaP(001)(2x4) and for Ga-rich GaP(001)(2x4)md are represented respectively in (b) and (d).

2.5.4.2. GaP(001) surface energies

In such a case, the relation to calculate the surface energy is:

$$\gamma_{non-polar} = \frac{E_{slab} - N_{Ga}\mu_{GaP}^{GaP-bulk} - (N_P - N_{Ga})\mu_P}{2A} \quad \textbf{(2.21)}$$

where E_{slab} is the slab energy when the reconstruction is achieved, N_i is the number of the particles of the species *i* (where i is Ga, or P) of the slab, $\mu_{GaP}^{GaP-bulk}$ and μ_P are the chemical potential of the GaP bulk material and of the species P and A is the surface area (that is counted

two times for top and bottom surfaces).

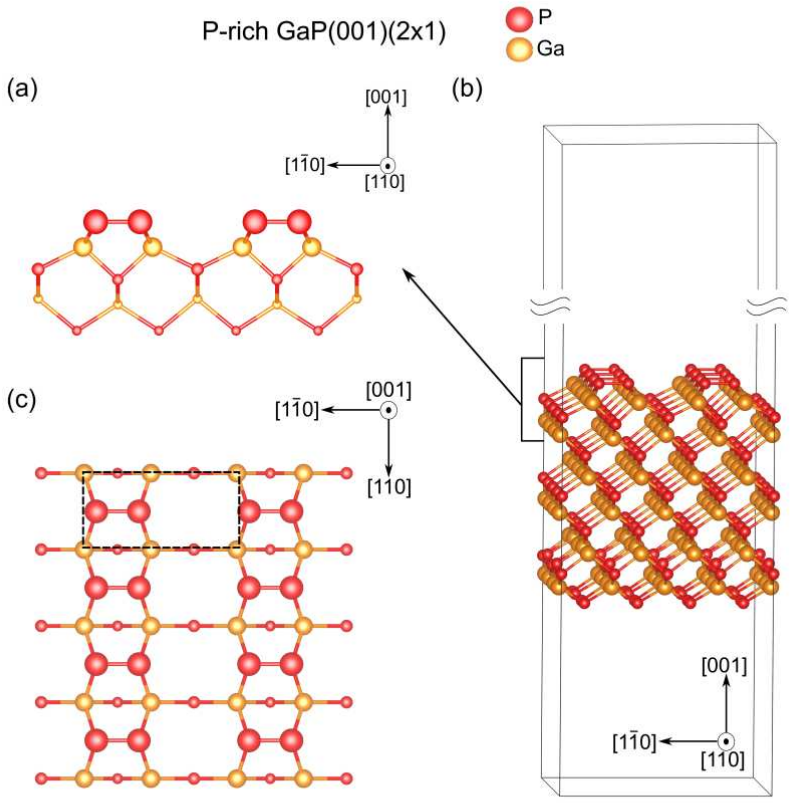

Figure 2.8 (a) Side profile and (c) top view over $[1\ \bar{1}\ 0]$, $[1\ 1\ 0]$ and $[0\ 0\ 1]$ axis for P-rich GaP(001)(2x1) surface. The slab built for the DFT calculations is represented in (b)

2.6.Polar GaP(114) and GaP(136) surfaces

The GaP(114) and the GaP(136) surfaces are polar [40], which means that the two surfaces of the slabs are formed by two different surfaces which are called type A and B. As a consequence, a different approach has been applied for these cases. It consists in considering the top surface as the one being investigated, and passivating the bottom one with fictitious hydrogen atoms. It will be explained in this section.

For DFT calculations $1s^{0.75}$, $1s^{1.25}$, $3s^2 3p^3$, and $4s^2 3d^{10} 4p^1$ were used as valence electrons for the fictitious H^* with a net charge of 0.75e to compensate P, and the fictitious H^* with a net charge of 1.25e to compensate Ga, for P and Ga atoms respectively. The two fictitious H^*, Ga and P atoms have been built with ATOM code, the pseudopotential generation distributed as part of the SIESTA software package.

2.6.1. GaP(114) and GaP(2 5 11) surface reconstructions

Type A and B polar surfaces were computed for each surface investigated. In particular, letter A (B) refers to P(Ga)-terminated surfaces.

For the GaP(114), two types of (2x1) reconstructions have been simulated: the P-rich GaP(114)A-α2(2x1) and the Ga-rich GaP(114)B-α2(2x1) which are similar to the ones already thoroughly investigated for the GaAs(114) [41]–[43]. Their side views are shown in **Figure 2.9(a) and (c).** The top views are also interesting. Indeed, in **Figure 2.9(e) and (f)** we can have a clear view of the reconstruction in the primitive cell (in the dashed lines). In each case, it is formed by two P- and Ga-dimers, as in the similar case of GaAs(114)[42]. The two GaP(114) bottom H*-passivated slabs are shown in **Figure 2.9(b) and (d)**. They have a thickness of about 25Å. The dark blue atoms are the fictitious hydrogens atoms bonded to the gallium atoms while the light blue ones, are the fictitious H* bonded to phosphorus atoms.

We used the same fictitious H* representation also for the GaP(136) passivated surface described in the next section. For the GaP(136) surfaces, we considered the reconstruction already studied for a similar case, which is the GaAs(2 5 11)[44]–[46]. This is due to the fact that the GaP(136) surfaces do not fulfill the ECM [27]. Therefore, it is necessary to add two P (Ga) atoms on the P-rich (Ga-rich) surface unit cell to fulfill the ECM criterion. As a consequence, three parallel slightly inclined P (Ga) dimers form in the surface unit cell, now lying on the (2 5 11) plane. The need to fulfill the ECM together with the fact that the (2 5 11) and (1 3 6) planes are very close (sustaining a leaning angle of ~2°) [45], [47] make strong arguments to work on the more stable GaP(2 5 11) surface rather than the (136). In the case of the GaP(2 5 11), the two reconstructions are named P-rich GaP(2 5 11)A-(1x1) and Ga-rich GaP(2 5 11)B-(1x1) (as

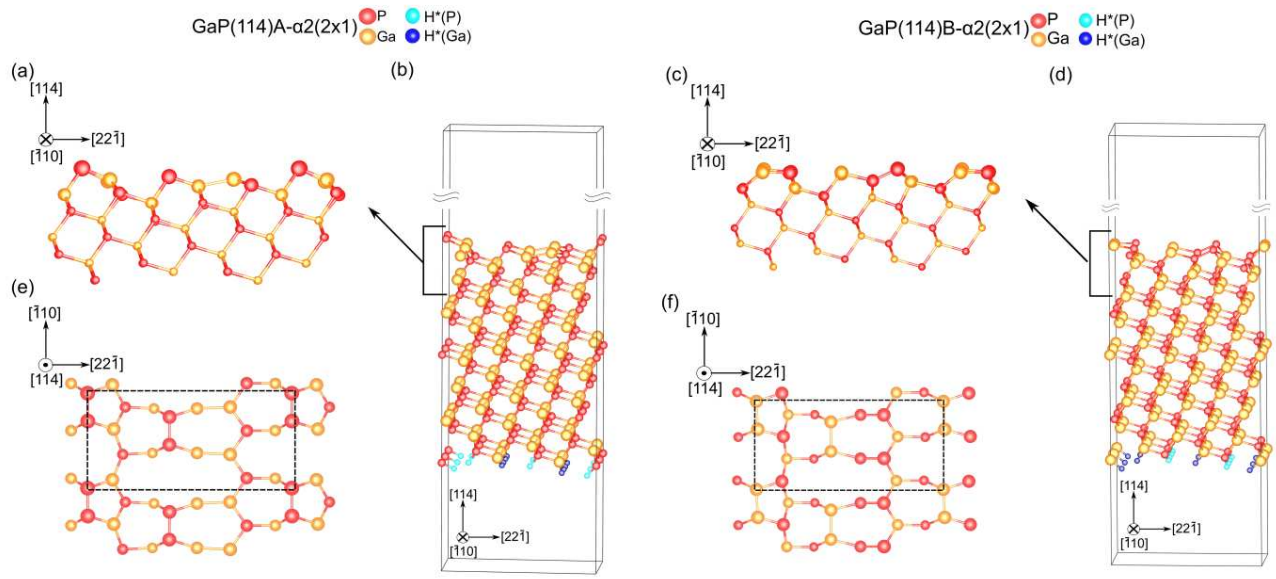

Figure 2.9 (a) and (c) side profile, (e) and (f) top view over $[1\quad 1\quad 4]$, $[\bar{1}\quad 1\quad 0]$and $[2\quad 2\quad \bar{1}]$axis, while the slab realized for the DFT calculations is represented in (b) and (d) with the surface investigated on top and the surface H*-passivated on the bottom for GaP(114)A-α2(1x1) and GaP(114)B-α2(1x1) surface respectively

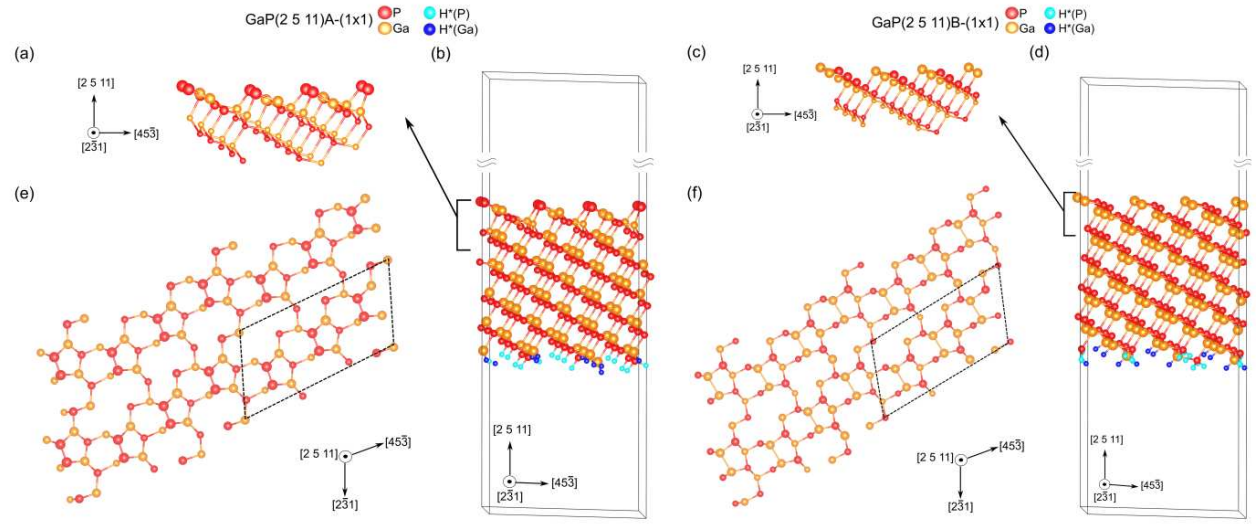

Figure 2.10 (a) and (c) side profile, (e) and (f) top view over $[2\quad 5\quad 11]$, $[2\quad \bar{3}\quad 1]$and $[4\quad 5\quad \bar{3}]$axis, while the slab realized for the DFT calculations is represented in (b) and (d) with the surface investigated on top and the surface H*-passivated on the bottom axis for GaP(2 5 11)A-(1x1) and GaP(2 5 11)B-(1x1) surface respectively

shown in similar works [44], [45]). Their side views are shown in **Figure 2.10 (a) and (b)**. Moreover, from the top views in **Figure 2.10(e) and (f)**) we can clearly see that the unit cells are tilted and made by 3 P and 3 Ga dimers respectively. The passivated slabs are depicted in **Figure 2.10(b) and (d)**. Their thicknesses are about 20Å.

2.6.2. Fictitious H*-passivation approach

In order to check the validity of the H*-passivation methodology, we compare in the following, two different methods: the H*-passivation approach and the one used for the non-polar surface (see above) on the simple non-polar P-rich GaP(001) (2x1) reconstruction. In the case of H*-passivation approach, the surface energy equation is therefore modified with respect to the symmetric case, by including a new term coming from the fictitious H^* atoms:

$$\gamma_{polar} = \frac{E_{slab} - N_{Ga}\mu_{GaP}^{GaP-bulk} - (N_P - N_{Ga})\mu_P - N_{H^*}^P \mu_{H^*}^P}{A} \quad \textbf{(2.22)}$$

where E_{slab} is the total energy of the slab with one side H*-passivated, $N_{H^*}^P$ the number of fictitious hydrogens bonded to the P atoms of the bottom surface and $\mu_{H^*}^P$ is their chemical potential.

The difficulty of this calculation is to determine the fictitious H* chemical potential $\mu_{H^*}^P$. Indeed, to do this, we first computed the total energy of the P-rich GaP(001)(2x1) slab with both-surfaces passivated by fictitious hydrogens H*. To this aim, all the Ga and P atoms were kept frozen in the bulk position while only the fictitious H* atoms where allowed to relax (the slab is shown in **Figure 2.11(a)**). Then, we applied the following equation to determine$\mu_{H^*}^P$:

$$\mu_{H^*}^P = \frac{E_{slab}^{H^*-passivated} - N_{Ga}\mu_{GaP}^{GaP-bulk} - (N_P - N_{Ga})\mu_P}{N_{H^*}} \quad \textbf{(2.23)}$$

where $E_{slab}^{H^*-passivated}$ is the total energy of the slab passivated on both sides. The both-side passivated slab, in **Figure 2.11(a),** is non-stoichiometric, *i.e* $N_P \neq N_{Ga}$. That is why, the $\mu_{H^*}^P$ must be expressed as a function of the chemical potential.

After that, we built a slab having the bottom surface passivated by the fictitious-H* kept in their positions of minimum energy. The top surface was allowed to relax in its P-rich GaP(001)

(2x1) reconstruction (see slab in **Figure 2.11(b)**). In particular, the top surface in addition to the subsurface (about 6Å) was allowed to relax into its minimum energy and all the others atoms were kept frozen in the bulk position.

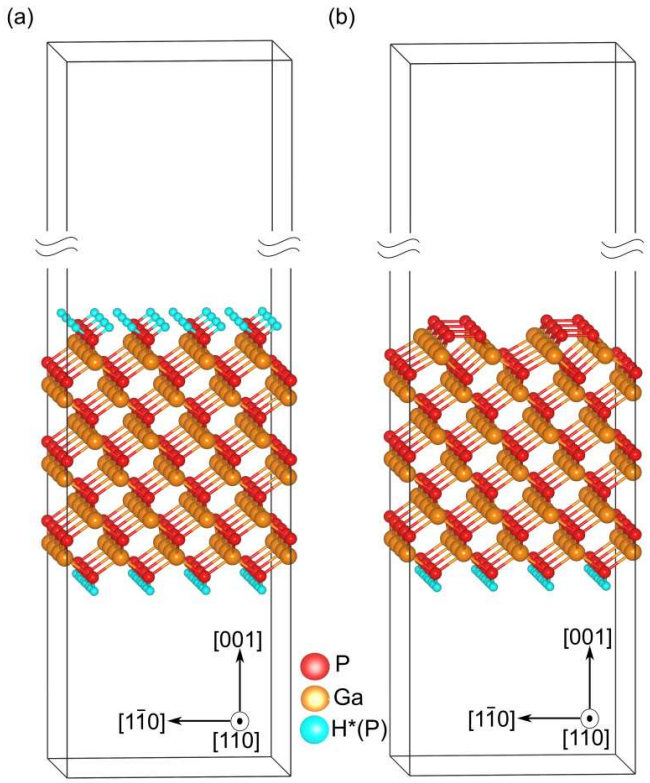

Figure 2.11 Slab built for determining: the fictitious H* chemical potential (a), the P-rich (2x1) surface energy using the H*-passivated surface on the bottom (b)

By applying in eq.**(2.22)**, $\mu_{H^*}^{P}$ found through eq.**(2.23)**, we finally determined the P-rich GaP(001)(2x1) surface energy which differs just of 0.49meV/Å^2 from the ones determined in the symmetric case. The values are shown in **Table 2.2**.

GaP(001) P-rich(2x1) reconstruction	N_{Ga}	N_P	P-rich Surface Energy (meV/Å^2)	Ga-rich Surface Energy (meV/Å^2)
Symmetric	96	112	57.19	87.10
H*-passivated	96	112	57.68	87.59

Table 2.2 Surface energies comparison between P-rich GaP(001) (2x1) with and without passivation

The validity of this approach being checked, we applied it to the polar GaP(114) and GaP(136) surfaces.

2.6.3. H*-passivation approach applied to GaP(114) and GaP(2 5 11) surfaces

The bottom surfaces of the slabs were passivated with fictitious H^* atoms [48] as it has been fruitfully demonstrated on a similar semiconducting GaAs crystal [44], [49], [50]. Contrary to the previous case explained in section 2.6.2, the surfaces are formed by both Ga and P atoms. Therefore, to determine the surface energy we need to include two new terms inherent to the fictitious H^* atoms $N_{H^*}^{Ga}\mu_{H^*}^{Ga} + N_{H^*}^{P}\mu_{H^*}^{P}$:

$$\gamma_{polar} = \frac{E_{slab} - N_{Ga}\mu_{GaP}^{GaP-bulk} - (N_P - N_{Ga})\mu_P - N_{H^*}^{Ga}\mu_{H^*}^{Ga} - N_{H^*}^{P}\mu_{H^*}^{P}}{A} \qquad \textbf{(2.24)}$$

where $N_{H^*}^{i}$ and $\mu_{H^*}^{i}$ are the number and the chemical potential of fictitious H^* bonded to the species *i* (where i is Ga, or P), and A is the reconstructed surface area. In our case, the polar GaP(114) surfaces studied are fulfilling the ECM criterion and are stoichiometric *i.e.*, ΔN=0, which means that the surface energy does not depends on the chemical potential μ_P. On the contrary, the GaP(2 5 11) surfaces are respecting the ECM but are non-stoichiometric, so here we have to consider these dependences. The slabs built, in both cases, to determine the value of the sum $\mu_{H^*}^{Ga} + \mu_{H^*}^{P}$ of the two chemical potentials of the fictitious H^* atoms, were similar to the one depicted in **Figure 2.11(a)**. For both GaP(114) and GaP(2 5 11) surfaces, $N_{H^*}^{Ga}$ and $N_{H^*}^{P}$ numbers of fictitious H^* atoms are exactly equal, so to simplify we can rename it as N_{H^*}. Finally, sum of the chemical potentials $\mu_{H^*}^{Ga} + \mu_{H^*}^{P}$ can be determined through this equation:

$$\mu_{H^*}^{Ga} + \mu_{H^*}^{P} = \frac{E_{slab}^{H^*-passivated} - N_{GaP}\mu_{GaP}^{GaP-bulk}}{N_{H^*}} \qquad \textbf{(2.25)}$$

where $E_{slab}^{H^*-passivated}$ is the energy of the slab when only the fictitious H^* atoms on the top and bottom have been minimized, N_{GaP} is the number of GaP pair within the slab and N_{H^*} and

$\mu_{GaP}^{GaP-bulk}$ have been already defined above.

The slabs, with H*-passivation on both sides for both GaP(114) and GaP(2 5 11) cases, are stoichiometric. Therefore, the sum $\mu_{H^*}^{Ga} + \mu_{H^*}^{P}$ of the fictitious hydrogen chemical potentials does not depend on the phosphorus chemical potential. To our experience, the sum $\mu_{H^*}^{Ga} + \mu_{H^*}^{P}$ of the two chemical potentials of the fictitious H^* highly depends on the studied surface and should not have the same value from one surface to another.

Finally, in order to strengthen the validation of the H*-passivation method in the case of GaP(114) surface, we also calculated the surface energy for the polar GaAs(114) as a test to compare with previous studies [50]. As a result, we found exactly the same surface energy for the As-rich GaAs(114)A-α2(2x1) reconstruction than the one given in ref. [50]. The values are reported in **Table 2.3**. Finally, the Ga-rich GaAs(114)B-α2(2x1) surface energy has also been estimated and a higher value by about 6.1 meV/Å² was found, as compared to the type A surface.

GaAs surface energies γ	As-rich (previous work) GaAs(114)A-α2(2x1)[50]	As-rich (this work) GaAs(114)A-α2(2x1)	Ga-rich (this work) GaAs(114)B-α2(2x1)
Ga-rich	53	53.0	59.1
As-rich	53	53.0	59.1

Table 2.3 GaAs surface energies γ, in units of meV/Å², for the GaAs(114)B-α2(2x1) and the GaAs(114)A-α2(2x1) reconstructions, compared to a previous study on the GaAs(114)A surface[50].

2.7.GaP(001), GaP(114) and GaP(2 5 11) surface energies

In **Figure 2.12**, all the GaP surfaces energies versus the chemical potential variations are shown. As mentioned above, the chemical potential $\Delta\mu_P$ has to vary between two extreme thermodynamic conditions: Ga-rich limit (i.e. bulk Ga will form preferentially) and P-rich limit (bulk P will form preferentially). In particular, the P-rich limit is when $\mu_P = \mu_P^{P-bulk}$ while the Ga-rich limit corresponds to the case when $\Delta\mu_P$ is equal to the GaP heat of formation ($\Delta H_f(GaP) =$ -0.928eV) which has been calculated with the black phosphorus phase and the orthorhombic α-Ga phase[28], [29].

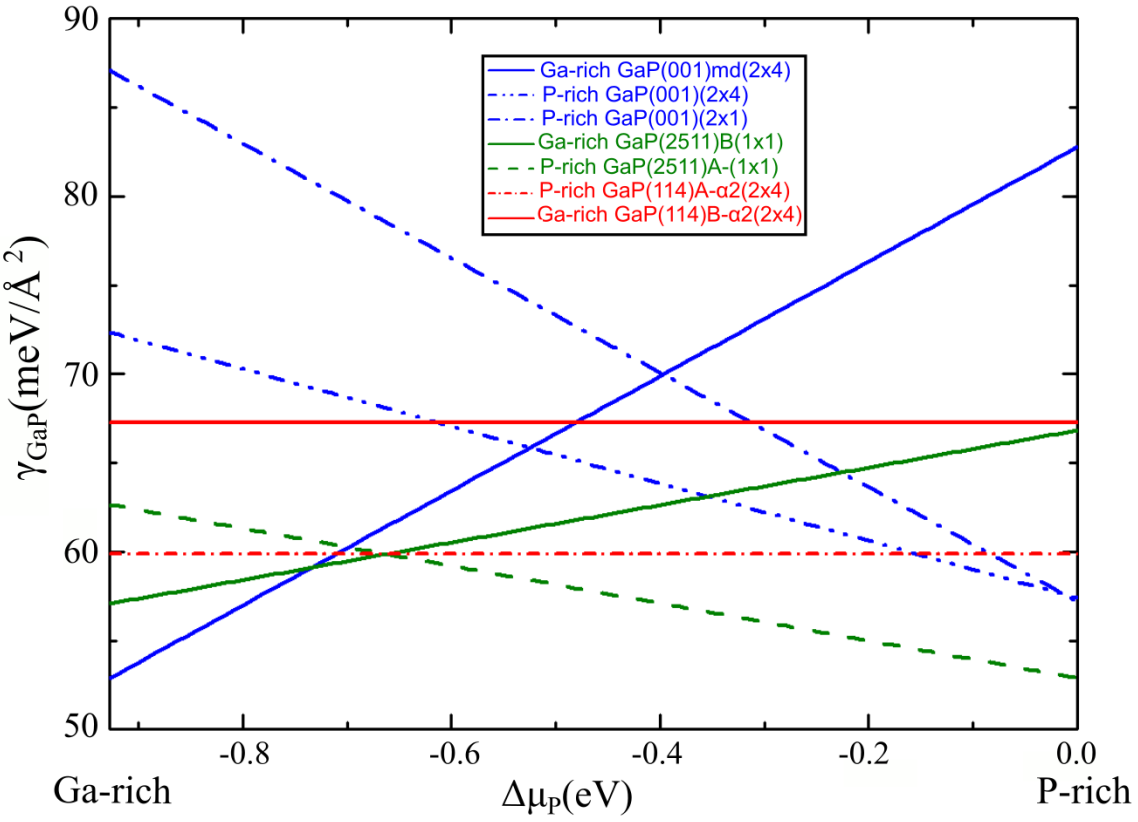

Figure 2.12 GaP(001), (114) and (2 5 11) surface energies as a function of the chemical potential

The slope of both the GaP(001) and GaP(2 5 11) surface energy curves (represented with blue and green curves respectively) is inherent to their stoichiometry. Indeed, all of them are non-stoichiometric, *i.e.*, $N_P \neq N_{Ga}$. In particular, in the case of the GaP(001) surfaces, we find ΔN=4 for the P-rich GaP(001)(2x4) while ΔN=-8 for the Ga-rich GaP(001)md(2x4) and ΔN=8 for the P-rich GaP(001)(2x1). For the GaP(2 5 11)A-(1x1) and the GaP(2 5 11)B-(1x1) surfaces ΔN is equal to 2 and -2 respectively. Finally, the GaP(114)A-α2(2x1) and the GaP(114)B-α2(2x1) surfaces are stoichiometric (ΔN=0) which implies that the surface energy is constant upon the variations of the chemical potential for these surfaces. Consequently, their surface energies (the red curves) are constant with the chemical potential. Their values are 59.9meV/$Å^2$ and 67.3meV/$Å^2$ respectively. In particular, the GaP(114)A-α2(2x1) surface is thermodynamically

more stable than the GaP(114)B-α2(2x1) surface, as already reported in previous works for the GaAs material. The GaAs(114)A surface energy was found to lie 3meV/$Å^2$ below the GaAs(114)B [43].

In the Ga-rich limit the most stable reconstructions are the Ga-terminated surfaces. The most stable one is the GaP(001)md(2x4) with an energy of 52.9meV/$Å^2$. The GaP(2 5 11)B-(1x1) has an energy just 4.2meV/$Å^2$ higher (dashed green line). The P-terminated reconstructions have a higher energy. Indeed, the GaP(2 5 11)B-(1x1) is energetically less favorable with an energy of 62.7meV/$Å^2$, the P-rich GaP(001) (2x4) has an energy of 72.4meV/$Å^2$ but the most unstable is the P-rich GaP(001)(2x1) with an energy of 87.1meV/$Å^2$. However, this is an expected result since this surface does not fulfill the ECM criterion.

In the P-rich limit the most stable surface is the P-rich GaP(2 5 11)A-(1x1) one, which has the lowest energy with a value of 52.9meV/$Å^2$. The similarity between the P-rich GaP(001)(2x4) and (2x1) surfaces reconstruction makes them having surface energies which differ just of 0.2meV/$Å^2$. The P-rich GaP (2 5 11)B-(1x1) has an energy value of 66.8meV/$Å^2$. The Ga-rich GaP(001)md(2x4) is here the most unstable with an energy of 82.8meV/$Å^2$. All the surface energies values are summarized in **Table 2.4**.

In conclusion, the surface energies of various (001), (114) and (2511) surfaces have been computed by DFT in this section, and summarized in table 4 and figure 12. While (001) surfaces are traditionally considered as the most stable surfaces, we here evidence that this conclusion is not straightforward for GaP, where (114) and (2511) surfaces have a remarkable stability. This will be discussed in Chapter 3 and Chapter 5.

2.8.GaP/Si interface energies

To clarify III-V/Si epitaxial processes, it is required to have an idea about the energy involved, and more specifically about the III-V/Si interface energies. In this part, we will focus on the determination of the absolute GaP/Si interface energy. So far, the GaP/Si interface energy has already been investigated in previous works. Indeed, results on the relative interface formation energy of the GaP on different Si surfaces has been already presented [31]. The

GaP surfaces Reconstructions	$\Delta N_{surface}$	Energy [meV/Å²]	
		P-rich	Ga-rich
	$(N_P - N_{Ga})/2$		
P-rich GaP(001) (2x1)	8	57.2	87.1
P-rich GaP(001) (2x4)	4	57.4	72.4
P-rich GaP(001) md(2x4)	-8	82.8	52.9
	$N_P - N_{Ga}$		
P-rich GaP(114)A-α2(2x1)	0	59.9	59.9
Ga-rich GaP(114)B-α2(2x1)	0	67.3	67.3
P-rich GaP(2 5 11)A-(1x1)	2	52.9	62.7
Ga-rich GaP(2 5 11)B-(1x1)	-2	66.8	57.1

Table 2.4 Summary of the computed GaP(001), (114) and (136) surface energies and surface stoichiometries

stability of the compensated GaP/Si(001) interface with respect to an abrupt one has been reported as well in references [32], [51] by calculating its relative formation energy. Compensated interfaces consist in intermixing Si-P or Si-Ga atoms at the interface layer. The most energetically stable compensated interfaces already known from the literature [51] are composed by Si/Ga(P) 0.5/0.5 ratio. They are called the 0.5 Si : 0.5 P–Ga and 0.5 Si : 0.5 Ga–P. These interfaces, unlike the abrupt ones, fulfill the ECM [32] which leads to a lower interface energy due to their higher stability. The determination of GaP/Si(001) absolute abrupt interface energy has also been attempted [52] but these studies were not taking into account the dependency to the chemical potential, as commented in reference [53]. Finally, a correct value of the GaP/Si(001) absolute abrupt interface energy has not been found yet.

In this section, we present our DFT calculations to determine the GaP/Si(001) absolute abrupt and compensated interface energies as a function of the chemical potential.

2.8.1. DFT common computational details

The slabs to determine the abrupt interfaces energies are shown in **Figure 2.13(a-d)**, while for the compensated case they are shown in **Figure 2.14(a-d)**. For each interface, the top surface is modeled by the stable reconstructions studied for the GaP(001): Ga-rich GaP(001)md (2x4) or P-rich GaP(001)(2x4) which obey to the ECM. All of the slabs are simulated with a 450Å-thick vacuum region. Moreover, to avoid any surface/interface interaction, both the GaP and Si bulk are, in each case, at least 20Å thick each. More precisely, the slab length of **Figure 2.13(a) and Figure 2.14(a)** is 42.31Å while that one for **Figure 2.13(b) and Figure 2.14(b)** is 43.62Å. Instead, the slabs in **Figure 2.13(c) and Figure 2.14(c)** are 45.04Å long and finally the **Figure 2.13(d) and Figure 2.14(d)** slab length is 40.95Å. For each slab, the basis vectors length are 15.44Å and 7.72Å. We choose the Si(001) as bottom surface of each case investigated. Finally, the entire GaP together with the two first layers of silicon at the interface was relaxed, while the rest has been frozen.

2.8.2. Compensated interfaces

Building compensated interfaces consists in intermixing Si-P or Si-Ga atoms at the interface layer. For this study, we took into account the most energetically stable structures [51] where the Si/Ga(P) ratio is 0.5/0.5. They are called the 0.5 Si : 0.5 P–Ga and 0.5 Si : 0.5 Ga–P. The most important difference with respect to the abrupt interfaces is that these intermixed ones fulfill the ECM [32] which leads to a lower interface energy because of their higher stability. The 0.5 Si : 0.5 P–Ga interfaces with P-rich GaP(001)(2x4) and Ga-rich GaP(001)md (2x4) surface are presented in **Figure 2.14(a) and (b)** respectively. While the 0.5 Si : 0.5 Ga–P with P-rich GaP(001)(2x4) and Ga-rich GaP(001)md (2x4) surface respectively, are shown in **Figure 2.14(c) and (d)**.

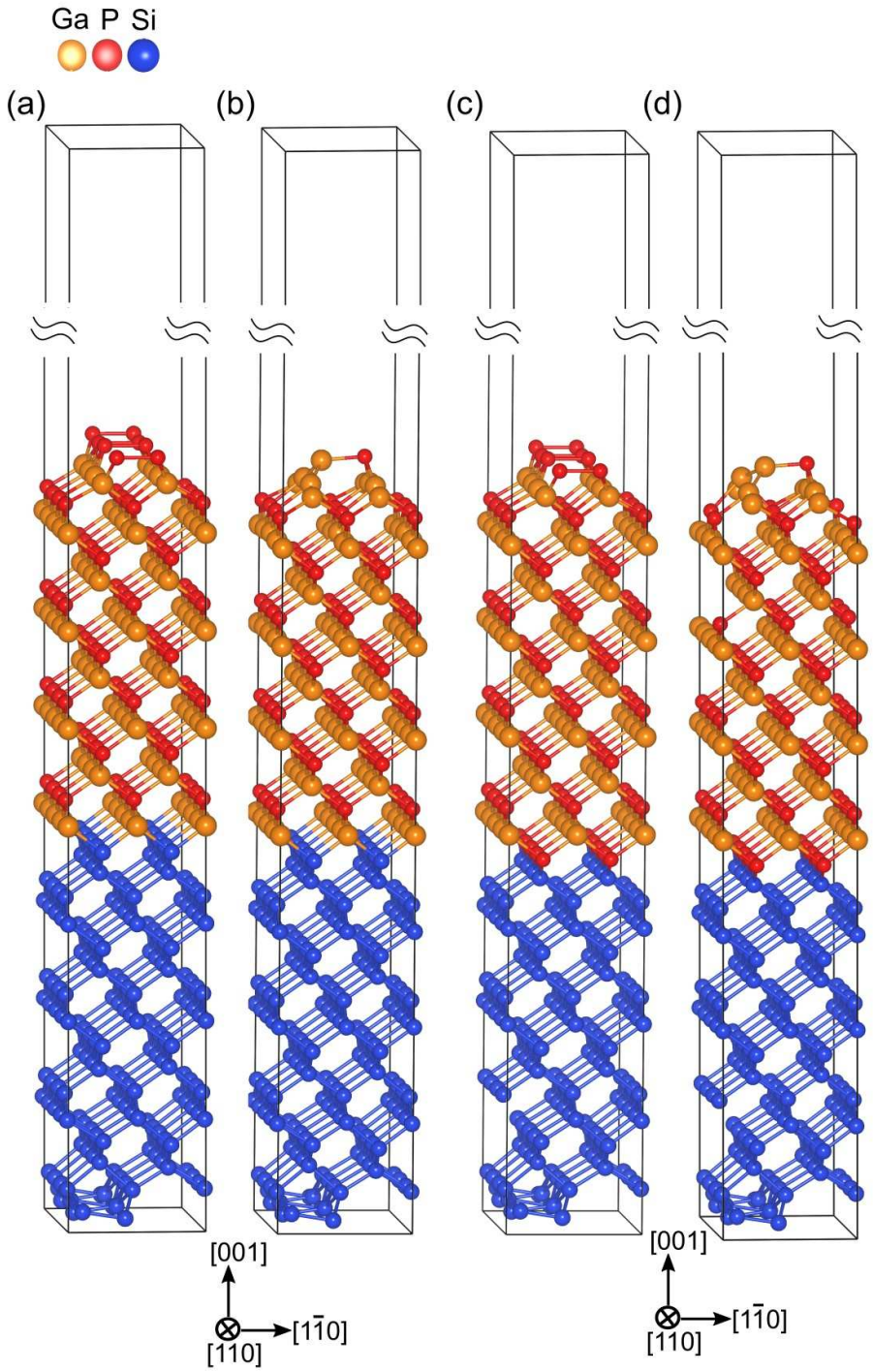

Figure 2.13 Slabs used for the DFT calculation of absolute interface energy of the Ga-Si interface with(a) P-rich GaP(001)(2x4) and(b) Ga-rich GaP(001)md (2x4) top surfaces reconstructions. Slabs used for the DFT calculation of absolute interface energy of the P-Si interface with(c) P-rich GaP(001)(2x4) and d) Ga-rich GaP(001)md (2x4) top surfaces reconstructions.

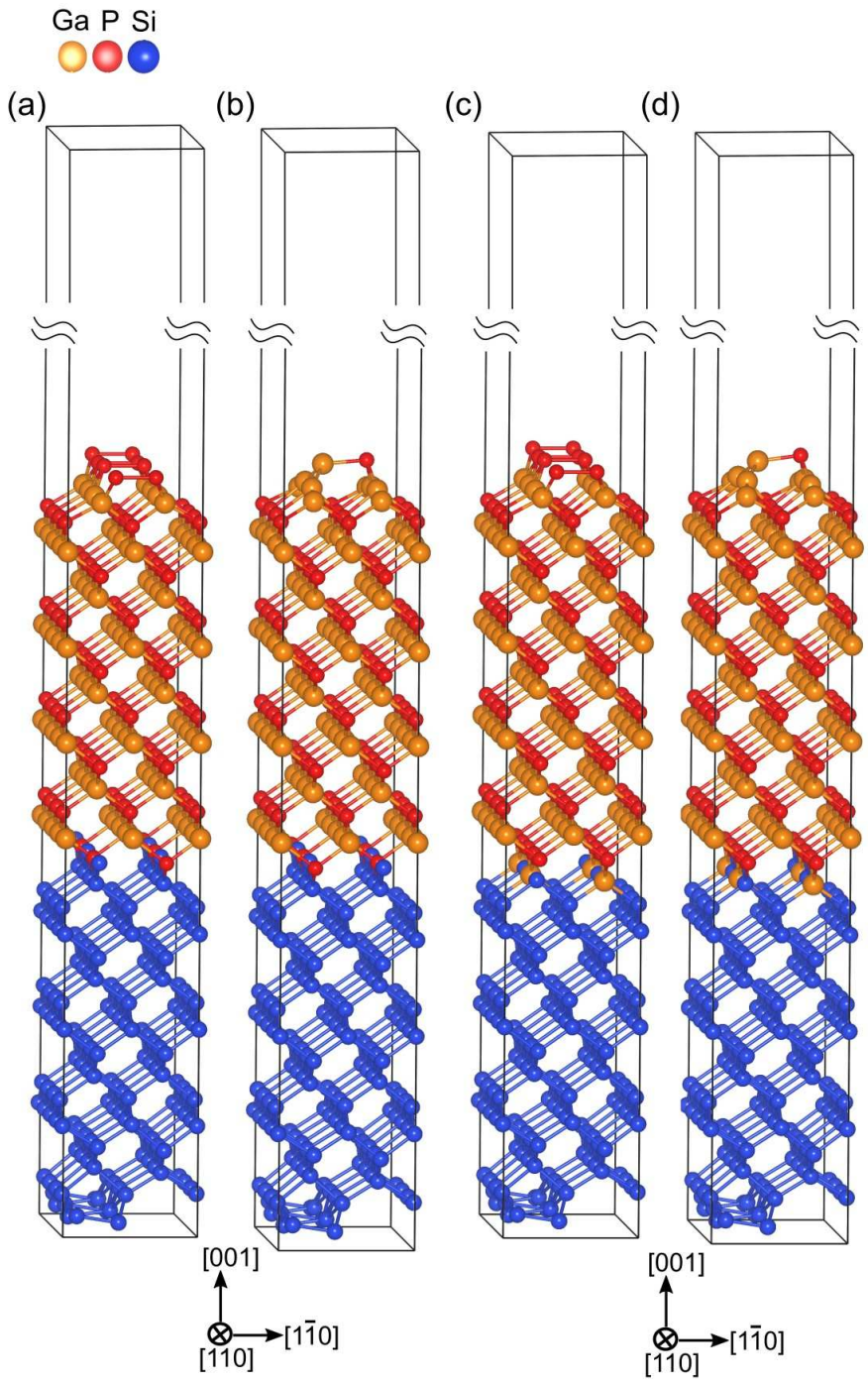

Figure 2.14 Slabs used for the DFT calculation of absolute interface energy of the 0.5 Si: 0.5 P–Ga compensated interface with (a) P-rich GaP(001)(2x4) and (b) Ga-rich GaP(001)md (2x4) top surfaces reconstructions. Slabs used for the DFT calculation of absolute interface energy of the 0.5 Si : 0.5 Ga–P compensated interface with (c) P-rich GaP(001)(2x4) and (d) Ga-rich GaP(001)md (2x4) top surfaces reconstructions.

2.8.3. Abrupt and compensated interface energies calculation

In the following, the interface energy will be noted ${}^{X}\gamma_{Z}^{Y}$, and expressed in meV/Å². X makes reference to the studied interface. Y and Z are the top and bottom specific surfaces of the slabrelated to the two considered materials. We are aware that the interface energies do not depend theoretically of the used top and bottom surfaces, but different slabs have been used to validate the method, and check uncertainties on the result. Here, the X interfaces for Silicon and GaP materials are Si-Ga or Si-P, abrupt or compensated.

	N [N_P-N_{Ga}]	Energy [meV/Å²]	
		P-rich	Ga-rich
Abrupt interfaces			
${}^{Si-Ga}\gamma_{\text{GaP (001) 2x4}}^{\text{Si (100)}}$	-4	72.0	40.8
${}^{Si-Ga}\gamma_{\text{GaP (001) 2x4md}}^{\text{Si (100)}}$	-4	69.7	38.5
${}^{Si-P}\gamma_{\text{GaP (001) 2x4}}^{\text{Si (100)}}$	+4	25.9	57.1
${}^{Si-P}\gamma_{\text{GaP (001) 2x4md}}^{\text{Si (100)}}$	+4	27.3	58.4
Compensated interfaces			
${}^{0.5Si:0.5P-Ga}\gamma_{\text{GaP (001) 2x4}}^{\text{Si (100)}}$	0	28.3	28.3
${}^{0.5Si:0.5P-Ga}\gamma_{\text{GaP (001) 2x4md}}^{\text{Si (100)}}$	0	26.2	26.2
${}^{0.5Si:0.5Ga-P}\gamma_{\text{GaP (001) 2x4}}^{\text{Si (100)}}$	0	24.7	24.7
${}^{0.5Si:0.5Ga-P}\gamma_{\text{GaP (001) 2x4md}}^{\text{Si (100)}}$	0	22.1	22.1

Table 2.5 Abrupt and compensated GaP/Si interface energies computed by DFT. N is the stoichiometry of the interface

The equation is the following:

$$ {}^{X}\gamma_{Z}^{Y} = \frac{E_{slab}^{int} - \sum_{i=Y,Z}(E_{bulk}^{i} + A\gamma_{surf}^{i})}{A} \quad \textbf{(2.26)} $$

where E_{slab}^{int} is the total energy of the slab, E_{bulk}^{i} and γ_{surf}^{i} are respectively the energy of the bulk material i and the specific surface energy for material i (with Y and Z). Then, we can rewrite this overall relation for our specific case such as:

Interfaces	ΔN_{slab}	$\Delta N_{surface}^{Top}$	$\Delta N_{interface}$
$Si-Ga\gamma_{\text{GaP (001) 2x4}}^{\text{Si (100)}}$	-2	2	-4
$Si-Ga\gamma_{\text{GaP (001) 2x4md}}^{\text{Si (100)}}$	-8	-4	-4
$Si-P\gamma_{\text{GaP (001) 2x4}}^{\text{Si (100)}}$	6	2	+4
$Si-P\gamma_{\text{GaP (001) 2x4md}}^{\text{Si (100)}}$	0	-4	+4
$\text{0.5Si:0.5P}-\text{Ga}\gamma_{\text{GaP (001) 2x4}}^{\text{Si (100)}}$	2	2	0
$\text{0.5Si:0.5P}-\text{Ga}\gamma_{\text{GaP (001) 2x4md}}^{\text{Si (100)}}$	-4	-4	0
$\text{0.5Si:0.5Ga}-\text{P}\gamma_{\text{GaP (001) 2x4}}^{\text{Si (100)}}$	2	2	0
$\text{0.5Si:0.5Ga}-\text{P}\gamma_{\text{GaP (001) 2x4md}}^{\text{Si (100)}}$	-4	-4	0

Table 2.6 Abrupt and compensated interfaces stoichiometry $\Delta N_{interface} = \Delta N_{slab} - \Delta N_{surface}^{Top}$

$$ {}^{X}\gamma_{Z}^{Y} = \frac{E_{slab}^{int} - N_{GaP}\mu_{GaP}^{GaP-bulk} - (N_P - N_{Ga})\mu_P - N_{Si}E_{bulk}^{Si} - A\gamma_{surf}^{Si} - A\gamma_{surf}^{GaP}}{A} \quad \textbf{(2.27)} $$

where E_{slab}^{int} is defined above, N_{GaP} is the number of GaP pairs, N_{Ga} and N_P are respectively the number of Ga and P atoms of the slab investigated, $\mu_{GaP}^{GaP-bulk}$ and μ_P are the chemical potentials of the bulk GaP and of the species P and A is the surface area. E_{bulk}^{Si} is the silicon bulk energy while N_{Si} is the number of silicon atoms. γ_{surf}^{Si} and γ_{surf}^{GaP} are the specific bottom and top surface energy per unit area. The chemical potential of species P varies in the same interval

range than the GaP surfaces case (see previous sections). All the energy values are summarized in **Table 2.5**.

We can see that the abrupt interface energy varies with the chemical potential while the compensated ones are constant. This is related to their stoichiometry which can be determined by the following equation:

$$\Delta N_{slab} = \Delta N_{surface}^{Top} + \Delta N_{interface} + \Delta N_{GaP}^{Bulk} \quad \textbf{(2.28)}$$

where ΔN_{slab} , $\Delta N_{surface}^{Top}$, $\Delta N_{interface}$ and ΔN_{GaP}^{Bulk} are respectively the slab, the top surface, the interface stoichiometry and the GaP bulk stoichiometry which is by definition equal to zero (without any doping). Their values are presented in **Table 2.6**.

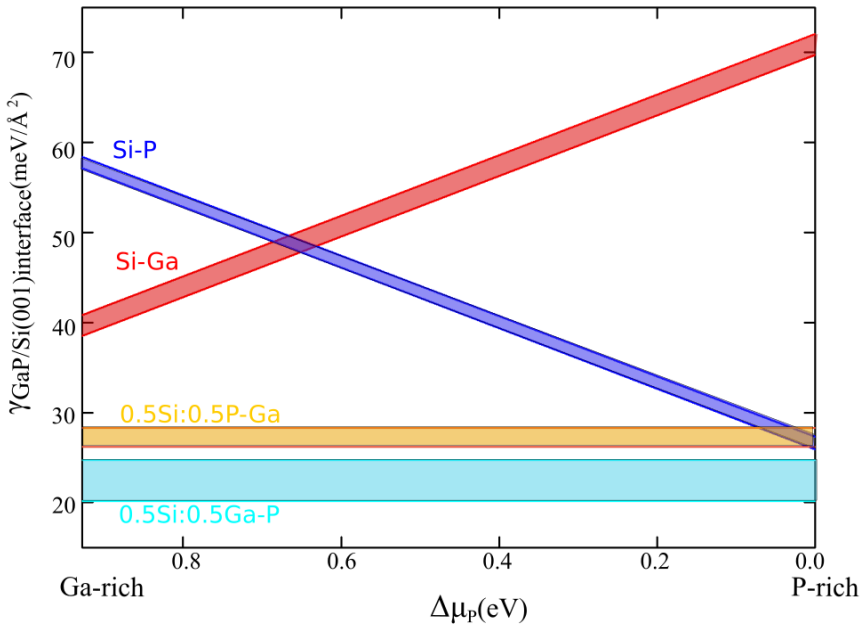

Figure 2.15 Interface energies incertitude diagram of both compensated an abrupt absolute interface energies computed by DFT. The width of each energy corresponds to the numerical uncertainty. As reported in [33] the compensated 0.5 Si : 0.5 Ga-P and 0.5 Si : 0.5 P-Ga energies are more stable with respect the abrupt ones because they fulfill the ECM criterion. Moreover, their energy do not vary with the chemical potential $\Delta\mu_P$, as expected because of their stoichiometry ($\Delta N=0$)

The width of each energy corresponds to the numerical uncertainty. Indeed, for verifying the results for a given interface, its absolute energy was determined by considering two different

surfaces. The energies associated to the two different cases determine the bounderies of each interval of uncertenity. Moreover, since the compensated interfaces are stoichiometric, their energies are constants with the chemical potential. Instead, the abrupt interfaces are not, so their energies vary with the chemical potential.

We can conclude that the Si-Ga interface is always more stable in Ga-rich environment while the Si-P interface is stable in the P-rich one. Moreover, this is independent of the kind of surface considered with a small numerical absolute error which is around 2.6 meV/$Å^2$. Finally, the absolute variation of the interface energy from P-rich to Ga-rich conditions is of 31.2meV/Å² for both Si-Ga and Si-P abrupt interface respectively, which is expected, given the opposite stoichiometry of the two interfaces. The compensated absolute interface energy is constant with the chemical potential, as expected because of their stoichiometry (ΔN=0), and the numerical absolute error is still small (2.35 meV/$Å^2$). The compensated and abrupt interface energy ranges as a function of the chemical potential are plotted in **Figure 2.15**.

2.9.Conclusions

In this chapter, we presented a thorough investigation of GaP and Si surface/interface energies by DFT. We have calculated the surface energies of Si(001) surfaces with and without steps. We have shown that the steps do not impact too much the silicon surface energy. We then computed the non-polar GaP(001) and polar GaP(114) and GaP(2 5 11) surface energies by using two different approaches depending on the different surfaces polarity. We verified the ECM criterion for every surface investigated, and showed that (114) and (2 5 11) facets are remarkably stable GaP surfaces. We also computed for the first time the absolute abrupt and compensated interface energies and confirmed the stability of the latter with respect to the first ones. The numerical errors associated to our DFT calculations are about 0.5meV for bulks, about 1.5meV/Å² for surfaces and 6meV/Å² for interfaces. However, we systematically compared, when possible, our results with the literature. Furthermore, interpretation of these results including errors does not affect the physic and the general tendency.

These results will be at the heart of the discussions and calculations performed Chapter 3 and Chapter 5.

References

[1] P. Hohenberg and W. Kohn, 'Inhomogeneous Electron Gas', *Phys. Rev.*, vol. 136, no. 3B, pp. B864–B871, Nov. 1964.

[2] W. Kohn and L. J. Sham, 'Self-Consistent Equations Including Exchange and Correlation Effects', *Phys. Rev.*, vol. 140, no. 4A, pp. A1133–A1138, Nov. 1965.

[3] D. R. Hartree, 'The Wave Mechanics of an Atom with a Non-Coulomb Central Field. Part II. Some Results and Discussion', *Mathematical Proceedings of the Cambridge Philosophical Society*, vol. 24, no. 1, pp. 111–132, Jan. 1928.

[4] V. Fock, 'Näherungsmethode zur Lösung des quantenmechanischen Mehrkörperproblems', *Z. Physik*, vol. 61, no. 1–2, pp. 126–148, Jan. 1930.

[5] L. H. Thomas, 'The calculation of atomic fields', *Mathematical Proceedings of the Cambridge Philosophical Society*, vol. 23, no. 5, pp. 542–548, Jan. 1927.

[6] P. a. M. Dirac, 'Note on Exchange Phenomena in the Thomas Atom', *Mathematical Proceedings of the Cambridge Philosophical Society*, vol. 26, no. 3, pp. 376–385, Jul. 1930.

[7] J. P. Perdew, K. Burke, and M. Ernzerhof, 'Generalized Gradient Approximation Made Simple', *Phys. Rev. Lett.*, vol. 77, no. 18, pp. 3865–3868, Oct. 1996.

[8] J. P. Perdew, K. Burke, and M. Ernzerhof, 'Generalized Gradient Approximation Made Simple [Phys. Rev. Lett. 77, 3865 (1996)]', *Phys. Rev. Lett.*, vol. 78, no. 7, pp. 1396–1396, Feb. 1997.

[9] J. M. Soler *et al.*, 'The SIESTA method for *ab initio* order- *N* materials simulation', *Journal of Physics: Condensed Matter*, vol. 14, no. 11, pp. 2745–2779, Mar. 2002.

[10] E. Artacho *et al.*, 'The SIESTA method; developments and applicability', *Journal of Physics: Condensed Matter*, vol. 20, no. 6, p. 064208, Feb. 2008.

[11] E. Artacho, D. Sanchez-Portal, P. Ordejon, A. Garcia, and J. M. Soler, 'Linear-Scaling ab-initio Calculations for Large and Complex Systems', *physica status solidi (b)*, vol. 215, no. 1, pp. 809–817, Sep. 1999.

[12] N. Troullier and J. L. Martins, 'Efficient pseudopotentials for plane-wave calculations', *Physical Review B*, vol. 43, no. 3, pp. 1993–2006, Jan. 1991.

[13] T. Hom, W. Kiszenik, and B. Post, 'Accurate lattice constants from multiple reflection measurements. II. Lattice constants of germanium silicon, and diamond', *J Appl Cryst, J Appl Crystallogr*, vol. 8, no. 4, pp. 457–458, Aug. 1975.

[14] M. S. Shur, *Handbook Series on Semiconductor Parameters*. World Scientific, 1996.

[15] R. M. Tromp, R. J. Hamers, and J. E. Demuth, 'Si(001) Dimer Structure Observed with Scanning Tunneling Microscopy', *Phys. Rev. Lett.*, vol. 55, no. 12, pp. 1303–1306, Sep. 1985.

[16] D. J. Chadi, 'Stabilities of single-layer and bilayer steps on Si(001) surfaces', *Phys. Rev. Lett.*, vol. 59, no. 15, pp. 1691–1694, Oct. 1987.

[17] R. J. Hamers, R. M. Tromp, and J. E. Demuth, 'Scanning tunneling microscopy of Si(001)', *Phys. Rev. B*, vol. 34, no. 8, pp. 5343–5357, Oct. 1986.

[18] D. J. Chadi, 'Atomic and Electronic Structures of Reconstructed Si(100) Surfaces', *Phys. Rev. Lett.*, vol. 43, no. 1, pp. 43–47, Jul. 1979.

[19] P. Bogusławski, Q.-M. Zhang, Z. Zhang, and J. Bernholc, 'Structure of monatomic steps on the Si(001) surface', *Phys. Rev. Lett.*, vol. 72, no. 23, pp. 3694–3697, juin 1994.

[20] D. E. Aspnes and J. Ihm, 'Biatomic Steps on (001) Silicon Surfaces', *Phys. Rev. Lett.*, vol. 57, no. 24, pp. 3054–3057, décembre 1986.
[21] A. Ramstad, G. Brocks, and P. J. Kelly, 'Theoretical study of the Si(100) surface reconstruction', *Phys. Rev. B*, vol. 51, no. 20, pp. 14504–14523, mai 1995.
[22] E. Artacho, D. Sanchez-Portal, P. Ordejon, A. Garcia, and J. M. Soler, 'Linear-scaling ab-initio calculations for large and complex systems', *physica status solidi (b)*, vol. 215, no. 1, pp. 809–817, Sep. 1999.
[23] J. Pack and H. Monkhorst, '"Special points for Brillouin-zone integrations"—a reply', *Phys. Rev. B*, vol. 16, no. 4, pp. 1748–1749, août 1977.
[24] C. Y. Zinchenko, N. L. Shwartz, Z. S. Yanovitskaja, and Y. N. Morokov, 'Ab Initio Calculations of the Si(001) Surface Reconstructions using Density Functional Theory', in *International Workshops and Tutorials on Electron Devices and Materials*, 2006, pp. 55–57.
[25] H. J. W. Zandvliet, 'Energetics of Si(001)', *Rev. Mod. Phys.*, vol. 72, no. 2, pp. 593–602, avril 2000.
[26] B. Li, A. Michaelides, and M. Scheffler, 'Density functional theory study of flat and stepped NaCl(001)', *Phys. Rev. B*, vol. 76, no. 7, p. 075401, août 2007.
[27] M. D. Pashley, 'Electron counting model and its application to island structures on molecular-beam epitaxy grown GaAs(001) and ZnSe(001)', *Phys. Rev. B*, vol. 40, no. 15, pp. 10481–10487, Nov. 1989.
[28] L. Cartz, S. R. Srinivasa, R. J. Riedner, J. D. Jorgensen, and T. G. Worlton, 'Effect of pressure on bonding in black phosphorus', *The Journal of Chemical Physics*, vol. 71, no. 4, pp. 1718–1721, Aug. 1979.
[29] H. Curien, A. Rimsky, and A. Defrain, 'Structure atomique d'une phase cristalline du gallium, instable a la pression atmospherique Locality: synthetic Sample: at T = 256.85 K', *Bulletin de la Societe Francaise de Mineralogie et de Cristallographie*, vol. 84, pp. 260–264, 1961.
[30] 'Basic Parameters of Gallium Phosphide (GaP)'. [Online]. Available: http://www.ioffe.ru/SVA/NSM/Semicond/GaP/basic.html. [Accessed: 20-Oct-2017].
[31] O. Romanyuk, T. Hannappel, and F. Grosse, 'Atomic and electronic structure of GaP/Si(111), GaP/Si(110), and GaP/Si(113) interfaces and superlattices studied by density functional theory', *Phys. Rev. B*, vol. 88, no. 11, p. 115312, Sep. 2013.
[32] O. Supplie *et al.*, 'Atomic scale analysis of the GaP/Si(100) heterointerface by in situ reflection anisotropy spectroscopy and ab initio density functional theory', *Phys. Rev. B*, vol. 90, no. 23, p. 235301, décembre 2014.
[33] V. Kumar and B. S. R. Sastry, 'Heats of formation of binary semiconductors', *phys. stat. sol. (b)*, vol. 242, no. 4, pp. 869–872, Mar. 2005.
[34] S. Mirbt, N. Moll, K. Cho, and J. D. Joannopoulos, 'Cation-rich (100) surface reconstructions of InP and GaP', *Physical Review B*, vol. 60, p. 13283, Nov. 1999.
[35] K. Luedge, P. Vogt, O. Pulci, N. Esser, F. Bechstedt, and W. Richter, 'Clarification of the GaP(001)(2x4) Ga-rich reconstruction by scanning tunneling microscopy and ab initio theory', *PHYSICAL REVIEW. B, CONDENSED MATTER AND MATERIALS PHYSICS*, vol. 62, no. 16, pp. 11046–11049, 2000.

[36] H. Döscher and T. Hannappel, 'In situ reflection anisotropy spectroscopy analysis of heteroepitaxial GaP films grown on Si(100)', *Journal of Applied Physics*, vol. 107, no. 12, p. 123523, juin 2010.
[37] O. Supplie, M. M. May, H. Stange, C. Höhn, H.-J. Lewerenz, and T. Hannappel, 'Materials for light-induced water splitting: In situ controlled surface preparation of GaPN epilayers grown lattice-matched on Si(100)', *Journal of Applied Physics*, vol. 115, no. 11, p. 113509, Mar. 2014.
[38] M. M. May, O. Supplie, C. Höhn, R. van de Krol, H.-J. Lewerenz, and T. Hannappel, 'The interface of GaP(100) and H 2 O studied by photoemission and reflection anisotropy spectroscopy', *New J. Phys.*, vol. 15, no. 10, p. 103003, 2013.
[39] O. Pulci *et al.*, 'First-principles study of InP and GaP(001) surfaces', *Computational Materials Science*, vol. 22, no. 1, pp. 32–37, Nov. 2001.
[40] Y. Zhang *et al.*, 'Pseudo-Hydrogen Passivation: A Novel Way to Calculate Absolute Surface Energy of Zinc Blende (111)/($\bar{1}\,\bar{1}\,\bar{1}$) Surface', *Scientific Reports*, vol. 6, no. 1, Apr. 2016.
[41] J. Márquez, P. Kratzer, and K. Jacobi, 'Structure and morphology of the As-rich and the stoichiometric GaAs(114)A surface', *Journal of Applied Physics*, vol. 95, no. 12, pp. 7645–7654, Jun. 2004.
[42] J. Márquez, P. Kratzer, L. Geelhaar, K. Jacobi, and M. Scheffler, 'Atomic Structure of the Stoichiometric GaAs(114) Surface', *Phys. Rev. Lett.*, vol. 86, no. 1, pp. 115–118, Jan. 2001.
[43] R. D. Smardon and G. P. Srivastava, 'Electronic structure of the GaAs (114) A-(2× 1) and GaAs (114) B-(2× 1) surfaces', *Phys. Rev. B*, vol. 72, juillet 2005.
[44] L. Geelhaar, J. Márquez, P. Kratzer, and K. Jacobi, 'GaAs(2511)$: A New Stable Surface within the Stereographic Triangle', *Phys. Rev. Lett.*, vol. 86, no. 17, pp. 3815–3818, Apr. 2001.
[45] Y. Temko, L. Geelhaar, T. Suzuki, and K. Jacobi, 'Step structure on the GaAs(2511) surface', *Surface Science*, vol. 513, no. 2, pp. 328–342, juillet 2002.
[46] K. Jacobi, L. Geelhaar, and J. Márquez, 'Structure of high-index GaAs surfaces – the discovery of the stable GaAs (2 5 11) surface', *Appl Phys A*, vol. 75, no. 1, pp. 113–127, Jul. 2002.
[47] R. Méndez-Camacho, V. H. Méndez-García, M. López-López, and E. Cruz-Hernández, 'New orientations in the stereographic triangle for self-assembled faceting', *AIP Advances*, vol. 6, no. 6, p. 065023, juin 2016.
[48] K. Shiraishi, 'A New Slab Model Approach for Electronic Structure Calculation of Polar Semiconductor Surface', *Journal of the Physical Society of Japan*, vol. 59, no. 10, pp. 3455–3458, Oct. 1990.
[49] N. Moll, A. Kley, E. Pehlke, and M. Scheffler, 'GaAs equilibrium crystal shape from first principles', *Phys. Rev. B*, vol. 54, no. 12, pp. 8844–8855, Sep. 1996.
[50] J. Márquez, P. Kratzer, L. Geelhaar, K. Jacobi, and M. Scheffler, 'Atomic Structure of the Stoichiometric GaAs(114) Surface', *Phys. Rev. Lett.*, vol. 86, no. 1, pp. 115–118, Jan. 2001.
[51] O. Romanyuk, O. Supplie, T. Susi, M. M. May, and T. Hannappel, 'Ab initio density functional theory study on the atomic and electronic structure of GaP/Si(001) heterointerfaces', *Phys. Rev. B*, vol. 94, no. 15, p. 155309, Oct. 2016.
[52] A. Beyer *et al.*, 'Pyramidal Structure Formation at the Interface between III/V Semiconductors and Silicon', *Chem. Mater.*, vol. 28, no. 10, pp. 3265–3275, mai 2016.

[53] T. Hannappel, O. Supplie, S. Bruckner, M. M. May, P. Kleinschmidt, and O. Romanyuk, 'Comment on pyramidal structure formation at the interface between III/V semiconductors and silicon', *arXiv:1610.01758 [cond-mat]*, Oct. 2016.

Chapter 3 : Description of III-V/Si epitaxial growth processes

Integrating monolithically III-V semiconductors on group-IV ones is often considered as the ultimate step for the co-integration of photonics (such as lasers, passive devices) with electronics, or the development of high efficiency multijunction solar cells [1], [2]. The main issues of polar on nonpolar epitaxy to overcome were soon identified in the early 80's [3],[4]. But since the interplay between three-dimensional (3D) growth modes, strain relaxation, antiphase domains, and other defects was never clarified, researchers preferentially developed defect filtering strategies using thick III-V buffers grown on silicon [5]. Reaching higher photonic integration levels now requires a deep understanding of the processes involved at the early stages of III-V/Si heterogeneous epitaxy. That is why they are going to be investigated in this chapter.

This work has been performed in collaboration with S. Charbonnier and P. Turban (IPR-*STM*), M. Vallet and A. Ponchet (CEMES-*TEM and Wulff-Kaishew analysis*), L. Pedesseau, R. Bernard, A. Létoublon, N. Bertru, A. Le Corre, and C. Cornet (FOTON- *GaP/Si MBE, AFM, DFT*), L. Cerutti , J.-B. Rodriguez and E. Tournié (IES-*GaSb/AlSb MBE*), S. Rennesson and F.Semond (CRHEA: *AlN/Si MBE*) and G. Patriarche and L. Largeau (C2N-S*TEM*). I was personally involved in the density functional theory (DFT) calculations for determining the surface and interface energies, interpretation of the experimental results and thermodynamic description.

The work reported here has been partly published in Physical Review Materials as a Rapid communication [6].

3.1.State-of-the-art

Summarizing the large literature on the subject is hopeless, but we would like to emphasize three major physical concepts about III-V/Si growth that are usually presented as implicit underlying statements and that are in close relationship with the present work.

First, the origin of antiphase domain (APD) formation is commonly attributed to either Si single steps or an incomplete group-III or group-V initial coverage of the Si surface (Chapter 1, Figure 1.18). This general picture, described in detail by Kroemer [3], is today considered as the main motivation for using misoriented Si substrates, in order to promote bi-step formation, and theoretically hamper the formation of antiphase boundaries.

Second, the origin of the commonly observed 3D islanding during III-V/Si growth was frequently ascribed to strain relaxation processes, for instance, in the case of GaAs on Si [4], [7] since most III-V semiconductors are lattice mismatched to the silicon. It was also noticed that for mismatched semiconductors, significant densities of dislocations are generated well before island coalescence. However, 3D islanding was also already reported in quasi-lattice-matched systems such as GaP/Si [8].

Finally, III-V/Si interface atomic arrangement was theoretically addressed on the basis of density functional theory (DFT) calculations. This was, for instance, discussed in relation to GaAs/Si [9] or more recently to GaP/Si [10]–[12]. Highlights were given on the fact that abrupt III-Si or V-Si interfaces are not always the most stable configurations, depending on the group-III/group-V chemical potentials. Indeed, some charge-compensated interdiffused interfaces following the electron counting model criteria [13] were found to be remarkably stable [10], [11], [14], [15].

3.1.1. 3D islanding of different III-V/Si systems

3D islanding is first investigated through three different III- V semiconductor materials because they allow one to span the initial epitaxial stress from compressive (AlSb/Si) to tensile (AlN/Si) through near zero (GaP/Si). To study the compressive epitaxial stress case, a GaSb/AlSb/Si system was investigated. Samples have been grown at IES and transmission electron microscopy (TEM) was performed at C2N. It is shown in **Figure 3.1(a).** The 6°-off (001) Si substrate was first prepared *ex situ* according to the procedure described in ref.[16] before being loaded into the molecular beam epitaxy (MBE) reactor. The substrate temperature was then ramped up to 800°C at ~ 20°C/min and then immediately cooled at the same rate down to 500°C, without any intentional flux (all shutter cells being kept closed). MBE growth was

initiated by simultaneous opening of Al and Sb shutters to grow 5 nm AlSb. Next, a thick GaSb layer was grown. The whole structure was grown at 500 °C, measured by a pyrometer, and the growth rates were 0.35 ML/s for AlSb and 0.65 ML/s for GaSb. The GaSb/Si sample has been observed in cross-sectional view by Scanning Transmission Electron Microscopy (STEM) on an aberration corrected microscope Titan Themis 200. The thin foil has been prepared by focused ion beam (FIB) following the [110] axis (parallel to the vicinal 6° misoriented surface steps). The FIB preparation has been followed by a cleaning with argon milling at low voltage (1.5kV) during nine minutes to remove the material redeposition (gallium and antimony) during the FIB process.

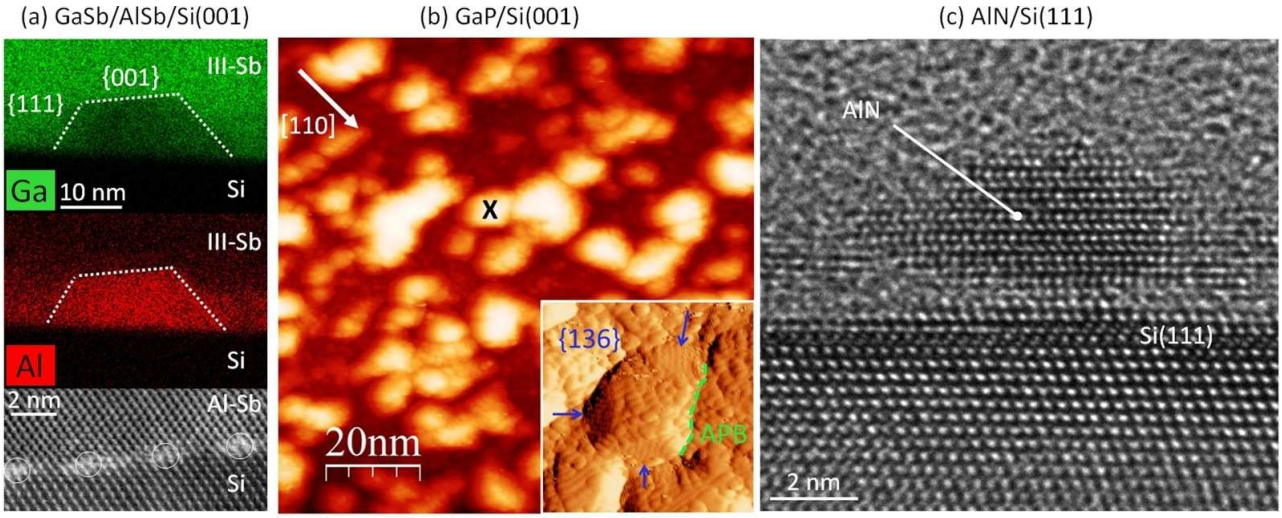

Figure 3.1 3D islanding in various III-V/Si material systems. (a) Cross-sectional STEM-EDX image of GaSb/AlSb layers grown on Si(001)- 6°-off, showing the Ga and Al concentrations, and high-resolution STEM imaging of the AlSb/Si interface; dislocations are surrounded. (b) Plan-view STM imaging of a 3-nm-thick GaP deposition on Si(001)-6°-off(100x100nm^2 ; vertical color scale: 0–5.1 nm). 20x20nm^2 inset shows the atomically resolved morphology of the individual island marked with a black cross, with {136} facets and an antiphase boundary. STM image was differentiated to enhance atomic contrasts. (c) Cross-sectional high-resolution TEM image of a 2-nm-thick AlN deposition on Si(111).

For the near zero epitaxial stress case, GaP/Si sample, presented in **Figure 3.1(b)**, has been grown by MBE on a HF-chemically prepared Si(001) substrate, with a 6° miscut toward the [110] direction [17]. Samples have been grown at FOTON, and transferred to IPR for STM measurements. The substrate has been heated at 800°C during 10 minutes to remove hydrogen

at the surface, and a 3-nm thick GaP/Si deposition was performed at 350°C, with a subsequent 500°C for 5 minutes annealing and a cooling under phosphorus following the approach developed in previous studies, that avoids surface modifications during the subsequent As-decapping process in the Scanning Tunnelling Microscopy (STM) chamber [17]–[19]. During the 5 minutes annealing, the RHEED diagram did not evolve. After MBE growth, an amorphous thick As capping layer was deposited on the GaP/Si(001) films at cryogenic temperature, allowing the transfer of the sample to the ultra-high vacuum STM chamber experiment, as already discussed in ref. [20]. Complete thermal desorption of the As protective layer was obtained at 500°C and allows STM observations of the GaP films. STM was performed at room-temperature in the constant current mode of operation. Tungsten electro-chemically etched tips were used. Raw STM images were simply corrected by subtraction of a basal plane. The (136) crystallographic planes of the GaP island facets were unambiguously identified by measuring the facet angle with respect to the basal plane. This was further confirmed by identification of the atomic arrangement of the (136) facets previously observed in ref. [20]. We also note here that alternated growth technique such as migration enhanced epitaxy (MEE) are sometimes used to promote the 2D planarity of the layers [21]. However, STM measurements performed on GaP/Si suggest that alternated growth on the contrary leads to higher density of smaller islands, with earlier coalescence, which may be misinterpreted as a 2D layer in conventional resolution-limited atomic force microscopy. As previously shown in Chapter 2, section 2.5.1, it has been shown that {136} facets do not respect the electron counting model. Consequently, as already proposed in GaAs, the {136} facet reconstruction will be changed to the stable {2 5 11} one for the surface energy calculations. The very small difference of facets orientation remains fully compatible with the STM observations presented here. The full justification of this change has been explained in Chapter 2.

To investigate the case of tensile stress, AlN/Si sample (**Figure 3.1(c)**) has been grown by MBE in a RIBER Compact 21S reactor at CHREA. A cold-neck solid source is used for Al whereas ammonia is used as N source (NH_3-MBE). The nominal Si(111) substrate is HF-chemically prepared. After introduction in the growth chamber, the substrate is heated at 780°C to desorb hydrogen atoms, giving rise to a (7 x 7) surface reconstruction. In order to promote large and

well defined terraces, the Si substrate was flashed at 1200°C (read by a pyrometer). While cooling down, we observe serval orders of the (7 x 7) surface reconstruction, indicating that the Si surface is clean and well ordered. Then the AlN nucleation starts at 600°C, following the procedure described [22], and the growth temperature is raised up to 1030°C. The AlN growth rate is of 100nm/h. For the purpose of this study, a very thin AlN layer is grown without rotation, which results in a nominal thickness varying from 1.6 to 2.3-nm along the substrate diameter. The AlN/Si sample for TEM observation (at CHREA) is prepared using a conventional technique, involving mechanical thinning followed by ion-milling using Ar^+ at 0.5-5 keV, by pure mechanical wedge polishing or by focused ion beam. Cross-sectional view is observed in a JEOL 2100F microscope.

In **Figure 3.1(a)**, the STEM energy-dispersive x-ray spectroscopy (EDX) images are given for AlSb/Si-6°-off islands (5 nm), buried in a GaSb matrix, with corresponding Ga and Al contrasts. A high-resolution transmission electron microscopy (TEM) image of the interfacial misfit dislocation network is also given. **Figure 3.1(b)** displays the STM in-plane image of a 3-nm GaP/Si-6°-off deposition, a very early stage of growth, as compared to previous studies [18], [19]. The inset shows the atomically resolved typical morphology of one individual island at the surface, where {136} facets can unambiguously be identified [20], together with a trench that shows the emergence of an antiphase boundary. **Figure 3.1(c)** shows the cross-sectional high-resolution TEM image of a 2-nm AlN/Si(111) deposition.

From these experiments, some important conclusions can already be made. First, in the various experiments performed on the three material systems, 3D islands were always observed, and the presence of a wetting layer was not clearly or systematically evidenced (see **Figure 3.1(a) and (c),** for instance), which confirms the partial wetting of III-V on Si, i.e., the Volmer-Weber growth mode, independently of the strain state [7], [8]. We believe that this is a general behavior of III-V/Si heteroepitaxial systems even when alternated growth techniques are used [21]. We will strengthen this assumption later on. Here, we note that the III-V/Si Volmer-Weber growth mode does not *a priori* hamper the Si surface to be terminated with a single monoatomic layer of group-III, group-V, or another element rising from the epitaxial reactor background. The impact of such a passivating layer will be discussed later.

It is also remarkable that in both AlSb and AlN material systems, the misfit is so large that the III-V material relaxes very rapidly. Even if the relaxation process is not similar in Sb- and N-based materials, complete strain relief is nearly achieved at only 1 nm of the interface. **Figure 3.1(a)** also illustrates that the island size is much larger than the typical distances between dislocations. It was already reported that dislocations appear well before the islands coalesce [7], and we note that the observed islands are nearly perfectly faceted well after crystal plastic relaxation. This suggests that the elastic relaxation of strain [23] is not contributing significantly to the energy balance of individual islands. Here, we conclude that surface/interface energies play a crucial role in III-V/Si 3D islanding.

The last important conclusion that can be drawn from the experiments is the monodomain character of the observed single islands. In **Figure 3.1(b)**, most of the individual grains have a homogeneous morphology. The largest homogeneous islands (without APDs) are likely a consequence of smaller islands coalescing. Neighboring smaller islands are also visible, with a clear separation between them that seems to hamper the coalescence (shown with the green dashed line in the inset of **Figure 3.1(b)**). The atomic structure of one individual island shown in the inset of **Figure 3.1(b)** evidences the monodomain character of the island and the presence of {136} facets. Therefore, from cross-sectional TEM and plan-view STM experiments it is clear that individual III-V/Si islands remain monodomain. This observation is in agreement with the work of Akahane *et al.* [24] where individual AlSb or GaSb islands on Si were observed, as illustrated in **Figure 3.2**. The anisotropy of individual islands was demonstrated along either the [110] or the [1-10] silicon crystallographic axis, demonstrating the monodomain character of the single islands, and the overall bidomain distribution of the island population. The size of the islands presented in **Figure 3.1 (a) and (b)** is also interesting. Both GaP and AlSb epilayers were grown on Si(001)- 6°-off substrates, where atomic (biatomic) steps are separated on average by 1.29 (2.58) nm. Monodomain islands are significantly larger (10 nm), which contradicts the usual correlation made between monoatomic Si steps and APB formation (Chapter 1, Figure 1.18)[3].

To complete the picture, we note that the average spacing between islands (10 nm) in **Figure 3.1(b)** corresponds well to the APD correlation length measured on the thicker epilayers

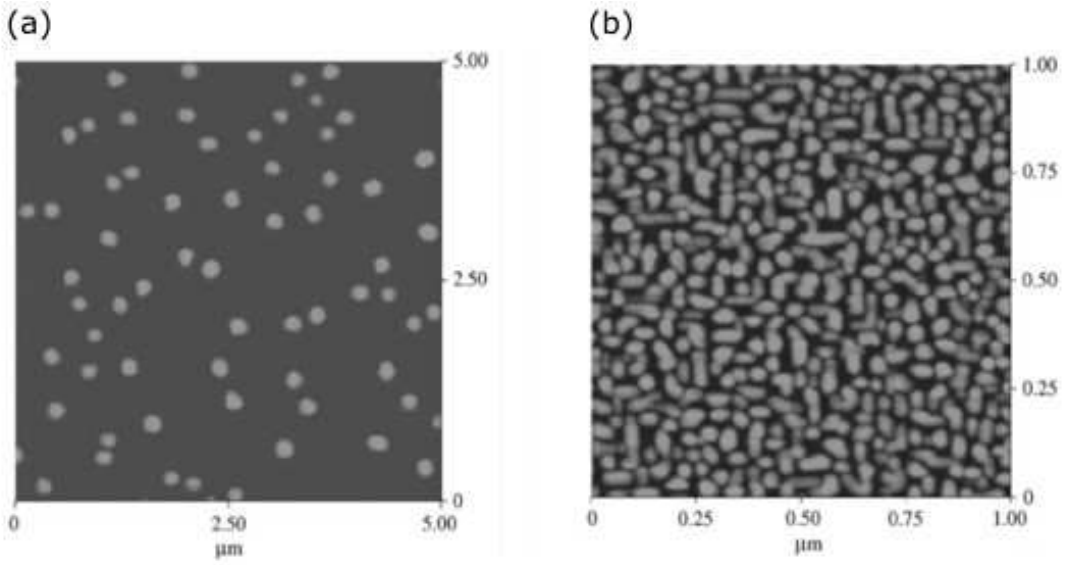

Figure 3.2 (a) 5x5µm^2 AFM image of 5nm GaSb island grown on Si substrate (b) 1x1µm^2 AFM image of 5no AlSb islands grown on Si substrate

grown under the same conditions (8–12 nm) [25]. Finally, the impact on the structural quality of III-V/Si epilayers by III-V islands coalescence was highlighted [8], [26].

In the following, we will discuss in terms of thermodynamics the 3D islands formation focusing on the GaP/Si system, through the surface and interface energies estimated by *ab-initio* calculations explained in Chapter 2.

3.1.2. Solid wetting theory applied to GaP/Si

In a first and general description, the III-V/Si wetting properties can be examined within the Young-Dupré spreading parameter Ω [27]:

$$\Omega = \gamma^{S}_{(Si)} - \gamma^{S}_{(III-V)} - \gamma^{i}_{(III-V/Si)} \quad \textbf{(3.1)}$$

where $\gamma^{S}_{(III-V)}$ and $\gamma^{S}_{(Si)}$ are the surface energies of the most stable III-V facet that would be involved in the two-dimensional (2D) growth on the substrate and of the silicon surface, respectively, and $\gamma^{i}_{(III-V/Si)}$ is the interface energy between the III-V semiconductor and the Si. A positive value of Ω corresponds to perfect wetting conditions, while a negative value corresponds to partial wetting, *i.e.*, a Volmer-Weber growth, or perfect nonwetting conditions.

However, the evaluation of Ω requires the accurate determination of surface and interface energies, which has been done for GaP in this work.

			Energy (meV/Å²)	
Surface/interface	Details	Reconstruction	P-rich	Ga-rich
Si(001)	Flat	c(2 × 4)	92.8	
Si(001)	D_B step	$p(2 \times 2)$	89.3	
Si(001)	S_B step	$p(2 \times 2)$	89.2	
Si(001)	S_A step	$c(2 \times 4)$	87.1	
GaP(001)	P-rich	(2×4)	57.4	72.4
GaP(001)	Ga-rich	(2×4)-md	82.8	52.9
GaP(136)	Type A	(1×1)	52.9	62.7
GaP(136)	Type B	(1×1)	66.8	57.1
GaP-Si	Abrupt Ga-Si	(1×1)	72.0	40.8
GaP-Si	Abrupt P-Si	(1×1)	29.7	60.9

Table 3.1 GaP and Si surface and interface energies determined by DFT

To this aim, different absolute surfaces and interface energies of interest were computed via DFT calculations (as illustrated in Chapter 2). The silicon surface energy was already widely discussed [28]–[30]. Silicon surfaces with or without steps have been considered in this work, and we found that the presence of steps at the silicon surface (at least for a miscut below or equal to 6°) does not significantly change the silicon surface energy range (87-93 meV/$Å^2$). For GaP the situation is different, as the surface energies depend on the reconstruction of the facet, on the chemical potential, and therefore on the growth conditions used (P or Ga rich). Calculations show that the {136} surface energies of GaP are in the same range as the {001} ones, as already found for GaAs [31]. Finally, abrupt Ga-Si or P-Si (001) GaP/Si interface energies also depend on the chemical potential [10], [11]. In a first approximation, we do not consider the charge compensated interfaces that may further stabilize the interface [11]. The results obtained from *ab-initio* calculations explained in Chapter 2, were reported in **Table 3.1**.

The spreading parameter Ω is then plotted in **Figure 3.3(a)** as a function of the phosphorus chemical potential variation $\Delta\ \mu_p = \mu_p - \mu_p^{P-bulk}$ (μ_p is the chemical potential of P

atoms, μ_p^{P-bulk}; see details in Chapter 2), where the right (left) side corresponds to P-rich (Ga-rich) limit conditions [10].

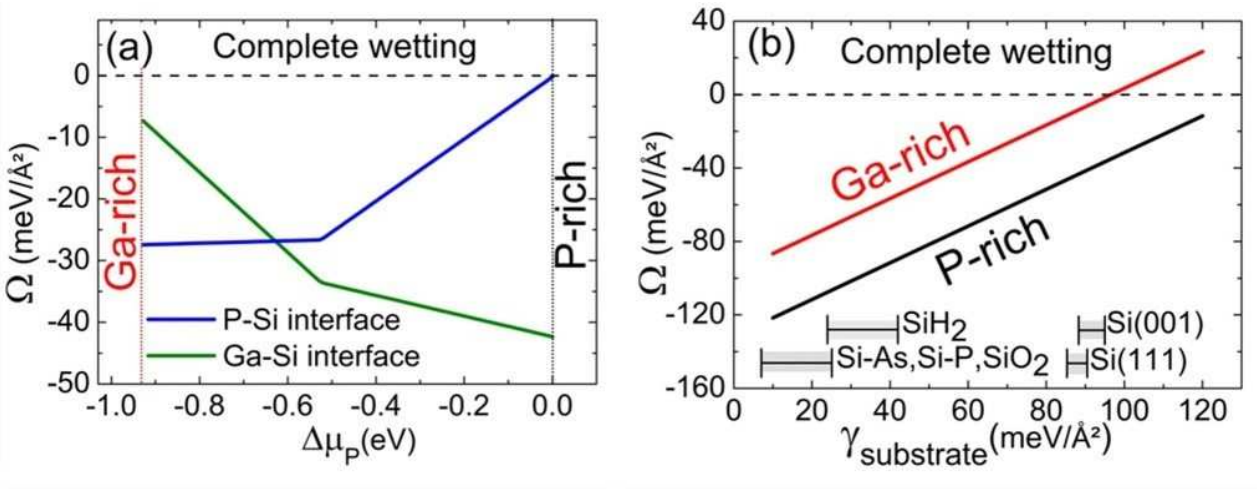

Figure 3.3 (a) Spreading parameter vs the chemical potential variation for the deposition of GaP/Si, with P-Si and Ga-Si abrupt interfaces. (b) Spreading parameter vs substrate surface energy in P- and Ga-rich conditions with a Ga-Si interface

The calculation is presented both for the P-Si and the Ga-Si abrupt interfaces, with a D_B -stepped Si surface. The most stable {001} surface reconstruction was always considered at a given value of the chemical potential, explaining the slope variation of Ω around -0.52 eV. Regardless of the chemical potential and the interface, Ω remains negative, indicating partial wetting conditions, even if in extreme P-rich conditions with a P-Si abrupt interface, the accuracy of the DFT calculation does not allow one to conclude unambiguously on the sign of Ω in this very narrow window. Considering that most III-V semiconductors have the same surface energy orders of magnitude, this conclusion (partial wetting conditions) can be extended to most III-V semiconductors deposited on Si. In the following, the abrupt Ga-Si interface will be chosen for illustration.

In **Figure 3.3(b)**, the spreading parameter is plotted as a function of the substrate surface energy in P- and Ga-rich conditions. Ω increases with the substrate surface energy, as expected by definition. In the same plot, we have also reported typical surface energy ranges of some

commonly used starting Si surfaces (passivated or unpassivated) already considered in the literature, such as Si(001), Si(111), SiH_2, SiAs, SiP, or SiO_2 (e.g., Refs. [32] or [33]). Here, Si*X* stands for the *X*-terminated Si surface. The vertical positioning of the different Si*X* surfaces has no physical meaning. The impact of surface pretreatment or orientation on interface energy is not taken into account. We here conclude that any Si surface pretreatment or passivation will tend to stabilize the highly reactive nude Si surface, and thus favor partial wetting conditions, strongly reducing the hope to reach complete III-V/Si wetting conditions in real epitaxial chambers where the passivation can be intentional or nonintentional.

3.2.Free-energy calculations from the equilibrium shape given by the Wulff-Kaishew theorem

To complete the picture at the submonolayer scale, and evaluate the relative contributions of stress relaxation and surface/interface energies, one needs to compute the free energy variations during the epitaxial growth of III-V/Si islands. To this aim, the precise knowledge of the equilibrium shape (the most stable island geometry) is needed, that is usually given by the so-called Wulff-Kaishew theorem [34]. In the following, I will remind the approach proposed by Wulff and Kaishew to determine the crystal shape in equilibrium conditions.

The notion of equilibrium shape (ES) has been a subject discussed since the end of XIXth century when Gibbs [35] stated that the equilibrium shape of a free crystal, at constant volume, is the one that minimizes its total surface free energy. The subject was also discussed by Curie [36] who introduced a proportional relation between h_i (distance from the center of the crystal shape to the surface S_i) and the surface free energy γ_i ,without specifying the constant of proportionality [35]. In 1901, Wulff's theorem [34], [37] clarified the proportionality γ_i/h_i, defining the equilibrium shape as the inner part of a polyhedron formed by i facets (having a surface energy γ_i) perpendicular to directions n, at distances h_i from the ES center called Wulff point in **Figure 3.4(a)**. The theorem had no proofs but it was later demonstrated by different authors such as Liebmann, Laue and I.N Stranski [35],and references herein.

The Wulff theorem derived by I.N Stranski with the so-called generalized Gibbs-Thomson equation [38], reads:

$$\frac{\Delta\mu}{2v} = \frac{\gamma_i}{h_i} \qquad \textbf{(3.2)}$$

where $\Delta\mu$ is the thermodynamic supersaturation given by $k_B T \ln(P/P_\infty)$, where k_B is the Boltzmann constant while P and P_∞ are the vapor pressure and the crystal vapor saturation pressure. Finally v is the volume occupied by each molecule, transferred from vapor phase to the crystal. The equation **(3.2)** states that the ESs, whatever their size, are self-similar [34], as shown in **Figure 3.5(a)** where the self-similar ESs have a common Wulff point O. This is the case for a free crystal.

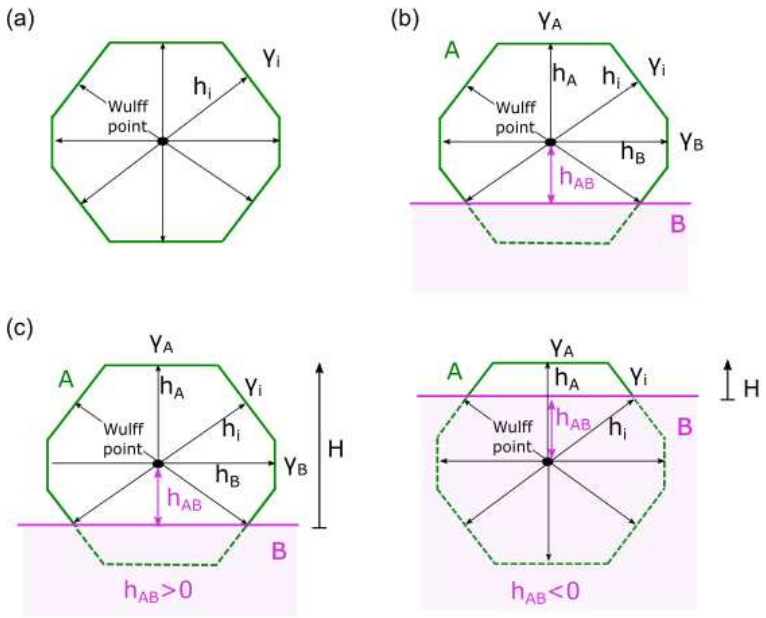

Figure 3.4 (a) Free crystal polyhedral equilibrium shape formed by i facets of surface S_i (and surface energy γ_i) perpendicular to directions n at distances h_i from the Wulf point. (b) ES for a supported crystal where $h_A(h_B)$ is the distance of the facets parallel (Perpendicular) to the interface, with surface S_A (S_B) and surface energy $\gamma_A(\gamma_B)$. h_{AB} is the distance from the Wulf point and the interface. (c) $H = h_A + h_{AB}$ varies as a function of the position of the crystal with respect to the substrate, when the interface is above (below) the Wulf point $h_{AB} > 0$ ($h_{AB} < 0$)

The equation changes when a crystal, of matter A for instance, is deposited on a substrate B. Indeed, the latter must be taken into account to determine the crystal equilibrium shape. Kaishew [39] explained (in the case of a non-coherent epitaxial growth) how the Wulff ES

is affected by the presence of a substrate as illustrated in **Figure 3.4(b)**, where the polyhedral crystal A (in green) is accommodated on a substrate B. The interface AB is represented with a pink line. The polyhedron's planes parallel (perpendicular) to substrate have a surface $S_A(S_B)$, a surface energy per unit area $\gamma_A(\gamma_B)$ and a distance $h_A(h_B)$ from the Wulff point. The latter can be above or below the substrate as a function of h_{AB} that is the distance between the Wulff point and the interface AB (with interface energy per unit area γ_{AB}). This point will be explained in detail in the following. Finally, the distance from the interface to the crystal surface S_A is H= $h_A + h_{AB}$. See **Figure 3.4(c).** In the case of the Wulff-Kaishew theorem, the free energy change ΔF to form the crystal is given by [40]:

$$\Delta F = \Delta F_{\mu} + \Delta F_{S\&i} = -N\Delta\mu + \sum_i \gamma_i S_i + S_i(\gamma_{AB} - \gamma_B) \quad \textbf{(3.3)}$$

The first term $\Delta F_{\mu} = -N\Delta\mu$ represents the chemical work spent to form the crystal where Δμ is the supersaturation and N is the number of molecules in the crystal. These parameters were already mentioned previously. The second term $\Delta F_{S\&i} = \sum_{i\neq AB} \gamma_i S_i + S_{AB}(\gamma_{AB} - \gamma_B)$ is related to the formation of the surface and interfaces for a crystal having i facets of area S_i whose surface energy is $\gamma_i S_i$, while S_{AB} is the contact area, $\gamma_{AB}$is the interfacial energy per unit area and γ_B is the surface energy per unit area for the free substrate B [34]. By applying the minimum of the crystal free energy given by $d\Delta F = 0$ [40], Wulff-Kaishew theorem is expressed as:

$$\frac{\gamma_i}{h_i} = \frac{\Delta\mu}{2v} = \frac{\gamma_{AB} - \gamma_B}{h_{AB}} \quad \textbf{(3.4)}$$

Equation **(3.4)** can be written as:

$$\frac{h_{AB}}{h_i} = \frac{\gamma_{AB} - \gamma_B}{\gamma_i} \quad \textbf{(3.5)}$$

Thus, when $\gamma_{AB} - \gamma_B > 0$ ($\gamma_{AB} - \gamma_B < 0$), $h_{AB} > 0$ ($h_{AB} < 0$), the Wulff point is above (below) the interface, as illustrated In **Figure 3.4(c).**

It is possible to write the equation **(3.4)** as a function of the adhesion coefficient between two crystals, which expresses the energy needed to separate them. It is given by the following equation [40]:

$$\beta = \gamma_A - \gamma_{AB} + \gamma_B = 2\gamma_A + \Omega \qquad \textbf{(3.6)}$$

thus, equation **(3.4)** becomes:

$$\frac{\gamma_i}{h_i} = \frac{\Delta\mu}{2v} = \frac{\gamma_A - \beta}{h_{AB}} \qquad \textbf{(3.7)}$$

That can be written as:

$$\frac{h_{AB}}{h_i} = \frac{\gamma_A - \beta}{\gamma_i} \qquad \textbf{(3.8)}$$

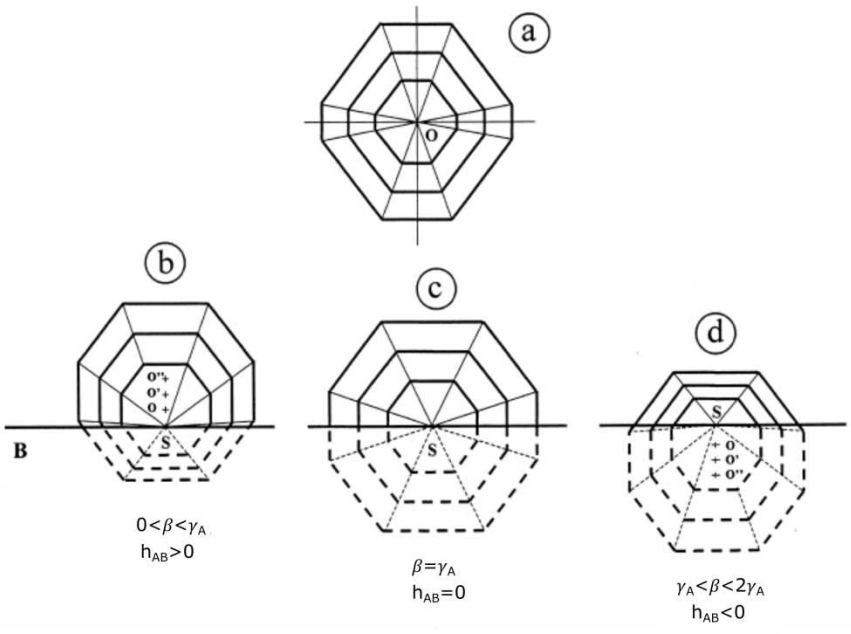

Figure 3.5 ES in the Wulf-Kaishew theorem hypothesis. (a) In the case of a free crystal (β =0) the ES are self smilar and they have a common Wulf point. In the case of a supported crystal the Wulf point moves ($O \longrightarrow O' \longrightarrow O''$) (b) above the interface when $h_{AB} > 0$ and $\beta < \gamma_A$(c) at the interface ($O = O' = O''$= S) when $\beta = \gamma_A$ and $h_{AB} = 0$ and (d) below the interface when when $h_{AB} < 0$ and $\gamma_A < \beta$. In these three cases, since $\beta < 2\gamma_A$ the growth is 3D. Courtesy of [34]

In conclusion, according to the Wulff-Kaishew theorem, the self-similarity is preserved but the ES is truncated by the substrate. This truncation is taken into account by the adhesion coefficient β.

To summarize, the crystal growth is achievable when the chemical potential variation is positive ($\Delta\mu > 0$), which means that the vapor partial pressure is greater than the crystal vapor saturation pressure. Otherwise the crystal growth is not achieved [40]. When $\Delta\mu$>0, different growth modes can be identified as a function of the adhesion coefficient value: when β =0, the crystal is free (Wulff's theorem conditions) **Figure 3.5(a)**. The 3D growth region corresponds to values when $\beta - 2\gamma_A < 0$, thus when Ω<0. These are the partial wetting conditions which correspond to Volmer-Weber growth. Otherwise, we are in the 2D growth conditions (complete wetting) [40]. In the 3D growth (when $\beta - 2\gamma_A < 0$) the self-similar ES varies and the Wulff point moves (as mentioned above) as a function of h_{AB} which depends on β. Indeed, when 0< β <γ_A and $h_{AB} > 0$, the ESs are bottom-truncated polyhedrons with Wulff point above the interface (**Figure 3.5(b)**) ; when β =γ_A and $h_{AB} = 0$, the ESs are half-truncated self-similar polyhedrons with the Wulff point at the interface (**Figure 3.5(c)**); finally when $\gamma_A < \beta$ <$2\gamma_A$ and $h_{AB} < 0$ the ESs are truncated from the top so that just the summit emerges from the substrate. The Wulff point is below the interface. This is illustrated in **Figure 3.5(d).**

3.2.1. Wulff-Kaishew theorem applied to GaP/Si system

In the following we now compare two different situations: a 2D GaP island (with a one monolayer height, growing laterally) and a 3D truncated pyramidal GaP island in its Wulf-Kaishew equilibrium shape growing in an homothetic way on the silicon substrate, as depicted in **Figure 3.6(a).** A careful STM image analysis has been performed on the data of **Figure 3.1(b)**, which gives an average island height of 2.5 nm, and an average diameter of 11 nm, which leads to an average (miscut included) island contact angle of 27.04°. Among the different stable facets observed with GaP or GaAs materials that are mainly lying around the {001}, {111}, {136}, and {114}ones [20], [31], the measured contact angle can only correspond to the {136} ones (theoretical contact angle of 27.8°). We therefore model the GaP 3D islands by truncated

pyramidal structures composed of facets with an angle α=27.8°, having the surface energy of {136} facets. As explained in Chapter 2, the surface energy of this facet is taken from the {2511} one as it is the most stable configuration, and respects the electron counting model criterion. The pyramid has a square basis (length b_1), a {001} facet on top (length b_2), and grows in a homothetic way during the initiation steps. Truncated pyramid islands are chosen at their equilibrium shape determined by the Wulff-Kaishew theorem (section 3.2) [34] as schematized in a side-view in **Figure 3.6(b).** The height h_{AB} in our case is negative, that is why the Wulff point is positioned below the interface.

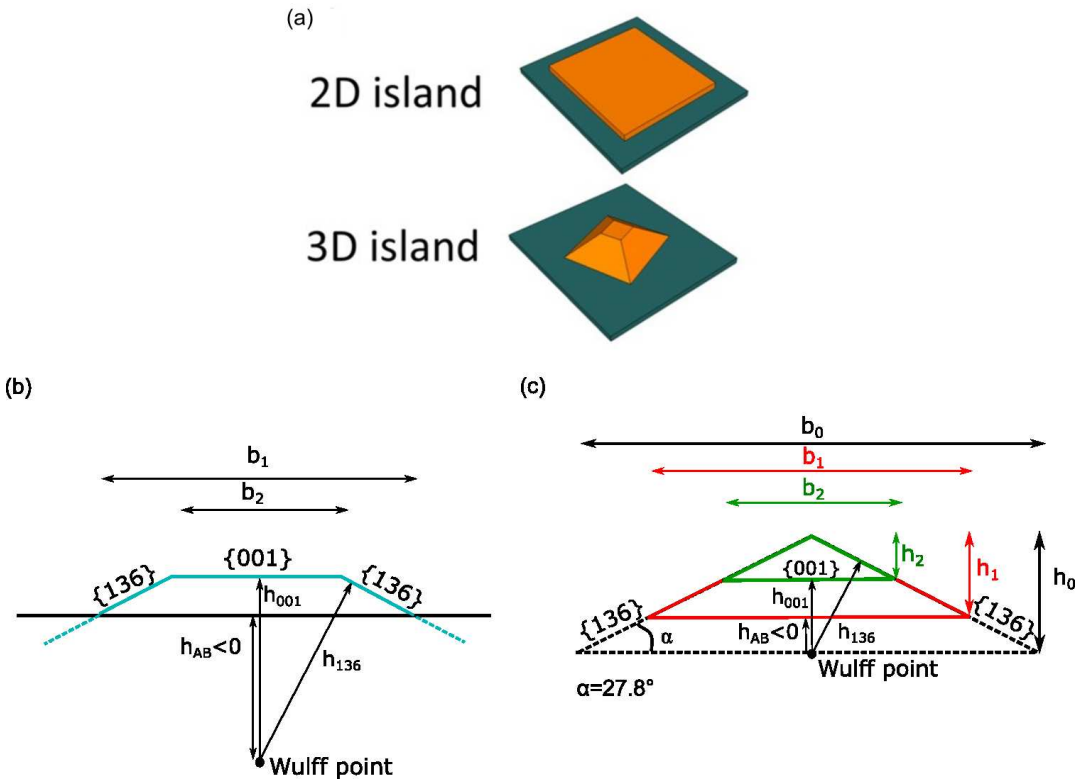

Figure 3.6 (a) Sketch of the 2D and 3D GaP islands on Si. (b) Side view of the GaP trapezoidal ES formed by (001) and (136) facets (b) the pyramidal composition to determine the ratio b_2/b_1 of the GaP ES which is given by $P=P_1-P_2$; The three pyramids P_0, P_1 and P_2 have square basis b_0,b_1,b_2, height h_0,h_1 and h_2 respectively and they are formed by four 136 facets; h_{001} is the distance between the wulf point and the (001) surface which corresponds to the top facet of the ES, h_{136} is the distance between the Wulf point and the (136) facets and h_{AB} is the distance between the interface, which is the basis of the ES, and the Wulf point.

To determine the equilibrium shape parameters, we considered three pyramids P_0, P_1, P_2 with a square basis length b_0, b_1, b_2, and height h_0, h_1, h_2 respectively. Each one formed by four {136} equivalent facets. The trapezoidal shape, we are interested in, is given by the difference between the two pyramids P=P1-P2 with b_2 as the basis on the top and b_1 the one on the bottom. A side view of the scheme, we considered to determine our ES, is illustrated in **Figure 3.6(c)** with the following pyramids: in black P_0, in red P_1 and in green P_2. The heights h_{001} and h_{136} are the distances between the {001} and {136} facets respectively, and the Wulff point.

The aspect ratio b_2/b_1 defining the ES is then calculated. Thus, we need to know the two pyramids P1 and P2 aspect ratios (b_1/h_1 and b_2/h_2 respectively). b_2/b_1 is given by:

$$\frac{b_2}{b_1} = \frac{h_2}{h_1} \tag{3.9}$$

From the scheme in **Figure 3.6(c)**, we also can determine h_{136}, h_0, h_2 and , h_1 which are given by the following equations:

$$h_{136} = sin(\alpha)\left(\frac{b_0}{2}\right) \tag{3.10}$$

$$h_0 = tg(\alpha)\left(\frac{b_0}{2}\right) \tag{3.11}$$

$$h_2 = h_0 - h_{001} \tag{3.12}$$

$$h_1 = h_0 + h_{\mathrm{AB}} \tag{3.13}$$

h_{AB} , in equation **(3.13)**, is an algebraic value that thus can be negative. From the Wulff theorem we know that:

$$\frac{\gamma_{001}}{\mathrm{h}_{001}} = \frac{\gamma_{136}}{\mathrm{h}_{136}} \tag{3.14}$$

Using equation **(3.10)** it comes:

$$h_{001} = \frac{h_{136}}{\gamma_{136}}\,\gamma_{001} = \sin(\alpha)\left(\frac{b_0}{2}\right)\frac{\gamma_{001}}{\gamma_{136}} \qquad \textbf{(3.15)}$$

Substituting **(3.11)** and **(3.15)** in **(3.12)** we find h_2:

$$h_2 = \sin(\alpha)\left(\frac{b_0}{2}\right)\left(\frac{1}{\cos(\alpha)} - \frac{\gamma_{001}}{\gamma_{136}}\right) \qquad \textbf{(3.16)}$$

For determining h_1, we need to know h_{AB} which is given by the Wulff-Kaishew theorem:

$$\frac{\gamma_{001}}{h_{001}} = \frac{\gamma_{AB} - \gamma_B}{h_{AB}} \qquad \textbf{(3.17)}$$

$$h_{AB} = \frac{h_{001}}{\gamma_{001}}\,(\gamma_{AB} - \gamma_B) = \sin(\alpha)\left(\frac{b_0}{2}\right)\frac{\gamma_{AB} - \gamma_B}{\gamma_{136}} \qquad \textbf{(3.18)}$$

substituting **(3.11)** and **(3.18)** in the **(3.13)** we can express h_1 as:

$$h_1 = \sin(\alpha)\left(\frac{b_0}{2}\right)\left(\frac{1}{\cos(\alpha)} + \frac{\gamma_{AB} - \gamma_B}{\gamma_{136}}\right) \qquad \textbf{(3.19)}$$

Finally, the ratio b_2/b_1 is given by inserting equations **(3.16)** and **(3.19)** in **(3.9)**

$$\frac{b_2}{b_1} = \frac{\gamma_{136} - \gamma_{001}\cos(\alpha)}{\gamma_{136} + (\gamma_{AB} - \gamma_B)\cos(\alpha))} \qquad \textbf{(3.20)}$$

From the surface energies determined in Chapter 2, in P-rich conditions, b_2/b_1=0.05, while in Ga-rich conditions, b_2/b_1= 0.60. The aspect ratio is therefore highly dependent of the growth conditions used. We note here that the same analysis was recently performed by members of the ANTIPODE project on AlSb/Si islands [41].

Instead, for the modeling of the 2D GaP island on Si, we model the top surface by a conventional {001} facet and keep a one monolayer height thickness; the 2D island is only

growing laterally. The edge energy is neglected, which gives a lower limit estimated around 10^3 for the total number of atoms composing the island.

3.2.2. Total free energy variation during the GaP/Si epitaxial growth

So far, the lattice mismatch between the crystal and the substrate was not considered. Indeed, in the GaP/Si ES presented in section 3.2.1, the elastic strain relaxation has been considered negligible. This will be confirmed in the following. In 2000, Muller and Kern [34] generalized the Wulff-Kaishew theorem taking into account the lattice mismatch. Indeed, they introduced the contribution of the epitaxial strain in the equilibrium crystal shape. They schematized the thermodynamic process to find the equilibrium shape of an epitaxial strained crystal as illustrated in **Figure 3.7**. After the formation of a polyhedral crystal shape from an infinite reservoir of a crystal matter A (step 1), the crystal is accommodated on the substrate through an homogenous strain (step 2). The crystal shape formed in step 2 does not minimize its total free energy thus, it undergoes to an elastic relaxation which makes the crystal coherently strained to the substrate, lowering its elastic energy leading to the equilibrium shape. At the end of this process, the 3D crystal and the substrate are inhomogeneously strained [34].

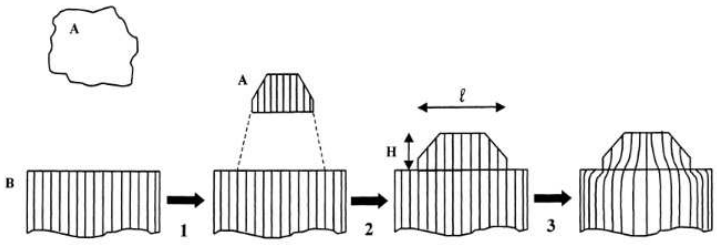

Figure 3.7 Scheme of the thermodynamic process to form a crystal A coherently strained on a substrate B. Step 1, formation; step 2, homogeneous deformation for accommodation then adhesion; Step 3, inhomogeneous relaxation. Courtesy of [34]

The free energy variation for describing this thermodynamic process is given by:

$$\Delta F = \Delta F_{\mu} + \Delta F_e + \Delta F_{S\&i} = -N\Delta\mu + \varepsilon_0 m^2 VR + \sum_{i \neq AB} \gamma_i S_i + S_{AB}(\gamma_{AB} - \gamma_B) \quad \textbf{(3.21)}$$

Where, with respect to the **(3.3)** a third term ΔF_e, related to the elastic energy stored by the relaxed system, is considered. In this term $\Delta F_e = \varepsilon_0 m^2 VR$, ε_0 is a combination of elastic coefficients of A, $m = (\mathrm{b} - \mathrm{a})/\mathrm{a}$ is the epitaxial misfit between the crystal A of lattice constant a and the substrate B with a lattice constant b, V is the volume of the deposited crystal A and R (whose values belong to the range 0<R<1) is a relaxation energy factor.

A detailed explanation of the **(4.21)** applied in our case is reported in the following. The total free-energy variation during the GaP/Si growth is calculated for the different 2D or 3D island configurations (illustrated in **Figure 3.6(a)**) by using equation **(3.21)** [34]. In our case ΔF corresponds to the difference of free energy between an initial thermodynamic state with a total atom number *N* related to the sum of Ga and P atoms in a vapor reservoir together with a nude Si substrate, and a final state where the GaP crystal is formed on the Si. Thus, the first term is the chemical work needed to form the bulk crystal from an infinite reservoir. For the molecular beam epitaxy of GaP using a P_2 source, it becomes:

$$\Delta F_{\mu} = NK_b T ln\left(\frac{P_{Ga}(P_{P_2})^{1/2}}{P_{Ga-\infty}(P_{P_2-\infty})^{1/2}}\right) \quad \textbf{(3.22)}$$

where *T* is the growth temperature, *N* the number of condensed atoms, P_X the partial pressure of species *X*, $\mathrm{P_{X-\infty}}$ the saturation partial pressure of species *X*, and k_B the Boltzmann constant. While *T* and P_X are extracted directly from growth conditions, the saturation pressures have been precisely calibrated in Ref.[42](section 2.5.4.1) for GaP. The second term is associated with the elastic energy stored and is defined as:

$$\Delta F_e = RF_0 m^2 V = R\Delta {F_e}^{2D} \quad \textbf{(3.23)}$$

where m is the epitaxial misfit between the deposited material and the substrate, *V* the volume of the deposited crystal F_0, a combination of the elastic coefficients C_{ij} , and *R* the relaxation energy factor [34]. ${\Delta F_e}^{2D}$ is the elastic energy of a biaxially strained 2D layer [34]. Here, we take R=1 for the 2D GaP island growing on Si, and R=0.7 for the free elastic energy variation of the ΔF_e-3D GaP island [43]. Finally, for a cubic crystal stressed in a (001) plane, F_0 is expressed as

($C_{11} + C_{12} - 2\frac{{C_{12}}^2}{C_{11}}$). The third term corresponds to the formation of surfaces and interfaces, which is rewritten in the present case,

$$\Delta F_{S\&i} = \sum_j \gamma^S_{(III-V),j} S_{(III-V),j} + S_{(III-V)/Si}(\gamma^i_{(III-V/Si)} - \gamma^S_{(Si)}) \quad \textbf{(3.24)}$$

where $\gamma^S_{(III-V),j}$ and $\gamma^S_{(Si)}$ are the surface energies of the *j* th III-V facet and of the silicon surface, respectively, $\gamma^i_{(III-V/Si)}$ is the interface energy between the III-V semiconductor and the Si, $S_{(III-V),j}$ the surface of the *j* th III-V facet, and $S_{(III-V)/Si}$ the contact surface between the III-V and the Si. In this work, we neglect the vibrational contribution to the free energy, which is not expected to impact the main conclusions [44].

The ΔF_{μ}, ΔF_e and $\Delta F_{S\&i}$ are plotted in **Figure 3.8** for both Ga- and P-rich conditions, and for the two types of islands, as a function of an increasing number of atoms. The energy gain provided by the crystal formation ΔF_{μ} is partly counterbalanced by both ΔF_e and $\Delta F_{S\&i}$, the elastic and surface/interface contributions. A first conclusion that can be drawn is that, regardless of the phosphorus chemical potential, surface and interface energies always make a larger contribution to the energy variation than the elastic energy contribution. We also see that the contribution of the elastic energy is so weak that the relaxation of strain has no impact on the island morphology, which is thus mainly defined by surface/interface competition. Here, we note that *R* depends on the island shape. The energy gain provided by the transition of an equilibrium Wulff-Kaishew island (*R* = 0.7) and a similar nontruncated island (*R* = 0.6) is not sufficient to compensate the increase in the corresponding surface energy. This also applies for an island with {111} facets, where *R* = 0.3. Therefore, the gain provided by elastic relaxation is always several orders of magnitude lower than the corresponding surface/interface energy cost and therefore will not have any influence on the island shape. We finally evidence that, at a small deposited number of atoms, 2D islands may be more stable than 3D ones. A precise description of this process would, however, require taking into account edge energies, which is beyond the scope of this work.

The importance of elasticity can be also discussed for other III-V semiconductors. For instance, the maximization of elastic energy in AlSb assuming a biaxial stress with R = 0.005

leads to ΔF_e ≈$7.5x10^2$eV for 10^6atoms. This remains lower than typical surface/interface free-energy variations. In addition, a significant contribution of misfit dislocations to the interface energies is also expected for mismatched systems. In the intermediate case of GaAs, where the relaxation occurs after some monolayers, elastic energy is expected to more seriously impact the island shape before relaxation occurs [34]. In any case, after plastic relaxation, surface and interface energy competition is clearly the most important contribution to the free-energy variation, and has a prominent role in defining the shape of the initial III-V/Si islands.

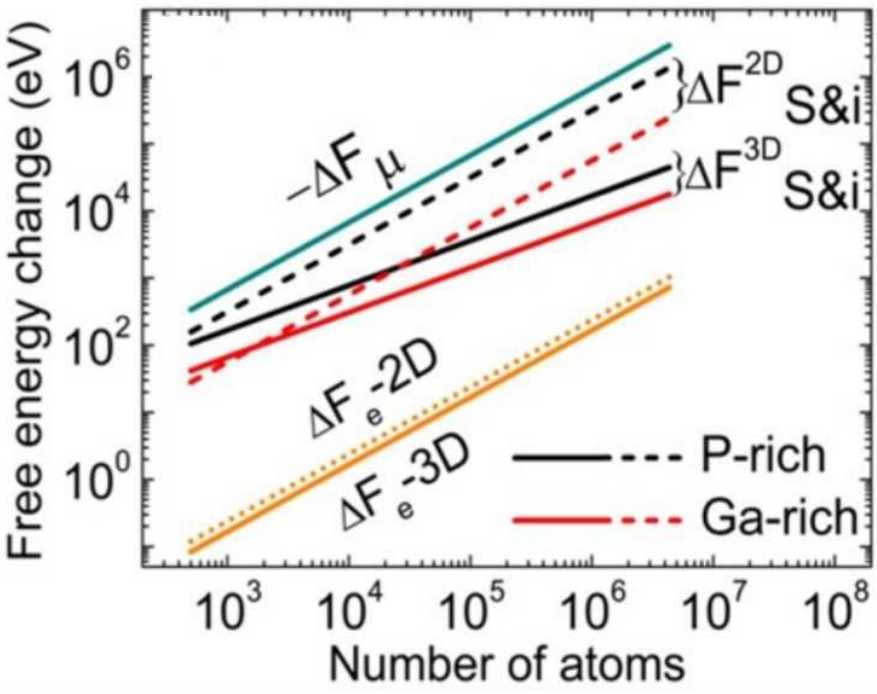

Figure 3.8 The different contributions (ΔF_{μ}, ΔF_e, $\Delta F_{S\&i}$) to the free-energy variation for 3D and 2D GaP/Si islands with a Ga-Si interface

3.3.General description of the III-V/Si epitaxial growth

From these experimental and theoretical findings, it becomes clear that the physics of III-V/Si epitaxial growth is driven by the competition between III-V surface energies, Si surface energies,

and the III-V/Si interface energy. The main growth steps can be then derived and are represented in **Figure 3.9**.

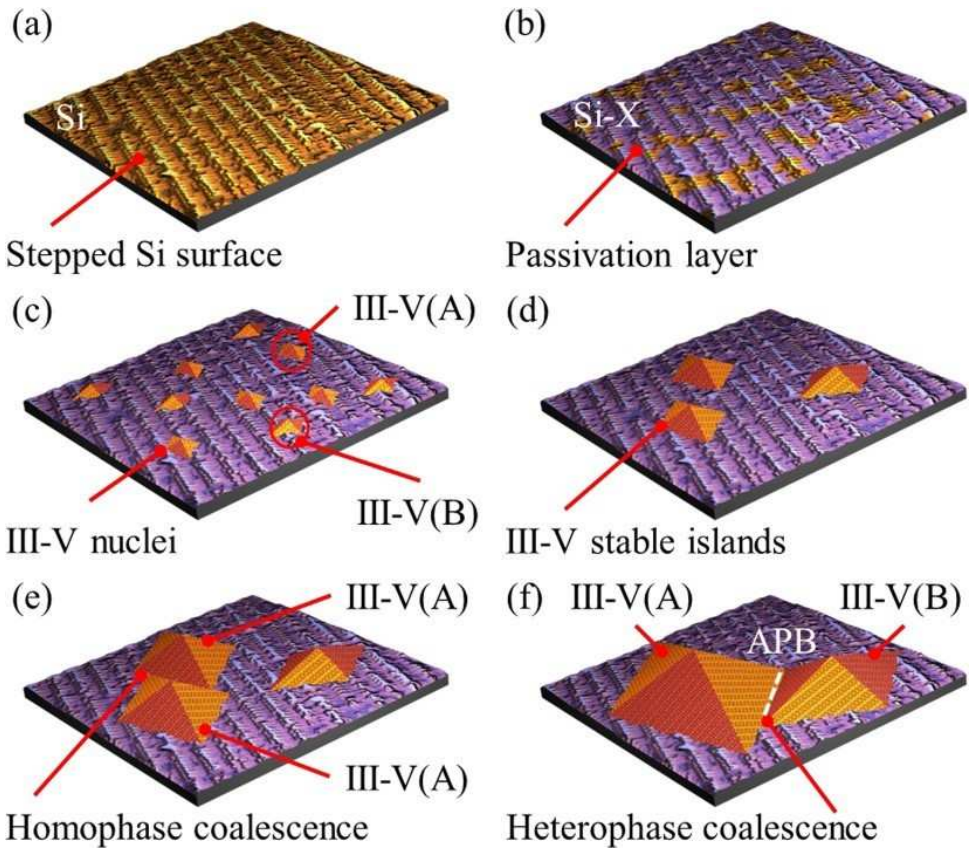

Figure 3.9 Description of the proposed III-V/Si Growth steps, with (a) the 35×35nm2 STM image of a stepped starting Si surface. The Si surface is then covered (b) at least partially with a 2D passivation layer. Nucleation starts (c) with local epitaxial relationships and crystal polarity. Some stable islands then grow (d), independently of Si steps. If two islands of the same phase coalesce (e), they will form a larger island. If two islands having different phases coalesce (f), antiphase boundaries will appear.

Step (i): A thermal pretreatment of the Si surface possibly allows organizing Si steps [in monoatomic or biatomic layers for (001) substrates], giving rise to a statistically dominant monodomain or bidomain distribution at the Si surface. A 35×35 nm² STM image of a Si(001)-6°-off surface is provided for a realistic illustration in **Figure 3.9(a)**, but the same process occurs on Si(111). We note here, that perfect monodomain surfaces is usually not achieved in realistic conditions, different polarities of the Si surface are observed at the surface most of the times.

Step (ii): The very reactive silicon surface is covered with a 2D complete or incomplete passivating layer (**Figure 3.9(b)**). This can be accomplished intentionally with hydrogen, for instance, in chemical vapor deposition reactors, or unintentionally with growth chamber residual atmosphere exposure, group-V initial exposure such as Si-As, Si-N, Si-Sb, or Si-P, or group-III initial exposure. This lowers the Si surface energy [see **Figure 3.3(b)**), and promotes partial wetting conditions.

Step (iii): The nucleation starts and forms 2D or 3D small nuclei that can appear and disappear. This step is kinetically driven. The crystal polarity (we will use A and B to distinguish the two possible phases) of each nucleus is defined locally with respect to the silicon surface local orientation [**Figure 3.9(c)**].

Step (iv): Stable 3D islands are formed and grow (**Figure 3.9(d)**). The epitaxial relationship and (if necessary) dislocation network (including tilt, twist) are determined locally. Each island is monophase, because the energy cost to form an antiphase boundary is too large. Consequently, once an island is stable, its polarity is preserved during its subsequent growth by an adaptation of the charge-compensated interface structure, regardless of the nature of the steps at the surface. The density of such stable islands directly defines the subsequent density/size of APDs.

This density is fully determined by the kinetics of nucleation [45], mainly imposed by the migration of group-III atoms, *i.e.*, growth temperature, nature of group-III atoms used, V/III ratio, but also the vicinality used (numbers of steps at the surface), and the nature of the passivation layer at the Si surface. The comparison between Al and Ga group-III atoms in Ref. [24] perfectly illustrates this point. Indeed, a higher density of stable islands is obtained for AlSb/Si as compared to GaSb/Si, because the Al adatom diffusion length is known to be significantly lower than the one of Ga. Kinetics also explains why APDs observed in the literature are usually larger (*i.e.*, lower density) on nominal substrates than on vicinal ones, due to the Ehrlich-Schwoebel barrier at the step edges during the diffusion processes.

Step (v): Islands cover a large part of the Si surface, and coalescence occurs. If the two islands have the same phase, homophase coalescence leads to the formation of a larger island (**Figure 3.9(e)**). In this process, different tilt, twist, and dislocation network structures within individual islands may impact the structural quality of the coalesced island. If the two islands have different phases, heterophase coalescence necessarily leads, in addition to all the previous

structural considerations, to the formation of an antiphase boundary (**Figure 3.9(f)**). The generation of APDs in III-V/Si epilayers is therefore not governed by the surface density of the monoatomic steps, as is usually suggested [3]. It is related to the initial ratio between type-A and type-B terraces area on Si surface before the III-V overgrowth.

3.4.Conclusions

Overall, we finally conclude that most of the structural defects usually formed during III-V/Si epitaxy (twist, tilt, imperfect dislocation networks, or APDs) fundamentally originate from the partial wetting of III-V semiconductors on silicon, without a significant impact of elasticity. This generalized description of III-V/Si growth processes opens different routes to deeply cointegrate photonics and electronics, or for the development of high efficiency photovoltaic or even water splitting devices.

References

[1] C. Cornet, Y. Léger, and C. Robert, *Integrated Lasers on Silicon*. ISTE-Elsevier, 2016.
[2] D. Derkacs, R. Jones-Albertus, F. Suarez, and O. Fidaner, 'Lattice-matched multijunction solar cells employing a 1 eV GaInNAsSb bottom cell', *J. Photon. Energy*, vol. 2, no. 1, pp. 021805–1, 2012.
[3] H. Kroemer, 'Polar-on-nonpolar epitaxy', *J. Cryst. Growth*, vol. 81, no. 1–4, pp. 193–204, Feb. 1987.
[4] C.-H. Choi, R. Ai, and S. Barnett, 'Suppression of three-dimensional island nucleation during GaAs growth on Si(100)', *Physical Review Letters*, vol. 67, no. 20, pp. 2826–2829, Nov. 1991.
[5] S. Chen *et al.*, 'Electrically pumped continuous-wave III–V quantum dot lasers on silicon', *Nat Photon*, vol. 10, no. 5, pp. 307–311, May 2016.
[6] I. Lucci *et al.*, 'Universal description of III-V/Si epitaxial growth processes', *Phys. Rev. Materials*, vol. 2, no. 6, p. 060401, juin 2018.
[7] R. Hull and A. Fischer-Colbrie, 'Nucleation of GaAs on Si: Experimental evidence for a three-dimensional critical transition', *Applied Physics Letters*, vol. 50, no. 13, pp. 851–853, Mar. 1987.
[8] F. Ernst and P. Pirouz, 'Formation of planar defects in the epitaxial growth of GaP on Si substrate by metal organic chemical-vapor deposition', *Journal of Applied Physics*, vol. 64, no. 9, pp. 4526–4530, Nov. 1988.
[9] J. E. Northrup, 'Energetics of GaAs island formation on Si(100)', *Physical Review Letters*, vol. 62, no. 21, pp. 2487–2490, May 1989.

[10] O. Supplie *et al.*, 'Atomic scale analysis of the GaP/Si(100) heterointerface by in situ reflection anisotropy spectroscopy and ab initio density functional theory', *Phys. Rev. B*, vol. 90, no. 23, p. 235301, Dec. 2014.
[11] O. Romanyuk, O. Supplie, T. Susi, M. M. May, and T. Hannappel, 'Ab initio density functional theory study on the atomic and electronic structure of GaP/Si(001) heterointerfaces', *Phys. Rev. B*, vol. 94, no. 15, p. 155309, Oct. 2016.
[12] A. Beyer *et al.*, 'Pyramidal Structure Formation at the Interface between III/V Semiconductors and Silicon', *Chem. Mater.*, vol. 28, no. 10, pp. 3265–3275, May 2016.
[13] M. D. Pashley, 'Electron counting model and its application to island structures on molecular-beam epitaxy grown GaAs(001) and ZnSe(001)', *Phys. Rev. B*, vol. 40, no. 15, p. 10481, Nov. 1989.
[14] O. Romanyuk, T. Hannappel, and F. Grosse, 'Atomic and electronic structure of GaP/Si(111), GaP/Si(110), and GaP/Si(113) interfaces and superlattices studied by density functional theory', *Physical Review B*, vol. 88, no. 11, Sep. 2013.
[15] P. Kumar and C. H. Patterson, 'Dielectric Anisotropy of the GaP / Si (001) Interface from First-Principles Theory', *Physical Review Letters*, vol. 118, no. 23, Jun. 2017.
[16] K. Madiomanana *et al.*, 'Silicon surface preparation for III-V molecular beam epitaxy', *Journal of Crystal Growth*, vol. 413, pp. 17–24, Mar. 2015.
[17] T. Quinci *et al.*, 'Defects limitation in epitaxial GaP on bistepped Si surface using UHVCVD–MBE growth cluster', *Journal of Crystal Growth*, vol. 380, pp. 157–162, Oct. 2013.
[18] Y. P. Wang *et al.*, 'Abrupt GaP/Si hetero-interface using bistepped Si buffer', *Applied Physics Letters*, vol. 107, no. 19, p. 191603, Nov. 2015.
[19] P. Guillemé *et al.*, 'Antiphase domain tailoring for combination of modal and 4^{-} -quasi-phase matching in gallium phosphide microdisks', *Opt. Express, OE*, vol. 24, no. 13, pp. 14608–14617, Jun. 2016.
[20] C. Robert *et al.*, 'Electronic, optical, and structural properties of (In,Ga)As/GaP quantum dots', *Phys. Rev. B*, vol. 86, no. 20, p. 205316, Nov. 2012.
[21] Y. Takagi, H. Yonezu, K. Samonji, T. Tsuji, and N. Ohshima, 'Generation and suppression process of crystalline defects in GaP layers grown on misoriented Si(1 0 0) substrates', *J. Cryst. Growth*, vol. 187, no. 1, pp. 42–50, Avril 1998.
[22] F. Semond *et al.*, 'Molecular Beam Epitaxy of Group-III Nitrides on Silicon Substrates: Growth, Properties and Device Applications', *physica status solidi (a)*, vol. 188, no. 2, pp. 501–510, Dec. 2001.
[23] J. Tersoff and F. K. LeGoues, 'Competing relaxation mechanisms in strained layers', *Phys. Rev. Lett.*, vol. 72, no. 22, pp. 3570–3573, May 1994.
[24] K. Akahane, N. Yamamoto, S. Gozu, A. Ueta, and N. Ohtani, 'Initial growth stage of GaSb on Si(001) substrates with AlSb initiation layers', *Journal of Crystal Growth*, vol. 283, no. 3–4, pp. 297–302, Oct. 2005.
[25] P. Guillemé *et al.*, 'Second harmonic generation in gallium phosphide microdisks on silicon: from strict 4^{-} to random quasi-phase matching', *Semicond. Sci. Technol.*, vol. 32, no. 6, p. 065004, 2017.
[26] J. B. Rodriguez, K. Madiomanana, L. Cerutti, A. Castellano, and E. Tournié, 'X-ray diffraction study of GaSb grown by molecular beam epitaxy on silicon substrates', *Journal of Crystal Growth*, vol. 439, pp. 33–39, Apr. 2016.

[27] A. Dupré and P. Dupré, *Théorie mécanique de la chaleur*. Gauthier-Villars, 1869.
[28] G.-H. Lu, M. Huang, M. Cuma, and F. Liu, 'Relative stability of Si surfaces: A first-principles study', *Surface Science*, vol. 588, no. 1–3, pp. 61–70, Aug. 2005.
[29] D. J. Chadi, 'Stabilities of single-layer and bilayer steps on Si(001) surfaces', *Phys. Rev. Lett.*, vol. 59, no. 15, pp. 1691–1694, Oct. 1987.
[30] P. Bogusławski, Q.-M. Zhang, Z. Zhang, and J. Bernholc, 'Structure of monatomic steps on the Si(001) surface', *Physical Review Letters*, vol. 72, no. 23, pp. 3694–3697, Jun. 1994.
[31] L. Geelhaar, J. Márquez, P. Kratzer, and K. Jacobi, 'GaAs(2 5 11): A New Stable Surface within the Stereographic Triangle', *Phys. Rev. Lett.*, vol. 86, no. 17, p. 3815, avril 2001.
[32] D. K. Biegelsen, R. D. Bringans, J. E. Northrup, M. C. Schabel, and L.-E. Swartz, 'Arsenic termination of the Si(110) surface', *Physical Review B*, vol. 47, no. 15, pp. 9589–9596, Apr. 1993.
[33] J. E. Northrup, 'Structure of Si(100)H: Dependence on the H chemical potential', *Physical Review B*, vol. 44, no. 3, pp. 1419–1422, Jul. 1991.
[34] P. Müller and R. Kern, 'Equilibrium nano-shape changes induced by epitaxial stress (generalised Wulf–Kaishew theorem)', *Surface Science*, vol. 457, no. 1, pp. 229–253, juin 2000.
[35] R. Kern and P. Müller, 'From Wulff Kaishew' theorem to nanodots', in *Nanoscale phenomena and structures*, Ed. D.Kashchiev, Pr Drinov Pub. House, 2008, pp. 23–41.
[36] P. Curie, 'Sur la formation des cristaux et sur les constantes capillaires de leurs différentes faces', *Bulletin de Minéralogie*, vol. 8, no. 6, pp. 145–150, 1885.
[37] P. Müller and R. Kern, 'Equilibrium shape of epitaxially strained crystals (Volmer–Weber case)', *Journal of Crystal Growth*, vol. 193, no. 1, pp. 257–270, Sep. 1998.
[38] C. A. Johnson, 'Generalization of the Gibbs-Thomson equation', *Surface Science*, vol. 3, no. 5, pp. 429–444, Dec. 1965.
[39] R.Kaishew, *Arbeitstagung fetsköper Phys.*, p. 81, 1952.
[40] S. Andrieu and P. Müller, *Les Surfaces solides : concepts et méthodes*. EDP Sciences, 2012.
[41] A. Ponchet, G. Patriarche, J. B. Rodriguez, L. Cerutti, and E. Tournié, 'Interface energy analysis of III–V islands on Si (001) in the Volmer-Weber growth mode', *Appl. Phys. Lett.*, vol. 113, no. 19, p. 191601, Nov. 2018.
[42] N. N. Ledentsov, *Growth Processes and Surface Phase Equilibria in Molecular Beam Epitaxy*. Springer Science & Business Media, 1999.
[43] A. Ponchet, D. Lacombe, L. Durand, D. Alquier, and J.-M. Cardonna, 'Elastic energy of strained islands: Contribution of the substrate as a function of the island aspect ratio and inter-island distance', *Applied Physics Letters*, vol. 72, no. 23, pp. 2984–2986, Jun. 1998.
[44] C. G. Van de Walle and J. Neugebauer, 'First-Principles Surface Phase Diagram for Hydrogen on GaN Surfaces', *Physical Review Letters*, vol. 88, no. 6, Jan. 2002.
[45] J. A. Venables, G. D. T. Spiller, and M. Hanbucken, 'Nucleation and growth of thin films', *Rep. Prog. Phys.*, vol. 47, no. 4, p. 399, 1984.

Chapter 4 : Silicon growth and surface control for III-V/Si integration

In this chapter, we focus on the chemical or physical preparation and homoepitaxial growth of silicon for further III-V semiconductor deposition. The reduction of contaminants either by annealing or by growth processes is first discussed. We then study the evolution of the monodomain/bidomain Si surface property, under different growth conditions, on nominal and vicinal substrates. Finally, we investigate the possibility to propagate or annihilate Antiphase Boundaries (APBs) by using thin AlGaP marker layers.

This work has been performed in close collaboration with T. Rohel, R. Gautheron-Bernard and C. Cornet (FOTON Institute: *MBE, UHV-CVD, RHEED, AFM*), S.Charbonnier and P.Turban (IPR: *STM*), M. Vallet and A. Ponchet (CEMES: *TEM*). I was personally involved in UHVCVD sample growth, RHEED&AFM measurements and analysis.

In order to improve the III-V overgrowth on the Si substrate it is important to have a high quality (with low contaminant density, and monodomain) silicon starting surface, as mentioned in Chapter 3. In this chapter, a particular effort is done on the explanation of the different strategies we adopted, in order to avoid the risk of contamination and also to control the steps organization on Si(001) surface, whose atomistic description has been already introduced in detail in Chapter 2.

4.1. Si(001) surface chemical preparation and growth by UHV-CVD

Silicon surface chemical or physical treatment is the first step before any III-V or Si epitaxial growth. Indeed, it allows in principle to remove the oxide, and to limit the surface contamination. In the following section, the surface treatments are introduced and the silicon growth process used is described.

4.1.1. Si(001) surface treatments

Si(001) surface preparation is necessary for avoiding the presence of contaminants, such as oxygen or carbon atoms [1], in order to have a smooth and defect-free substrate. Indeed, the surface is highly sensitive to contaminants and very few of them can cause a rough and defective surface which can be detrimental either for the following III-V overgrowth or Si homoepitaxial growth.

The silicon surface cleaning has been widely studied [2]. Indeed, ex-situ chemical surface treatments [3], [4] or in-situ through gases or thermal treatments [5]–[8] have been reported. Especially, it was found that in-situ thermal treatments can impact the surface roughness and can also induce contaminant diffusion on the Si(001) surface, resulting in undesired surface reconstructions [9], [10]. Nevertheless, thermal treatments can be a strategy of choice, but one needs to be able to heat the silicon wafer at 900°C. This requirement is usually impossible in most III-V MBE chambers. In the following, most of the samples presented will be chemically prepared, otherwise it will be mentioned.

One detrimental effect due to the presence of contaminants is related to their impact on the steps behavior on the Si(001) surface. This effect was studied in collaboration with IPR. Nominal <100 +/-0.2°> off 0.3° towards <110 +/- 0.1°> and vicinal <100 +/-0.2°> off 6° towards <110> silicon surfaces were analyzed at IPR. First, surfaces preparation consisting in a HF treatment followed by ozonolysis was performed at FOTON. To this aim, the wafers were first dipped in HF 1% solution for 90 seconds. Then, they were exposed under UV/O_3 for 10 minutes (ultraviolet ozonolysis [11]–[13]) to remove contaminants [11], [14] such as carbon, organics or metal particles. The SiO_2 layer, formed after this stage on the Si surface, was removed by IPR through an in-situ annealing (1h at 1000°C) under a chamber pressure of 10^{-10}mbar. After that, they analyzed the surfaces by scanning tunneling microscopy (STM), as shown in **Figure 4.1**. Nanometric crystallites are observed at the surface. We attribute the formation of these crystallites to the presence of residual amount of C on the silicon surface. Indeed, it is reported that annealing above 600 °C favors the appearance of β-SiC crystallites [15]. On the nominal 0.3°-off Si(001) surface (see **Figure 4.1(a)**), these SiC crystallites modify significantly the step distribution at the surface, hampering the formation of stable D_B biatomic steps. Instead, it

does not happen on Si(001) 6°-off surface, where the correspondent D_B-step terraces periodicity of 2.6nm has been observed on a large scale, independently of crystallite formation at the surface (**Figure 4.1(b)**).The big bump on the bottom right corner of **Figure 4.1(b)** is a STM tip effect which is likely related to the presence of a SiC crystallite underneath. We note that the annealing temperature used before STM imaging is much larger than the typical T°C used in the MBE chambers. The steps organization is thus expected to be much less regular at the surface in conventional III-V/Si MBE growth conditions.

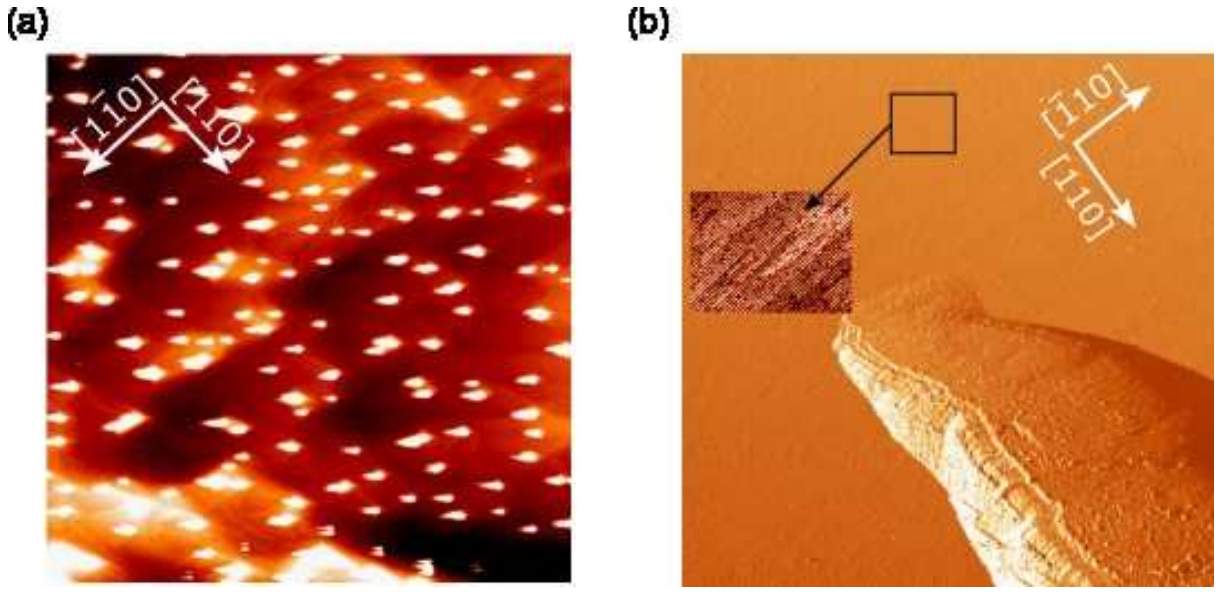

Figure 4.1 (a)1x1μm^2 STM image of a Si(001) 0.3°-off surface with SiC crystallites that are typically [2-4]nm height (b) 300x300μm^2 STM image of a Si(001) 0.6°-off surface both realized after annealing for 1h at 1000°C under a chamber pressure of 10^{-10}mbar. Initial accidental C-contamination leads to SiC crystallites formation acting as pining centers for the monoatomic steps (IPR).

Besides wafer chemical cleaning, another important step to avoid contaminants formation consists in cleaning and heating the wafer molybdenum holder before any subsequent growth. In the FOTON institute, this process is achieved by the following steps: almost 100mL and few drops of bromine are poured and homogenized in a crystallizer. The wafer holder is then immersed into the solution for few minutes and it is rinsed two times: first with methanol and after with deionized water. It is transferred into the oven heated up at

120°C. Finally, the molybdenum holder with a sacrificed wafer is degassed in the ultrahigh vacuum chemical vapor deposition (UHV-CVD) chamber, by annealing at 1100°C for 10 minutes.

4.1.2. Si growth under UHV-CVD

It is well-known that Si(001) homoepitaxial growth under UHV-CVD is governed by two main phenomena: i) hydrogen desorption and ii) silane (SiH_4) absorption[16]–[19]. The latter consists in the SiH_4 decomposition by forming tri-hydrides (SiH_3), di-hydrides (SiH_2) and mono-hydrides (SiH) on the silicon surface [18]–[21]. These reactions are described by the equations in **Figure 4.2(a)** where *db* stands for "dangling bonds" and the single and double underlining indicate the number of surface bonds of a Si or H atom [18], [19]. The SiH_4 decomposition is represented in **Figure 4.2(b)** where the silicon atoms are in blue, the hydrogen atoms are the empty circles and the Db, in red, are the dangling bonds. Due to the presence of hydrides species, the surface will have different phases ((3x1), (2x1) and (1x1)) as a function of the growth temperature. At temperatures lower than 20°C, SiH_4 molecules bond to dangling bonds by releasing hydrogen atoms. These bonds form tri-hydrides (SiH_3) which correspond to the 1x1 surface phase. With the increasing of the temperature, di-hydrides (SiH_2) appear on the surface (3x1 phase). Nevertheless, at temperature below 100°C all the hydrides species mentioned can be detected, and the (1x1) phase is commonly observed, as a result of the coverage with a mixture of them [20], [22]. SiH_2 and SiH_3 are highly unstable, indeed they will desorb at temperatures higher than 300°C leaving the surface covered by mono-hydrides (2x1 phase). The hydrogen released by the hydrides species is then desorbed.

The hydrogen desorption has been widely studied [16], [24]–[26]. It desorbs completely at temperature is higher than 600°C [16], [27]. The reaction is given by the last equation of **Figure 4.2(a).** In particular, two peaks called β_1 and β_2 were found respectively at 475°C for hydrogen desorption from mono-hydrides (SiH) and around 340°C from di-hydrides (SiH_2). The β_3 peak related to the hydrogen desorption from SiH_3 was found to overlap β_2 [16], [19], [27]. Finally, the Si(001) growth can be divided in three main regimes. They are represented in **Figure 4.3** where the growth rate is plotted as a function of the inverted growth temperature $10^3/T_g$. At low temperature, the hydrogen desorption is weak. In this regime, the growth rate depends on

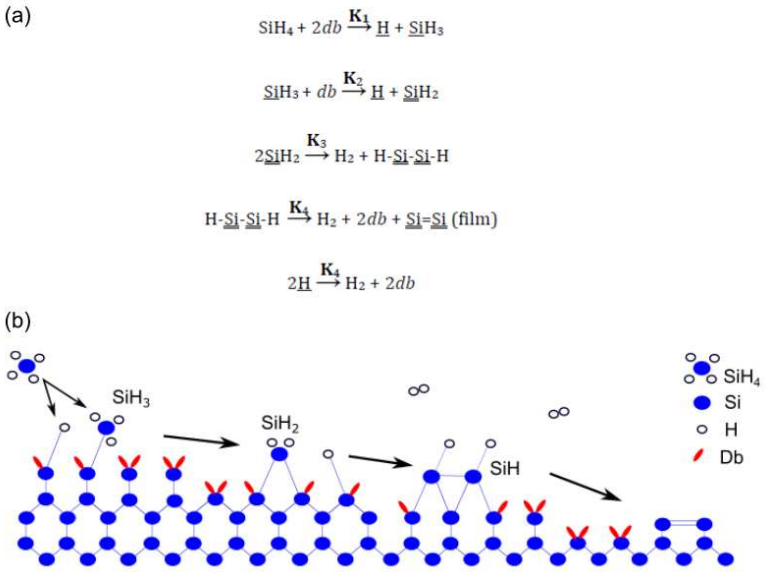

Figure 4.2 SiH_4 decomposition reactions which form trihydrides (SiH_3), dihydrides (SiH_2) and monohydrides (SiH**)** (a) equations [18], [19] and (b) scheme. Courtesy of [23]

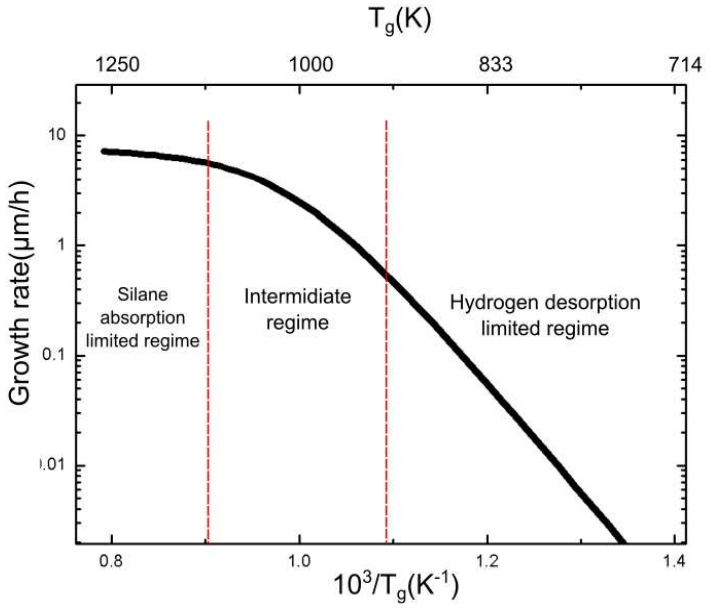

Figure 4.3 Silicon growth rate as a function of the temperature for a given silane flux

how many free-sites are available for silane molecules absorption. At temperatures higher than 600°C, when the hydrogen is completely desorbed, the growth is limited by the silane absorption, and thus strongly depends on the chamber silane pressure. At intermediate temperatures, the growth is controlled by the competition between silane absorption and hydrogen desorption.

4.1.3. Homoepitaxial Si(001) growth in standard growth conditions

In this thesis, in order to study the surface quality, an ex-situ surface cleaning procedure followed by a Si homoepitaxial growth process was performed. At the beginning of my thesis, I repeated the reference sample that was obtained in previous works. The details of the chemical treatments and standard growth conditions used will be described now. On this basis, we will be able to compare the improvements that were achieved or not.

The ex-situ surface cleaning done in this thesis work, consists in a chemical treatment developed by T. Nguyen Than, and used in ref.[4] at FOTON Institute, inspired by the work of Takahagi *et al.*[11]. Indeed, the latter showed a high surface quality by preparing the surface with a simple UV/HF treatment. This method proved its efficiency also for the III-V/Si growth[28], [29]. Y. Ping Wang *et al.* at FOTON Institute reached a high silicon surface quality through a similar cleaning treatment called “optimized HF process”. The surface quality is improved by reducing the time during which the surface is exposed to chemical products [4]. The first step consists in removing the native oxide layer of the silicon surface together with other contaminants. This step, as mentioned above, is achieved by dipping the wafer in HF 1% bath for 90 seconds. Then, oxidation is performed by using ultraviolet ozonolysis [11]–[13] where the wafer is exposed under UV/O_3 for 10 minutes to fix contaminants [11], [14]. This step forms a few nm-thick SiO_2 layer which is removed by dipping a second time the wafer in the HF 1% for 90 seconds. This “last HF” process is performed in the MBE-UHVCVD room to guarantee rapid loading in UHV chambers. The surface hydrogenation, achieved in this final step, is fundamental to promote its passivation [30]–[32]. The hydrogen is then removed in-situ by annealing at low temperature (400-500°C) as described hereafter.

Finally, we grow a 1µm-thick homoepitaxial Si layer on Si(001) 6°-off by taking the same growth conditions thanks to which a smooth surface was already achieved in previous works at FOTON Institute before the beginning of my thesis [27]. The growth conditions used on the Si(001) 6°-off substrate are described in **Figure 4.4(a).** After the ex-situ surface treatment the wafer is loaded into the UHV-CVD chamber at a residual chamber pressure of P_R=8x10^{-10}Torr, the temperature is then linearly raised up to the desired value T_g=820°C. Just before the temperature reaches the value T_0 (corresponding to the first desorption peak β_1), the silicon surface is exposed to a very low silane flux (P_{SiH4}=0.01Torr) to avoid any recontamination. Indeed, without hydrogen passivation the silicon surface is very reactive and may easily be contaminated by the chamber residual atmosphere. When T_g is reached, the silane flux is changed to P_{SiH_4}=5Torr for 1h. Finally, the temperature is cooled down by quenching under vacuum. In the meantime, the surface reconstruction is analysed in real-time by reflection high-energy electron diffraction (RHEED) through an electron beam incident (angle range: 0.3°-0.5°) on the surface plane, working at 29keV and 1.5A. A 2xn surface reconstruction, associated to a statistically dominant monodomain surface, is obtained as illustrated in **Figure 4.4(b)** [33]. Indeed, due to the narrow terraces length which is around 2.58nm for double-steps on Si(001) 6°-off substrate[27], the steps look as a grating like staircase when the beam is parallel to the [1-10] direction. Thus, the RHEED diagram splits by forming a xn pattern[33]. Instead, when the beam is parallel to the [110] direction, a 2x pattern is observed. The RHEED patterns along the two azimuths are presented in **Figure 4.4(b).** The 5x5µm^2 atomic force microscopy (AFM) image in **Figure 4.4(c)** shows a smooth surface (RMS=0.65nm). Nevertheless, the absence of hydrogen passivating the surface, during the cooling, favors the formation of impurities. Indeed, 1nm-height islands are visible at the surface level (AFM image of **Figure 4.4(c)**). As discussed previously, we attribute this observation to the presence of SiC crystallites that form when heating a C-contaminated Si surface [34] as shown in the 5x5µm^2 AFM image in **Figure 4.4(c)**. We confirmed the results obtained by previous PhD students using the same growth procedure at FOTON institute [27].

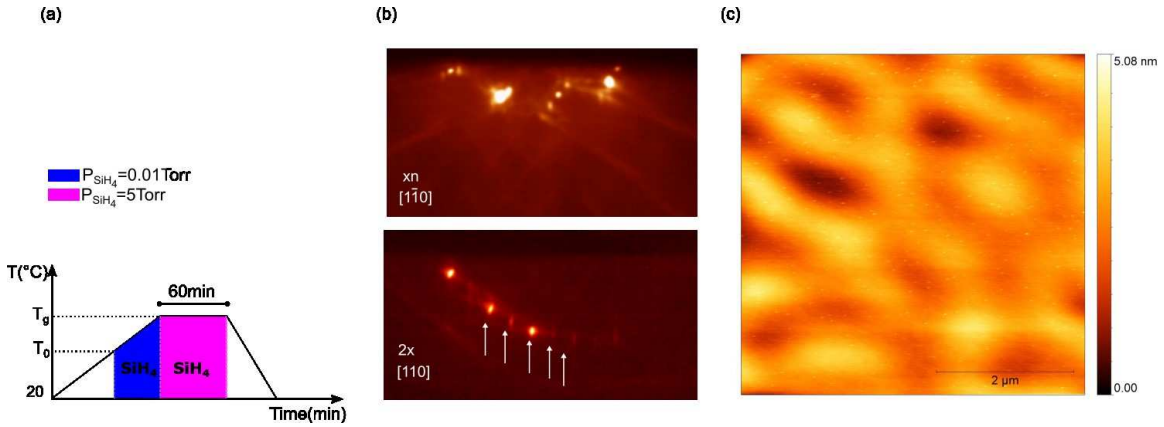

Figure 4.4 (a) Si Growth sequence used at FOTON laboratory at the beginning of my thesis [27] (b) RHEED patterns on Si-6°-off substrates: a 2x reconstruction is observed on the [110] azimuth while a xn reconstruction is observed on the [1-10] azimuth
(c) Corresponding 5x5µm AFM image of the sample after the growth

In conclusion, the standard growth conditions used at FOTON Institute at my arrival are not sufficient to have a contaminants free surface. In order to improve the surface quality, we worked on different strategies to be able to avoid the presence of impurities on the silicon surface. They are presented in the following section. First, we studied how the chemical preparation and products impact on the surface morphology and reconstructions through a high temperature annealing process. We then, annealed the silicon surface under H_2 and SiH_4 in order to protect the Si surface upon contamination.

4.2.Toward a contamination-free Si(001) surface

In order to study the impact of the cleaning treatements (and especially the chemical products) on the surface morphology and reconstruction, we annealed under UHV two Si(001) surfaces with a 0.3° miscut angle towards [110], one of which was ex-situ chemically prepared (H-terminated surface, with the procedure described previously) before being loaded inside the UHV-CVD chamber. The other one was loaded as-received. In this case, the silicon surface is covered by a native oxide (SiO_2) layer of 2-3nm. Once the samples were loaded into the UHV-CVD chamber (residual chamber pressure P_R=8.9x10^{-10}Torr), they were heated up to the

annealing temperature T_a=1095°C for 2 minutes at a work chamber pressure of P_w=5.7x10^{-8}Torr. Finally, the samples were cooled down by quenching to room temperature.

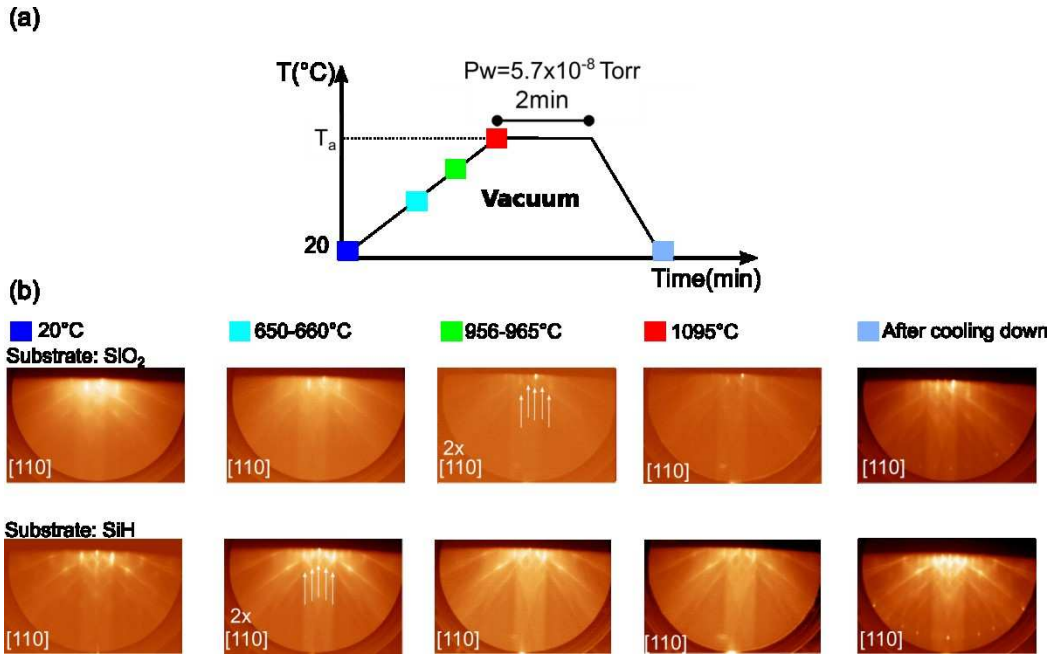

Figure 4.5 (a) Scheme of the annealing procedure under a residual chamber pressure P_R=8.9x10^{-10}Torr, and a work chamber pressure of P_w=5.7x10^{-8}Torr at T_a=1095°C for both the cases investigated (with a SiO_2 or SiH surfaces**)**. Different colors are used to higlight the temperatures corresponding to the RHEED patterns along the [110] azimuth in (b)

This procedure is illustrated in **Figure 4.5(a)**. We monitored the surfaces reconstruction by RHEED along the [1-10] and [110] azimuth. The RHEED on the [110] azimuth is shown as a function of the temperature in **Figure 4.5(b)**. At room temperature (blue square), modulated and broad diffraction streaks of the x1 pattern are observed in both cases [27], [35]. We note that the diffuse part of the RHEED signal is less intense for the chemically cleaned H-terminated silicon surface (SiH) case, which indicates a better surface organization with the H-terminated surface. Also, kikuchi lines are less sharp in the RHEED pattern of SiO_2 substrate. When the temperature reaches almost 650-660°C (light blue square), the hydrogen is completely desorbed from the SiH surface and a clear 2x reconstruction appears. Instead, on the other case, the 2x reconstruction appears at higher temperatures around 956°C (green square), corresponding to the oxyde desorption. After, in both cases the 2x reconstruction is preserved

at higher temperatures and it becomes sharper after the cooling down at room temperature. Also, when the temperature is cooled down a second order Laue zone appears in the RHEED pattern of both the surfaces, but it is sharper in the case of SiH surface. On the [1-10] azimuth, a x2 reconstruction is observed. The superposition of (2x1) and (1x2) surface reconstructions gives rise to a (2x2) apparent RHEED diagram that is associated to a bi-domain surface. If we compare the two surfaces reconstructions as a function of the temperature, we can see that overall, the RHEED patterns are much sharper in the case of the SiH surface indicating a better surface organization than the one obtained in the other case. Moreover, the x2 reconstruction is obtained at lower temperature when the wafer is ex-situ chemically cleaned (due of course to the different desorption temperatures of SiH and SiO_2), reducing the thermal budget and duration of the annealling process.

Now, looking at corresponding 5x5µm^{2}AFM images of **Figure 4.6(b) and (c)**, contaminants are still observed on both surfaces, with and without chemical preparation (SiH and SiO_2). From this comparison, we conclude that the chemical HF pretreatment of the Si may not be responsible of the presence of contaminants at the surface. Another possible source of contamination is the presence of carbon atoms in the residual atmosphere of the chamber. Therefore, in the following, we will study some strategies to protect the silicon surface, especially in the high temperature range, when the silicon surface is highly reactive.

4.2.1. Annealing of Si(001) under an H_2 or SiH_4 atmosphere

As mentioned in the previous section, by annealing under vacuum (P_R=8.9x10^{-10}Torr) the silicon wafer, a contaminants-free surface has not been achieved (See **Figure 4.6(b) and (c)**). Thus, under the hypothesis that the contaminants have more chance to deposit on a nude and highly reactive Si surface, we will try to keep the surface covered during all the process. Especially, we investigated the two following strategies: annealing under H_2 and under SiH_4.

In order to avoid contamination, the first strategy analysed, which is very conventional in CVD to protect the nude Si surface, consisted in annealing under hydrogen during all the process (from initial room temperature to final room temperature). We therefore annealed the different surfaces, with and without chemical preparation (with a SiH or SiO_2 terminated surface), under

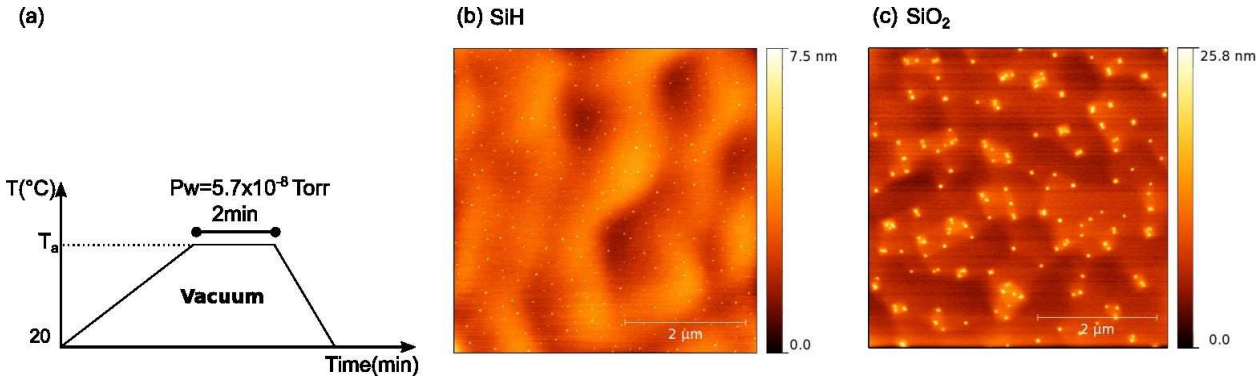

Figure 4.6 (a) scheme of the annealing procedure under under ultra high vacuum (residual chamber pressure P_R=8.9x10^{-10}Torr) and a work chamber pressure of P_w=5.7x10^{-8}Torr at T_a=1095°C; 5x5µm^2 AFM images of the surface samples under investigation: (b) ex-situ chemically cleaned,H-teminated, Si(001) surface (SiH) and (c) surface covered by a native oxide (SiO_2) layer

60sccm hydrogen (corresponding to a partial pressure P_p=9x10^{-3}Torr) until the temperature reaches T_a=1095°C for 2 minutes and goes down to room temperature.The growth sequence is presented in **Figure 4.7(a)**. The 5x5µm^2 AFM images in **Figure 4.7(b) and (c)** shows the silicon surfaces after annealing. In both cases, contaminants are still observed at the surface. Nevertheless, the maximum pressure of hydrogen delivered by the UHV-CVD experiment at FOTON Institute is lower than the pressure usually used in common CVD systems. Some works have also shown that for higher hydrogen pressure and annealing temperatures, hydrogen can impact on the Si(001) steps organization. Indeed, a double-layer stepped surface, starting from a single stepped nominal Si(001) surface 0.15° misoriented towards the [110] direction, was obtained after 10min annealing at 900°C under a high H_2 pressure of 600Torr [36]. Brückner *et al*. have obtained Da-type steps, cooling from 1000°C to 500°C, at 950mbar of H_2 pressure, on a Si(001) surface 2° misoriented in the [011] direction [37]. While, under vapor phase epitaxy (VPE) conditions, Volz *et al.* observed double steps formation on a homoepitaxial silicon buffer deposited on exact Si(001). It was achieved by annealing at 950°C for 10min under 950mbar H_2 pressure [8]. Therefore, in our case with such a low hydrogen pressure, the protection of the silicon surface upon contamination was not achieved here.

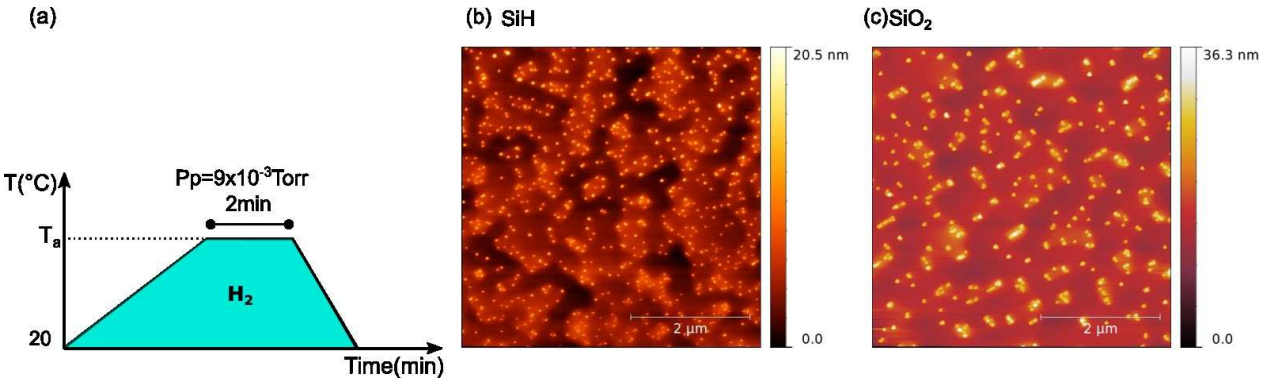

Figure 4.7 (a) scheme of the annealing procedure under hydrogen (60sccm) under H_2 partial pressure P_P=9x10^{-3}Torr at T_a=1095°C; 5x5µm^2 AFM images of the samples under investigation: (b) ex-situ chemically cleaned,H-teminated, Si(001) surface (SiH) and (c) surface covered by a native oxide (SiO_2) layer

In the following, we propose to protect the surface by annealing under SiH_4. In **Figure 4.4**, we have shown that the standard Si growth conditions are not good enough to avoid impurities formation on Si surface. In these growth conditions, the quenching at room temperature is done under vacuum, which means that the silicon surface is not protected, especially at the beginning of the quenching at high temperature. Thus, by supposing that in this stage the Si surface, being nude and reactive, have more chance to be contaminated, we performed a new homoepitaxial growth where the surface is always exposed to SiH_4 flux. Indeed, we kept a low silane flux (P_{SiH_4}=0.01Torr) while rising up the temperature to T_g =830°C and also, during the quenching (P_{SiH_4}=0.02Torr) in order to prevent the formation of SiC crystallites and contaminants absorption as well (residual chamber pressure P_R=1.3x10^{-9}Torr). The growth scheme is presented in **Figure 4.8(a)**. The surface was analyzed in real-time by RHEED and after the growth by AFM. By RHEED measurements, a 2xn diagram is observed at the end of 1h growth but the reconstruction is not preserved during the quenching **Figure 4.8(b)**. A phase transition, due to step bunching [38] and meandering instabilities [39], makes the surface phase changing from 2xn to 2x2 after the quenching at room temperature **Figure 4.8(b)**. The surface becomes bi-domain. This change could be related to the temperature-dependence of the adatoms diffusion anisotropy on the Si(001)[40]. In particular, the atoms arranges in terraces having a length of 30-70 nm in the [110] and 600-1200 nm in the [-110] direction, as shown in the 5x5µm^2 AFM image in **Figure 4.8(c).** An important conclusion is that

we are not able to identify contaminants at the surface. We therefore drastically reduced the surface contaminants with respect to **Figure 4.4(c)**.

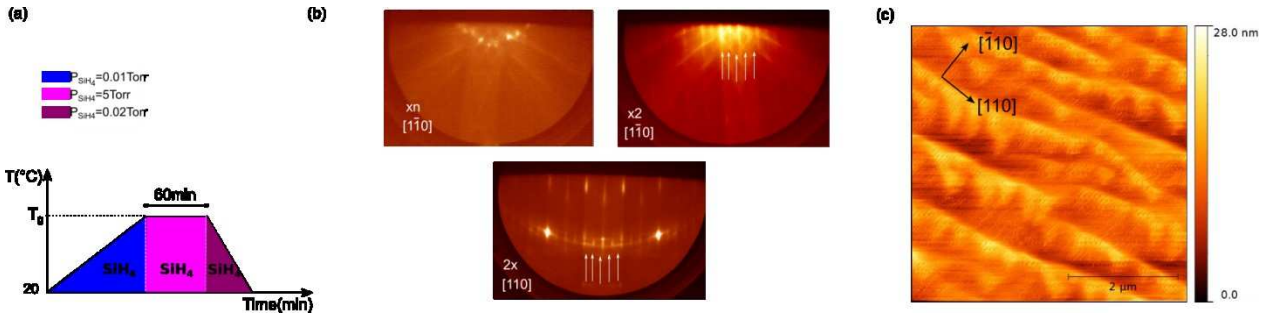

Figure 4.8 (a) Scheme of the Si growth sequence exposing the surface under SiH_4 flux from the beginning till the end of the procedure (b) 2xn and 2x2 reconstruction observed by RHEED just after 60min growth and at room temperature respectively (c) 5x5µm^2 AFM image of the Si(001)-6°-off after growth

4.3.Silicon surface reconstruction vs growth conditions

In our work presented in the Chapter 3, we have shown that the kind of atomic steps does not impact on the formation of APDs as previously suggested [41]. Instead, the ratio between type-A and type-B terraces area [42] plays an important role in the III-V overgrowth and APDs generation. Based on this conclusion, in this part of the thesis we focused on the study of the growth conditions for having of a statistically dominant mono-domain surface on both vicinal and nominal Si(001) substrates.

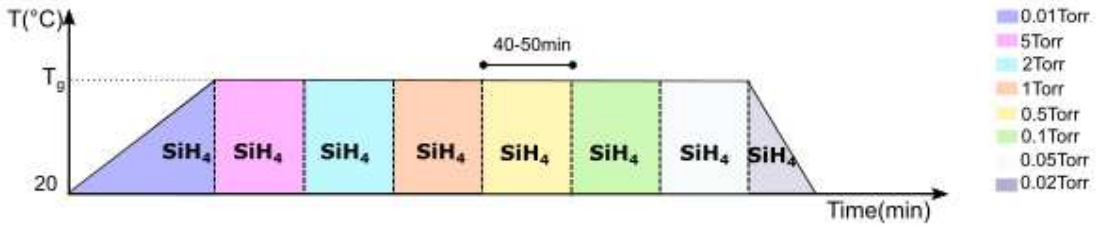

Figure 4.9 Scheme of the growth sequence used for surface reconstruction study under different SiH_4 pressures at constant growth temperature Tg. Each color refers to the different silane pressure used. After increasing the temperature to Tg under P_{SiH4}=0.01Torr, the deposition time is 40-50min for each silane pressure except in the case of P_{SiH4}=0.02Torr where it is 2min

In order to study the Si(001) surface reconstructions, we performed the silicon growth under SiH_4. In particular, the silane pressure was varied at constant temperature T_g. Nominal <100 +/- 0.2°> off 0.3° towards <110 +/- 0.1°> and vicinal <100 +/-0.2°> off 6° towards <110> Si surfaces were analyzed. The study was performed at four different T_g: 727°C, 778°C, 828°C, 868°C for the vicinal case and 751°C, 772°C, 818°C, 862°C for the nominal case. The growth sequence is illustrated in **Figure 4.9**. While increasing the temperature to T_g, the surface is exposed to a low silane flux (P_{SiH_4}=0.01Torr). The ramping rate is almost 20°C/min, thus the time to reach T_g varies as a function of the desired growth temperature. Once reached the desired T_g value, the silane pressure is changed to 5, 2, 1, 0.5, 0.1, and 0.05Torr. Each one is kept constant for almost one hour under the hypothesis that it is enough to stabilize the surface phase without any influence from the previous growth conditions. Finally, the silane flux is changed to 0.02Torr for 2 minutes and the temperature is quenched. We studied by RHEED measurement the surface reconstruction along both the [1-10] and [110] azimuth.

The plot of the surface phase diagram along the [1-10] azimuth, in the case of the vicinal Si(001) (6°-off) substrate, is presented in **Figure 4.10(a)**. We can see that at low temperatures a 3D growth mode is observed (3D growth mode is also observed on the [110] azimuth), whatever the silane pressure. For a Silane flux in the [0.01-1]Torr range, increasing the temperature around 776°C, a x2 pattern is observed while a 2x appeared on the other azimuth. The 2x2 RHEED diagram of these growth conditions suggests the formation of a bi-domain surface. When increasing the temperature until 860°C, while remaining in the same pressure range a change from a x2 to a xn reconstruction is observed (2x on the other azimuth). We therefore observe a transition to a growth mode promoting the formation of narrow terraces related to the presence of bi-atomic steps. The surface becomes monodomain. Nevertheless, for high silane flux values (P_{SiH_4}=5, 2Torr corresponding to a partial pressure P_p= $1.1x10^{-2}$, $4.4x10^{-3}$ Torr) and at temperatures above 820°C, a xn reconstruction with some spots suggesting a rough surface are present. A x2 pattern appears on the other azimuth. The surface quality, observed at lower pressure, is not preserved at higher pressure because of the high silane flux which limits the adatoms surface diffusion. RHEED images are illustrated in **Figure 4.10(b)**. Overall, in the

growth conditions studied, three main silicon growth regions can be identified moving from a rough 3D to a smooth mono-domain 2xn passing through a bi-domain 2x2. An improvement of

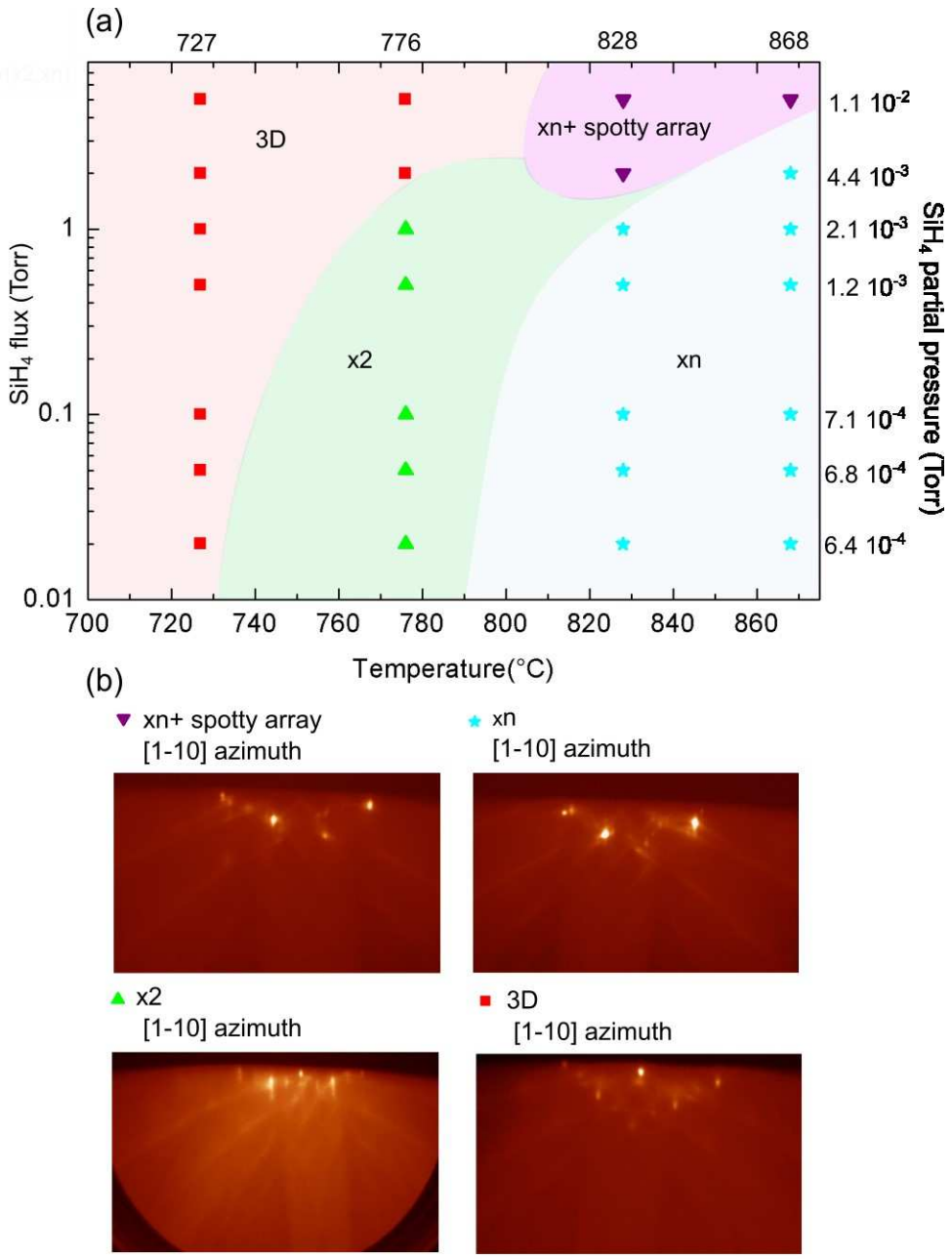

Figure 4.10 (a) Si(001) 6°-off Pressure-Temperature phase diagram . By RHEED analyis along the [1-10] azimuth, three main regions can be identified :3D, x2 (bidomain), xn (monodomain). A monodomain surface is obtained at higher temperatures (b) Rheed patterns corresponding to each region is identified on the plot in (a)

the surface quality is achieved when working at higher temperature greater than 727°C while keeping silane pressure below 1-0.5Torr. Moreover, working at such a low silane pressure for a fixed T_g, and during the cooling down step, have allowed to protect the surface from contaminants but also to preserve the surface reconstruction after the quenching to room temperature. In particular, at T_g≥828°C for pressures below 1-0.5Torr we were able to preserve the monodomain surface protecting it from contaminants at the same time.

In the case of the "nominal" (0.3°-off) Si(001) surfaces the phase diagram is presented in **Figure 4.11(a)**. We still see a 3D growth mode at low temperature whatever the silane flux (the same observation is performed on the other azimuth). Increasing the temperature to 772°C, the adatoms rearrange in terraces in a x2 reconstruction which is preserved till 862°C (a 2x pattern being observed on the [110] azimuth). We can see that at higher silane flux (from P_{SiH_4}= 5 to 0.5 Torr and a partial pressure P_P= $1.1x10^{-2}$ to $1.2x10^{-3}$ Torr) at 772°C, the 3D reconstruction changes to x2 through a transition area between P_{SiH4}=2 Torr and P_{SiH4}=1Torr, where both reconstructions are present. The RHEED is not very sharp. A diffuse RHEED pattern is also found at P_{SiH_4}=from 5 to 0.5 Torr at higher temperature above 800°C, where a x2 reconstruction is present with some spots suggesting a rough surface. The origin of these spots is not clear yet. The RHEED patterns are presented in **Figure 4.11(b)**. Overall, we can identify two main areas moving from a rough 3D to a smooth 2x2 bi-domain configuration. Indeed, an improvement of surface quality was obtained for T_g≥772°C, keeping low silane pressures (below 0.5Torr) achieving a 2x2 reconstruction. As in the case of the vicinal surface, keeping low silane pressures below 0.5Torr for fixed T_g, and also during the cooling down step, has permitted to preserve the surface reconstruction after the quenching to room temperature and to protect it from contaminants. Nevertheless, a mono-domain surface was not observed by RHEED measurement for the low miscut angle nominal Si substrate.

Finally, for both cases investigated we verified that it is possible to control the Si terraces length as a function of the Si growth conditions. In the case of the vicinal Si(001) (6°-off) substrate, through this study we were able to define a range of temperatures and pressures favorable for achieving a mono-domain surface (from P_{SiH_4} =1Torr to 0.02Torr, partial pressure

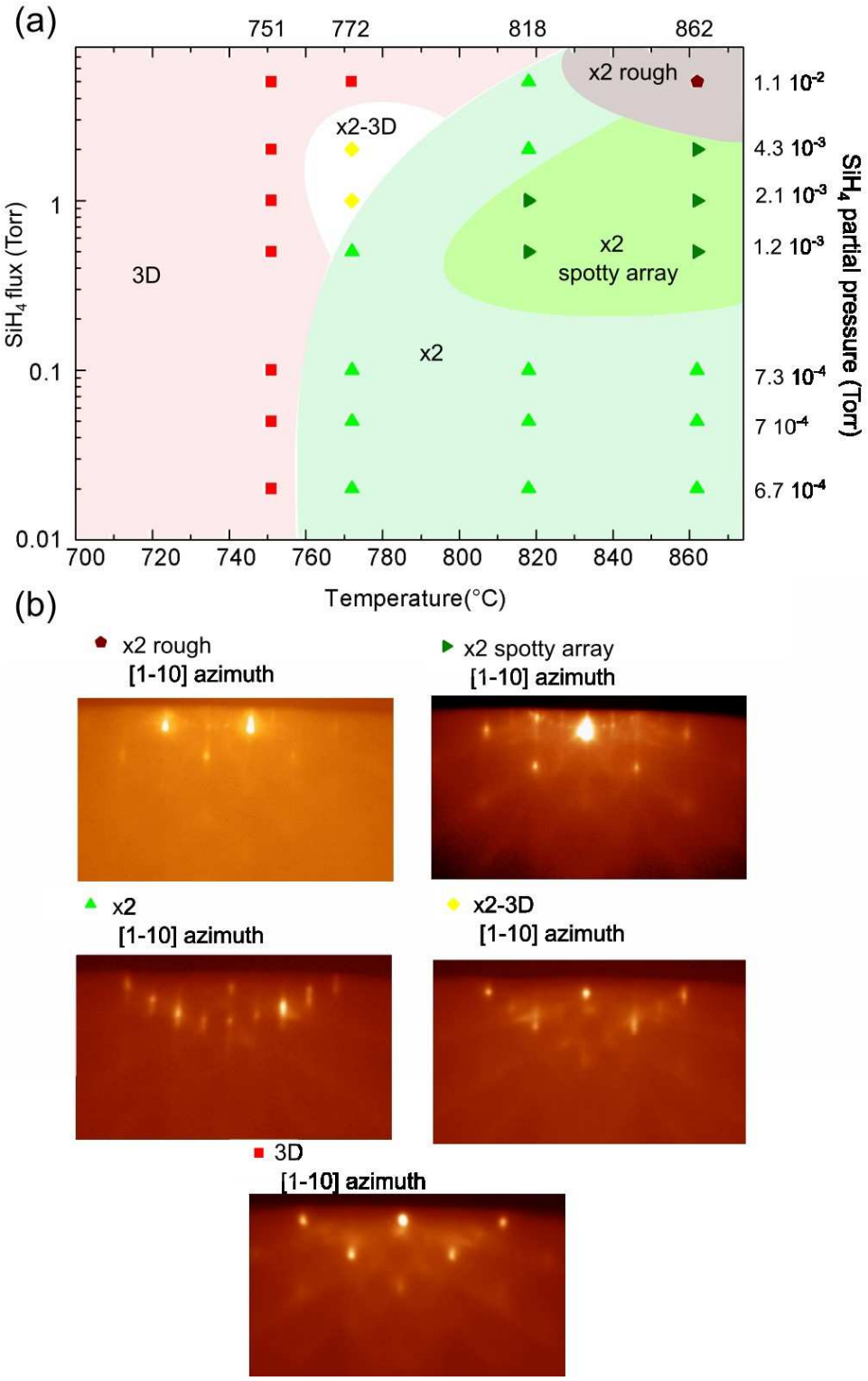

Figure 4.11 (a) Si(001) 0.3°-off Pressure-Temperature phase diagram . By RHEED analyis along the [1-10] azimuth, two main regions can be identified : 3D, x2 together with some transition areas. No monodomain surface is obtained (b) Rheed patterns corresponding to each region is identified on the plot in (a)

from P_P= 2.1x10^{-3} to 6.4x10^{-4} Torr and T_g≥828°C). The case is different for the nominal Si(001) (0.3°-off)where the monodomain was not observed by RHEED. Nevertheless, a good quality bi-domain surface has been observed at low silane pressure P_{SiH_4} =0.5Torr to 0.02Torr, partial pressure from P_P= 7.3x10^{-4} to 6.7x10^{-4}Torr and T_g≥772°C. Working with a nominal Si(001) surface with a low miscut (±0.5°) while having a mono-domain surface could permit to limit the APDs formation during the MBE process while keeping a CMOS-compatible approach [8], such as the one developed by the NAsP company in Marburg by MOCVD[8]. The experimental conditions needed to achieve this monodomain surface surface will need to be clarified by UHVCVD. Further work is needed to define the growth conditions and substrate miscut specifications in order to observe a mono-domain surface.

4.4.Antiphase boundaries in GaP/Si epitaxial layers

The APBs are detrimental for applications such as lasers, since they are electrical and optical active structural defects [41], [43]. On the contrary, APD engineering can be useful in the field of non-linear optics conversion schemes [44]. In the general context of the III-V on Si growth, the presence of APDs results in a large surface roughness [45].

As mentioned in Chapter 1, we focus on the heteroepitaxial growth of GaP on Si at FOTON Institute. Indeed, this system, thanks to the low lattice mismatch, presents a very low dislocation density. At the beginning of my thesis, previous works showed the ability to annihilate antiphase boundaries by using AlGaP marker layers [44]. In this work, we want to show that it is possible to control the vertical extent of APDs for further developments of non-linear photonic devices.

4.4.1. APDs annihilation

The efficiency of AlGaP markers in promoting APDs annihilation was already demonstrated in [44]. To go deeper in this study, we grew three GaP on Si samples by varying the distance between the first AlGaP marker and the GaP/Si interface. For each sample, we first grew a contaminant-free Si buffer layer on a Si(001) 6°-off substrate. The Si homoepitaxy growth

procedure is the same as the one illustrated in **Figure 4.8(a)**. Each sample presents the same RHEED pattern with a 2xn reconstruction at growth temperature (statistically dominant monodomain surface), moving to a 2x2 one during the quenching, demonstrating the reproducibility of the silicon homoepitaxial growth process. After the silicon growth, the wafer is transferred, through a UHV transfer tunnel (P_R=10^{-9}Torr), to the molecular beam epitaxy (MBE) reactor for the GaP overgrowth [28]. Before the III-V overgrowth, the 2x2 surface reconstruction is cross-checked by RHEED inside the MBE reactor. The GaP overgrowth starts after degassing the Si substrate, by annealing at 800°C in order to desorb the hydrogen, and cooled down to room temperature.

Each sample is composed of three GaP layers separated by two 2nm-thick $Al_{0.2}GaP$ markers. In order to study the first marker impact on the APDs annihilation, the distance between the first marker and the GaP/Si interface is varied from 5, 10 to 30nm. For achieving the same total thickness in all the samples, the second GaP layer thickness is 55, 50 and 30nm respectively. The second $Al_{0.2}GaP$ marker is in each case grown at 62nm from the interface. The last GaP layer is 30nm-thick in each sample. The GaP growth is first performed by migration enhanced epitaxy (MEE) at 350°C. Then, at the first marker level, the growth is performed by using a conventional MBE continuous growth mode at 550°C. Previous works have shown that the same growth sequence without AlGaP does not lead to APDs annihilation [46]. Finally the temperature is increased to 580°C for growing the second $Al_{0.2}GaP$ marker and the last GaP layer, that is the standard temperature used for the growth of GaP by MBE. The samples structures and transmission electron microscopy (TEM) images are given in **Figure 4.12**. TEM images were performed at the CEMES. In these images, the $Al_{0.2}GaP$ markers can be identified by their darker contrast with respect to the GaP layers.

The samples present occasionally some micro-twins (MT) and stacking faults. Indeed, X-ray measurements, performed by a colleague with a PhD thesis in progress at the FOTON institute, have shown that the percentage of MTs is 0.20%, 0.10% and 0.03% for the samples with the marker at 5, 10, 30nm from the interface respectively. Even if the samples have a low defects density, their presence suggest that the transfer procedure between the two growth chambers can be still improved.

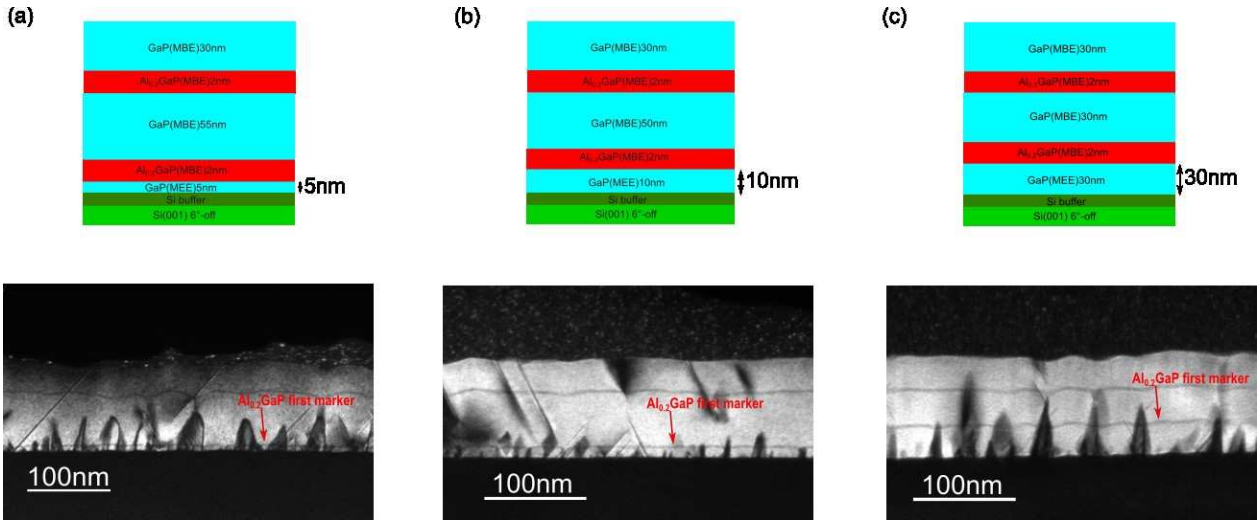

Figure 4.12 GaP on Si samples grown to study the AlGaP markers effect on APDs annihilation. The first marker distance from the GaP/Si is different in each sample. It is 5nm in (a), 10nm in (b), and 30nm in (c). In each figure, the sample structure is illustrated above while below the TEM image is presented.

By analyzing the impact of the first markers on the APDs annihilation, we can see that in **Figure 4.12(a),** where the first marker is at 5nm from the interface, the APDs annihilation happens mostly very close to the second marker. As a consequence the annihilated APDs have a strong effect on the surface topology as we can see by the induced surface roughness in **Figure 4.13(a)** [45]. In **Figure 4.12(b)** the first marker is at 10nm far from the GaP/Si interface. Most of the APDs annihilate in the first GaP layer and the sample surface appears smoother with respect to the first case. This suggests that APDs annihilation is mainly due to the presence of the first marker. When the marker is at 30 nm from the GaP/Si interface (**Figure 4.12(c)**), some APDs annihilate between the first and the second marker affecting the surface. Nevertheless, we observe a clear correspondence between the first marker position and the APDs annihilation. We can conclude that the best case is represented by the sample where the first marker is positioned at 10nm from the interface. The worst case is the first one (marker at 5nm) because in this case, the presence of an AlGaP marker has much less influence on APDs annihilation. A reason for this could be that at 5nm, the coalescence of initial 3D islands is not fully achieved,

and therefore antiphase boundaries are not perfectly formed, that limits the impact of the AlGaP marker layer.

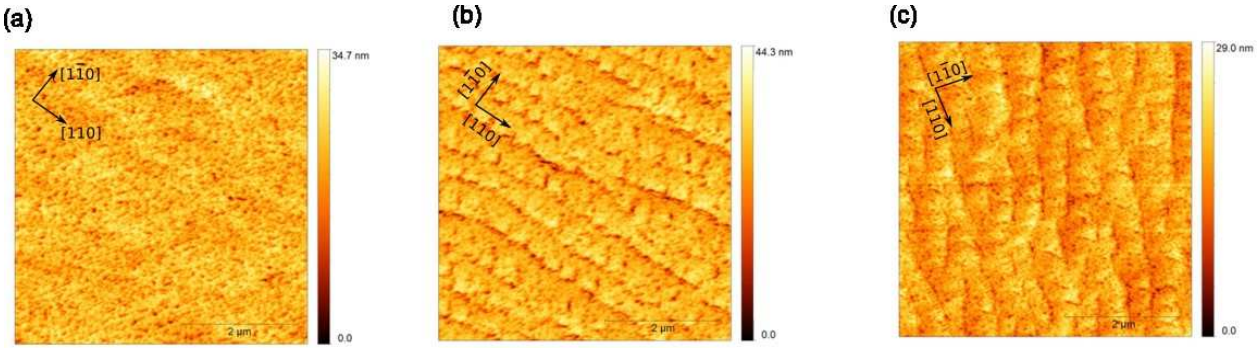

Figure 4.13 5x5µm^2 AFM images of the surfaces of the samples whose growth sketch is shown in Figure 4.12. The first marker is at 5nm (a), 10nm (b), and 30nm (c) far from the GaP/Si interface.

Moreover, if we look at the 5x5µm AFM images of the three samples surfaces in **Figure 4.13**, we can see that when the marker is at 5 nm from the interface (**Figure 4.13(a)**), 1.2-1.4µm large blurry terraces appear on the surface where the GaP atoms arrangement is mostly elongated in the [1-10] direction. When the marker is at 10 or 30nm (**Figure 4.13(b) and (c)** respectively) from the interface, the GaP surface is structured in 350-530nm large terraces along the [1-10] direction. The terraces length in these last two cases, is comparable to the one on the Si buffer used as reference in **Figure 4.8(c)**.

Anyway, we can conclude here that: (i) the markers seem to be effective for controlling the vertical propagation of APDs, which could be useful in the non-linear photonics field (ii) the AFM images confirmed the important role of the silicon buffer in affecting the GaP surface morphology. Finally, even if these are preliminary results, we believe that this is a first step towards the precise control of the APDs vertical extent.

4.4.2. APBs electrical characterization

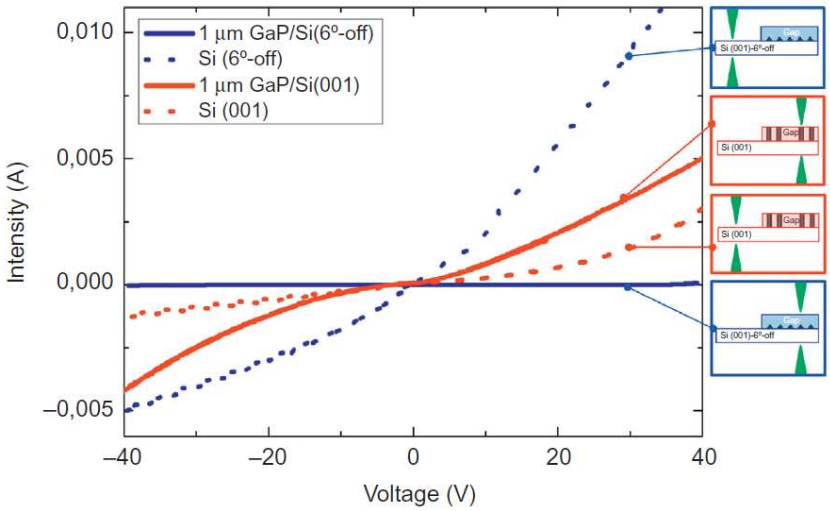

Figure 4.14 Current-voltage I(V) curves performed in Top-Bottom configuration on two samples composed of 1 µm-thick GaP grown by MBE on Si. Red lines are related to the sample grown on a Si(001) substrate with emerging APBs, and blue lines are related to the sample grown on a Si (001)-6 degree-off substrate with early annihilation (10-20nm) of APBs. Dashed lines are I(V) curve of the sole substrate, while solid lines are the I(V) curves of the whole GaP/Si stacking. [47]

Previous works performed by Tea *et al.* [43] predict that APBs can act as conduction channels for charge carriers, which can have consequences (advantages or drawbacks) for the photonic devices.

In order to better understand APBs electrical properties, we grew two GaP/Si samples: one with emerging APDs and one with annihilated APDs. To this aim, two 1µm-thick GaP on Si samples were grown by MBE on nominal (0.3°-off) and vicinal (6°-off) Si(001) respectively. The growth procedure is described in [28]. For each sample we performed I(V) measurements where metal contacts were used in a top-bottom configuration. In particular, for each sample we measured the current through the Si substrate and also considering the GaP layer to study the APDs contribution. In the first case, the metallic contacts were taken at the top and bottom of the silicon substrate. While, in the second case the top contact was taken on the GaP top layer

and the other contact was taken on the silicon substrate bottom side. The I(V) curve are plotted in **Figure 4.14**.

A non-zero current is measured through the Si substrate for each sample. While, when considering also the GaP layer, no current flows through the sample where APDs are annihilated. The situation is different in the case of emerging APBs. Similar behavior was also discussed by Feifel *et al.* [48]. These preliminary studies are coherent with the prediction made by Tea *et al*. [43]. Thus, further detailed studies have to be performed to fully understand APBs electrical properties.

4.5.Conclusions

To summarize, in this chapter we focused on achieving a good quality silicon surface from which the III-V overgrowth is strongly affected. Unlike the previous works achieved at FOTON Institute, we were able to protect the Si substrates from contaminants. This result was obtained by annealing the silicon surface under silane flux during all the process from starting room temperature to final room temperature. In order to investigate the growth conditions to get a monodomain surface which is targetted to limit APDs formation in the III-V overgrowth, we studied the silicon growth under SiH_4 by varying the growth temperature and silane pressure for both nominal <100 +/-0.2°> off 0.3° towards <110 +/- 0.1°> and vicinal <100 +/-0.2°> off 6° towards <110> Si surfaces. We found an improvement of the surface quality when working at high growth temperatures (T_g≥727°C for the vicinal case and T_g≥772°C for the nominal case) and at low silane pressure (0.02Torr≤P_{SiH_4}<1Torr). Otherwise, a rough sourface is observed on both surfaces. In the case of the vicinal 6°-off silicon substrate, at the pressure range mentioned above and at T_g around 776°C, a bidomain surface (2x2 reconstruction) is formed while at higher temperatures (in a range 820°C<T_g<870°C) a statistically dominant monodomain surface (2xn reconstruction) is observed. Instead, in the case of the nominal 0.3°-off silicon substrate, a smooth bidomain silicon surface (2x2 reconstruction) was observed at low silane pressure range (P_{SiH_4} =0.5Torr to 0.02Torr) for growth temperature T_g≥727°C. In this case, we did not observed by RHEED measurement a monodomain surface. However, maybe the growth conditions just

mentioned above, for which we achieved a smooth and bidomain substrate, could be the starting point for further studies to improve the nominal surface quality with the aim to obtain a monodomain surface.

In the context of the III-V overgrowth, during the GaP growth on Si, we confirmed the AlGaP markers efficiency in promoting APDs annihilation. We showed that the distance of the first marker from the interface is relevant in the APDs annihilation. Indeed the marker looses its efficiency when it is too close (5nm) to the interface. We also studied the electrical properties of APBs, that are coherent with the prediction made by Tea *et al.* [43], and also the recent experimental measurements published in the literature[48]. We especially demonstrated that current flows from the Si substrate through the GaP layer with emerging APBs while no current flows when APDs are annihilated. Further studies have to be done to fully understand their electrical properties and more quantitatively the APD annihilation process [8], [45], [49], [50].

References

[1] M. Maeder, A. Ramírez, and A. Zehe, 'A RHEED study of as-received and atomically clean Silicon surfaces in UHV-environment', *Superficies y vacío*, no. 9, pp. 242–244, 1999.

[2] K. Reinhardt and W. Kern, *Handbook of Silicon Wafer Cleaning Technology*. William Andrew, 2018.

[3] W. Kern, 'The Evolution of Silicon Wafer Cleaning Technology', *J. Electrochem. Soc.*, vol. 137, no. 6, pp. 1887–1892, Jun. 1990.

[4] Y. Ping Wang *et al.*, 'Abrupt GaP/Si hetero-interface using bistepped Si buffer', *Appl. Phys. Lett.*, vol. 107, no. 19, p. 191603, Nov. 2015.

[5] H. Döscher, S. Brückner, A. Dobrich, C. Höhn, P. Kleinschmidt, and T. Hannappel, 'Surface preparation of Si(100) by thermal oxide removal in a chemical vapor environment', *Journal of Crystal Growth*, vol. 315, no. 1, pp. 10–15, Jan. 2011.

[6] A. Ishizaka and Y. Shiraki, 'Low Temperature Surface Cleaning of Silicon and Its Application to Silicon MBE', *J. Electrochem. Soc.*, vol. 133, no. 4, pp. 666–671, Apr. 1986.

[7] A. Aßmuth *et al.*, 'The role of atomic hydrogen in pre-epitaxial silicon substrate cleaning', *Applied Surface Science*, vol. 253, no. 20, pp. 8389–8393, Aug. 2007.

[8] K. Volz *et al.*, 'GaP-nucleation on exact Si (001) substrates for III/V device integration', *Journal of Crystal Growth*, vol. 315, no. 1, pp. 37–47, Jan. 2011.

[9] H. Nörenberg and G. A. D. Briggs, 'The Si(001) c(4×4) surface reconstruction: a comprehensive experimental study', *Surface Science*, vol. 430, no. 1, pp. 154–164, Jun. 1999.

[10] L. V. Arapkina, V. A. Yuryev, V. M. Shevlyuga, and K. V. Chizh, 'Phase transition between (2 × 1) and c(8 × 8) reconstructions observed on the Si(001) surface around 600°C', *Jetp Lett.*, vol. 92, no. 5, pp. 310–314, Sep. 2010.
[11] T. Takahagi, I. Nagai, A. Ishitani, H. Kuroda, and Y. Nagasawa, 'The formation of hydrogen passivated silicon single-crystal surfaces using ultraviolet cleaning and HF etching', *Journal of Applied Physics*, vol. 64, no. 7, pp. 3516–3521, Oct. 1988.
[12] K. Choi, T.-J. Eom, and C. Lee, 'Comparison of the removal efficiency for organic contaminants on silicon wafers stored in plastic boxes between UV/O3 and ECR oxygen plasma cleaning methods', *Thin Solid Films*, vol. 435, no. 1, pp. 227–231, Jul. 2003.
[13] M. Tabe, 'UV ozone cleaning of silicon substrates in silicon molecular beam epitaxy', *Appl. Phys. Lett.*, vol. 45, no. 10, pp. 1073–1075, Nov. 1984.
[14] K. Miki, K. Sakamoto, and T. Sakamoto, 'Surface preparation of Si substrates for epitaxial growth', *Surface Science*, vol. 406, no. 1, pp. 312–327, May 1998.
[15] G. O. Krause, 'Observations of ß-SiC formation on reconstructed Si surfaces', *physica status solidi (a)*, vol. 3, no. 4, pp. 899–906, Dec. 1970.
[16] F. Hirose, M. Suemitsu, and N. Miyamoto, 'Surface Hydrogen Desorption as a Rate-Limiting Process in Silane Gas-Source Molecular Beam Epitaxy', *Jpn. J. Appl. Phys.*, vol. 29, no. 10A, p. L1881, Oct. 1990.
[17] F. Hirose, M. Suemitsu, and N. Miyamoto, 'High Quality Silicon Epitaxy at 500°C using Silane Gas-Source Molecular Beam Technique', *Jpn. J. Appl. Phys.*, vol. 28, no. 11A, p. L2003, Nov. 1989.
[18] D. W. Greve and M. Racanelli, 'Growth Rate of Doped and Undoped Silicon by Ultra-High Vacuum Chemical Vapor Deposition', *J. Electrochem. Soc.*, vol. 138, no. 6, pp. 1744–1748, Jun. 1991.
[19] J. Spitzmüller, M. Fehrenbacher, M. Pitter, H. Rauscher, and R. J. Behm, 'Local arrangement of silylene groups on Si(100)2\ifmmode\times\else\texttimes\fi{}1 after ${\mathrm{SiH}}_{4}$sdecomposition', *Phys. Rev. B*, vol. 55, no. 7, pp. 4659–4664, Feb. 1997.
[20] R. J. Hamers and Y. Wang, 'Atomically-Resolved Studies of the Chemistry and Bonding at Silicon Surfaces', *Chem. Rev.*, vol. 96, no. 4, pp. 1261–1290, Jan. 1996.
[21] H. Rauscher, 'The interaction of silanes with silicon single crystal surfaces: microscopic processes and structures', *Surface Science Reports*, vol. 42, no. 6, pp. 207–328, May 2001.
[22] C. C. Cheng and J. T. Yates, 'H-induced surface restructuring on Si(100): Formation of higher hydrides', *Phys. Rev. B*, vol. 43, no. 5, pp. 4041–4045, Feb. 1991.
[23] T. Quinci, 'Composant photovoltaïque innovant à base d'hétérojonction GaP/Si', thesis, Rennes, INSA, 2015.
[24] C. Kisielowski-Kemmerich and W. Beyer, 'Hydrogen desorption from crystalline silicon and its modification due to the presence of dislocations', *Journal of Applied Physics*, vol. 66, no. 2, pp. 552–558, Jul. 1989.
[25] L. K. Orlov and T. N. Smyslova, 'Hydrogen desorption from the surface under the conditions of epitaxial growth of silicon layers from monosilane in vacuum', *Semiconductors*, vol. 39, no. 11, pp. 1275–1279, Nov. 2005.

[26] K. Sinniah, M. G. Sherman, L. B. Lewis, W. H. Weinberg, J. T. Yates, and K. C. Janda, 'New Mechanism for Hydrogen Desorption from Covalent Surfaces: The Monohydride Phase on Si(100)', *Phys. Rev. Lett.*, vol. 62, no. 5, pp. 567–570, Jan. 1989.
[27] T. T. Nguyen, 'Sillicon photonics based on monolithic integration of III-V nanostructures on silicon', phdthesis, INSA de Rennes, 2013.
[28] T. Quinci *et al.*, 'Defects limitation in epitaxial GaP on bistepped Si surface using UHVCVD–MBE growth cluster', *Journal of Crystal Growth*, vol. 380, pp. 157–162, Oct. 2013.
[29] K. Madiomanana *et al.*, 'Silicon surface preparation for III-V molecular beam epitaxy', *Journal of Crystal Growth*, vol. 413, pp. 17–24, Mar. 2015.
[30] M. Takahashi, Y.-L. Liu, H. Narita, and H. Kobayashi, 'Si cleaning method without surface morphology change by cyanide solutions', *Applied Surface Science*, vol. 254, no. 12, pp. 3715–3720, Apr. 2008.
[31] H. Kim and R. Reif, 'Ex situ wafer surface cleaning by HF dipping for low temperature silicon epitaxy', *Thin Solid Films*, vol. 305, no. 1, pp. 280–285, Aug. 1997.
[32] H. Angermann, 'Passivation of structured p-type silicon interfaces: Effect of surface morphology and wet-chemical pre-treatment', *Applied Surface Science*, vol. 254, no. 24, pp. 8067–8074, Oct. 2008.
[33] J. Zhu, K. Brunner, and G. Abstreiter, 'Step characterization on vicinal Si surfaces by reflection high-energy electron diffraction at arbitrary azimuths', *Applied Surface Science*, vol. 137, no. 1, pp. 191–196, Jan. 1999.
[34] S. Baunack and A. Zehe, 'A study of UV/Ozone cleaning procedure for silicon surfaces', *physica status solidi (a)*, vol. 115, no. 1, pp. 223–227, Sep. 1989.
[35] V. V. Balashev, V. V. Korobtsov, T. A. Pisarenko, and E. A. Chusovitin, 'Influence of defects in a silicon dioxide thin layer on the processes of silicidation in the Fe/SiO2/Si(001) system', *Phys. Solid State*, vol. 51, no. 3, pp. 601–607, Mar. 2009.
[36] M. Martin *et al.*, 'Toward the III–V/Si co-integration by controlling the biatomic steps on hydrogenated Si(001)', *Appl. Phys. Lett.*, vol. 109, no. 25, p. 253103, Dec. 2016.
[37] S. Brückner, H. Döscher, P. Kleinschmidt, O. Supplie, A. Dobrich, and T. Hannappel, 'Anomalous double-layer step formation on Si(100) in hydrogen process ambient', *Phys. Rev. B*, vol. 86, no. 19, p. 195310, Nov. 2012.
[38] J. Mysliveček *et al.*, 'Step bunching during Si(001) homoepitaxy caused by the surface diffusion anisotropy', *MRS Online Proceedings Library Archive*, vol. 749, ed 2002.
[39] G. S. Bales and A. Zangwill, 'Morphological instability of a terrace edge during step-flow growth', *Phys. Rev. B*, vol. 41, no. 9, pp. 5500–5508, Mar. 1990.
[40] C. Schelling *et al.*, 'Kinetic and strain-driven growth phenomena on Si(001)', *physica status solidi (a)*, vol. 201, no. 2, pp. 324–328, Jan. 2004.
[41] H. Kroemer, 'Polar-on-nonpolar epitaxy', *J. Cryst. Growth*, vol. 81, no. 1–4, pp. 193–204, Feb. 1987.
[42] O. Supplie *et al.*, 'Atomic scale analysis of the GaP/Si(100) heterointerface by in situ reflection anisotropy spectroscopy and ab initio density functional theory', *Phys. Rev. B*, vol. 90, no. 23, p. 235301, décembre 2014.
[43] E. Tea *et al.*, 'Theoretical study of optical properties of anti phase domains in GaP', *Journal of Applied Physics*, vol. 115, no. 6, p. 063502, Feb. 2014.

[44] P. Guillemé *et al.*, 'Antiphase domain tailoring for combination of modal and 4^{-} -quasi-phase matching in gallium phosphide microdisks', *Opt. Express, OE*, vol. 24, no. 13, pp. 14608–14617, Jun. 2016.
[45] A. C. Lin, M. M. Fejer, and J. S. Harris, 'Antiphase domain annihilation during growth of GaP on Si by molecular beam epitaxy', *Journal of Crystal Growth*, vol. 363, pp. 258–263, Jan. 2013.
[46] M. Bahri, 'Caractérisation structurale des hétérostructures à base de GaSb et de GaP épitaxiées sur silicium (001)', thesis, Paris Saclay, 2016.
[47] C. Cornet, M. Da Silva, C. Levallois, and O. Durand, 'Chapter 28 - GaP/Si-Based Photovoltaic Devices Grown by Molecular Beam Epitaxy', in *Molecular Beam Epitaxy (Second Edition)*, M. Henini, Ed. Elsevier, 2018, pp. 637–648.
[48] M. Feifel *et al.*, 'Direct Growth of III–V/Silicon Triple-Junction Solar Cells With 19.7% Efficiency', *IEEE Journal of Photovoltaics*, vol. 8, no. 6, pp. 1590–1595, Nov. 2018.
[49] Y. Ping Wang *et al.*, 'Quantitative evaluation of microtwins and antiphase defects in GaP/Si nanolayers for a III–V photonics platform on silicon using a laboratory X-ray diffraction setup', *J Appl Cryst, J Appl Crystallogr*, vol. 48, no. 3, pp. 702–710, Jun. 2015.
[50] I. Németh, B. Kunert, W. Stolz, and K. Volz, 'Heteroepitaxy of GaP on Si: Correlation of morphology, anti-phase-domain structure and MOVPE growth conditions', *Journal of Crystal Growth*, vol. 310, no. 7, pp. 1595–1601, Apr. 2008.

Chapter 5 : Surface texturation of GaP on Si for water splitting applications

In this chapter we focus on the formation of large scale textured GaP template monolithically integrated on Si developed by using surface energy engineering, for water splitting applications. The stability of (114)A facets is first discussed**,** based on scanning tunneling microscopy (STM) images, transmission electron microscopy (TEM) and atomic force microscopy (AFM). These observations are then discussed in terms of thermodynamics through density functional theory calculations. A stress-free nano-patterned surface is obtained by molecular beam epitaxy (MBE), composed of a regular array of GaP (114)A facets over a 2 inches vicinal Si substrate. The advantages of such textured (114)A GaP/Si template in terms of surface gain, band-lineups and ohmic contacts for water splitting applications are finally discussed.

This work has been performed in collaboration with S. Charbonnier and P. Turban (IPR-*STM*), M. Vallet and A. Ponchet (CEMES-*TEM*), Y. Léger, T. Rohel, N. Bertru, A. Létoublon, L. Pedesseau and C. Cornet (FOTON- *GaP/Si MBE, AFM, DFT*), J.-B. Rodriguez, L. Cerutti and E. Tournié (IES-*GaSb/AlSb MBE*), G. Patriarche (C2N-S*TEM*). I was personally involved in density functional theory (DFT) calculations and AFM measurements; I contributed to TEM and STM analysis; I also contributed to the discussion about water splitting applications.

Most of the results presented in this chapter have been published in advanced functional materials [1].

5.1.Introduction to PEC water splitting

Solar photoelectrochemical (PEC) water-splitting devices have attracted interest for decades with the ultimate objective to convert and store the solar energy into clean hydrogen fuel [2], [3] at a lower production cost and environmental impact. Indeed, more than 90% of the hydrogen production is today made by steam methane reforming which releases carbon monoxide/dioxide and heat into the atmosphere while global warming is an issue [4]. The conversion of solar energy into hydrogen production through a water-splitting process assisted

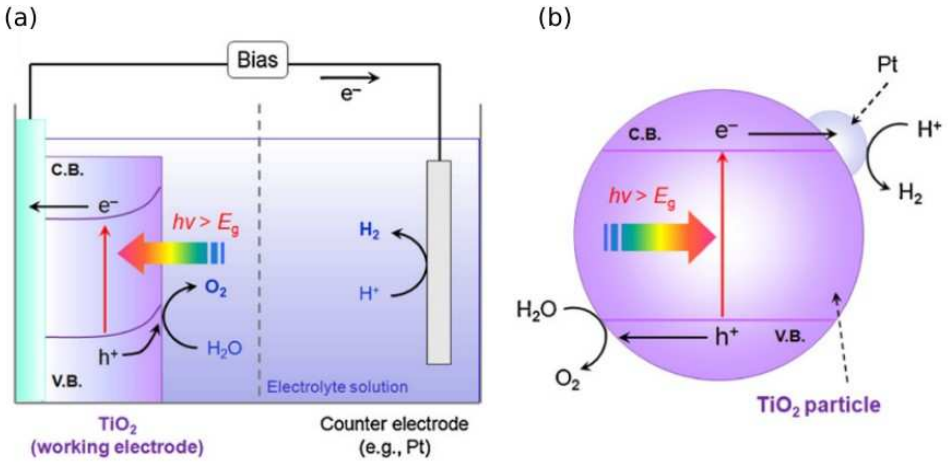

Figure 5.1 (a) PEC water splitting device scheme using a TiO_2 working electrode and (b) a short circuit model of a PEC cell. Courtesy of [8]

by photosemiconductor catalysts [5], [6] is definitely the most promising technology for the near-future with potentially plethora of hydrogen provided in a clean and sustainable manner. The PEC water splitting research was triggered by Honda and Fujishima in 1970s [2]. A PEC device consists in two electrodes (a semiconductor and a counter-electrode) immersed in an aqueous electrolyte solution [7]. When the semiconductor material is irradiated with energy greater than its bandgap, electrons-holes pairs are generated. Thanks to the bias applied, the electrons migrate through the semiconductor bulk reaching the counter-electrode surface where they are responsible for the water hydrogen half-reaction (HER) **(5.2).** Instead, the holes reach the working-electrode surface for the water oxidation half-reaction (OHR) **(5.3)**. An example of the device scheme is shown in **Figure 5.1(a)**, where the working electrode is made by TiO_2 and the counter one by Pt. They were the materials used by Honda and Fujishima to develop the first PEC water splitting device. A metal-semiconductor short circuit model, where the anode and cathode are connected without the need of an external circuit, is another example to realize the PEC water splitting (**Figure 5.1(b)**). The equation which governs the water splitting reaction is the following:

$$2H_2O \rightarrow 2H_2 + O_2 \qquad \textbf{(5.1)}$$

While the two half reactions are:

$$\text{HER: } 2H^+ + 2e^- \rightarrow H_2 \qquad E^0_{reduction} = 0\text{V} \qquad \textbf{(5.2)}$$

$$\text{OER: } 2H_2O + 4h^+ \rightarrow O_2{+}4H^+ \qquad E^0_{oxidation} = +1.23\text{V} \qquad \textbf{(5.3)}$$

To achieve the overall water splitting reaction, the bottom of the conduction band at the photocathode must be lower than the reduction potential of H^+ to H_2 (0 V vs. NHE at pH 0), while the top of the photoanode valence band must be more positive than the oxidation potential of H_2O to O_2 (1.23 V vs. NHE). Therefore, the minimum photon energy thermodynamically required to drive the reaction is 1.23eV. The potential energy diagram is presented in **Figure 5.2**. Because of an additional overpotential due to the energy losses during the solar energy conversion (such as charge transfer, electron/holes recombination), the suitable bandgap for achieving the PEC water splitting increases from 1.23eV to a value of 1.6-2.2eV.

After the pioneering work of Honda and Fujishima [2], different semiconductors materials have been used to improve the PEC water splitting devices performances. The requirements for a material to be suitable for this application are specifics. Indeed, in addition to the bandgap and band position, an "ideal" material should have efficient charge carrier separation and transportation in the bulk semiconductor, strong catalytic activity and stability. Some of the compatibles semiconductors materials are schematized with their bandgap value in the graph of **Figure 5.3**. We can see that GaP is also of interest for PEC water splitting devices because of its bandgap energy which can be tailored by using GaP-based alloys for improving devices performances. An efficient solar water splitting was already achieved in 1998 with a p-$GaInP_2$/GaAs tandem cell [9]. So far, different studies have been performed to increase the solar-to-hydrogen conversion efficiency (STH) up to 19% (reaching a value of 0.85 of the theoretical limit efficiency) [10]–[12]. Recently unbiased water splitting with 2% STH efficiency using new materials based on $GaSb_{0.03}P_{0.97}$ alloy has been reported in [13].

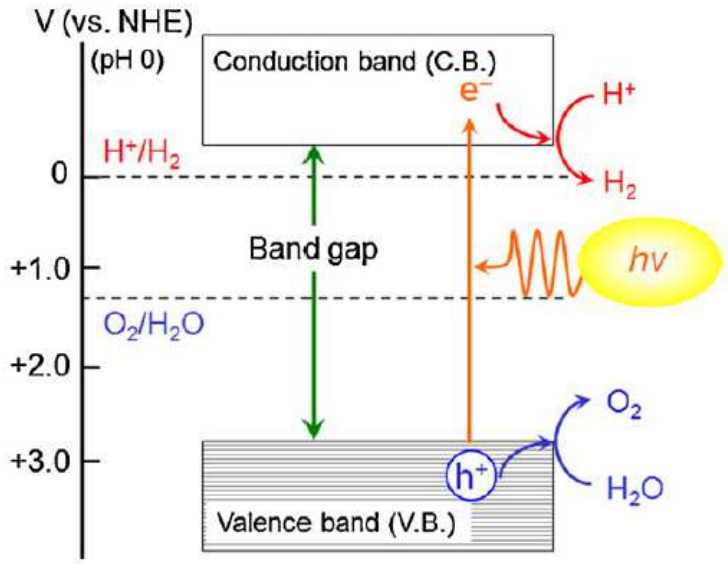

Figure 5.2 Potential energy diagram for achieving the overall photocatalytic water splitting reaction using a semiconductor system. Courtesy of [14]

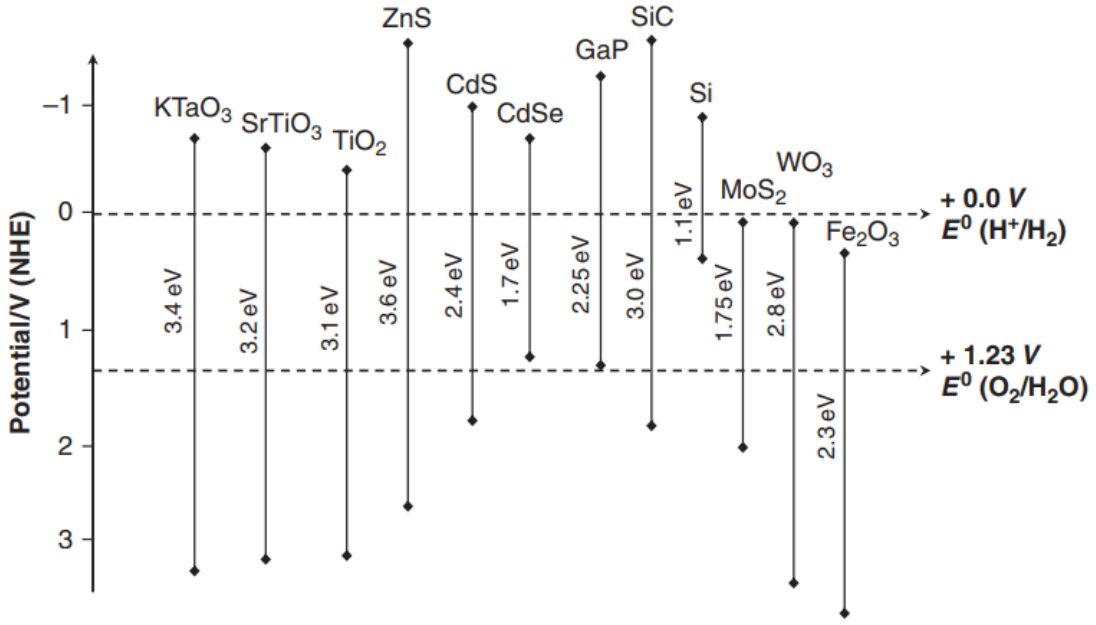

Figure 5.3 Band-gap energy and relative band position of different semiconductors with respect to the potentials (NHE) for water slitting reaction. Courtesy of [15]

5.2.GaP and PEC water splitting devices

Many recent proposals deal with the use of the GaP semiconductor as a photoelectrode in PEC devices [16], especially because its bandgap energy (2.26 eV) is larger than the 1.73 eV photopotential needed for water splitting [17]. Using this idea, demonstrations of GaP-based PEC devices [18]–[21] and descriptions of the physics/chemistry of the standard GaP surface [22], its interaction with water [23], [24] and hydrogen generation [25] were reported.

To enhance conversion efficiency of GaP-based PEC devices, strategies like surface functionalization [20], use of plasmon resonant nanostructures [26] or integration of nanowires [27] were considered. Meanwhile, it was demonstrated recently that the texturation of surfaces at the electrode level greatly enhances the efficiency of $BiVO_4$ photoanodes in PEC devices [28]. Structuration of semiconductor surfaces can be performed by lithography techniques [29], chemical processes [30], [31], nanowires, or by a self-organization during the epitaxial process of the material itself [32]. This last approach is usually driven by crystal strain-relief processes, it simplifies the post-growth device processing but does not offer large degrees of freedom, while keeping a crystal quality compatible with operating devices. The need for a scalable PEC device, in view of its very large scale integration was also pointed out [33]. In this regard, GaP presents several advantages. Among them, its monolithic integration on silicon leads to a high crystal quality, due to the low lattice mismatch between GaP and Si (0.36% at room temperature) [34].

5.3.Experimental results

To design efficiently a textured semiconductor surface, a good knowledge of the non-(001) most stable surfaces is needed. Stable facets are easily identified in stress-induced nanostructures, such as quantum dots [35]. But it is also possible to use stress-free surface structures whose formation is highly correlated to emerging defects as for instance, antiphase domains (APDs) separated by emerging anti-phase boundaries (APBs) [36]. In this regard, a 10nm-thick GaP has been grown on a freshly prepared HF-last Si(001) substrate. Before starting the GaP/Si(001) growth process, the silicon substrate has been annealed at 800°C in order to desorb the hydrogen. With this preparation (without Si buffer layer), the Si surface remains bidomain. After that, the GaP was grown at 350°C by molecular beam epitaxy using migration

enhanced epitaxy (MEE) (see ref. [34], [37], [38] for growth procedure and apparatus description). This layer was further annealed at 500°C. An amorphous As capping layer was then deposited at cryogenic temperatures to avoid any air contamination during transfer to the scanning tunneling microscope (STM) ultra-high vacuum (UHV) chamber, as explained in ref. [35], [39].

Figure 5.4(a) shows the STM image of the 10nm-thick GaP/Si surface. Two antiphase domains are observed. Each domain is first characterized by a large (001) surface where the dimers are aligned along the local [1-10] directions. Different facets can be identified at the boundaries where the two domains coalesce. Amongst the different facets observed, {136}, {113} and (114)A and B are clearly identified by their angle and surface reconstructions. Especially, as highlighted in **Figure 5.4(a)**, the surface is quantitatively mainly covered by {114} and (001) facets. The stability of GaAs{114}A or InGaAs {114}A facets was already widely discussed in the literature [40]–[42]. The work of Yamada *et al*., who performed STM investigations, showed low kink density and a highly uniform surface structure for the GaAs{114}A facets. Marquez *et al.* also observed a well-ordered GaAs(114)A-α2(2x1) reconstruction, discussing its relative stability with respect to the GaAs(001)A-β2(2x4) one with ab-initio calculations. This was already commented in Chapter 2.

5.4.GaP textured surface on Si vicinal substrate

To promote {114}A surface texturation, we need thermodynamic conditions where the energy of the {114}A facetted surface is lower than the {001} one, i.e. by developing a surface energy engineering approach. To this aim, a 1 µm-thick GaP sample was grown on a vicinal Si (001)-6°-off substrate. Corresponding TEM and AFM images and profiles are shown in **Figure 5.4(b),(c),(d)**. In this sample most of the APDs were annihilated within the first 20nm, by using AlGaP filtering layers, as demonstrated in the TEM image of ref.[34] and shown in **Figure 1.19.** The remaining GaP is grown at 580°C, with an intermediate beam equivalent pressure (BEP) V/III ratio of 4. The crystal growth was monitored in-situ using Reflection High Energy Electron Diffraction (RHEED) experiments. The 1µm thickness is well above the critical thickness, and X-ray diffraction experiments (not shown here) reveal an overall full relaxation of the GaP crystal.

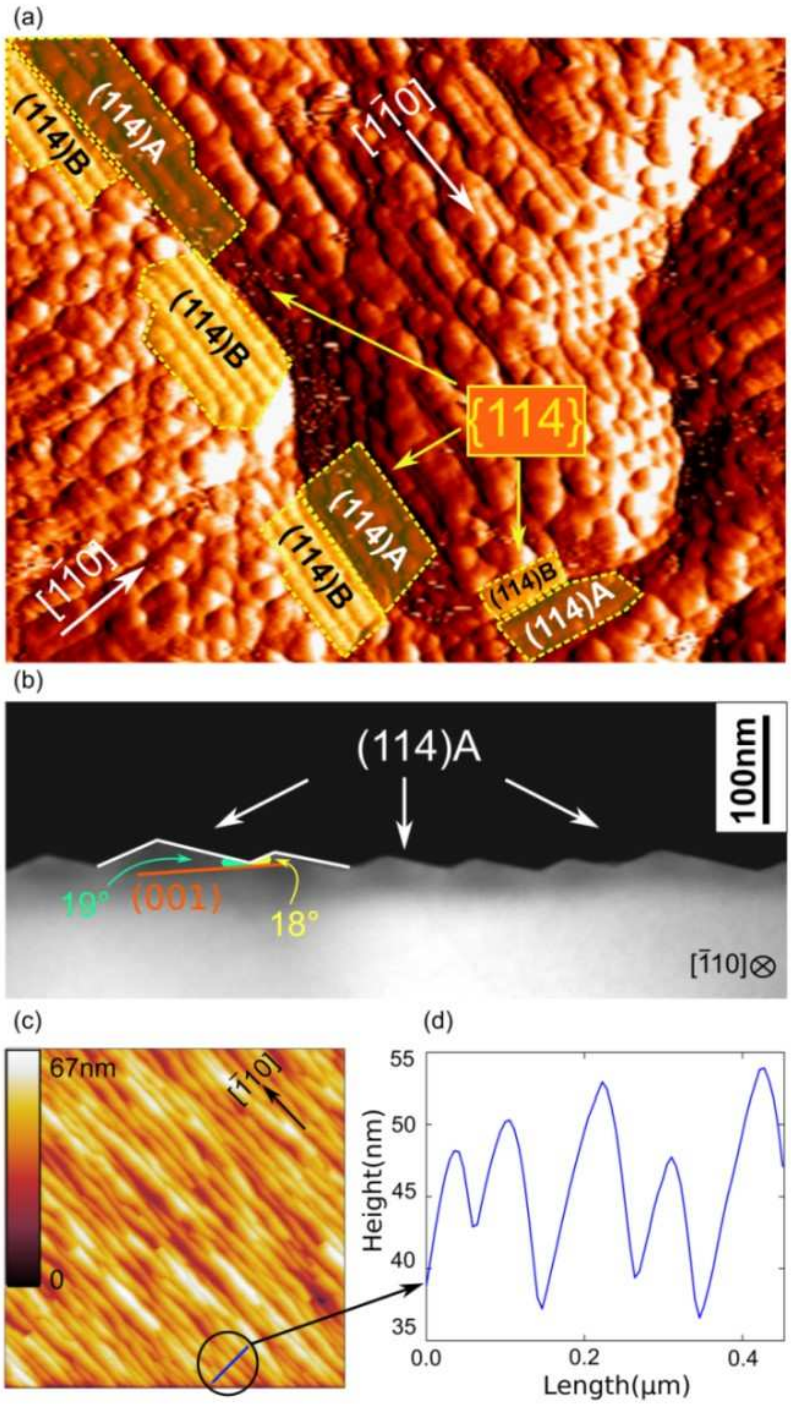

Figure 5.4 (a) 25x30 nm² STM image of a bi-domain 10nm-thick GaP on Si(001) evidencing the presence of numerous (114)A and B facets at the antiphase boundaries edges (b) TEM image of 1µm-thick GaP-on Si 6°-off ((c) 3 µm *3 µm AFM image of the surface of the same sample as b) and (d) a profile taken by small region of the AFM image. TEM and AFM observations show the (114)A faceting of the GaP surface

Figure 5.4(b) shows the <110> cross-sectional TEM image of the sample. The surface presents a saw-tooth profile along the lateral <110> direction. All facets have an angle with the (001) plane between 18° and 20°, close to the theoretical angle calculated for the {114} facets that is θ =19.48°. The average distance between two maxima is 100 nm with a dispersion of 40%. In the TEM image, left-oriented and right-oriented (114)A facets present different widths. The saw-tooth asymmetry allows compensating the 6°-miscut of the silicon substrate. It is important to note that (001) facets are completely missing. We also point out that (114) facets are parallel to the step edges direction of the vicinal silicon substrate, suggesting that the direction of the substrate miscut determines the dominant polarity of the grown GaP, but we will see that the situation is more complex later on. We also note that emerging dislocation density remains low on this relaxed sample, because of the low lattice mismatch. Interestingly, these facets were also observed by RHEED. During the growth a thin and streaky pattern, orientated with a 15-20° angle from the conventional (001) usual RHEED diffraction direction was observed. Even if the RHEED apparatus used in this study does not allow to determine precisely the observed reconstruction, diffraction lines were found to be remarkably thin as compared to the usual (2x4) (001) GaP ones, suggesting a good planarity of the facets. We also note here that similar observations were done on more than ten different samples, grown in the same conditions, showing the reproducibility of the process.

The resulting surface pattern is also highlighted in **Figure 5.4(c)** where a plan-view AFM image is shown. The corresponding saw-tooth profile is also given in **Figure 5.4(d)**. Here, the measured profile is smoother than the one obtained with TEM measurements, because of AFM tip convolution effects. A strong anisotropy of the surface structuration is revealed. The typical length of one facet is larger than 2µm, to be compared to the 100nm average distance between saws tooth profile. The surface anisotropy confirms that antiphase domains have been well annihilated, over the observed 3x3µm² surface. The morphologies observed by TEM and AFM thus clearly show that in these conditions the (001) GaP surface is unstable against (114)A faceting. It experimentally suggests that the surface energy of the (114)A surface over cos(θ) is here lower than the (001) surface energy. Interestingly, it is worth mentioning that a similar

growth on the GaP native substrate does not lead to any {114} surface structuration indicating that growth on the vicinal silicon substrate impacts the surface properties.

5.5.AlSb/GaP(001): texturation without vicinality

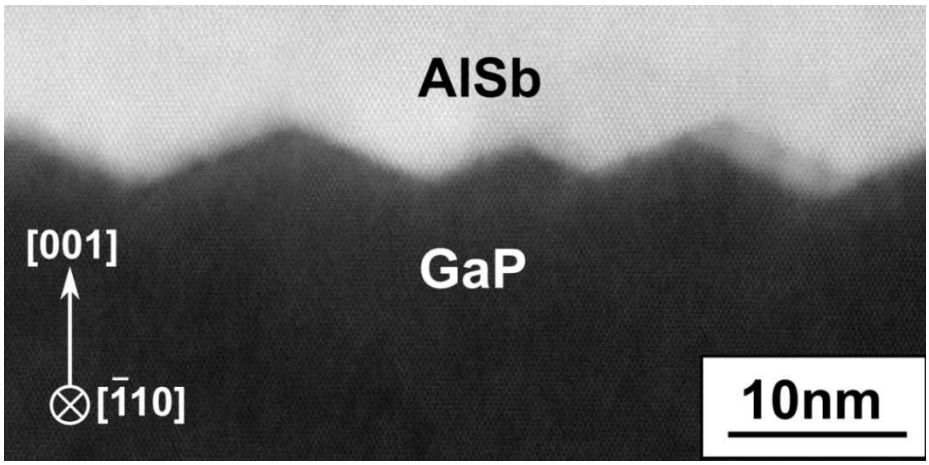

Figure 5.5 Bright field STEM image of the AlSb/GaP(001) interface of a 100nm-thick GaSb/AlSb/GaP(001) sample

Beyond the use of a vicinal substrate, we have also observed that changing group-V atmosphere above the surface on a nominal GaP substrate, can be another strategy for surface energy engineering promoting a textured-surface formation on GaP. Indeed, the textured behavior was obtained simply exposing the GaP surface under Sb atmosphere as shown in **Figure 5.5** which represents the cross-sectional TEM image of the heterointerface in an AlSb/GaP sample. In this sample, a GaP homoepitaxial layer was first grown on GaP (001) substrate. The sample was then cooled down to cryogenic temperatures, and an amorphous Sb capping layer was used to protect the sample from air contamination. The sample was transferred to another MBE chamber, and heated at 500°C to desorb the Sb. AlSb was then grown at 500°C, with a 0.35ML/s growth rate [43]. The interface presents here a similar shed-like behavior. The facets are now symmetric, due to the absence of miscut on this sample, and the average lateral and vertical amplitudes are much smaller. The pattern is supposed to have formed during the heating of the GaP surface covered by antimony indicating that the change of group-V exposure generated a lowering of high index surface energies vs nominal GaP surface energies. This could open the

way for a large scale stress-free, miscut-free GaP surface texturation. This also provides additional degree of freedom on the control of lateral periodicity of the GaP pattern, which we think can be controlled between few nanometers until the micrometer scale.

Beside III-Vs systems, a similar surface energy engineering strategy has also been developed to control the growth morphology by promoting a 2D-3D transition for growing self-assembled II-VI and nitride quantum dots (QDs) [44]–[46]. Indeed, in both the cases, the Stranski–Krastanow (SK) transition was interpreted as a surface energy change due to a saturation of the dangling bonds by changing the species exposure. Nevertheless, all the present observations demonstrate that there is a real competition between the growth of a (001) surface and the (114)A faceting.

5.6.DFT computational details

The stability of the {114} facets is discussed thermodynamically in the following. The density functional theory (DFT) has been used to estimate the surface energy of the (001) non-polar GaP surface and the (114) A and B polar GaP surfaces in Chapter 2. Here is the summary of the surfaces of interest considered in Chapter 2. Every surface considered in this work fulfills the Electron Counting Model (ECM) [47]. For both (001) and {114} facets, P-rich and Ga-rich reconstructions are considered. In the case of the non-polar GaP(001) surface, two different (2x4) reconstructions are simulated.

For the Ga-rich GaP(001) surface, the GaP(001)md(2x4) [48], [49] reconstruction (where md stands for mixed dimers) is assumed. This reconstruction is often considered for Ga-rich conditions in the literature [22], [24], [50]. For the P–rich GaP(001) surface, different stable structures were proposed [51] and H-passivated reconstructions were considered for Metal-Organic Chemical Vapor Deposition growth or in the context of water splitting applications [24], [52], [53]. In this study where samples are grown by MBE, we use a simple anion (P)-rich GaP(001) surface that fulfills the ECM criteria as proposed for GaAs[47]. We believe that any change of this reconstruction does not qualitatively affect the main conclusions of the study.

For the polar GaP(114) surfaces, two types of (2x1) reconstructions have been simulated: the Ga-rich GaP(114)A-α2(2x1) and the P-rich GaP(114)B-α2(2x1) which are similar to the ones already thoroughly investigated for the GaAs(114) [41], [54], [55].

In **Figure 5.6**, the surfaces energies versus the chemical potential variations are shown for GaP(001) and GaP(114) surfaces. The slope of the P-rich GaP(001)(2x4) and Ga-rich GaP(001)md(2x4) surface energy curves (respectively the green and blue one) is inherent to their stoichiometry. Indeed, both GaP(001)(2x4) surfaces are non-stoichiometric, *i.e.*, $N_P \neq N_{Ga}$. In particular, we find $\Delta N_{surface}$ =4 for the P-rich GaP(001)(2x4) case while $\Delta N_{surface}$ =-8 for the Ga-rich GaP(001)md(2x4) one ($\Delta N_{surface}$ has been defined in Chapter 2). Instead, the GaP(114)A-α2(2x1) and the GaP(114)B-α2(2x1)surfaces are stoichiometric (ΔN=0). Consequently, their surface energies (respectively the pink and brown curve) are constant with the chemical potential. Their values are about 59.9meV/Å^2 and 67.3meV/Å^2 respectively.

The chemical potential μ_P has to vary between two extremes thermodynamic conditions: Ga-rich limit (i.e. bulk Ga will form preferentially) and P-rich limit (bulk P will form preferentially). In particular, the P-rich limit is when $\mu_P = \mu_P^{P-bulk}$ while the Ga-rich limit corresponds to case when $\Delta\mu_P$ is equal to the GaP heat of formation ($\Delta H_f(GaP)$ = -0.928eV) which has been calculated with the black phosphorus phase and the orthorhombic α-Ga phase [56], [57].

For the Ga-rich limit the most stable reconstruction is the Ga-rich GaP(001)md(2x4) with a value of 52.9meV/Å^2 while in the P-rich limit the most stable one is the P-rich GaP(001)(2x4) with a value of 57.4meV/Å^2. The GaP(114)A-α2(2x1)surface is thermodynamically more stable than the GaP(114)B-α2(2x1) surface, as already reported in previous works for the GaAs material. The GaAs(114)A surface energy was found to lie 3meV/Å^2 below the GaAs(114)B [55]. In the interval from Ga-rich up to $\Delta\mu_P = -0.70$eV, then from $-0.70eV < \Delta\mu_P < -0.16eV$ and finally from $\Delta\mu_P = -0.16$eV to P-rich conditions, the lowest surface energies are the ones of Ga-rich GaP(001)md(2x4), GaP(114)A-α2(2x1) and P-rich GaP(001)(2x4) respectively**.** Overall, the surface energy of the GaP(114)A-α2(2x1) is the lowest over a wide $\Delta\mu_P$ intermediate range (almost 60% of the full $\Delta\mu_P$ range) as compared to the GaP(001) surface energies. However, to predict the possible destabilization of the (001) surface by (114)A faceting, one should consider

$\gamma_{\mathrm{GaP(114)A-\alpha2(2x1)}}/\cos(\Theta)$ (dashed pink line in **Figure 5.6**), where Θ=19.48° is the angle between the GaP(114) and the GaP(001) surfaces. We can see that this corrected surface energy is still lower than the GaP (001) ones in almost 30% of the full $\Delta\mu_P$ range ($-0.60eV < \Delta\mu_P < -0.36eV$), traducing a destabilization of the (001) surface by GaP(114)A-α2(2x1) faceting. In contrast, the GaP(114)B-α2(2x1) surface obviously cannot destabilize the (001) surface, in agreement with experimental observations.

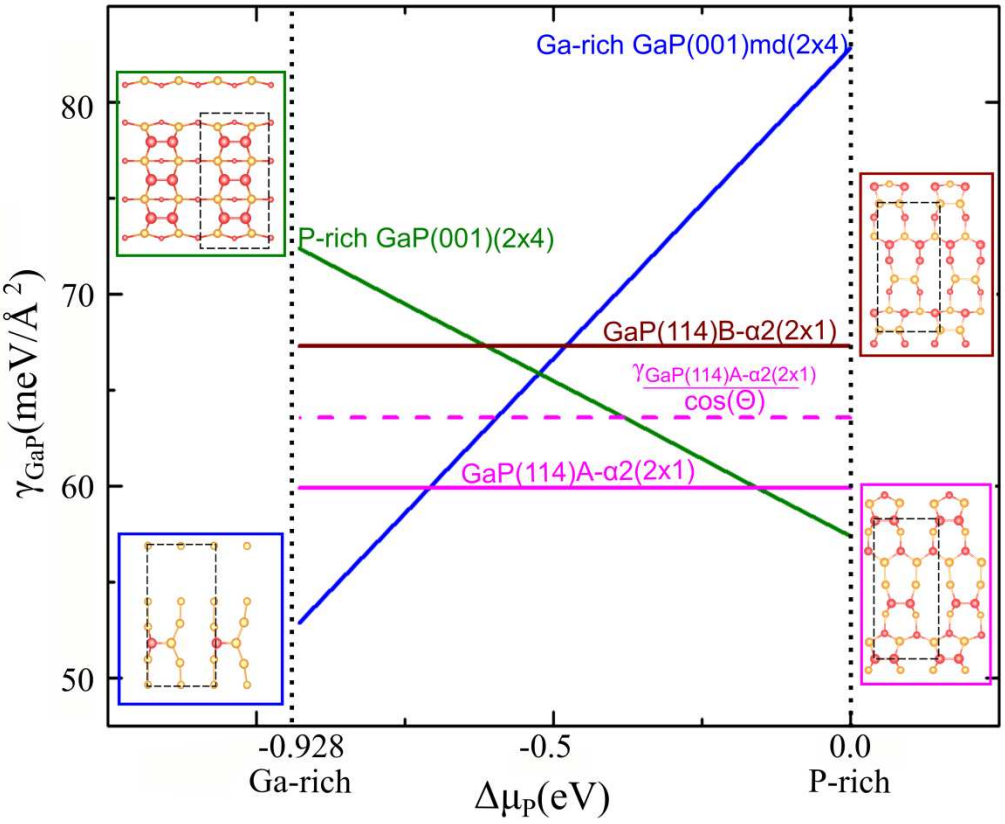

Figure 5.6 GaP surface energies γ versus the phosphorus chemical potential variation $\mathbf{\Delta\mu_P}=\mu_P-\mu_P^{\mathbf{P-bulk}}$. The dashed black lines represent the thermodynamic boundaries allowed for $\mathbf{\Delta\mu_P}$: $\mathbf{\Delta H_f(GaP)[=-0.928eV]} < \mathbf{\Delta\mu_P} < 0$

We note that although the destabilization of the (001) GaP surface by (114)A faceting is predicted by DFT in homoepitaxy, it has not been experimentally observed on GaP substrate yet. This shows that the heteroepitaxial growth on the silicon substrate changes the surface energies balance. Note that a small shift of about +2 or -2 meV/Å^2 in the surface energy of the

(114)A or (001) surfaces, respectively, would be sufficient to inhibit the destabilization in the DFT prediction. This suggests that the destabilization regime is highly sensitive to small variations of surface properties. Although the relaxation degree of the GaP layer on Si is very high, a small residual stress induced by the heteroepitaxy cannot be ruled out and could explain why the destabilization was observed on Si and not on GaP substrates. An eventual anisotropic effect induced by vicinal Si substrates should be further investigated by comparisons of growth on vicinal and nominal substrates. We also point out that the GaP(001)-oriented surfaces on vicinal Si substrates were already obtained in previous works with different growth conditions [36], [58], [59].

5.7.Textured surface on Si, over a 2-inch wafer

Even if a stress-free and textured GaP template on Si substrate has been obtained, the question of sample homogeneity is still raised, in the general context of a very large scale integration. In order to check the homogeneity of the anisotropic surface texturation over a 2-inch wafer, optical surface control is the most efficient approach. For this aim, a 3µm GaP/Si was grown in the same conditions as the 1µm-thick GaP/Si sample. Similar RHEED observations (streaky misorientated RHEED pattern) were obtained during the growth. The average distance between the ridges significantly increased, as compared to the 1µm GaP/Si and reached 400 nm. Therefore, the pattern dimension becomes of the same order of magnitude that the visible light wavelength.

To study the sample optical properties, we used as a reference object a metal box, labelled “INSA” (See **Figure 5.7(a),(b)**). Then, the reflection/diffusion properties of light coming from this object are observed at the center of the sample surface. Ambient lightning is added, on the right side of the picture. Two pictures of the experiment performed exactly in the same conditions are given in **Figure 5.7(a),(b)**. The same sample has been used in both figures, but the sample has been simply rotated by 90°. An arrow gives the Si [110] direction of the sample on both images. Two distinct areas are observed on this sample: (i) the central area of the sample, that correspond to nearly 90% of the total sample surface, starting from the center, and (ii) the

crown area, corresponding to the edges of the sample (10% of the total sample surface on the outskirts of the sample). In the central area of the surface sample in **Figure 5.7(a)**, the edge of the metal box and the INSA logo are well and precisely reflected indicating that diffusion does not occur significantly. The sample appears mirror-like. If the sample azimuth is rotated by 90° (**Figure 5.7(b)**), a "milky" surface behavior appears indicating important contribution of light diffusion. These results suggest a strong and homogeneous anisotropy of surface texturation over 90% of the 2-inch sample.

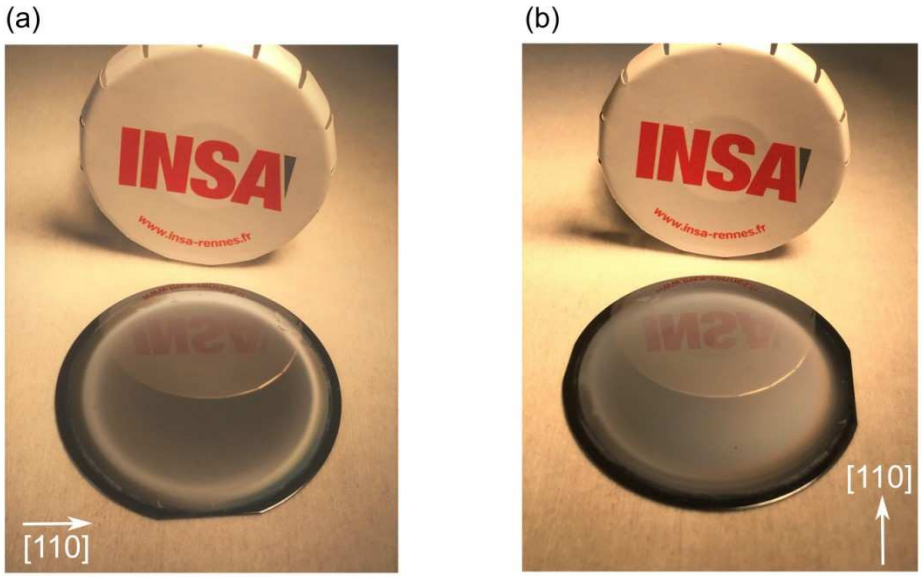

Figure 5.7(a) study of light reflection on the 2-inch wafer of GaP(114)/Si 6°-off surface rotated by 90° with respect to (b)

We then conclude that the central area of the sample is perfectly monodomain, and that {114}A textured surface have been obtained homogeneously over nearly 2 inches. **Figure 5.7(a),(b)** shows also a more intriguing feature with this patterned surface. Indeed, for light parallel to [110], the central area appears mirror-like and the crown appears with a white "milky" behavior. On the opposite, when the light direction is along the [-110], the central area appears "milky", the crown appears mirror-like. This shows that a {114}A textured surface has also been obtained in the crown area, but its orientation is turned by 90°, as compared to the central area. These opposite light effects, at the center and at the edge of the sample, suggest

that the majority domains developed in these two areas are different. These two areas are therefore in antiphase one for the other. A giant antiphase boundary is therefore expected at the separation between the central area and the crown area. We assume that the formation of these two different domains could be due to the inhomogeneity of growth temperatures and fluxes in the central area and in the crown area during the sample growth. Further works will be needed to clarify this finding. Nevertheless, a large scale {114}A textured GaP surface has been successfully obtained in this work on a silicon substrate.

5.8.Benefits of using the stress-free nanopatterned GaP(114)A surface for water splitting applications

We now discuss the relevance of GaP(114)A surfaces for water splitting applications. Indeed, beyond the high thermal stability and the benefit of the free post-processing aspect, there are other advantages in terms of optical and electrical devices properties inherent to the GaP material. Firstly, the electric device properties can benefit from the GaP direct growth on Si substrate where the ohmic contact can be realized easily to connect an external circuit. Indeed, the realization of ohmic contacts on the GaP remains very challenging because of its large bandgap [60], while for the Si substrate it is a well-known process which simplifies the device fabrication. Moreover, the band lineup of the GaP/Si hetero-interface is another advantage. Indeed, GaP and Si have a large bandgap difference ($E_g^{Si} = 1.12$eV, E_g^{GaP} =2.26eV at 300K) and their bandgap alignment is of type I favoring the extraction of the photo-generated carriers in the GaP photocatalyst through the Si substrate, when a potential is applied. We also point out that if GaP naturally fits photocathode requirements, quasi lattice-matched AlGaP [61] can also be grown on Si, that lowers the alloy valence band to reach photoanode adapted band lineups [62]. Finally, in the water splitting reaction, the catalyst surface area plays an important role since it constitutes the main part where the oxidation occurs. It means that a stable and high catalyst surface area is beneficial for the water splitting efficiency providing more active sites for the photocatalytic reaction [63]–[66]. Here, thanks to the surface texturation, a larger surface area has also been gained with respect to the planar one. The gain can be easily quantified since we know the GaP{114}A facets angle. The GaP (001) and GaP (114)A surface areas are linked

with $S_{GaP(001)} = \cos\theta S_{GaP(114)}$, where $\cos\theta \approx 0.94$. Consequently, we expect a surface gain of 6 %. Moreover, the textured surface may enable a more efficient light trapping into the material, where the direct expected consequence is an increase of light absorption which enhances the photo-generated carrier density.

5.9.Conclusions

A large scale textured surfaces were achieved by growing micrometer-thick GaP layers on vicinal Si(001) substrates, thanks to the instability of the (001) GaP surface against (114)A faceting. This destabilization is also predicted by DFT calculations of GaP(001)(2x4), GaP(001)md(2x4), and GaP(114)-α2(2x1) surface energies. We propose to use this surface energy engineering to develop large scale textured GaP templates monolithically integrated on Si, for water splitting applications. We believe that this nano-patterning approach could also benefit to various other applications, such as window layers in photovoltaic solar cells, nano-fluidic applications, surface nano-functionalization, or biologic sensors.

References

[1] I. Lucci *et al.*, 'A Stress-Free and Textured GaP Template on Silicon for Solar Water Splitting', *Advanced Functional Materials*, vol. 28, no. 30, p. 1801585, Jul. 2018.
[2] A. Fujishima and K. Honda, 'Electrochemical Photolysis of Water at a Semiconductor Electrode', *Nature*, vol. 238, no. 5358, pp. 37–38, Jul. 1972.
[3] M. G. Walter *et al.*, 'Solar Water Splitting Cells', *Chemical Reviews*, vol. 110, no. 11, pp. 6446–6473, Nov. 2010.
[4] J. M. Ogden, 'Prospects for building a hydrogen energy infrastructure', *Annu. Rev. Energy. Environ.*, vol. 24, no. 1, pp. 227–279, Nov. 1999.
[5] H. Li, Y. Zhou, W. Tu, J. Ye, and Z. Zou, 'State-of-the-Art Progress in Diverse Heterostructured Photocatalysts toward Promoting Photocatalytic Performance', *Adv. Funct. Mater.*, vol. 25, no. 7, pp. 998–1013, février 2015.
[6] R. Marschall, 'Semiconductor Composites: Strategies for Enhancing Charge Carrier Separation to Improve Photocatalytic Activity', *Adv. Funct. Mater.*, vol. 24, no. 17, pp. 2421–2440, mai 2014.
[7] R. van de Krol and M. Grätzel, Eds., *Photoelectrochemical Hydrogen Production*. Springer US, 2012.

[8] K. Maeda, 'Photocatalytic water splitting using semiconductor particles: History and recent developments', *Journal of Photochemistry and Photobiology C: Photochemistry Reviews*, vol. 12, no. 4, pp. 237–268, décembre 2011.
[9] O. Khaselev and J. A. Turner, 'A Monolithic Photovoltaic-Photoelectrochemical Device for Hydrogen Production via Water Splitting', *Science*, vol. 280, no. 5362, pp. 425–427, Apr. 1998.
[10] J. L. Young, M. A. Steiner, H. Döscher, R. M. France, J. A. Turner, and T. G. Deutsch, 'Direct solar-to-hydrogen conversion via inverted metamorphic multi-junction semiconductor architectures', *Nature Energy*, vol. 2, no. 4, p. 17028, Apr. 2017.
[11] M. M. May, H.-J. Lewerenz, D. Lackner, F. Dimroth, and T. Hannappel, 'Efficient direct solar-to-hydrogen conversion by *in situ* interface transformation of a tandem structure', *Nature Communications*, vol. 6, p. 8286, Sep. 2015.
[12] W.-H. Cheng *et al.*, 'Monolithic Photoelectrochemical Device for Direct Water Splitting with 19% Efficiency', *ACS Energy Lett.*, vol. 3, no. 8, pp. 1795–1800, Aug. 2018.
[13] A. Martinez-Garcia *et al.*, 'Unassisted Water Splitting Using a GaSbxP(1−x) Photoanode', *Advanced Energy Materials*, vol. 8, no. 16, p. 1703247, Jun. 2018.
[14] K. Maeda and K. Domen, 'New Non-Oxide Photocatalysts Designed for Overall Water Splitting under Visible Light', *J. Phys. Chem. C*, vol. 111, no. 22, pp. 7851–7861, Jun. 2007.
[15] R. M. Navarro, F. del Valle, J. A. Villoria de la Mano, M. C. Álvarez-Galván, and J. L. G. Fierro, 'Photocatalytic Water Splitting Under Visible Light: Concept and Catalysts Development', in *Advances in Chemical Engineering*, vol. 36, H. I. de Lasa and B. Serrano Rosales, Eds. Academic Press, 2009, pp. 111–143.
[16] E. E. Barton, D. M. Rampulla, and A. B. Bocarsly, 'Selective Solar-Driven Reduction of CO_2 to Methanol Using a Catalyzed p-GaP Based Photoelectrochemical Cell', *Journal of the American Chemical Society*, vol. 130, no. 20, pp. 6342–6344, May 2008.
[17] B. Kaiser, D. Fertig, J. Ziegler, J. Klett, S. Hoch, and W. Jaegermann, 'Solar Hydrogen Generation with Wide-Band-Gap Semiconductors: GaP(100) Photoelectrodes and Surface Modification', *ChemPhysChem*, vol. 13, no. 12, pp. 3053–3060, Aug. 2012.
[18] D. Cedeno, A. Krawicz, P. Doak, M. Yu, J. B. Neaton, and G. F. Moore, 'Using Molecular Design to Control the Performance of Hydrogen-Producing Polymer-Brush-Modified Photocathodes', *The Journal of Physical Chemistry Letters*, vol. 5, no. 18, pp. 3222–3226, Sep. 2014.
[19] M. Malizia, B. Seger, I. Chorkendorff, and P. C. K. Vesborg, 'Formation of a p–n heterojunction on GaP photocathodes for H_2 production providing an open-circuit voltage of 710 mV', *J. Mater. Chem. A*, vol. 2, no. 19, pp. 6847–6853, 2014.
[20] A. M. Beiler, D. Khusnutdinova, S. I. Jacob, and G. F. Moore, 'Chemistry at the Interface: Polymer-Functionalized GaP Semiconductors for Solar Hydrogen Production', *Industrial & Engineering Chemistry Research*, vol. 55, no. 18, pp. 5306–5314, May 2016.
[21] O. M. Williams, J. W. Shi, and M. J. Rose, 'Photoelectrochemical study of p-GaP(100)|ZnO|AuNP devices: strategies for enhanced electron transfer and aqueous catalysis', *Chem. Commun.*, vol. 52, no. 58, pp. 9145–9148, 2016.
[22] O. Supplie, M. M. May, H. Stange, C. Höhn, H.-J. Lewerenz, and T. Hannappel, 'Materials for light-induced water splitting: In situ controlled surface preparation of GaPN epilayers

grown lattice-matched on Si(100)', *Journal of Applied Physics*, vol. 115, no. 11, p. 113509, Mar. 2014.
[23] B. C. Wood, E. Schwegler, W. I. Choi, and T. Ogitsu, 'Hydrogen-Bond Dynamics of Water at the Interface with InP/GaP(001) and the Implications for Photoelectrochemistry', *Journal of the American Chemical Society*, vol. 135, no. 42, pp. 15774–15783, Oct. 2013.
[24] M. M. May, O. Supplie, C. Höhn, R. van de Krol, H.-J. Lewerenz, and T. Hannappel, 'The interface of GaP(100) and H 2 O studied by photoemission and reflection anisotropy spectroscopy', *New J. Phys.*, vol. 15, no. 10, p. 103003, 2013.
[25] X. Zhang and S. Ptasinska, 'Distinct and dramatic water dissociation on GaP(111) tracked by near-ambient pressure X-ray photoelectron spectroscopy', *Phys. Chem. Chem. Phys.*, vol. 17, no. 5, pp. 3909–3918, 2015.
[26] J. Qiu, G. Zeng, P. Pavaskar, Z. Li, and S. B. Cronin, 'Plasmon-enhanced water splitting on TiO_2 -passivated GaP photocatalysts', *Phys. Chem. Chem. Phys.*, vol. 16, no. 7, pp. 3115–3121, 2014.
[27] A. Standing *et al.*, 'Efficient water reduction with gallium phosphide nanowires', *Nature Communications*, vol. 6, p. 7824, Jul. 2015.
[28] J. Zhao *et al.*, 'High-Performance Ultrathin $BiVO_4$ Photoanode on Textured Polydimethylsiloxane Substrates for Solar Water Splitting', *ACS Energy Letters*, vol. 1, no. 1, pp. 68–75, Jul. 2016.
[29] Y. S. Jung, J. B. Chang, E. Verploegen, K. K. Berggren, and C. A. Ross, 'A Path to Ultranarrow Patterns Using Self-Assembled Lithography', *Nano Letters*, vol. 10, no. 3, pp. 1000–1005, Mar. 2010.
[30] Y. Shin and S. Lee, 'Self-Organized Regular Arrays of Anodic TiO_2 Nanotubes', *Nano Letters*, vol. 8, no. 10, pp. 3171–3173, Oct. 2008.
[31] W. Lu and D. Kim, 'Patterning Nanoscale Structures by Surface Chemistry', *Nano Letters*, vol. 4, no. 2, pp. 313–316, Feb. 2004.
[32] C. Teichert, 'Self-organization of nanostructures in semiconductor heteroepitaxy', *Physics Reports*, vol. 365, no. 5–6, pp. 335–432, Aug. 2002.
[33] B. Turan, J.-P. Becker, F. Urbain, F. Finger, U. Rau, and S. Haas, 'Upscaling of integrated photoelectrochemical water-splitting devices to large areas', *Nature Communications*, vol. 7, p. 12681, Sep. 2016.
[34] P. Guillemé *et al.*, 'Antiphase domain tailoring for combination of modal and 4^- -quasi-phase matching in gallium phosphide microdisks', *Opt. Express, OE*, vol. 24, no. 13, pp. 14608–14617, Jun. 2016.
[35] C. Robert *et al.*, 'Electronic, optical, and structural properties of (In,Ga)As/GaP quantum dots', *Phys. Rev. B*, vol. 86, no. 20, p. 205316, Nov. 2012.
[36] K. Volz *et al.*, 'GaP-nucleation on exact Si (001) substrates for III/V device integration', *Journal of Crystal Growth*, vol. 315, no. 1, pp. 37–47, Jan. 2011.
[37] Y. Ping Wang *et al.*, 'Quantitative evaluation of microtwins and antiphase defects in GaP/Si nanolayers for a III–V photonics platform on silicon using a laboratory X-ray diffraction setup', *J Appl Cryst, J Appl Crystallogr*, vol. 48, no. 3, pp. 702–710, Jun. 2015.
[38] T. Quinci *et al.*, 'Defects limitation in epitaxial GaP on bistepped Si surface using UHVCVD-MBE growth cluster', *Journal of Crystal Growth*.

[39] N. Esser, U. Resch-Esser, M. Pristovsek, and W. Richter, 'Scanning-tunneling-microscopy study of InP(001) surfaces prepared by UHV decapping of metal-organic vapor-phase-epitaxy-grown samples', *Phys. Rev. B*, vol. 53, no. 20, pp. R13257–R13259, mai 1996.
[40] T. Yamada, H. Yamaguchi, and Y. Horikoshi, 'Evaluation of the highly coherent surface structure of the GaAs (411)A plane using scanning tunneling microscopy', *Journal of Crystal Growth*, vol. 150, pp. 421–424, mai 1995.
[41] J. Márquez, P. Kratzer, L. Geelhaar, K. Jacobi, and M. Scheffler, 'Atomic Structure of the Stoichiometric GaAs(114) Surface', *Phys. Rev. Lett.*, vol. 86, no. 1, pp. 115–118, Jan. 2001.
[42] A. Ponchet, A. L. Corre, A. Godefroy, S. Salaün, and A. Poudoulec, 'Influence of stress and surface reconstruction on the morphology of tensile GaInAs grown on InP(001) by gas source molecular beam epitaxy', *Journal of Crystal Growth*, vol. 153, no. 3, pp. 71–80, août 1995.
[43] I. Lucci, C. Cornet, M. Bahri, and Y. Léger, 'Thermal Management of Monolithic Versus Heterogeneous Lasers Integrated on Silicon', *IEEE Journal of Selected Topics in Quantum Electronics*, vol. 22, no. 6, pp. 35–42, Nov. 2016.
[44] F. Tinjod, B. Gilles, S. Moehl, K. Kheng, and H. Mariette, 'II–VI quantum dot formation induced by surface energy change of a strained layer', *Appl. Phys. Lett.*, vol. 82, no. 24, pp. 4340–4342, juin 2003.
[45] F. Tinjod, I.-C. Robin, R. André, K. Kheng, and H. Mariette, 'Key parameters for the formation of II–VI self-assembled quantum dots', *Journal of Alloys and Compounds*, vol. 371, no. 1, pp. 63–66, mai 2004.
[46] B. Damilano, N. Grandjean, F. Semond, J. Massies, and M. Leroux, 'From visible to white light emission by GaN quantum dots on Si(111) substrate', *Appl. Phys. Lett.*, vol. 75, no. 7, pp. 962–964, août 1999.
[47] M. D. Pashley, 'Electron counting model and its application to island structures on molecular-beam epitaxy grown GaAs(001) and ZnSe(001)', *Phys. Rev. B*, vol. 40, no. 15, pp. 10481–10487, Nov. 1989.
[48] S. Mirbt, N. Moll, K. Cho, and J. D. Joannopoulos, 'Cation-rich (100) surface reconstructions of InP and GaP', *Physical Review B*, vol. 60, p. 13283, Nov. 1999.
[49] K. Luedge, P. Vogt, O. Pulci, N. Esser, F. Bechstedt, and W. Richter, 'Clarification of the GaP(001)(2x4) Ga-rich reconstruction by scanning tunneling microscopy and ab initio theory', *PHYSICAL REVIEW. B, CONDENSED MATTER AND MATERIALS PHYSICS*, vol. 62, no. 16, pp. 11046–11049, 2000.
[50] H. Döscher and T. Hannappel, 'In situ reflection anisotropy spectroscopy analysis of heteroepitaxial GaP films grown on Si(100)', *Journal of Applied Physics*, vol. 107, no. 12, p. 123523, juin 2010.
[51] O. Pulci *et al.*, 'First-principles study of InP and GaP(001) surfaces', *Computational Materials Science*, vol. 22, no. 1, pp. 32–37, Nov. 2001.
[52] P. H. Hahn, W. G. Schmidt, F. Bechstedt, O. Pulci, and R. Del Sole, 'P-rich GaP(001)(2x1)/(2x2) surface: A hydrogen-adsorbate structure determined from first-principles calculations', *Phys. Rev. B*, vol. 68, no. 3, p. 033311, juillet 2003.
[53] A. M. Frisch, W. G. Schmidt, J. Bernholc, M. Pristovsek, N. Esser, and W. Richter, '(2×4) GaP(001) surface: Atomic structure and optical anisotropy', *Phys. Rev. B*, vol. 60, no. 4, pp. 2488–2494, juillet 1999.

[54] J. Márquez, P. Kratzer, and K. Jacobi, 'Structure and morphology of the As-rich and the stoichiometric GaAs(114)A surface', *Journal of Applied Physics*, vol. 95, no. 12, pp. 7645–7654, Jun. 2004.
[55] R. D. Smardon and G. P. Srivastava, 'Electronic structure of the GaAs (114) A-(2× 1) and GaAs (114) B-(2× 1) surfaces', *Phys. Rev. B*, vol. 72, juillet 2005.
[56] L. Cartz, S. R. Srinivasa, R. J. Riedner, J. D. Jorgensen, and T. G. Worlton, 'Effect of pressure on bonding in black phosphorus', *The Journal of Chemical Physics*, vol. 71, no. 4, pp. 1718–1721, Aug. 1979.
[57] H. Curien, A. Rimsky, and A. Defrain, 'Structure atomique d'une phase cristalline du gallium, instable a la pression atmospherique Locality: synthetic Sample: at T = 256.85 K', *Bulletin de la Societe Francaise de Mineralogie et de Cristallographie*, vol. 84, pp. 260–264, 1961.
[58] T. J. Grassman *et al.*, 'Control and elimination of nucleation-related defects in GaP/Si(001) heteroepitaxy', *Appl. Phys. Lett.*, vol. 94, no. 23, p. 232106, juin 2009.
[59] A. C. Lin, M. M. Fejer, and J. S. Harris, 'Antiphase domain annihilation during growth of GaP on Si by molecular beam epitaxy', *Journal of Crystal Growth*, vol. 363, pp. 258–263, Jan. 2013.
[60] M. Henini, Ed., *Molecular Beam Epitaxy, Second Edition: From Research to Mass Production*, 2 edition., vol. after Charles, Cornet et al. in Chapter 31. GaP/Si based photovoltaic devices grown by MBE. S.l.: Elsevier, 2018.
[61] R. Tremblay *et al.*, 'MBE growth and doping of AlGaP', *Journal of Crystal Growth*, vol. 466, pp. 6–15, mai 2017.
[62] C. G. Van de Walle and J. Neugebauer, 'Universal alignment of hydrogen levels in semiconductors, insulators and solutions', *Nature*, vol. 423, no. 6940, pp. 626–628, print juin 2003.
[63] S. Licht, B. Wang, S. Mukerji, T. Soga, M. Umeno, and H. Tributsch, 'Efficient Solar Water Splitting, Exemplified by RuO2-Catalyzed AlGaAs/Si Photoelectrolysis', *J. Phys. Chem. B*, vol. 104, no. 38, pp. 8920–8924, Sep. 2000.
[64] K. T. Fountaine, H. J. Lewerenz, and H. A. Atwater, 'Efficiency limits for photoelectrochemical water-splitting', *Nat Commun*, vol. 7, Dec. 2016.
[65] W. Jiang, X. Jiao, and D. Chen, 'Photocatalytic water splitting of surfactant-free fabricated high surface area NaTaO3 nanocrystals', *International Journal of Hydrogen Energy*, vol. 38, no. 29, pp. 12739–12746, Sep. 2013.
[66] Z. Zou, J. Ye, K. Sayama, and H. Arakawa, 'Direct splitting of water under visible light irradiation with an oxide semiconductor photocatalyst', *Nature*, vol. 414, no. 6864, p. 625, Dec. 2001.

Conclusions and perspectives

This thesis work was part of the ANTIPODE project which aimed to clarify the main steps at the very early stage of the III-V on Si 3D-growth and defects generation. In particular, this thesis focused on the study of GaP/Si 3D-growth supported by density functional theory calculations and on achieving experimentally a silicon surface adapted to III-V overgrowth.

In **Chapter 1**, the state of the art of different III-V on Si integration approaches was presented together with devices developed for photonics and energy applications. Emphasis was given to the monolithic approach which is very promising for very large scale integration (VLSI) techniques. The different challenges due to the III-V/Si direct growth together with strategies adopted for avoiding or controlling them were introduced. Nevertheless, one of the main issues remain the generation of antiphase domains (APDs) which are structural defects whose total suppression or control at the early stage of growth is still under investigation.

In **Chapter 2**, Si and GaP non-polar and polar absolute surface energies and absolute interface energies of GaP/Si were calculated by density functional theory simulations. First, the calculations for determining the surface energies of the Si(001) with and without step, showed that the presence of the step does not impact significantly the silicon surface energy. The GaP surface energies for the most stable facets experimentally observed, such as {001}, {136}, {114} were determined as a function of the chemical potential. Finally, the abrupt and compensated GaP/Si absolute interface energies were determined confirming the stability of the compensated one with respect to the abrupt one.

In **Chapter 3,** the main steps of the III-V/Si early stage of growth and defects generation were clarified. First, the analysis of the different III-V on Si materials systems showed similar 3D-monodomain islands formation. This suggested the importance of surface and interface energies in the III-V/Si 3D islanding process. GaP/Si heterostructure wetting properties were studied, and it was demonstrated that partial wetting is always achieved whatever the phosphorus chemical potential. This effect is even reinforced by the Si surface passivation. Through the calculation of the free energy change for both a 2D and 3D GaP/Si island, we have

calculated that the contribution of the elastic energy is negligible with respect to the one of surface and interface energies. This result can be extended to most of III-V/Si systems, confirming that III-V/Si islands morphology is mainly governed by a competition between surface and interface energies. On this basis, we clarified the main steps of the III-V/Si growth showing that the partial wetting is at the origin of the defects generation such as antiphase domains

In **Chapter 4**, silicon surface quality has been experimentally studied for improving III-V overgrowth. We first developed a new strategy to protect the Si(001) surface from contaminants. Then, different Si growth conditions were investigated to determine silicon growth parameters allowing to reach a monodomain surface. Overall, with this study, we have highlighted the importance (on both 0.3°-off nominal and 6°-off vicinal Si(001)) of working at high temperatures and low silane pressures for improving the silicon surface quality. Moreover, we confirmed the role of AlGaP marker layers for controlling the antiphase domains vertical propagation in GaP/Si samples. These samples were grown on the silicon substrate developed with the new strategy, demonstrating the reproducibility of the Si surface quality achieved. Finally, the GaP/Si antiphase boundaries were electrically characterized. With this study, we demonstrated that current flows from the Si substrate through the GaP layer with emerging APBs while no current flows when APDs are annihilated.

In **Chapter 5**, a micrometer-thick GaP template grown on Si by surface energy engineering for photoelectrochemical (PEC) water splitting applications was presented. We showed that this growth is governed by the competition between {001} and {114} surface energies. Indeed, the {114} facets formation on the GaP surface is achieved due to their stability against the {001}. These results are well explained by DFT calculations presented in Chapter 2. The homogeneity of the anisotropic surface texturation over a 2-inch wafer was also demonstrated. Finally, we presented the advantages of using such a textured GaP surface monolithically grown on Silicon for PEC water splitting applications.

Perspectives

From the work presented in this thesis, we believe that the ratio between Type-A and Type-B terraces surface area plays a crucial role in the APDs formation rather than the kind of atomic step (monoatomic or biatomic) as claimed usually in the literature. That is why achieving a monodomain surface, in particular on a nominal substrate compatible with CMOS technology, is a key challenge to improve the III-V overgrowth avoiding APDs generation. Even if impressive results were already demonstrated by Marburg University (NAsP company), the further total absence or ultimate control of APDs could permit to open the route toward high efficiency, high performances, and low cost materials for photonic or energy applications, overcoming the defect filtering strategies adopted nowadays by most of the researchers.

Moreover, the surface energy engineering is very promising for realizing nano-structured templates going beyond the limits of lithography. In the context of energy application, we believe that the nano-patterning approach could be used to develop large scale textured GaP-based templates monolithically integrated on Si, for water splitting applications.

Overall, three fundamental aspects still need to be clarified: (i) the real impact of the miscut (angle and direction) during III-V/Si, (ii) the impact of antiphase boundaries on light emission or absorption, (iii) the impact of antiphase boundaries on transport properties. Further research efforts will be needed in the future to deeply investigate these points.

Appendices

A. Density functional theory (DFT)

In the following paragraph the errors per unit surface area related to the GaP/Si surfaces and interfaces energy calculations (Chapter 2) are presented in detail.

In the case of the Si(001) surface energies calculation, the surface energy is given by the following equation:

$$\gamma^{S}{}_{(Si)} = \frac{E_{slab} - N_{Si}\mu_{Si-bulk}}{2A} \quad \textbf{(A.1)}$$

Thus, the error per unit surface area associated to the silicon surface energy is given by two contributions. One is related to the total energy of the slab $\varepsilon_{E_{slab}}$ which is given by the sum $\varepsilon_{cutoff\&kkk}+\varepsilon_{Lvacuum}$. The first term of the sum is the cutoff and K-points energy-related error and the second one is the vacuum length-related error. The other contribution is the error given by the bulk energy calculation $\varepsilon_{N_{Si}\mu_{Si-bulk}}$. The values of each contribution are approximated to:

- $\boldsymbol{\varepsilon_{E_{slab}}} = \varepsilon_{cutoff\&kkk}+\varepsilon_{Lvacuum} \approx 120\text{meV}+25\text{meV} \approx \mathbf{150meV}$
- $\boldsymbol{\varepsilon_{N_{Si}\mu_{Si-bulk}}} \approx 192x0.04meV \approx \boldsymbol{8meV}$

The Si(001) super cell has been built with a surface area of 237.2 Å^2. Finally, the overall error per surface area associated to the Si(001) surface energy can be overestimated to a value of almost $1\text{meV}/\text{Å}^2$.

In the following we present the calculations for estimating the error per unit surface area related to the GaP surfaces energies. We are going to show the case of the GaP(114) surface. Nevertheless, the calculations are similar for the other two cases studied (GaP(001) and GaP (2511)). The GaP(114) surface energy is given by the following equation:

$$\gamma_{polar} = \frac{E_{slab} - N_{Ga}\mu_{GaP}^{GaP-bulk} - N_{H^*}(\mu_{H^*}^{Ga} - \mu_{H^*}^{P})}{A} \quad \textbf{(A.2)}$$

In this case, besides the total slab energy error $\boldsymbol{\varepsilon_{E_{slab}}}$ (whose value is the same as the one estimated for the Si(001)) and the GaP bulk energy error $\boldsymbol{\varepsilon_{N_{Ga}\mu_{GaP}^{GaP-bulk}}}$, one has to consider also the contribution of the error related to the fictitious hydrogen chemical potentials $\boldsymbol{\varepsilon_{N_{H^*}(\mu_{H^*}^{Ga}-\mu_{H^*}^{P})}}$. The values of these two terms are the following:

- $\boldsymbol{\varepsilon_{N_{Ga}\mu_{GaP}^{GaP-bulk}}} \approx 74\text{x}0.07\text{meV} \approx \mathbf{5meV}$
- $\boldsymbol{\varepsilon_{N_{H^*}(\mu_{H^*}^{Ga}-\mu_{H^*}^{P})}} \approx \mathbf{153meV}$

The GaP(114) super cell has been built with a surface area of 131.6 Å^2. By considering each value in the equation **(A.2)**, the overall error per surface area associated to the GaP(114) surface energy can be then overestimated to a value of almost 2.5meV/Å^2.

Finally, in the following we are going to show the error related to the GaP/Si interfaces energies. To this aim we took into account the compensated 0.5:0.5 P-Si/Ga interface. The calculations are similar for the other kinds of GaP/Si interfaces investigated in Chapter 2. The equation for determining the compensated 0.5:0.5 P-Si/Ga interface energy is the following:

$$\gamma_{Int} = \frac{E_{slab} - N_P\mu_{GaP}^{GaP-bulk} - (N_{Ga} - N_P)\Delta\mu_P - N_{Si}\mu_{Si-bulk} - A\gamma^S{}_{(Si)} \quad - A\gamma^S{}_{(GaP)}}{A} \qquad \textbf{(A.3)}$$

In this case we have the following errors contributions: the total slab energy error $\boldsymbol{\varepsilon_{E_{slab}}}$, the Si(001) and GaP(001) bulk energy errors $\boldsymbol{\varepsilon_{N_{Si}\mu_{Si-bulk}}}$ and $\boldsymbol{\varepsilon_{N_{Ga}\mu_{GaP}^{GaP-bulk}}}$ respectively**,** the Si(001) and GaP(001) total surface energy errors and the phosphorous chemical potential variation error $\boldsymbol{\varepsilon_{(N_{Ga}-N_P)\Delta\mu_P}}$**.** The error relatet to the interface energy calculation has been finally overestimated to 4.86meV/Å^2. This value has been determined by considering that, for this particular interface, the numbers of gallium, phosphorous and silicon atoms is respectively $N_{Ga} = 65$, $N_P = 61$, $N_{Si} = 124$ and the surface unit area is A=119.2 Å^2.

B. Molecular beam epitaxy and ultra-high vacuum chemical vapor deposition

In order to realize the III-V/Si molecular beam epitaxy (MBE) growth, the FOTON institute has installed from 2010 a RIBER ultra-high vacuum chemical vapor deposition (UHV-CVD) reactor dedicated to group IV near the existing RIBER compact 21 solid source MBE chamber for III-V growth. They are connected by a ultra-high vacuum(UHV) tunnel kept at 10^{-10}Torr thanks to ionic pumps. This system allows the growth of a silicon buffer layer in situ prior to subsequent III-V overgrowth.

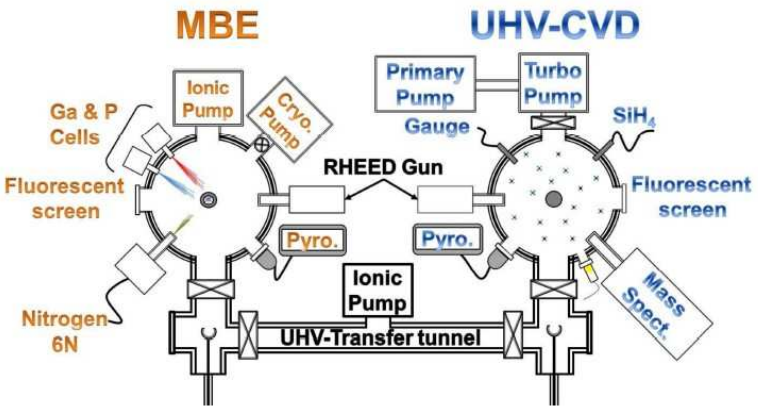

Figure B.1 Schematic representation of the UHVCVD-MBE growth cluster. UHV-CVD chamber connected to the MBE reactor by a UHV transfer tunnel kept at 10^{-9}Torr[1]

- UHV-CVD

In this thesis work, I was particularly involved in close collaboration with R. Gautheron-Bernard in the Silicon growth under UHV-CVD.

The UHV-CVD reactor is composed by an oven which heats the substrate at temperatures up to 1100°C. The temperature is measured by a pyrometer working in the range of 500°C to 1500°C. There are also four active gases injection lines (SiH_4, diluted AsH_4, diluted B_2H_6 and H_2) controlled by mass-flows or Baratrons gauges. The vacuum inside the UHV-CVD chambers is kept by a pumping system formed by a primary pump and a turbo pump which permits to have a high vacuum of 10^{-10} Torr. At a constant active gas flow rate it is possible to work either in “low pressure mode” or “high pressure mode” condition through the use of a by-

pass control between the pumping system and the growth chamber. In this work, the by-pass control allows us to work also in "high pressure mode" conditions achieving chamber pressures around 10^{-2}Torr-10^{-1}Torr. The pressure inside the chamber is measured by an extractor gauge (which works in the pressure range of 10^{-12} – 10^{-4}Torr). During both the growth and annealing processes, the gauge is carefully turned off for avoiding to be damaged. A Transmitter gauge (pressure range of $4x10^{-4}$ – 750Torr) is used to monitor the chamber pressure during the processes. Finally, a mass spectrometer is installed on the reactor to identify the species present in the growth chamber and to ensure absence of contaminants. A RHEED apparatus (Appendix C) enables in-situ surface analysis during UHV-CVD growth.

- MBE growth process

Molecular beam epitaxy is a non-equilibrium growth technique which allows to deposit thin films on a heated crystalline substrate in a ultrahigh vacuum (UHV) environment ($<10^{-10}$Torr). This environment corresponds to the free molecular flow regime which means that the collisions between atoms during their path to the substrate are almost negligible.

MBE reactor:

The MBE reactor is connected to a pumping system which permits to achieve a vacuum of 10^{-10} Torr and a working pressure of 10^{-5} to 10^{-7}Torr. Group-III elements (Ga, In, Al) are provided through conventional Knudsen effusion cells containing pure metal solid sources. The group-V elements (P, As, Sb) are supplied via a thermal effusion cell where heated solid sources of these elements (released as tetramer such as P_4 and As_4) are cracked (by the valved-cracker cell) in P_2 and As_2 molecules. The MBE reactor is also composed by a RHEED apparatus for in-situ layers characterizations. Also in this reactor a mass spectrometer is installed for identifying the species present inside and the presence of contaminants. See Figure B.1.

Different physical processes can occur during the MBE growth: adsorption, desorption and diffusion of adatoms, islands nucleation, nucleation on second-layer island, diffusion to a lower terrace. A thermodynamic description, based on surface and interface energies competition, can be used to distinguish three main growth modes during the MBE hetero-

epitaxial crystal growth [2], [3] (see **Figure B.2**). Illustration is made here by considering the deposition of a III-V semiconductor on Si:

(i) Frank- Van de Merve growth (layer-by-layer) when surface energy of the substrate is higher than the sum of the III-V/Si interface and III-Vs surface energies ($\gamma^{S}{}_{(Si)} \geq \gamma^{S}{}_{(III-V)} + \gamma^{i}{}_{(III-V/Si)}$). This growth mode corresponds to perfect wetting conditions.

(ii) Volmer-Weber growth when the substrate surface energy is weaker than the sum of the III-V/Si interface and III-Vs surface energies ($\gamma^{S}{}_{(Si)} < \gamma^{S}{}_{(III-V)} + \gamma^{i}{}_{(III-V/Si)}$). Thus, it corresponds to partial wetting conditions.

(iii) Stranski-Krastanow growth when the substrate surface energy is almost the same as the sum of the III-V/Si interface and III-Vs surface energies ($\gamma^{S}{}_{(Si)} \approx \gamma^{S}{}_{(III-V)} + \gamma^{i}{}_{(III-V/Si)}$). It can be considered as an intermediate case between the first two growth modes.

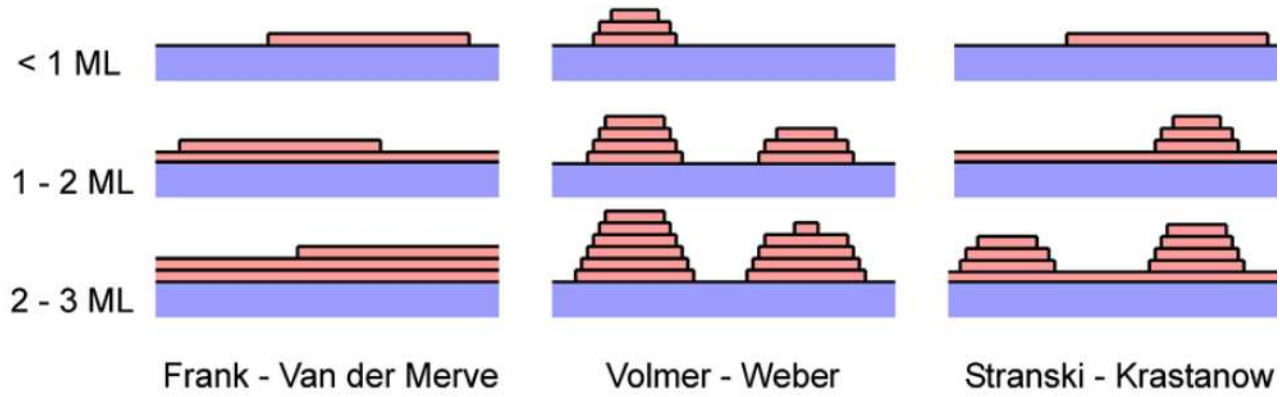

Figure B.2 Three different MBE growth mode**:** Frank- Van de Merve ($\gamma^{S}{}_{(Si)} \geq \gamma^{S}{}_{(III-V)} + \gamma^{i}{}_{(III-V/Si)}$), Volmer-Weber($\gamma^{S}{}_{(Si)} < \gamma^{S}{}_{(III-V)} + \gamma^{i}{}_{(III-V/Si)}$) and Stranski-Krastnow($\gamma^{S}{}_{(Si)} \approx \gamma^{S}{}_{(III-V)} + \gamma^{i}{}_{(III-V/Si)}$)[2]

GaP growth process:

For growing GaP on Si substrate a two-step growth process [1] is used taking inspiration from Grassman *et al*.[4]. It consists of a low temperature migration enhanced epitaxy (MEE)

growth, which allows having a very smooth surface at the early stage of growth, followed by the conventional molecular beam epitaxy (MBE) growth mode. Before the GaP overgrowth, the silicon substrate is firstly heated to 800°C in order to desorb the hydrogen and ramped down to 350°C for growing 40 ML-thick (about 10 nm) GaP by MEE. The first MEE sequence consists in forming a Ga/Si interface. Indeed, starting by Ga element, instead of P, enables to decrease the surface roughness (see ref. [5], and references therein). Thus, first 0.9 ML of Ga is deposited at a growth rate of 0.1 ML/sec., followed by a 4 sec. growth interruption. An exposure to phosphorus overpressure for P deposition ends the first MEE sequence. The following MEE cycle starts after 60 sec. growth interruption. These cycles are repeated until a 40ML-thickness is reached. After MEE, the growth is continued by MBE to suppress defects such as microtwins and annihilate antiphase domains[4], [6]–[9]. Standard MBE growth temperatures 500-600°C are used during this part of the growth.

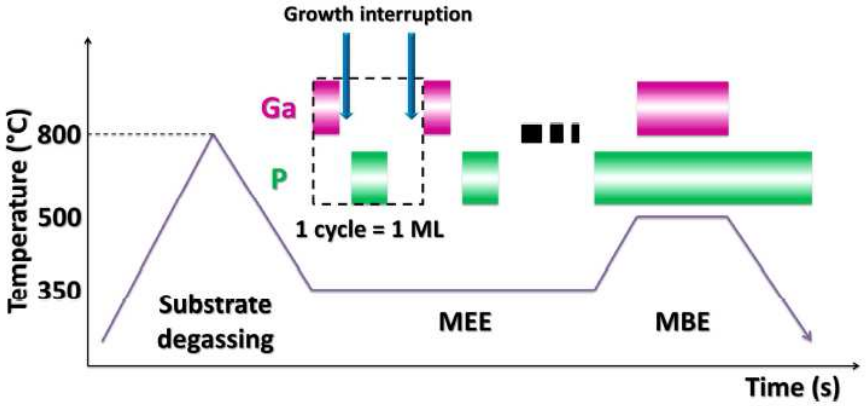

Figure B.3 Two steps III-V on Si growth process: Silicon substrate degassing followed by MEE and MBE [10]

C. Atomic force microscopy

During this thesis work, I was particularly involved in the silicon surfaces analysis by atomic force microscopy (AFM). The AFM is a method for studying the topology of the sample surface, scanning it with a tip (typically made by Si_3N_4 or Si) fixed on the extremity of a

deformable cantilever. Its interaction with the surface sample can happen through different types of forces: Van Der Waals force, capillarity forces, electrostatic or magnetic, depending on the sample. The AFM principle is scanning the surface sample by monitoring the cantilever deflection through a feedback mechanism.

The AFM apparatus is formed by an optical system composed of a laser source and a quadrant photodiode detector that permits to record the cantilever spatial variation, as illustrated in **Figure C.1**. Indeed, the laser source is focalized on the cantilever extremity and it is reflected back to the photodiode which converts the light in electrical energy producing a signal proportional to the cantilever deflection. The sample is positioned on a cylindrical piezoelectric (PZT) tube which, by shrinkage and expansion, allows the sample to move on the three axes (x, y, z) for keeping constant the interactions between the tip and the surface. Before the measurement, a parameter called set-point which characterizes the strength of interaction between the tip and the surface is fixed.

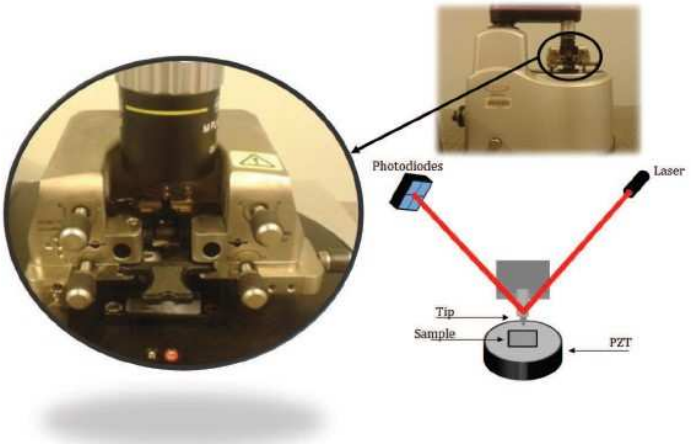

Figure C.1 2007 Veeco di Innova setup of the FOTON institute at INSA Rennes [11]

In the FOTON institute we use the AFM 2007 Veeco di Innova experimental setup, allowing 100x100 µm² images with a *Z* scale maximum amplitude of ~6 µm (**Figure C.1**).

A force-distance curve can better explain what happens in terms of interactions between the tip and the sample through attractive and repulsive forces when the cantilever approaches the sample. At the beginning, the cantilever is away from the surface thus, no forces act (**Figure C.2(A)**). When the cantilever approaches the sample, it undergoes to attraction and repulsion

forces which could make the cantilever deflect upwards and downwards(**Figure C.2(B)**). When the tip is brought into contact with the sample (**Figure C.2(C)**), the cantilever deflection increases a little more. **Figure C.2(D)and (E)** represent the case where the retraction starts and the cantilever is brought far from the surface.

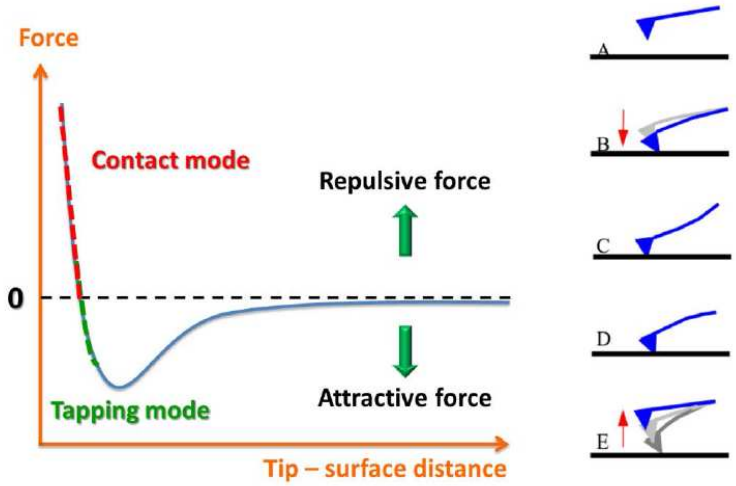

Figure C.2 Force profile when the distance between the tip and the surface changes [5]

The force exerted between the sample surface and the tip is essentially given by the Hook's law:

$$F = -kZ \qquad \textbf{(C.1)}$$

where F is the force proportional to the cantilever Z deviation through the cantilever stiffness k. There are two kind of AFM operation mode: *contact mode* and *tapping mode*. In the *contact mode*, the type of force is repulsive and the tip scans over the surface maintaining the cantilever vertical deviation at a constant level. Before starting the measurement, the laser is adjusted at the end of the cantilever and the reflected spot is positioned as a reference at the center of the photodiode. During the scanning, the deflection is recorded by the optical system and it is compared by a DC feedback loop to the set-point level. The resulting error signal from the amplifier is used to actuate the PZT, moving the sample in order to maintain constant the tip/sample interaction by applying the required voltage.

The *tapping mode* alternatively uses both the attractive and repulsive forces. The cantilever is oscillating at its resonance frequency, normal to the sample. It alternately contacts

the surface and lifts off. The amplitude of oscillations is affected by the interactions forces between the tip and the sample surface. In this case, the feedback loop aims to maintain a constant oscillation amplitude keeping constant the average distance between the cantilever and the surface. This tapping mode causes less damages with respect to the other operation modes because of the fewer contacts. Thus, it is useful for fragile surfaces which could be damaged when scanned in contact mode.

D. Reflection high energy electron diffraction

In this thesis work, I was involved in performing in-situ reflection high energy electron diffraction (RHEED) analysis for studying the silicon surface reconstruction, in close collaboration with R. Gautheron-Bernard.

The RHEED analysis allows having information on the atomic arrangement of the surface sample and on the growth rate by analyzing the RHEED oscillation as a function of the growth mode. The RHEED apparatus is composed of an electron gun that produces and accelerates an electron beam. The latter is diffracted on the sample surface while a fluorescent screen detects the reflected electron beam. In order to analyze in real time the silicon surface reconstruction, the electron gun is equipped by a differential pumping system. It allows to analyze the surface reconstruction under high pressure of active gas, up to $5x10^{-2}$ Torr and with a working energy of the electrons of 30keV. The electron energy used in this work is 28keV. The incident angle is very small, in a range of 0.3°-0.5°. At these angles values the beam does not penetrate deeply in the sample (just few Å). Thus, the electron beam “sees” a 2D crystal whose reciprocal lattice is made by rods perpendicular to its surface.

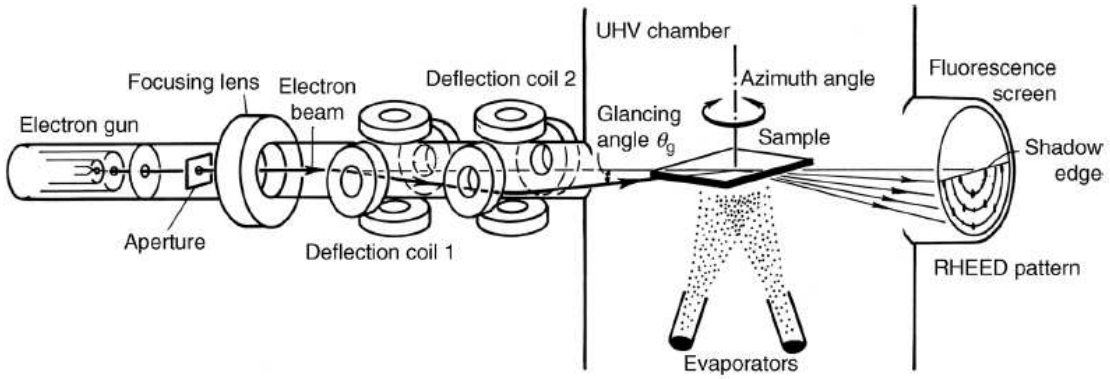

Figure D.1 Scheme of the RHEED apparatus of a ultrahigh vacuum (UHV) chamber. Courtesy of [12]

When the magnitude of the incident beam wave vector $\vec{k}$ equals the one of the diffracted beam $\overrightarrow{k'}$, the elastic diffraction is achieved. In this case the Ewald sphere centered on the sample and of radius $\overrightarrow{k'}$, (2π/λ), intersects the reciprocal rods. This conditions is expressed as :

$$\vec{k} - \overrightarrow{k'} = \vec{G} \qquad \textbf{(D.1)}$$

It means that the diffracted vector is a reciprocal lattice vector $\vec{G}$ (**Figure D**.2**(a)**). When this condition is fulfilled, some spots organized in concentric circles are observed on the screen. These are the so-called Laue zones (**Figure D**.2**(b)**). The electrons inelastically diffracted form on the RHEED pattern the so-called Kikuchi lines (**Figure D**.2**(b)**). The electron beam wavelength (Å) is given by [13] :

$$\lambda = \frac{h}{\sqrt{2.m.E}} \qquad \textbf{(D.2)}$$

Where h is the Plank 's constant, m is the electron mass and E is the electron energy. Thus, for high energies used, the wavelength is very small and the Ewald sphere radius is very large and it appears almost flat in the reciprocal rods areas. For this reason, we see a streaky diffraction pattern.

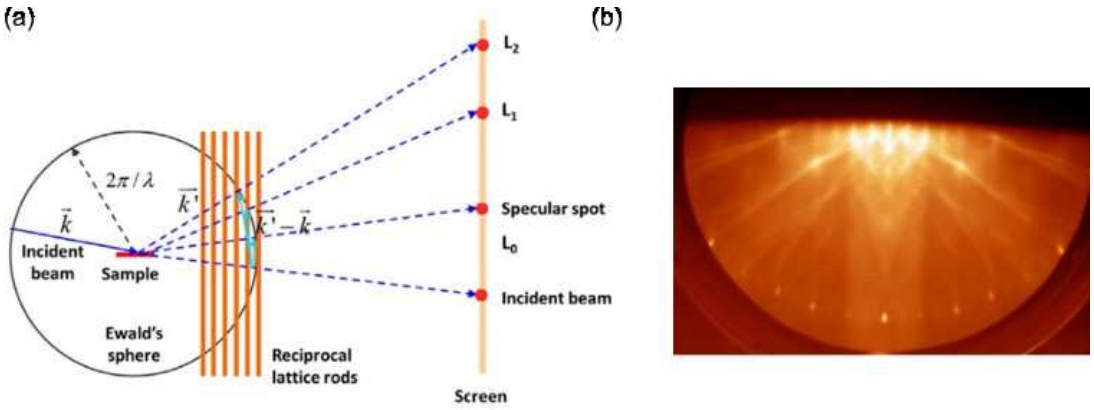

Figure D.2 (a) scheme of the RHEED pattern formation where L_0 , L_1 and L_2 are the zeroth, the first and the second order Laue zones [5]. (b) The kikuchi lines and Laue zone observed on the ex-situ chemically cleaned Si(001) 0.3°off misoriented toward the [110] direction, described in Chapter 4.

Different surface atoms arrangement are associated to different RHEED patterns, as explained in the literature by S. Hasegawa [12] . The different patterns are illustrated in **Figure D.3** where the case of a perfectly 2D monocrystalline surface is presented in **Figure D.3(a).** Its diffraction pattern is formed by Laue zones consisting in elongated spots. In **Figure D.3(b)** the surface is poly-crystalline and its reciprocal space is given by thick rods. When the rods intersect the Ewald sphere, elongated and thicker diffraction spots form on the screen. The presence of terraces can complicate a little bit more the reciprocal rods formed and so the diffraction pattern. Moreover, as the interference of the reflected beam from lower and upper terraces can be either constructive or destructive, the intensity of each rod can be modulated. **Figure D.3(c)** corresponds to a two level stepped surface while **Figure D.3(d)** is the case of a rough surface with multilevel terraces. Here the rods intensity is modulated forming sharper nodes separated by broader weaker areas (**Figure D.3(d)**). In the case of a vicinal surface, the rods are perpendicular to the terraces. Other fine rods are perpendicular to the overall surface, thus they are slightly inclined. These are present inside the rods normal to the terraces. As a result, inclined streaks are observed on the screen, see **Figure D.3(e)** . Finally for a 3D surface, (**Figure D.3(f)**), the electron beam is transmitted through the 3D islands and diffracted in different directions creating a diagram of spots.

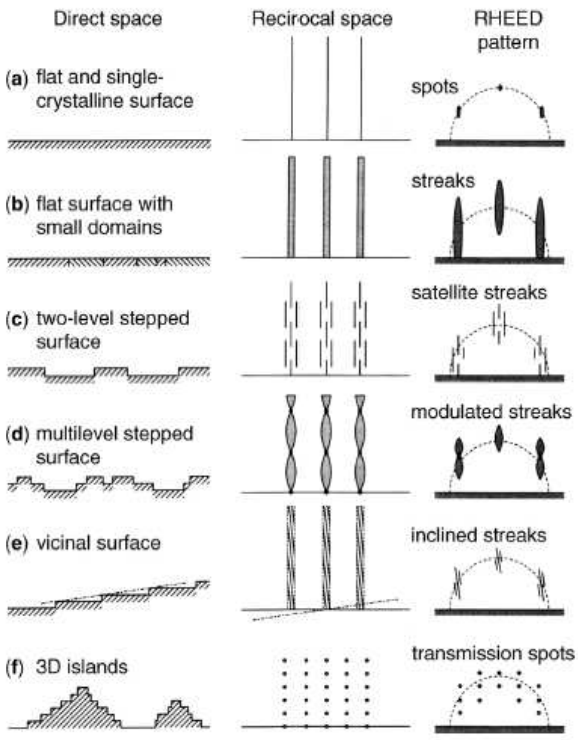

Figure D.3 Scheme of different type of surfaces: their real morphology, the reciprocal space and the corresponding RHEED pattern. Courtesy of [12]

RHEED analysis is very useful to monitor growth modes and growth rates. Indeed, it is possible to detect the three main type of MBE growth modes (see figure 2 in appendix B): Frank-van der Marve (layer-by-layer) growth where the RHEED pattern is formed by streaks corresponding to a 2D surface with a diffraction patterns dependent with the kind of surface investigated (see **Figure D.3(a-e)**) ; Volmer-Weber (3D-islanding) growth where the spots indicate a rough 3D-islands surface (see **Figure D.3(f)**); Stranski-Krastanov (layer-plus-islands) growth where formation of a 2D wetting layer (streaky pattern, see **Figure D.3(a-e)**) is followed by the 3D-islands formation (spots **Figure D.3(f)**). Moreover, RHEED is very useful during homeopitaxial Si growth (or during annealing procedures) under ultrahigh vacuum chemical vapor deposition (UHV-CVD) for in-situ investigating the surface atoms arrangement as showed in this thesis for Si(001) in chapter 4.

Finally, the growth rate can be detected as a function of the oscillatory intensity of the reflected beam (**Figure D**.4). Indeed, during a layer-by-layer growth the starting surface is flat at the beginning. Then, a second flat layer is formed passing through the formation of 2D islands. Thus, the intensity of the specular spot, which is higher when the surface is flat, becomes weaker during the islands formation when the surface looks rough. Finally, the intensity becomes higher again when a flat and continuous layer is formed.

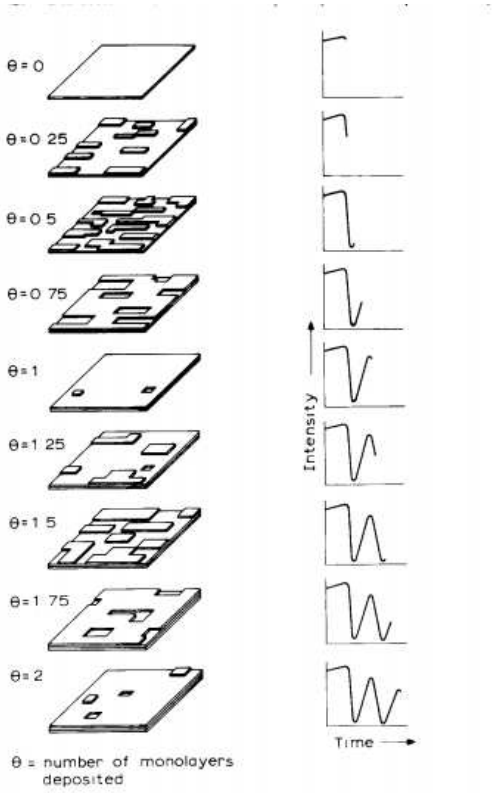

Figure D.4 The intensity modulated by the surface morphology during the layer-by-layer growth. Courtesy of [12].

References

[1] T. Quinci *et al.*, 'Defects limitation in epitaxial GaP on bistepped Si surface using UHVCVD–MBE growth cluster', *Journal of Crystal Growth*, vol. 380, pp. 157–162, Oct. 2013.

[2] U. W. Pohl, *Epitaxy of Semiconductors: Introduction to Physical Principles*. Springer Science & Business Media, 2013.

[3] K. Reichelt, 'Nucleation and growth of thin films', *Vacuum*, vol. 38, no. 12, pp. 1083–1099, Jan. 1988.

[4] T. J. Grassman *et al.*, 'Control and elimination of nucleation-related defects in GaP/Si(001) heteroepitaxy', *Appl. Phys. Lett.*, vol. 94, no. 23, p. 232106, juin 2009.

[5] T. T. Nguyen, 'Sillicon photonics based on monolithic integration of III-V nanostructures on silicon', phdthesis, INSA de Rennes, 2013.

[6] Y. Ping Wang *et al.*, 'Quantitative evaluation of microtwins and antiphase defects in GaP/Si nanolayers for a III–V photonics platform on silicon using a laboratory X-ray diffraction setup', *J Appl Cryst, J Appl Crystallogr*, vol. 48, no. 3, pp. 702–710, Jun. 2015.

[7] Y. Ping Wang *et al.*, 'Abrupt GaP/Si hetero-interface using bistepped Si buffer', *Appl. Phys. Lett.*, vol. 107, no. 19, p. 191603, Nov. 2015.

[8] P. Guillemé *et al.*, 'Antiphase domain tailoring for combination of modal and 4^{-} -quasi-phase matching in gallium phosphide microdisks', *Opt. Express, OE*, vol. 24, no. 13, pp. 14608–14617, Jun. 2016.

[9] A. C. Lin, M. M. Fejer, and J. S. Harris, 'Antiphase domain annihilation during growth of GaP on Si by molecular beam epitaxy', *Journal of Crystal Growth*, vol. 363, pp. 258–263, Jan. 2013.

[10] Y. Wang, 'Structural analyses by advanced X-ray scattering on GaP layers epitaxially grown on silicon for integrated photonic applications', phdthesis, INSA de Rennes, 2016.

[11] T. Quinci, 'Composant photovoltaïque innovant à base d'hétérojonction GaP/Si', thesis, Rennes, INSA, 2015.

[12] S. Hasegawa, 'REFLECTION HIGH-ENERGY ELECTRON DIFFRACTION', p. 14.

[13] A. Ichimiya, P. I. Cohen, and P. I. Cohen, *Reflection High-Energy Electron Diffraction*. Cambridge University Press, 2004.

Résumé

La photonique sur silicium consiste à intégrer des composants et des circuits photoniques sur des plaquettes de silicium sur isolant (SOI). Elle est née de l'idée d'appliquer à la photonique les avantages technologiques de la fabrication des composants silicium à faible coût. De plus, elle vise également à dépasser les limites des interconnexions électriques par des communications optiques à haut débit sur puce et intra-puce. Depuis les travaux pionniers de Soref *et al.* en 1985 [1], la recherche en photonique sur silicium a été stimulée par la réalisation de nombreux dispositifs de photonique intégrée, tels que les modulateurs ou les photodétecteurs. Une avancée majeure dans la technologie nanophotonique intégrée CMOS a été rapportée en 2012 par IBM, intégrant côte à côte des composants électriques et optiques avec une technologie 90 nm [2]. Cependant jusqu'à présent, l'intégration des lasers sur puce reste un défi. Néanmoins, dans le cadre de la photonique intégrée sur puce, la co-intégration des semi-conducteurs III-V sur Si est une stratégie réaliste pour améliorer les performances des dispositifs photoniques intégrés [3]. En effet, elle combine les bonnes propriétés optiques des semi-conducteurs III-V couplées à la technologie mature du silicium [4]. En particulier, l'approche monolithique est une technique d'intégration très prometteuse, comme l'a rappelé INTEL (conférence ECOC) en 2018. En effet, cette approche permet la croissance directe des III-V sur silicium dans un schéma appelé "front-end" dont l'avantage majeur est d'être directement compatible avec des schémas d'intégration à très grande échelle (VLSI) [4]. Néanmoins, elle doit faire face à différents défis tels que la formation de défauts à l'interface III-V/Si, dont la formation de domaines d'antiphase (APDs) due à la croissance directe des matériaux III-V (polaires) sur silicium (non polaire) [5]. L'origine de la formation des domaines d'antiphases (APD) est communément attribuée soit à une couverture incomplète du substrat Si, sans marche, par le groupe III ou V, ou à une la présence des marches de Si comme illustré en **Figure 1**. En 1987, Kroemer [5] a expliqué en détail ce mécanisme de formation. Depuis lors, ce mécanisme est considéré comme la principale motivation pour l'utilisation d'un substrat de Si désorienté. Cependant, le contrôle et la compréhension de la génération mais aussi de la propagation des défauts aux premiers stades précoce de la croissance III-V/Si est encore un sujet très débattu par de nombreux groupes de recherche.

Cette thèse s'inscrit dans le cadre du projet ANR intitulé "Advanced aNalysis of III-V/Si nucleaTIon for highly integrated PhOtonic Devices" (ANTIPODE) (soutenu par l'Agence Nationale de la Recherche - subvention n° 14-CE26-0014-01). Il vise à clarifier la phase initiale de la croissance monolithique des semi-conducteurs III-V sur Si. En particulier, il avait pour but d'établir les liens étroits entre le mode de croissance 3D, la relaxation des contraintes et la génération des APDs. Ainsi, les principaux objectifs du projet ANTIPODE sont: (i) la compréhension du mécanisme de nucléation 3D des semi-conducteurs III-V sur silicium (y compris la génération de défauts pendant la coalescence) mais aussi les mécanismes de relaxation de contrainte associés (ii) la nature et le rôle des charges d'interface sur la croissance et la génération de défauts (iii) l'influence de la surface initiale de silicium.

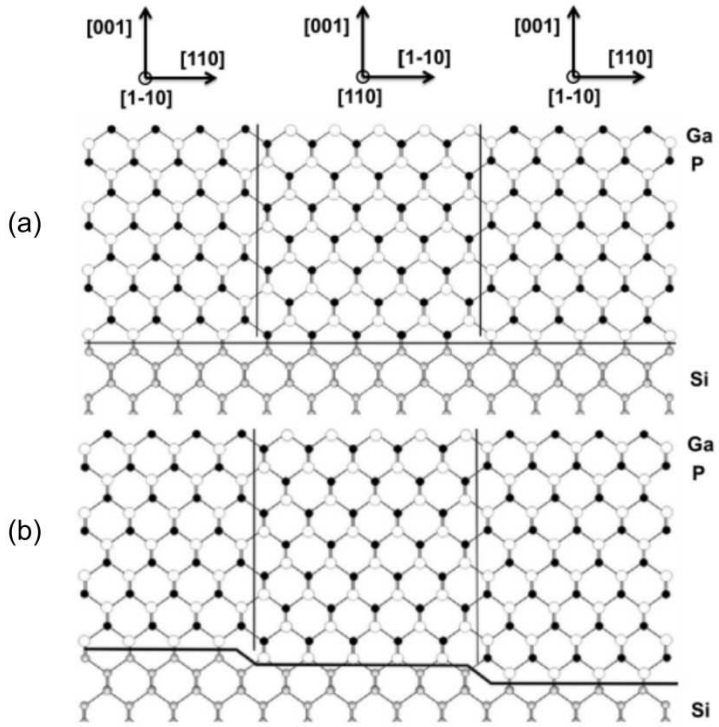

Figure 1 Formation de domaines d'antiphase due à (a) une couverture incomplète du substrat Si par le groupe III ou le groupe V ou (b) à la presence des marches atomiques à la surface Si **[6]**

L'objectif de cette thèse est d'étudier ce qui se passe au tout début de la croissance du système GaP sur Si pour les applications en photonique ou dans le domaine de l'énergie. En

effet, le système GaP/Si est très intéressant parce qu'il présente un très faible désaccord de maille (0,3 %). Avec l'aide de la théorie, la thèse vise à déterminer, par des calculs de théorie de la fonctionnelle de la densité (DFT), i) les énergies absolues de surface et d'interface du système GaP/Si, ii) à comprendre leur rôle dans le mode de croissance 3D GaP/Si et dans la formation d'une surface texturée de GaP sur Si iii) à confronter ces énergies avec d'autres valeurs de système III-V sur Si. Enfin, elle vise à étudier expérimentalement les conditions de croissance nécessaires pour l'obtention d'une surface de silicium promettant une recroissance III-V de bonne qualité. La plupart des surfaces stables du GaP sur Si ont été étudiées avec des interfaces GaP/Si abruptes mais aussi compensées, par la méthode DFT.

Tout d'abord, nous avons calculé l'énergie de surface Si(001) avec et sans marches atomiques [7]. Ensuite, les reconstructions les plus stables connues dans la littérature pour GaP [8], [9] ont été considérées. Un premier résultat montre que la présence de marche ne change pas significativement l'énergie de surface du silicium (**Tableau 1**).

	Type de reconstruction	Energie de surface (meV/Å^2)
Si(001)	c(4x2)	92.8
S_B-step Si(001)	p(2x2)	89.1
S_A-step Si(001)	c(4x2)	87.1
D_B-step Si(001)	p(2x2)	89.3

Tableau 1 Energies de surface calculées par DFT pour le Si(001)

Pour les surfaces de GaP, les surfaces les plus stables observées expérimentalement {001}, {114}, et {136} [8]–[16] ont été étudiées. Pour ces travaux, le modèle de comptage d'électrons (ECM) [17] a été pris en compte pour trouver les configurations des surfaces les plus énergétiquement stables. Par exemple, les surfaces GaP(136) ne remplissent pas l'ECM [17]. Ainsi, la nécessité de respecter l'ECM couplée avec un angle d'inclinaison de ~2° entre les plans (2 5 11) et (1 3 6) [15], [18], nous a convaincu de travailler sur la surface GaP(2 5 11) plus stable plutôt que sur la (136). Toutes ces énergies de surfaces sont reportées dans la **Figure 2 (a).**

Les énergies des interfaces abruptes et compensées ont aussi été calculées par DFT. Ces simulations ont confirmé que les interfaces compensées sont nettement plus stables que les interfaces abruptes. Les énergies d'interface compensées et abruptes en fonction du potentiel chimique sont représentées sur le graphique en **Figure 2 (b).**

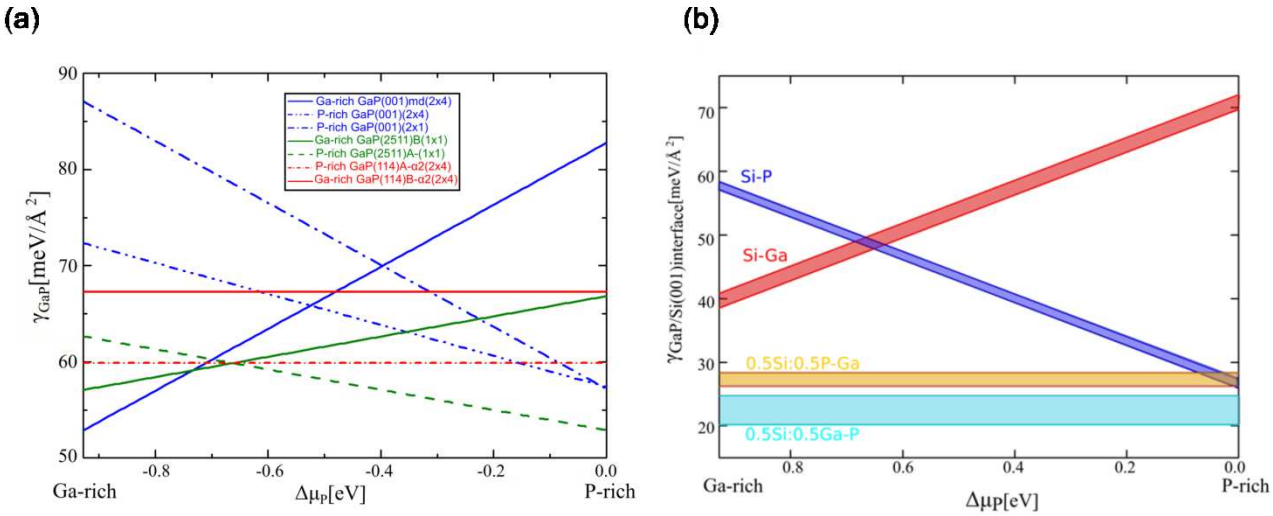

Figure 2 (a) Energies de surface en fonction du potentiel chimique pour les surfaces (001), (114) et (2 5 11) (b) Diagramme des énergies d'interface absolues compensées et abruptes calculées par DFT. Un pinceau coloré représente les incertitudes sur les énergies d'interface. Comme indiqué dans la référence [33], les énergies des interfaces compensées 0,5 Si : 0,5 Ga-P et 0,5 Si : 0,5 P-Ga sont plus stables par rapport aux énergies des interfaces abruptes car elles remplissent le critère ECM. De plus, leur énergie ne varie pas en fonction du potentiel chimique $\Delta\mu_P$, comme prévu par la théorie en raison de leur stoechiométrie ($\Delta N=0$)

Dans le contexte de l'intégration monolithique des matériaux III-V sur le Si, les processus impliqués dans les premiers stades de l'épitaxie hétérogène III-V/Si ont ensuite été étudiés: i) l'interaction entre les modes de croissance tridimensionnels (3D), ii) la relaxation des contraintes, et iii) la formation des domaines d'antiphase et des autres défauts. Les îlots 3D de III-V sur Si sont étudiés dans trois systèmes de matériaux semi-conducteurs III-V différents. Ainsi, cette étude a permis de couvrir la contrainte épitaxiale initiale de la compression (AlSb/Si) à la tension (AlN/Si) en passant par le cas d'une contrainte quasi nulle (GaP/Si) (**Figure 3**) . De cette analyse, il est apparu que le mouillage partiel de III-V sur Si, c'est-à-dire le mode de croissance Volmer-Weber, est observé indépendamment de l'état de déformation [19], [20]. Nous avons également observé que les îlots sont presque parfaitement facettés bien après la

relaxation plastique cristalline. Cela suggère que la relaxation élastique de la contrainte [21] ne contribue pas de manière significative au bilan énergétique de chaque îlot. Le rôle crucial des énergies de surface et d'interface dans la formation des îlots 3D III-V sur Si a ainsi été mis en évidence. De plus, les résultats expérimentaux montrent que les îlots sont mono-domaines.

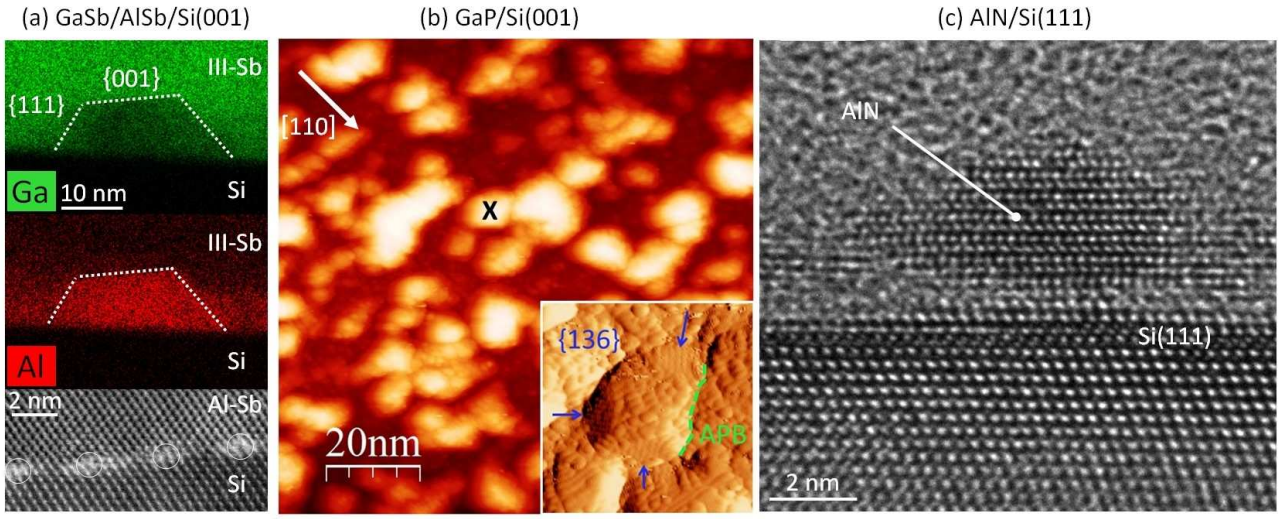

Figure 3 Îlotage 3D dans différents systèmes de matériaux III-V/Si. (a) Image STEM-EDX en coupe transversale de couches de GaSb/AlSb épitaxiées sur Si (001) - 6°-off, montrant les concentrations de Ga et d'Al, et image STEM haute résolution de l'interface AlSb/Si, les dislocations sont entourées. (b) Image STM en vue plane d'un dépôt de GaP de 3 nm d'épaisseur sur Si (001) - 6°-off ($100*100nm^2$, échelle de couleurs verticale : 0-5,1 nm). L'encadré $20*20nm^2$ montre la morphologie à résolution atomique de l'îlot individuel marqué d'une croix noire, avec des facettes {136} et une paroi d'antiphase. c) Image TEM à haute résolution en coupe transversale d'un dépôt d'AlN de 2 nm d'épaisseur sur du Si(111).

Thermodynamiquement, nous avons aussi discuté de la formation d'îlots 3D du système GaP/Si, grâce aux énergies absolues de surface et d'interface estimées par les calculs DFTs. Les propriétés de mouillage du système GaP/Si ont été étudiées révélant que le mouillage partiel est toujours obtenu quelle que soit la valeur du potentiel chimique μ_P. De plus, le mouillage partiel est encore favorisé par la passivation de surface Si (**Figure 4-gauche(a) et (b)**). La variation totale de l'énergie libre pendant la croissance de GaP/Si est calculée pour différentes configurations d'îlots 2D ou d'îlots 3D pyramidal tronqué de GaP (correspondant à leur forme d'équilibre de Wulf-Kaishew) (**Figure 4-gauche(c) et (d)**) [22]. L'analyse des différentes contributions montre, indépendamment du potentiel chimique du phosphore, que les

contributions des énergies absolues de surface et d'interface sont toujours dominantes par rapport à la contribution de l'énergie élastique. Cette contribution de l'énergie élastique n'a donc pas un impact majeur sur la morphologie des îlots. En conséquence, la morphologie des îlots est principalement reliée à la compétition entre les énergies de surface et d'interface. (**Figure 4-gauche-(d)**). Ces conclusions peuvent être étendues à tous les III-V sur Si au regard des ordres de grandeur. De plus, un mécanisme de croissance généralisé aux III-V sur silicium a été proposé pour clarifier la formation des défauts liés au mouillage partiel, dont la formation des APDs (**Figure 4-droit**).

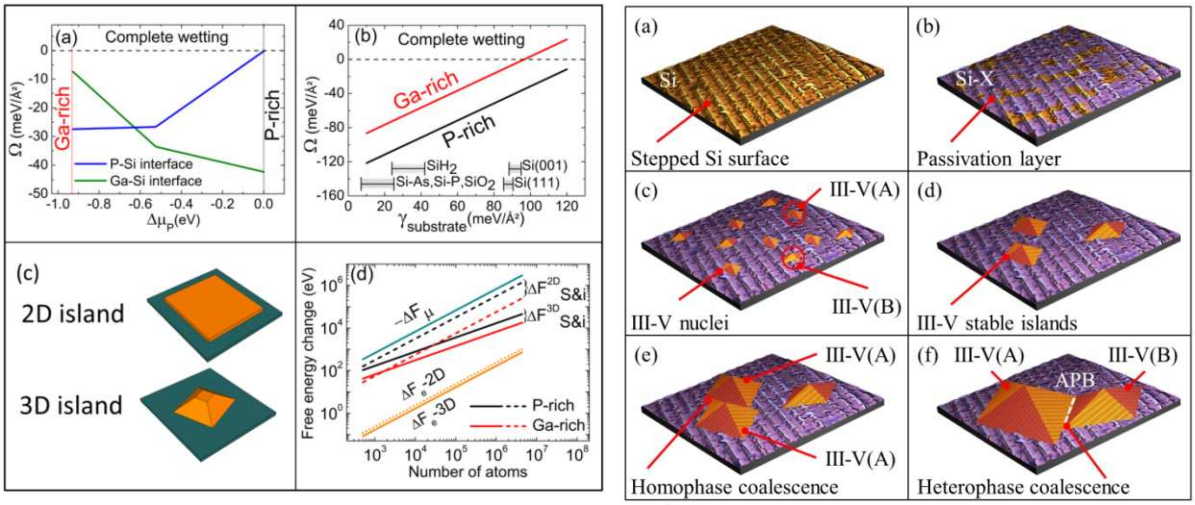

Figure 4 Gauche (a) Paramètre d'étalement en fonction de la variation du potentiel chimique pour le dépôt de GaP/Si, avec interfaces P-Si et Ga-Si abruptes. (b) Paramètre d'étalement en fonction de l'énergie de surface du substrat dans des conditions riches en P et des conditions riches en Ga avec interface Ga-Si. (c) Croquis des îlots 2D (contraintes) et 3D (relaxation élastique) en GaP sur Si. d) Les différentes contributions (ΔF_μ, $\Delta F_{S\&i}$, ΔF_e) de la variation d'énergie libre pour les îlots 3D et 2D GaP/Si avec interface Ga-Si. Droit: Description des étapes de croissance III-V/Si proposées, avec (a) l'image STM 35×35 nm² d'une surface de départ Si avec marche (composée de bisteps et de monosteps même sur des substrats mal orientés). La surface de Si est ensuite recouverte (b) au moins partiellement d'une couche de passivation 2D. La nucléation commence (c) la polarité des cristaux est définie localement par l'orientation locale du substrat de silicium. Certains îlots stables se développent ensuite (d), indépendamment des marches de Si. Lorsque 2 îlots de la même phase s'unissent (e), ils formeront un îlot plus grand. Lorsque 2 îlots ont des phases différentes et qu'ils fusionnent (f), des frontières d'antiphase apparaîssent.

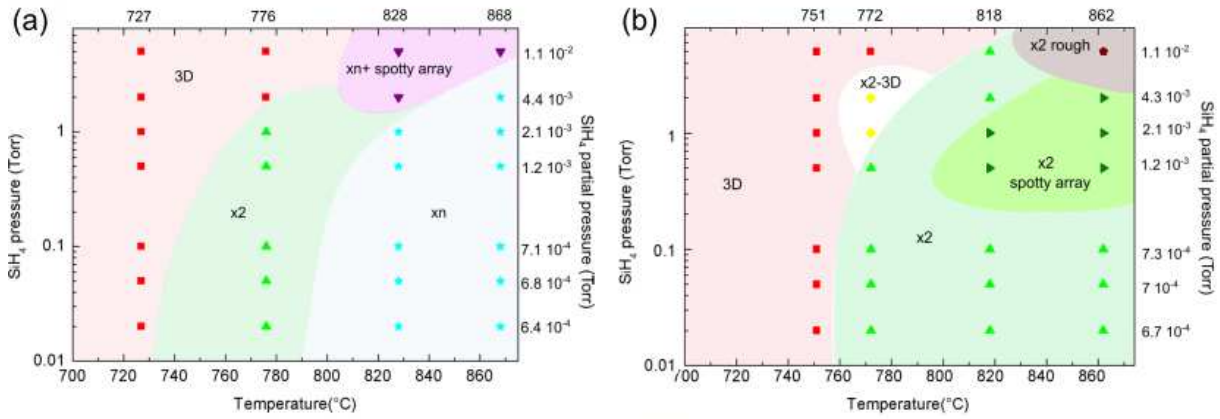

Figure 5 (a) Diagramme de phase Pression-Température obtenu pendant la croissance Si sur substrat Si-6°-off. Par l'analyse RHEED le long de l'azimut[1-10], trois régions principales peuvent être identifiées :3D, x2, xn (b) Diagramme de phase Pression-Température obtenu pendant la croissance Si sur substrat Si(001). Par l'analyse RHEED le long de l'azimut[1-10], deux régions principales peuvent être identifiées : 3D, x2 ainsi que certaines zones de transition. Aucune surface monodomaine n'est obtenue

Par la suite, une étude expérimentale approfondie a été réalisée pour étudier les propriétés à l'échelle atomique de la surface de silicium pendant et après sa croissance, par diffraction électronique de surface (RHEED), en vue d'une reprise de croissance de matériau III-V. Une nouvelle procédure pour protéger le substrat de Si(001) des contaminants a été mise en place. Par ailleurs, travailler avec i) une surface nominale Si(001) à faible désorientation (±0,5°) tout en ayant ii) une surface mono-domaine doit permettre d'éviter la formation d'APDs lors de la croissance épitaxiale. L'avantage principal de cette méthode est qu'elle est directement compatible avec l'approche CMOS [23]. C'est d'ailleurs cette approche qui est proposée par la société NAsP à Marburg par MOCVD [23]. Ainsi, afin d'étudier l'influence des conditions de croissance sur la polarité de la surface, nous avons étudié la croissance du silicium sous un flux de SiH_4 en fonction de la température de croissance et de la pression du silane. Ces études ont été réalisées pour des surfaces nominales et vicinales (6°-off) de Si(001). L'analyse montre dans certaines conditions, pour le cas Si(001) vicinal, la présence de surfaces bi-domaines ou mono-domaines de type xn (**Figure 5a)**). Par contre, pour le cas Si(001) nominal, quelques soient les conditions de croissance étudiées, une surface bi-domaine a été obtenue (**Figure 5(b)**).

Des études préliminaires ont été menées pour (i) démontrer la possibilité de propager ou d'annihiler les parois d'antiphase (APBs) en utilisant de fines couches d'AlGaP et ii) caractériser les propriétés électriques des APBs.

Enfin, dans le contexte des applications pour l'énergie, de nombreuses propositions récentes portent sur l'utilisation du semi-conducteur GaP comme photoélectrode dans les dispositifs appelés cellules photoélectrochimiques (PEC) [24]. En effet, son énergie de bande interdite (2,26 eV) est bien supérieure au photopotentiel de 1,73 eV nécessaire pour le bon fonctionnement des composants pour la photodissociation de l'eau[25]. Le GaP possède également un alignement de bande quasi parfait avec les niveaux redox de l'eau. Dans cette thèse, une surface de GaP nano-texturée sans contrainte a été réalisée par épitaxie par jets moléculaires sur un substrat vicinal de Si de 2 pouces (**Figure 6**)**.** Les avantages de l'utilisation de cette surface texturée à grande échelle pour développer des composants pour la photodissociation de l'eau ont aussi été discutés.

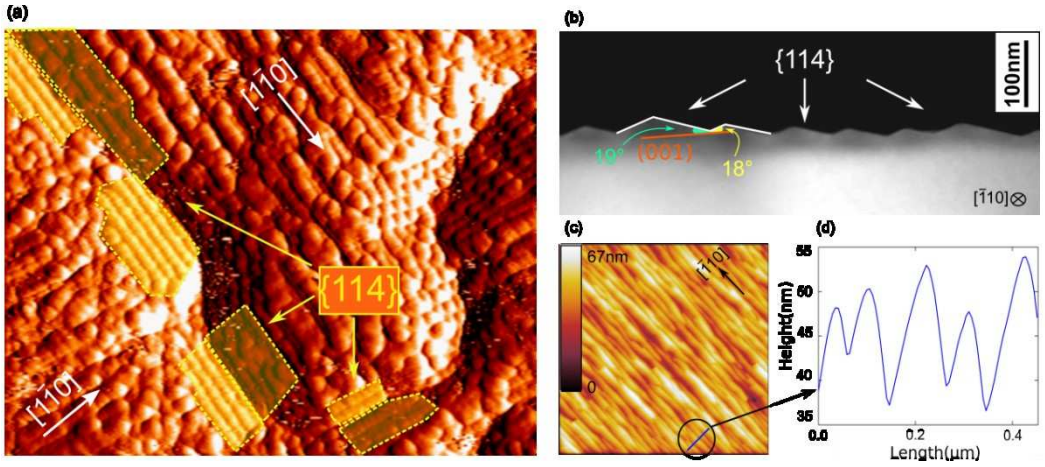

Figure 6 (a) 25x30 nm² STM image d'une surface GaP bi-domaine de 10 nm d'épaisseur sur Si(001) attestant la présence de nombreuses facettes (114)A et B sur les bords des parois antiphase (b) TEM image de GaP d'épaisseur 1µm sur Si 6°-off (c) 3 µm *3 µm AFM image de la surface du même échantillon que b) et (d) un profil pris par une petite région de l'image AFM. Les observations TEM et AFM montrent la facette (114)A de la surface du GaP

En conclusion, les résultats de recherche présentés dans ce travail de thèse permettent d'ouvrir la voie vers des matériaux pour des composants à haut rendement, à hautes performances et à faible coût pour des applications en photonique et dans le domaine de l'énergie. Ce travail va au-delà des stratégies de filtrage des défauts adoptées de nos jours par les chercheurs[26].

References

[1] R. A. Soref and J. P. Lorenzo, 'Single-crystal silicon: a new material for 1.3 and 1.6 µm integrated-optical components', *Electronics Letters*, vol. 21, no. 21, pp. 953–954, Oct. 1985.

[2] S. Assefa *et al.*, 'A 90nm CMOS integrated Nano-Photonics technology for 25Gbps WDM optical communications applications', in *Electron Devices Meeting (IEDM), 2012 IEEE International*, 2012, pp. 33.8.1-33.8.3.

[3] D. T. Spencer *et al.*, 'An optical-frequency synthesizer using integrated photonics.', *Nature*, vol. 557, no. 7703, pp. 81–85, May 2018.

[4] C. Cornet, Y. Léger, and C. Robert, *Integrated Lasers on Silicon*. ISTE-Elsevier, 2016.

[5] H. Kroemer, 'Polar-on-nonpolar epitaxy', *J. Cryst. Growth*, vol. 81, no. 1–4, pp. 193–204, Feb. 1987.

[6] I. Nemeth, 'Transmission electron microscopic investigations of heteroepitaxial III/V semiconductor thin layer and quantum well structures', 2008. .

[7] D. J. Chadi, 'Stabilities of single-layer and bilayer steps on Si(001) surfaces', *Phys. Rev. Lett.*, vol. 59, no. 15, pp. 1691–1694, Oct. 1987.

[8] S. Mirbt, N. Moll, K. Cho, and J. D. Joannopoulos, 'Cation-rich (100) surface reconstructions of InP and GaP', *Physical Review B*, vol. 60, p. 13283, Nov. 1999.

[9] O. Pulci *et al.*, 'First-principles study of InP and GaP(001) surfaces', *Computational Materials Science*, vol. 22, no. 1, pp. 32–37, Nov. 2001.

[10] K. Luedge, P. Vogt, O. Pulci, N. Esser, F. Bechstedt, and W. Richter, 'Clarification of the GaP(001)(2x4) Ga-rich reconstruction by scanning tunneling microscopy and ab initio theory', *PHYSICAL REVIEW. B, CONDENSED MATTER AND MATERIALS PHYSICS*, vol. 62, no. 16, pp. 11046–11049, 2000.

[11] J. Márquez, P. Kratzer, and K. Jacobi, 'Structure and morphology of the As-rich and the stoichiometric GaAs(114)A surface', *Journal of Applied Physics*, vol. 95, no. 12, pp. 7645–7654, Jun. 2004.

[12] J. Márquez, P. Kratzer, L. Geelhaar, K. Jacobi, and M. Scheffler, 'Atomic Structure of the Stoichiometric GaAs(114) Surface', *Phys. Rev. Lett.*, vol. 86, no. 1, pp. 115–118, Jan. 2001.

[13] R. D. Smardon and G. P. Srivastava, 'Electronic structure of the GaAs (114) A-(2× 1) and GaAs (114) B-(2× 1) surfaces', *Phys. Rev. B*, vol. 72, juillet 2005.

[14] L. Geelhaar, J. Márquez, P. Kratzer, and K. Jacobi, 'GaAs(2511)$: A New Stable Surface within the Stereographic Triangle', *Phys. Rev. Lett.*, vol. 86, no. 17, pp. 3815–3818, Apr. 2001.

[15] Y. Temko, L. Geelhaar, T. Suzuki, and K. Jacobi, 'Step structure on the GaAs(2511) surface', *Surface Science*, vol. 513, no. 2, pp. 328–342, juillet 2002.
[16] K. Jacobi, L. Geelhaar, and J. Márquez, 'Structure of high-index GaAs surfaces – the discovery of the stable GaAs (2 5 11) surface', *Appl Phys A*, vol. 75, no. 1, pp. 113–127, Jul. 2002.
[17] M. D. Pashley, 'Electron counting model and its application to island structures on molecular-beam epitaxy grown GaAs(001) and ZnSe(001)', *Phys. Rev. B*, vol. 40, no. 15, pp. 10481–10487, Nov. 1989.
[18] R. Méndez-Camacho, V. H. Méndez-García, M. López-López, and E. Cruz-Hernández, 'New orientations in the stereographic triangle for self-assembled faceting', *AIP Advances*, vol. 6, no. 6, p. 065023, juin 2016.
[19] R. Hull and A. Fischer-Colbrie, 'Nucleation of GaAs on Si: Experimental evidence for a three-dimensional critical transition', *Applied Physics Letters*, vol. 50, no. 13, pp. 851–853, Mar. 1987.
[20] F. Ernst and P. Pirouz, 'Formation of planar defects in the epitaxial growth of GaP on Si substrate by metal organic chemical-vapor deposition', *Journal of Applied Physics*, vol. 64, no. 9, pp. 4526–4530, Nov. 1988.
[21] J. Tersoff and F. K. LeGoues, 'Competing relaxation mechanisms in strained layers', *Phys. Rev. Lett.*, vol. 72, no. 22, pp. 3570–3573, May 1994.
[22] P. Müller and R. Kern, 'Equilibrium nano-shape changes induced by epitaxial stress (generalised Wulf–Kaishew theorem)', *Surface Science*, vol. 457, no. 1, pp. 229–253, juin 2000.
[23] K. Volz *et al.*, 'GaP-nucleation on exact Si (001) substrates for III/V device integration', *Journal of Crystal Growth*, vol. 315, no. 1, pp. 37–47, Jan. 2011.
[24] E. E. Barton, D. M. Rampulla, and A. B. Bocarsly, 'Selective Solar-Driven Reduction of CO_2 to Methanol Using a Catalyzed p-GaP Based Photoelectrochemical Cell', *Journal of the American Chemical Society*, vol. 130, no. 20, pp. 6342–6344, May 2008.
[25] B. Kaiser, D. Fertig, J. Ziegler, J. Klett, S. Hoch, and W. Jaegermann, 'Solar Hydrogen Generation with Wide-Band-Gap Semiconductors: GaP(100) Photoelectrodes and Surface Modification', *ChemPhysChem*, vol. 13, no. 12, pp. 3053–3060, Aug. 2012.
[26] S. Chen *et al.*, 'Electrically pumped continuous-wave III–V quantum dot lasers on silicon', *Nat Photon*, vol. 10, no. 5, pp. 307–311, mai 2016.

List of publications/conferences

a) –Publications and proceedings

Publications:

***I. Lucci**, S. Charbonnier, L. Pedesseau, M. Vallet, L. Cerutti, J.-B. Rodrigue, E. Tournié, R. Bernard, A. Létoublon, N. Bertru, A. Le Corre, S. Rennesson, F. Semond, G. Patriarche, L. Largeau, P. Turban, A. Ponchet and C. Cornet "* A universal description of III-V/Si epitaxial growth processes *",* Physical Review Materials, 2 (6), pp.060401(R) (2018).

***Ida Lucci**, Simon Charbonnier, Maxime Vallet, Pascal Turban, Yoan Léger, Tony Rohel, Nicolas Bertru, Antoine Létoublon, Jean-Baptiste Rodriguez, Laurent Cerutti, Eric Tournié, Anne Ponchet, Gilles Patriarche, Laurent Pedesseau, and Charles Cornet "* A stress-free and textured GaP template on silicon for solar water splitting *",* Adv. Funct. Mater. 28, 1801585 (2018).

**I. Lucci, C. Cornet, M. Bahri, Y. Léger "*Thermal management of monolithic vs heterogeneous lasers integrated on silicon *", IEEE Journal of Selected Topics in Quantum Electronics - special issue on Silicon Photonics, accepted (2016).*

b) –Invited talks

***I. Lucci,** S. Charbonnier, L. Pedesseau, M. Vallet, L. Cerutti, J.-B. Rodriguez, E. Tournié, R. Bernard, A. Létoublon, N. Bertru, A. Le Corre, S. Rennesson, F. Semond, G. Patriarche, L. Largeau, P. Turban, A. Ponchet, *C. Cornet," A universal mechanism to describe III-V epitaxy on Si.", Invited talk at EURO-MBE 2018 Conference, Lenggries, Germany,17-20 February 2019.*

C. Cornet, L. Chen, **I. Lucci, A. Ruiz, A. Beck, L. Pedesseau, and Y. Léger,"GaP-based materials for photonics and energy", Invited talk at SNAIA2018 - Smart Nanomaterials Conference, Ecole normale supérieure de Chimie- Paris, 10-13 December 2018.*

**I. Lucci, S. Charbonnier, L. Pedesseau, M. Vallet, L. Cerutti, J.-B. Rodrigue, E. Tournié, R. Bernard, A. Létoublon, N. Bertru, A. Le Corre, S. Rennesson, F. Semond, G. Patriarche, L. Largeau, P. Turban, A. Ponchet and C. Cornet"* III-V/Si 3D crystal growth: a thermodynamic description*", Invited Talk at EMN 3CG Meeting 2017, Berlin, 7-11 August 2017*

Y. Léger, R. Tremblay, **I. Lucci, C. Cornet. "*Laser integration challenges for on-chip optical interconnects *", Invited talks at OPTICS 2016 workshop, Dresden, 14-18 March 2016*

c) –Communications with international audience

**I. Lucci, S. Charbonnier, L. Pedesseau, M. Vallet, L. Cerutti, J.-B. Rodriguez, E. Tournié, R. Bernard, A. Létoublon, N. Bertru, A. Le Corre, S. Rennesson, F. Semond, G. Patriarche, L. Largeau, A. Ponchet, P. Turban and C. Cornet "*A universal mechanism to describe the III-V on Si growth growth by Molecular Beam Epitaxy*", Talk at the 20th International Conference on Molecular Beam Epitaxy (IC-MBE 2018), Shanghai, China.*

**I. Lucci, S.Charbonnier, M.Vallet, P.Turban, Y.Léger, T.Rohel, N. Bertru, A. Létoublon, J.-B.Rodriguez, L.Cerutti, E.Tournié, A. Ponchet, G. Patriarche, L.Pedesseau, and C.Cornet "*Large scale textured GaP(114) growth on vicinal Si

substrate by Molecular Beam Epitaxy for water splitting applications*", Poster at 20th International Conference on Molecular Beam Epitaxy (IC-MBE 2018), Shanghai, China.*

**I. Lucci, S. Charbonnier, L. Pedesseau, M. Vallet, L. Cerutti, J.-B. Rodriguez, E. Tournié, R. Bernard, A. Létoublon, N. Bertru, A. Le Corre, S. Rennesson, F. Semond, G. Patriarche, L. Largeau, A. Ponchet, P. Turban and C. Cornet "III-V/Si heterogeneous growth : thermodynamics and antiphase domains formation", Talk at the 34th International Conference on the Physics of Semiconductors (ICPS2018), Montpellier , France 29 July-3 August 2018*

I. Lucci", S. Charbonnier, L. Pedesseau, M. Vallet, L. Cerutti, J.-B. Rodriguez, E. Tournié, R. Bernard, A. Létoublon, N. Bertru, A. Le Corre, S. Rennesson, F. Semond, G. Patriarche, L. Largeau, A. Ponchet, P. Turban and C. Cornet"*A general III-V/Si growth process description*", Poster at 2018 E-MRS Spring Meeting (EMRS2018)Strasbourg , France 18-22 June 2018*

**I. Lucci, S.Charbonnier, M.Vallet, P.Turban, Y.Léger, T.Rohel, N. Bertru, A. Létoublon, J.-B.Rodriguez, L.Cerutti, E.Tournié, A. Ponchet, G. Patriarche, L.Pedesseau, and C.Cornet "(*114) GaP surface texturation on Si for water splitting", *Poster at 2018 E-MRS Spring Meeting (EMRS2018)Strasbourg , France 18-22 June 2018*

**M. Vallet, I. Lucci, M. Bahri, A. Létoublon, L. Largeau, G. Patriarche, C. Cornet and A. Ponchet, "*Role of marker layers on antiphase domains in GaP/Si heterostructures*", Talk at "Extended Defects in Semiconductors" (EDS) Conference, Les Issambres, France, 25-29 sept. 2016.*

**I. Lucci, S. Charbonnier , Y. Ping Wang, M. Bahri, M. Vallet , T. Rohel, R. Bernard, A. Létoublon, L. Largeau, G. Patriarche, A. Ponchet, O. Durand, L. Pedesseau, S. Gangopadhyay, P. Turban and C. Cornet "* Etude de la croissance cohérente de GaP/Si(001) en couche mince. *" Talk at IC-MBE 2016, Montpellier, France, 4-9 September 2016*

**I. Lucci, C. Cornet, M. Bahri and Y. Léger, "*Thermal management of monolithic and heterogeneous integrated lasers.*" Poster at CSW 2016, Toyama, Japan, 26-30 June 2016*

**S. Charbonnier, I. Lucci, S. Gangopadhyay, Y. Ping Wang, T. Rohel, R. Bernard, A. Létoublon, C. Cornet, P. Turban "* Scanning tunneling microscopy investigation of GaP epitaxial growth on nominal and vicinal Si(001) substrates for optoelectronic applications. *" Poster at EMRS 2016, Lille, France, 2-6 May 2016*

**I. Lucci, S. Charbonnier , Y. Ping Wang, M. Bahri, M. Vallet , T. Rohel, R. Bernard, A. Létoublon, L. Largeau, G. Patriarche, A. Ponchet, O. Durand, L. Pedesseau, S. Gangopadhyay, P. Turban and C. Cornet "*Relationship between antiphase domains, roughness and surface/interface energies during the epitaxial growth of GaP on Si. *" Poster at EMRS 2016, Lille, France, 2-6 May 2016*

d) –Communications with national audience

**I.Lucci, S. Charbonnier , S. Gangopadhyay, Y. Ping Wang, T. Rohel, R. Bernard, L. Pedesseau, A. Létoublon, C. Cornet and P. Turban "Etude de la croissance tridimensionnelle des III-V sur Silicium par DFT" Poster at GDR Pulse(PULSE 2017), Paris, France 2-5 October 2017*

*S. Charbonnier, *I. Lucci, S. Gangopadhyay, Y. Ping Wang, T. Rohel, R. Bernard, L. Pedesseau, A. Létoublon, C. Cornet and P. Turban , " GaP/Si(001) polar-on-nonpolar epitaxial growth revisited by scanning tunneling microscopy. " ,Talk at GDR Pulse(PULSE 2017), Paris, France 2-5 October 2017*

**I. Lucci , S. Charbonnier, Y. Ping Wang, M. Bahri, M. Vallet, T. Rohel, R. Bernard, A. Létoublon, L. Largeau ,G . Patriarche, A. Ponchet, O. Durand, L. Pedesseau, S. Gangopadhyay, P. Turban and C. Cornet "Integration of GaP on Si(001): understanding the origin of antiphase boundaries" Poster at* Journée *De Doctorants (JDD),Rennes, France, 1 June 2017*

**I. Lucci , S. Charbonnier, Y. Ping Wang, M. Bahri, M. Vallet, T. Rohel, R. Bernard, A. Létoublon, L. Largeau ,G . Patriarche, A. Ponchet, O. Durand, L. Pedesseau, S. Gangopadhyay, P. Turban and C. Cornet "3D GaP nucleation as*

the origin of the antiphase boundaries" Poster at Journées Surfaces et Interfaces (*JSI), Rennes, France, 25-27, January 2017*

***I. Lucci,** S. Charbonnier, Y. Ping Wang, M. Bahri, M. Vallet , T. Rohel, R. Bernard, A. Létoublon, L. Largeau, G. Patriarche, A. Ponchet, O. Durand, L. Pedesseau, S. Gangopadhyay, P. Turban and C. Cornet "* Etude de la croissance cohérente de GaP/Si(001) en couche mince. *" Talk at GDR PULSE 2016, Marseille, France, 18-22 July 2016*

S. Charbonnier, **I. Lucci, S. Gangopadhyay, Y. Ping Wang, T. Rohel, R. Bernard, A. Létoublon, C. Cornet and P. Turban, « Etude par microscopie à effet tunnel de la croissance épitaxiale de GaP sur substrats Si(001) nominaux et vicinaux pour l'optoélectronique. » Poster at GDR PULSE 2016, Marseille, France, 18-22 July 2016.*

e) – Selected seminars

***I. Lucci,** R. Bernard, L. Pedesseau, C. Cornet. Oral presentation for a reunion ANR: ANTIPODE T0+34, Rennes, 27-28 November 2018*

***I. Lucci,** R. Bernard, L. Pedesseau, C. Cornet. Oral presentation for a reunion ANR: ANTIPODE T0+24, Touluse, 12 January 2017*

***I. Lucci,** R. Bernard, L. Pedesseau, C. Cornet. Oral presentation for a reunion ANR: ANTIPODE T0+18, Valbonne, 8 June2016*

***I. Lucci,** R. Bernard, L. Pedesseau, C. Cornet. Oral presentation for a reunion ANR: ANTIPODE T0+13, Montpellier, 28 January 2016*

INSA de RENNES
Service des Formations

AVIS DU JURY SUR LA REPRODUCTION DE LA THESE SOUTENUE

Titre de la thèse:
Surface and interface contributions to III-V/Si hetero-epitaxial growth: Theory and Experiments

Nom Prénom de l'auteur : LUCCI IDA

Membres du jury :
- Monsieur MÜLLER Pierre
- Monsieur PEDESSEAU Laurent
- Monsieur TURBAN Pascal
- Madame BENOIT Magali
- Monsieur CORNET Charles
- Madame VOLZ Kerstin
- Monsieur HARMAND Jean-Christophe

Président du jury :

Date de la soutenance : 26 Février 2019

Reproduction de la these soutenue

☒ Thèse pouvant être reproduite en l'état
☐ Thèse pouvant être reproduite après corrections suggérées

Fait à Rennes, le 26 Février 2019

Signature du président de jury

Le Directeur,

M'hamed DRISSI

INSTITUT NATIONAL DES SCIENCES APPLIQUÉES - RENNES

UNIVERSITE MATIERE BRETAGNE MOLECULES LOIRE ET MATERIAUX

INSA RENNES

Titre : Contributions des surfaces et interfaces à la croissance hétéroépitaxiale III-V/Si : Théorie et Expériences

Mots clés : Photonique sur Silicium, croissance 3D, III-V/Si, GaP/Si, thermodynamique, DFT

Résumé : L'objectif de cette thèse est d'étudier les propriétés thermodynamiques et clarifier les toutes premières étapes de la croissance hétérogène de GaP sur Si (désaccord de maille de 0,3 %) pour les applications en photonique et dans le domaine de l'énergie. Tout d'abord, les énergies absolues de surfaces {001}, {136}, {114}, et d'interfaces abruptes et compensées de GaP/Si sont déterminées par des calculs de théorie fonctionnelle de la densité. L'étude des propriétés de mouillage de GaP/Si permet ensuite de démontrer que le mouillage total n'est jamais atteint dans ce système, quel que soit le potentiel chimique, et que cet effet est renforcé par la passivation de la surface du Si. Les calculs de variation d'énergie libre montrent l'importance des termes de surface et d'interface par rapport au terme d'énergie élastique dans la croissance 3D III-V/Si. Ces résultats sont généralisés à l'ensemble des systèmes III-V/Si. Un mécanisme pour la croissance III-V/Si est proposé pour clarifier les premières étapes de la croissance et expliquer la génération de défauts tels que les domaines d'antiphase, qui est reliée aux propriétés de mouillage partiel du système. Des études expérimentales ont été réalisées pour comprendre l'influence de la surface initiale du silicium lors de la reprise de croissance III-V. Ensuite, une étude préliminaire de l'efficacité de marqueurs AlGaP sur l'annihilation des parois d'antiphase et une première caractérisation des leurs propriétés électriques sont présentées. Enfin, une ingénierie d'énergie de surface est utilisée pour la réalisation d'une surface de GaP texturée, intégrée sur silicium, pour des applications dans le domaine de l'énergie.

Title : Surface and interface contributions to III-V/Si hetero-epitaxial growth: Theory and Experiments

Keywords : Silicon photonics, 3D-growth , III-V/Si, GaP/Si, thermodynamics, DFT,

Abstract: This thesis aims to investigate thermodynamic properties and epitaxial processes at the very early stages of GaP on Si heterogeneous growth for photonics and energy applications. The absolute {001}, {136}, {114} surfaces energies and abrupt and compensated interface energies of the GaP/Si material system are first determined by density functional theory (DFT) calculations. Furthermore, we studied the wetting properties of the GaP/Si through the surface and interface energies computed by DFT. We found that the partial wetting (observed experimentally) is always achieved whatever the chemical potential, and that it is even favoured by the silicon surface passivation. Through free energy change calculations, we have shown that the surface and interface energies play a crucial role in the III-V/Si 3D- growth while the impact of elastic energy contribution on surface island morphology is negligible. These conclusions are generalized to the various III-V/Si systems. A general III-V on Si growth mechanism is finally proposed to clarify the very early stages of growth and the defect generation (such as antiphase domains) that fundamentally originate from the partial wetting of III-V on Si. Experimental studies have been performed to understand the influence of the initial silicon surface on the III-V overgrowth. Furthermore, preliminary studies on AlGaP markers efficiency on antiphase domains annihilation and a first characterization of their electrical properties are also presented. Finally, surface energy engineering was used to demonstrate a textured GaP template monolithically grown on silicon that could be used for photoelectrochemical water splitting applications.